NUMERICAL EVALUATION OF ACOUSTIC GREEN'S FUNCTIONS

A thesis submitted to the University of Manchester
for the degree of Doctor of Philosophy
in the Faculty of Engineering and Physical Sciences

The University of Manchester

2014

Adrian R. G. Harwood

School of Mechanical, Aerospace & Civil Engineering

Contents

Word count approx. 52,400

List of Tables

List of Figures

The University of Manchester

Adrian R. G. Harwood
Doctor of Philosophy
Numerical Evaluation of Acoustic Green's Functions
December 10, 2014

The reduction of noise generated by new and existing engineering products is of increasing importance commercially, socially and environmentally. Commercially, the noise emission of vehicles, such as cars and aircraft, may often be considered a selling point and the effects of noise pollution on human health and the environment has led to legislation restricting the noise emissions of many engineering products. Noise prediction schemes are important tools to help us understand and develop a means of controlling noise. Acoustic problems present numerous challenges to traditional CFD-type numerical methods rendering all but the most trivial problems unsuitable. Difficulties relate to the length scale discrepancies which arise due to the relatively tiny pressure and density fluctuations of an acoustic wave propagating over large distances to the point of interest; the result being large computational domains to capture wave behaviour accurately between source and observer. Noise prediction may be performed using a *hybrid* Computational Aero-Acoustics (CAA) scheme, an approach to noise prediction which alleviates many issues associated with exclusively numerical or analytical approaches. Hybrid schemes often rely on knowledge of a Green's function, representing the scattering of the geometry, to propagate source fluctuations to the far-field. Presently, these functions only exist in analytical form for relatively simple geometries. This research develops principles for the robust calculation of Green's functions for general situations. In order to achieve this, three techniques to compute Green's functions for the Helmholtz equation within an extended class of 2D geometries are developed, evaluated and compared. Where appropriate, their extension to 3D is described. Guidance is provided on the selection of a suitable numerical method in practice given knowledge of the geometry of interest. Through inclusion of the numerical methods for the construction of Green's functions presented here, the applicability of existing hybrid schemes will be significantly extended. Thus, it is expected that noise predictions may be performed on a more general range of geometries while exploiting the computational efficiency of hybrid prediction schemes.

Declaration

No portion of the work referred to in the thesis has been submitted in support of an application for another degree or qualification of this or any other university or other institute of learning.

Copyright Statement

Acknowledgements

I would like to thank the patience and support of all my family, particularly my wife Kimberley, and also Mum and Dad, who have been there for every step of my long educational adventure and shared every high and low along the way.

Abbreviations

BEM	Boundary Element Method
BIE	Boundary Integral Equation
BVP	Boundary Value Problem
CAA	Computational Aero-Acoustics
CFD	Computational Fluid Dynamics
CHIEF	Combined Helmholtz Integral Equation Formulation
DGM	Discontinuous Galerkin Method
DNS	Direct Numerical Simulation
DRP	Dispersion-Relation-Preserving
DtN	Dirichlet-to-Neumann
FDM	Finite Difference Method
FEM	Finite Element Method
FW-H	Ffowcs-Williams-Hawkings
LBM	Lattice Boltzmann Method
LEE	Linearised Euler Equations
LES	Large Eddy Simulation
MAE	Matched Asymptotic Expansions
NRBC	Non-reflecting Boundary Condition
ODE	Ordinary Differential Equation
POD	Proper Orthogonal Decomposition
PSE	Parabolised Stability Equations
RANS	Reynolds-Averaged Navier Stokes

Nomenclature

a,b	Boundary Values, Interval Dimensions
A	Mathematical Constant
c	Constant, Speed of Sound, Interval Dimension
d	Interval Dimension
$\mathbf{D}$	Diagonal Matrix
f	Mapping Function, Source Function, Frequency
$\hat{G}$, G	Green's Function
h	Sinc Spatial Step Size
$\mathbf{H}$, $\mathbf{G}$	Influence Coefficient Matrices
$H_0^{(2)}$	Zeroth Hankel Function of the Second Kind
i	$sqrt{-}1$, Index
j	Index
k	Acoustic Plane Wave Number, Index
K	Mathematical Constant, Number of Type-3 Elements
l	Principal Dimension of Body
L	Length
m	Number of Sinc Nodes
M	Number of Terms in the DtN Expansion, Lower Limit of Sinc Expansion
n	Number of Vertex Points, Number of Mesh Points, Number of Nodes
N	Upper Limit of Sinc Expansion
p	Index
$\hat{q}$, q	Source Function/Strength, Boundary Value, Index
S	Boundary Surface, Translated Sinc Function
u	General Acoustic Variable
U	Flow Velocity

v, w	Weighting Function
$\mathbf{x}$	Observer Position Vector
$\bar{\mathbf{x}}$	Image Source Position Vector
$\mathbf{y}$	Source Position Vector
$\mathbf{Y}$	Kirchhoff Vector
z	Complex Coordinate in Physical Domain
α	Interior Angle of Polygon
γ_n	Wavenumber for Mode n
Γ	Boundary Curve
ζ	Complex Coordinate in Computational Domain
λ	Acoustic Wavelength
$\hat{\phi}$, ϕ	Velocity Potential, General Acoustic Variable, Conformal Map
$\phi*$	Free-Space Green's Function
Φ	Complex Potential
ψ	Stream Function, Normal Derivative of General Acoustic Variable
$\psi*$	Normal Derivative of the Free-Space Green's Function
ω	Angular Frequency

Chapter 1

Introduction

Awareness of the effects of new and existing engineering products on the environment and on human health is of increasing importance. In the world's cities in particular, the noise due to transport, infrastructure and industry negatively impacts the health and quality of life of the residents [63, 73, 145]. However, the reduction of noise emissions from engineering products can also have important commercial benefits. For example, quieter aircraft may be permitted to take-off and land during times for which these operations are currently prohibited resulting in more flights, and potentially more revenue, for airlines.

Noise is one form of pollution which has only been studied in earnest since the 1950s, largely motivated by an increase in commercial jet aircraft at the time [194]. However, in order to design means of controlling the physical processes involved in noise generation and propagation, it is essential to understand the underlying physical mechanisms. A critical tool which contributes to our understanding of noise emissions is a noise prediction scheme. Such schemes comprise one or more mathematical techniques which aim to achieve two goals:

1. Evolve the behaviour of a noise source at the point of generation over a given time interval;

2. Propagate this computed disturbance through a medium to another location where the noise is observed.

In Chapter 2 we discuss in detail the broad range of mathematical tools which exist to perform these tasks. Results, therefore, can vary widely in their fidelity when

compared to experimental measurements and a robust noise prediction scheme still remains far off. Part of the reason for this limited success is the conflicting demands of real acoustic problems on available analytical and numerical methods alike. Noise prediction schemes are required to find both the hydrodynamic and the acoustic components of the flow. The latter is governed by behaviour of a length scale much smaller than that of the former. Furthermore, the acoustic characteristics must be preserved by the scheme over distances of many acoustic wavelengths. We elaborate on the challenges acoustic problems present to computational methods later (see Section 2.1). Many means of addressing these known issues lead to calculations with prohibitively expensive computational resource requirements and despite the rapid development in computing technology, many realistic noise calculations remain impracticable.

The interaction of sound with complex geometrical features adds a significant degree of complexity to the problem being solved. Noise prediction schemes are therefore often designed to be applied within a simplified local geometry. This facilitates the prediction of a wider range of noise problems with available computational resources. The disadvantage is that scattering effects, including sound absorption, reflection, refraction, are often inaccurately represented. An example would be considering the noise generated by a jet engine attached to an aircraft wing by simply studying the behaviour of a jet of fluid leaving a nozzle. This reductionist approach to the real problem fails to incorporate the scattering effects of nearby fluid inhomogeneities such as the wing wake or shock systems, or of solid surfaces such as the rest of the engine nacelle, wing, pylon, fuselage and ground (if appropriate). There are many real acoustic problems in which these effects dominate the observed sound field and their omission introduces serious inaccuracies into the final solution. However, the results of such simplified studies have contributed significantly to our understanding of particular noise sources which we discuss in more detail in Section 2.1.7.

A particular class of noise prediction schemes, known as hybrid schemes, are capable of incorporating these neglected effects without appreciably increasing the computational demand of the calculation. The scheme consist of two distinct parts, which together, achieve the goals listed above. The part of the scheme responsible for propagating the noise allows for the scattering behaviour of the geometry to be captured in the form of a mathematical function known as a Green's function. Closed-form representations

of these functions are rare and, if mathematically tractable, require significant skill to construct analytically. It is for this reason that hybrid noise prediction schemes are designed such that either the geometry is simplified such that a closed-form description of the Green's function can be obtained for the the problem, or the part of the calculation designed to compute the source behaviour is applied to a wider region of space such that the complex geometry can be represented in the calculation. The former is selected most often as the latter would result in the calculation being prohibitively expensive and introduce a host of potential inaccuracies (see Section 2.1.2). An alternative (touted by Manoha *et al.* [215]) is to approximate the Green's function numerically by selecting appropriate numerical methods, and applying them within the geometry as an additional pre-processing part of the computation.

In order to investigate the feasibility of such an approach, Chapters 5 to 7 present three different methods for the numerical approximation of the Green's function within different classes of geometries. In each case, the method is developed, implemented and validated against a limited number of available analytical solutions. The rationale behind the choice of these particular approaches is discussed in Chapter 4. We first establish the context of this research project and identify its role in the wider activity of noise prediction.

Chapter 2

Noise Prediction Schemes

Here we establish the state of the art of noise prediction and the context of this research. We introduce, in Section 2.1, the methods available to perform noise prediction on aero-acoustic flows, and discuss the influence of the prevalent issues, including the specification and implementation of robust acoustic boundary conditions. We also consider specific applications and the challenges they present. We then specifically focus on the area of particular interest in this research – the calculation and use of Green's functions (Chapter 3) for scattering problems. Based on this discussion, the rationale behind the choice of methods for this research is presented in Chapter 4. A discussion of the literature associated with the chosen methods is given in the corresponding chapters where appropriate.

2.1 Computational Aero-Acoustics

Noise emission occurs in a wide variety of contexts. It is usual to classify noise problems based on either the propagation medium or the type of source. One particular class of noise problem which is of great importance is that of aero-acoustics. Aero-acoustic problems are typified by their sources, which arise due to unsteady air flow. Computational Aero-Acoustics (CAA) is an engineering discipline which aims to simulate the generation and propagation of acoustic fluctuations in fluid flow. Such flows comprise both hydrodynamic flow features as well as the acoustic fluctuations, the latter usually several orders of magnitude smaller in amplitude and of much smaller length-scale. In

many cases of interest, the observer is located in the far-field (a location many wavelengths away from the source itself). The distance over which fluctuations must be propagated is, therefore, typically much larger than the dimensions of the region of fluid responsible for the acoustic source. The aim of CAA is therefore to accurately compute the entire problem from source to observer such that accurate hydrodynamic and acoustic fields may be constructed. There are many schemes available to achieve this goal each with their related strengths and weaknesses. Despite the variety, the methods may be considered as belonging to one of three broad categories, numerical, analytical or hybrid approaches. These are discussed in more detail in the following sections.

2.1.1 Types of Computational Approaches

Many reviews on the subject of CAA have attempted to summarise and, to a certain extent, categorise the variety of methods available to perform acoustic calculations. One of the more recent and clearer attempts is the process flow chart of Colonius & Lele [71] (see Figure 6 therein) which segregates the types of methods based on modelling decisions. Even so, there are many emerging techniques which, due to their present lack of use in the field of CAA, did not find their way into this schematic or any presented in earlier literature. This is addressed here by presenting an alternative illustration of the methods of current and historical practice in Fig. 2.1. Categorisation is undertaken based on the nature of how the method is formulated and subsequently implemented. This was deemed appropriate as many of the practical issues associated with particular approaches are aligned to formulation and implementation. This graphic encompasses not only the numerical implementations of CAA – discretised systems of approximate equations – but also some exclusively analytical approaches which, although numerically implemented, are based on traditional integral formulations. Historically these latter approaches were used to model simple source behaviour and exactly predict wave propagation.

As illustrated in Fig. 2.1, the available methods can either be used in isolation or in combination, with available approaches consisting of:

1. **Exclusively numerical approaches**, which numerically solve some form of a

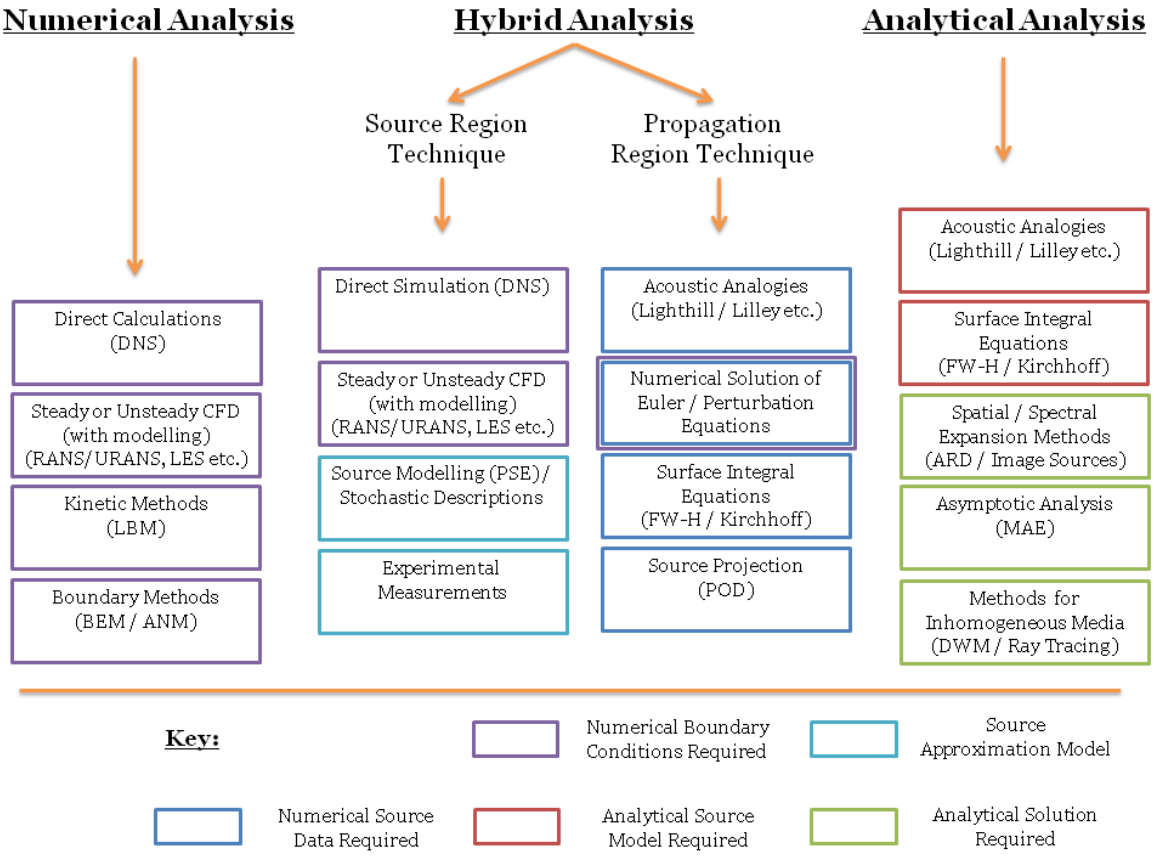

Figure 2.1: Illustration of many of the current variety of techniques available for the solution of acoustic problems

differential equation governing both the hydrodynamic and acoustic parts of the flow,

2. **Exclusively analytical approaches**, which propagate the acoustic radiation from an equivalent source representation or rely on a known form of solution to solve integral formulations of the governing differential equation,

3. **Hybrid methods**, which use the strengths of both types of method by suitably partitioning the domain and using a different method in each sub-domain.

Many studies choose a single approach for application to a particular problem but some initiate comparisons between one or more methods for one particular problem [18, 68, 69, 131, 170, 229, 294, 349] in order to highlight particular issues. In general, the choice of the author to apply one particular method over another is either driven by availability (or not) of computational resources or the lack of certain techniques having been applied to that problem in the past.
For a relatively recent review, which discusses usage of the most popular schemes, see Wang *et al.* [346]. The use of hybrid schemes in particular is reviewed by Bailly *et al.* [19]. We discuss applications of CAA schemes in Section 2.1.7.

2.1.2 Exclusively Numerical Approaches

In exclusively numerical approaches to sound field computation, Computational Fluid Dynamics (CFD) codes are applied to the Navier-Stokes (or a simplified set of) equations to compute the hydrodynamic sources as well as propagate the acoustic fluctuations to the observer. However, acoustic problems present a number of unique numerical challenges to which traditional CFD is poorly adapted. The pertinent issues [71, 77, 313, 314, 317, 318] are summarised below. Of the previous citations, the most recent include a summary of proposed means of addressing the issues (see also Ekaterinaris [96]).
The issues arise due to the very nature of acoustic problems: the propagation of tiny disturbances of potentially high frequency over large but finite distances. Specifically the following difficulties are noted:

1. Simulations must be unsteady throughout which increases the demand on computational resources as data at each time step must be computed and stored.

2. Waves of high frequency must be resolved over the numerical grid without ambiguity (aliasing).

3. The fluctuations being computed are very small – in most cases are of the same order of magnitude as truncation errors of common numerical schemes – hence very high-order schemes with low 'numerical noise' are necessary which often have a large computational stencil. Large stencils can result in a loss of precision at the domain boundary where the grid ends if the method reverts to a lower-order scheme in these regions. The high-order derivatives used in the scheme also require additional boundary conditions to be specified. It may not be possible to define these boundary conditions from the physical problem.

4. Interaction between the acoustic and hydrodynamic parts of the flow can be subtle but crucial to the observed sound field and must be captured by the numerical scheme, increasing demands on grid resolution and quality of modelling.

5. The waves propagate over a large distance and traditional CFD discretisation schemes introduce numerical dispersion and dissipation of the waves resulting in both non-physical solutions as well as an artificial decay of the already small fluctuation over the grid.

6. Since the domain over which the propagation takes place is finite, the truncation boundary (which is a non-physical boundary) must allow the passage of outgoing waves and in some cases, hydrodynamic flow components, without reflection. This can be achieved through the (often complex) implementation of non-reflecting boundary conditions. The boundary conditions are further complicated for problems where incoming waves are also required (see the discussion on boundary conditions in Section 2.1.6).

7. In order to successfully treat flow through or around complex geometries, unstructured meshes and/or overset grid methods may be considered [35]. Although this is not a feature specifically related to acoustic problems and can provide a

cost benefit for many complex hydrodynamic flow problems, their use for acoustic propagation increases the complexity and expense of noise prediction code.

Based on the above list, it is clear to see that the disparity in the length scales of an acoustic problem is the principal source of the issues. The length scale of the source flow features and region itself are vastly different to length scales of the propagating acoustic fluctuation and also the observer distance. Direct Numerical Simulation (DNS) is an approach which requires full discretisation of the governing differential equations of the fluid flow. This discretisation in both space and time must be capable of fully resolving all the length scales of the problem – both the large-scale hydrodynamic flow problem as well as any small-scale turbulent structures and of course the acoustic fluctuations themselves. All of the issues summarised above have been the subject of intense CAA research for some time. In particular, many of the issues have been successfully treated by introducing compact, high-order, spatial and temporal finite difference schemes for DNS. These schemes are designed to preserve the dispersion characteristics of the acoustic waves, use a reduced computational stencil than traditional schemes and exhibit minimal dissipation over the grid. The addition of artificial damping inhibits the growth of spurious waves generated by discretisation, ensuring an uncontaminated solution. The Dispersion-Relation-Preserving (DRP) code of Tam & Webb [316] is a popular choice, and this, as well as others, have been applied with highly accurate results [29, 37, 67–69, 72, 151, 213, 239, 273, 291]. The multi-size-mesh multi-time-step DRP, developed more recently [322] as a flexible extension to the original DRP code, is a means of addressing multiple length scale disparities of flow features by unstructuring the overall mesh; in other words using a uniform mesh in several partitioned sub-domains between which the mesh spacing and time step increase by a factor of two. Further optimisation of the scheme is still being actively pursued with Sengupta *et al.* [286] suggesting improvements to achieve near spectral accuracy and Si *et al.* [293] extending the DRP scheme to curvilinear grids.
To summarise, DNS schemes contain the following features:

1. High-order, low dissipation, spatial and temporal discretisation.

2. A grid providing a minimum number of points per wavelength to resolve even the highest frequency acoustic waves [278].

3. A discretisation which preserves dispersion characteristics and maintains phase information into the far-field.

4. Accurate non-reflecting boundary conditions at artificial boundaries, which must allow passage of all supported outgoing waves while preventing spurious reflections.

Many of the schemes developed to meet these requirements are of high computational cost, with typical aero-acoustic problems taking days or weeks to solve and direct simulations at high Reynolds number being well beyond current super-computing capabilities [338]. Furthermore, for high frequency (small wavelength) problems, very small time steps are required. This is due to the Courant-Friedrichs-Lewy (CFL) condition which, based on the selected spatial resolution of the scheme, defines the maximum allowable time step to ensure numerical stability. The small spacing required to resolve the acoustic waves in a spatial sense also, therefore, guarantees a small time step. This results in prohibitive storage requirements even for relatively short time histories.

Of the DNS schemes cited above, both explicit and implicit time-marching variations have been used. Explicit schemes use the information associated with the current time step to find the information at the next time step, whereas implicit schemes set up an equation involving information at the both current and next time steps, ultimately solving for the information at the next time step. Implicit schemes are especially useful for stiff systems where the time step would be impracticably small for stable solution, although are often more expensive than their explicit counterparts [95].

Despite the disadvantages discussed above, DNS results have helped the visualisation of many complex flows and in many cases improved our understanding of problems which have historically been difficult to treat analytically [39]. Hence, they remain a popular choice for noise prediction for many problems of interest.

As a means of reducing the computational cost associated with DNS schemes where the source flow is turbulent (as is the case in jet noise computations or vortex shedding applications), CFD numerical schemes make use of a turbulence model or description of vortex shedding [17, 21, 25, 30, 89, 271, 319, 340, 343]. Turbulence models improve the performance of the code in terms of execution time since all the length scales of

the turbulence do not need to be resolved by the grid. However, in problems where the turbulence is the principal source of noise, the acoustic field computed is highly sensitive to the quality of the turbulence model. The model must be able to accurately model the unpredictable and chaotic behaviour of the turbulence while capturing the complex interactions between the turbulence fluctuations and the mean flow if present. Also, turbulent eddies are usually convected over large distances and can decay slowly hence the behaviour must be represented over large spatial and temporal extents. Schemes featuring turbulence models, therefore, are often limited to simpler flows or localised regions of a more complex flow as part of a hybrid scheme.

The use of sub-grid scale methods is a useful compromise between DNS and traditional CFD by resolving only a proportion of the length scales of the problem. Large eddy simulation (LES) is a good way of capturing the turbulent/vortical flow features such as those witnessed in jet flows. More recent variations such as the Detached Eddy Simulation (DES) and Very Large Eddy Simulation (VLES) (see reviews by Singer *et al.* [295] and Ekaterinaris [96]), although more expensive than RANS-type modelling of turbulent flows, are still generally seen as a vast improvement on DNS in terms of execution time while maintaining an accuracy not achievable with cheaper approaches. However, use of LES exclusively to compute far-field data is still prohibitively expensive and, as with DNS, has become popular as a component of a hybrid scheme (see Section 2.1.4). A recent review on the use of LES in jet noise prediction is available by Bodony & Lele [36].

Other numerical techniques exist which split the acoustic radiation from the hydrodynamic field and solve the Linearised Euler Equations (LEE) or similar for the former [147, 148]. These kind of splitting approaches have decreased in popularity recently, driven by the recognition of the importance of the interaction between the acoustic field and the hydrodynamic flow field. For example, in the case of cavity resonances, the coupling between downstream scattering and upstream vortex shedding (acoustic feedback) is an integral part of the sound producing mechanism [199]. With respect to the LEE, it is important to recognise, that these equations neglect the physical viscous damping of the acoustic wave due to viscosity. The effects of this omission in terms of wave amplitude will become appreciable for propagation over large distances

and hence their use is generally restricted. Furthermore, the linearisation of the Euler equations used for the solution of the acoustic fluctuation can have a detrimental effect on the stability, since many non-linear stabilising terms are neglected. In fact, the Kelvin-Helmholtz instability, characteristic of shear layer problems, is supported by these equations and can contaminate the downstream acoustic solution as illustrated by Agarwal *et al.* [2]. The equations themselves contain 5 unknown variables – three velocity components, pressure and density. These variables can be grouped to show that the LEE support vorticity waves (velocity fluctuations convected with the mean flow) and entropy waves (density fluctuations convected with the mean flow) [13]. These can perturb the acoustic solution [314], particularly in shear flows where the modes couple with the acoustic modes. Artificial damping, mode decoupling or operator modification has been used in the past to address the problem with Prax *et al.* [256] suggesting source modification as an alternative.

There also exist a number of specially adapted numerical schemes for acoustic problems involving shockwaves, for example in supersonic jets. Numerical schemes need to be able to deal with the inevitable discontinuities in the solution while simultaneously capturing any radiation due to interaction with the shock-cell structures of the flow. These schemes both resolve the acoustic perturbations and maintain stability and accuracy across shock structures using MUSCL or (Weighted) Essential Non-Oscillatory ((W)ENO) or similar schemes in the neighbourhood of shock structures [53, 103, 153, 203, 298]. Lo *et al.* [200] use a shock-detection scheme to 'switch on' specific schemes in the neighbourhood of a shock and revert to standard LES elsewhere for a supersonic jet problem.

Finally, there are the more recent inclusions in the field, for example the Lattice Boltzmann Method (LBM). LBM is a numerical scheme based on the Boltzmann equation describing particle kinetics [58]. The LBM originated in the computation of 'Gas Automata' and the motivation behind applying it to fluid mechanics is that the macroscopic behaviour, observable in terms of flow features, is always driven by the microscopic behaviour of the material, which can be captured and related to macroscopic behaviour by the method. The actual numerical scheme used in practice is a simplified version of the full particle tracking algorithm to both maintain efficiency and eliminate statistical noise, and achieves an accuracy comparable to existing methods

for many applications to date.

Lew *et al.* [190] list the advantages of using LBM over conventional methods as:

1. Convection operators are linear – simpler discretisation;
2. The strain rate tensor (rate of change of fluid deformation) may be directly found – physically important quantity in understanding turbulent motion;
3. The methods are suitable for complex geometries due to the absence of Jacobians;
4. The algorithms are amenable to parallelisation.

However, they go on to say that for high Reynolds number flows, many of the models break down, although new formulations are becoming available to address these short-comings.

The LBM was first used for the simulation of acoustic waves by Buick *et al.* [51]. They describe the LBM as being able to deal with the length scale disparity of acoustic problems better than most traditional methods. Furthermore, boundary geometrical complexity has little effect on the efficiency of the method. A subsequent investigation by Crouse *et al.* [79] applied the method to a group of model acoustic problems. Their results indicate that for short propagation distances, the numerical dissipation is insignificant making LBM a good *local* means of solution. As the simulations were terminated before waves contacted the boundary, the quality of the boundary conditions were not investigated. The investigation into the LBM's potential for solving acoustic problems was then extended by Brès *et al.* [48]. This paper demonstrates that the method still suffers from a non-physical rate of dissipation but that it can be controlled to a degree by adhering to the resolution guidelines given. More recent advances due to Xu and Saugaut [357] improve upon these earlier formulations and hence LBM is fast becoming a popular means of treating noise-generating fluid flow [1, 49, 217, 287, 342, 351] and is recommended by [79] for fluid-structure interaction problems. The algorithm may also be coupled to turbulence models to allow application to jet noise problems [190]. In the context of this work, LBM can be seen as an alternative numerical scheme which, despite suffering many of the same drawbacks as finite-difference-based approaches, can be massively parallelised giving it a significant advantage in terms of execution time. However, the still method lacks accuracy and

robustness after long-term time evolution [48].

Although the limitation in terms of computational resources is a significant restriction on the use of exclusively numerical schemes, improved means of implementation have been recently pursued to address this. Hermite methods [11] are a means of implementation which lend themselves to parallelism – critical in the current environment of multi-core computing. They are methods which operate many times on local data and are relatively easy to implement. The most attractive feature is the ability to provide more arithmetic operations per memory access reducing the dependence on fast data transfer. The 'von Neumann bottleneck' (limit of data transfer rate between processor and memory) of 'exascale computing' is requiring a shift in 'algorithm mentality' and is the principle motivation for the development of Hermite methods [11]. Furthermore, Appelö *et al.* [10] state that Hermite methods can be combined with discontinuous Galerkin methods (such as the Boundary Element Method) to handle boundary conditions in a straight forward fashion. In the long term, it is suggested that LES and DNS are likely to provide a viable means of predicting the noise from large-scale turbulent structures in jets, since with the increasing computer power, DNS can be applied at higher and higher Reynolds numbers. However, the use of alternative techniques are always likely to be faster and hence universal use of exclusively numerical schemes is not expected.

2.1.3 Exclusively Analytical Approaches

The analysis of acoustic problems analytically remains important in the field of aeroacoustics as many analytical methods present an explicit description of the physical mechanisms of sound production and interactions obscured by many numerical calculations. A number of classical analytical techniques may be used to describe acoustic problems. One of the most useful and popular tools is the acoustic analogy. An acoustic analogy is an inhomogeneous differential equation written in a form which separates the propagation of the acoustic disturbances from the sources of these disturbances. With the acoustic disturbance being represented as a fluctuation about the relevant mean flow variables, the governing equation may be rearranged to produce a wave-like operator on one side of the equation and the remaining terms on the other side. The former governs the propagation of the disturbance from source to observer while the

latter are interpreted to be sources of the acoustic radiation. The first acoustic analogy was proposed in Lighthill's landmark 1952 paper [194] where the Navier-Stokes equations describing a fluctuating acoustic disturbance in a fluid flow were rearranged to form a linear wave equation. The wave operator on one side described the propagation, while the remaining terms were then viewed by Lighthill as the sources of sound in the fluid flow. Manipulating the source terms further allowed Lighthill to express them as the double divergence of a single quantity referred to as the 'Lighthill stress tensor'. The double divergence nature of the source term indicated that it was of quadrupole form.

Lighthill's analogy is built on the assumption of radiation into a quiescent medium – in other words the propagation takes place in a region with zero mean flow – as indicated by the linear wave operator. In addition, all the non-isentropic and viscous effects are incorporated in the source terms within the stress tensor. However, many applications of Lighthill's analogy omit the viscous terms (high Reynolds number of the fluctuation assumed) and assume isentropic behaviour leaving a single component of the stress tensor remaining. Under these assumptions, the physical interpretation of the analogy therefore reduces to that of a compact region of turbulence radiating linear density waves into the surrounding inviscid, isentropic, homogeneous fluid. Since its publication, there have been a number of numerical studies on this simplified problem alone [276, 352] where Lighthill's analogy has been used as a canonical result to assess the accuracy of the numerical procedures used.

Although this formulation appeared initially ideal for the study of jet noise [195], there are issues with analytical implementation due to the difficulty of expressing the stress tensor contents analytically [349]. Proudman [257] describes low Mach number, isotropic turbulence using statistical approach using dimensional analysis. This early attempt at describing the source analytically illustrates that qualitative results are possible with such approximate representations but in the absence of suitable experimental or numerical data, analytical source models for real acoustic sources are unlikely to produce results suitable for quantitative comparison.

Furthermore, more subtle flow effects are absent or at least disguised in the Lighthill source term which precludes a more universal application of the analogy. For example

the analysis by Ffowcs-Williams [117], omitting the presence of shockwaves, demonstrates a breakdown of Lighthill's 'eighth power law' [194] for the variation in jet noise with jet velocity as well as the description of the source as quadrupole when the mean flow is of high speed. This analysis concludes that the nature and efficiency of the source are dependent on the implicit cancellation of components of Lighthill's source term which can be difficult to calculate and are sensitive to inaccuracies.
Subsequently, there have been extensions or reformulations of Lighthill's analogy to explicitly account for different acoustic scenarios. Most notably by

- Curle [81] – considers the amplification and scattering effects of stationary solid bodies;
- Ffowcs-Williams & Hawking [119] – developed while studying the noise from helicopter rotor blades and practically incorporates the effects of moving bodies;
- Howe [156] – a reformulation of the problem in terms of vortex sound sources using the vortex sound theory approach of Powell [255];
- Phillips [253] – written in terms of a convected wave operator which separates out the non-linear convection and refraction effects, which would otherwise have to be described in the context of Lighthill's stress tensor;
- Lilley [196] – includes entropy convection omitted by Phillips;
- Goldstein [133] – a generalisation of a number of the previous analogies.

Goldstein's analogy [133] provides a more general approach to the construction of an acoustic analogy by splitting the governing equations into base flow and fluctuating flow components. The resulting equations are linearised Navier-Stokes equations with modified variables. The analogy is made between the fluctuations in a real flow and the linear inviscid fluctuations about an arbitrary base flow produced by appropriate stress and heat flux. These latter two terms are the source terms of the analogy, defined by the particular base flow selected. A number of base flows are considered by Goldstein with the uniform base flow shown [132, 133] to reduce the generalised analogy to the analogy attributed to Lilley [196].
The vortex sound formulation of Howe is a more suitable formulation for problems

involving vortex shedding [221]. Vorticity may be approximated by application of the Kutta condition and so a vorticity-based source is easier to predict than the turbulence-based source of Lighthill's analogy. Furthermore, the faster decay of vorticity over turbulence reduces the extent of the noise source itself. The time taken to compute the source may therefore be reduced as a rapidly decaying source restricts the size of the source domain. Crow [80] considers the effect of the size of the turbulent eddies on noise emission. He concludes that the analytical evaluation of the source integral required by applying Lighthill's actually becomes intractable if the source region becomes non-compact (in terms of the length of a turbulent eddy) due to the divergence of the integral.

The practical advantages of writing an acoustic analogy in terms of the stagnation enthalpy (as in vortex sound formulations) are considered by Doak [87] (and references therein). Stagnation enthalpy is seen as being the best choice of 'generalised acoustic field'. In other words, according to Doak, representing an acoustic problem in terms of the stagnation enthalpy allows the generation of an exact analogy with a convected wave operator on one side of the equation and a number of sources on the other. Crucially, these source terms are considered 'optimal' in that they represent distinct, local physical processes as best as possible. The variation presented by Doak, therefore, has many practical benefits over Lighthill's original analogy for more general flows where, in the latter, "physical processes such as refraction and/or diffraction of the sound waves in the actual fluid domain...are represented by a highly redundant set of 'equivalent quadrupole sources' in a fictitious 'classical acoustic' medium" [87].

There is also the issue of compliance with any underlying assumptions of the theory used to construct the analogy (i.e. the assumptions and modelling concerning the source and the medium through which the acoustic disturbance is propagating). Assumptions are usually made about the flow such that governing equations are reduced in complexity to a form more amenable to analytical solution. Knio *et al.* [180] show that the simplifying assumptions introduced by the acoustic analogy may actually over-simplify the source model and introduce errors in the acoustic calculations. The lack of availability of analytical expressions in many real cases, combined with a large number of simplifications, preclude the use of analytical techniques in isolation on many realistic problems. Specifically, those problems whose sources include turbulent

features may find that an accurate representation of the source in terms of analytical constructs is impossible. However, as was the case with Proudman [257], even simplified analytical techniques can provide useful qualitative insight into a number of complex phenomena. The discrete vortex model of Dai *et al.* [82] provides a qualitative description of the non-linear effects associated with the sound-vortex interaction of slits. The analytical results compare well with DNS results, only deviating in absolute values. The viscous effects absent in the analytical potential model are assumed, based on the agreement of the results, to not be a dominant absorption mechanism for high-intensity sound.

The application of analytical procedures to model problems is still an important exercise [77] in terms of providing a sound means of validating any new numerical methods. When applied to model problems, many analytical methods can be used to find an analytical expression for the radiated sound field. There are principally two ways of achieving this goal:

1. By representing the source field as a series of unsteady structures for which an analytical expression is available [118, 158, 180, 188]. Thus, an integral formulation, based on, for example, an acoustic analogy, can be used to find the value of the acoustic variable under consideration at an observer location (see Chapter 3);

2. Some form of known solutions to the equation subject to the given boundary conditions (eigenfunctions or fundamental solutions) can be superimposed to construct a solution to the overall field [3, 78, 366].

In the latter case, for more complex geometries, it is not uncommon for asymptotic solutions to be considered based on frequency or proximity to the source region or scattering geometry (near-field and far-field solutions). These asymptotic solutions may then be matched at some intermediate position using the method of Matched Asymptotic Expansions (MAE) [78, 188].

In the former case, when applying a suitable acoustic analogy, an integral method of solution has the significant advantage of requiring just a single integration to arrive at the value of the acoustic variable at a particular observer location [289]. However, as will become clearer later (Chapter 3), the success of using integral methods to solve acoustic analogies is limited by the availability of descriptions of the kernel of

the integral. Therefore, although the mathematical rigour and inherent accuracy of analytical approaches are highly desirable, the difficulties described above preclude their exclusive use for realistic acoustic problems.

2.1.4 Hybrid Approaches

The difficulties associated with numerical and analytical schemes are avoided with the use of hybrid schemes. These schemes combine the strengths of numerical approaches with elements of the analytical approaches to enable the accurate computation of complex source fields, as well as radiated acoustic fields, without significant computational cost. There are numerous configurations of hybrid schemes available, each of which are characterised by the combination of techniques used as illustrated by Yang *et al.* [359]. In general, the computational domain is partitioned at some near- to mid-field location and the source region, encompassing all complex flow features, is solved using a numerical procedure such as high-order CFD (specifically RANS or LES) or directly using DNS. The data, known on the boundary between the two domains, are then used as source data in an analytical method in order to rapidly and accurately propagate the sound to a far-field observer. Historically, hybrid schemes define the transition boundary between the source region and propagation region such that a linear wave equation, governing a region bereft of scattering surfaces, applies beyond the source region. The boundary conditions of the problem in this propagation region are simply ones of free-space – a radiation condition only. If the propagation region contains scattering features, we must consider a modification to traditional procedures to ensure this scattering behaviour is represented. One means of achieving this is the focus of this work.

2.1.4.1 Integral Propagation Techniques

Integral methods are one method which can be used to obtain the sound field given source information. In the general sense, these methods consider the integral of the governing equation (for example Lighthill's analogy) over the bounded acoustic medium. For the sake of this discussion, we assume the problem is three-dimensional and the integral is a volume integral. The application of Green's second theorem yields an integral equation which expresses the acoustic variable (usually the pressure

or density in the case of Lighthill) in terms of the sum of an integral over the volume and an integral over the bounding surface. Here, the acoustic variable is evaluated at a given observer location. Physically, the volume integral represents the sound due to the sources within the volume whereas the surface integral represents observed sound passing through the volume which has been generated outside the boundary.
The specification of the boundary conditions to be satisfied by the integral kernel (elaborated on in Chapter 3) is instrumental in defining special cases of this general integral equation. We consider in the following sections the two cases where the boundary conditions are defined such that a) the volume integral vanishes and b) the surface integral vanishes.

2.1.4.1.1 Surface Integral Techniques We may choose to define the boundary between source and observer regions such that it encompasses all the sources. In this case, the boundary conditions on the surface can be defined such that the surface acts as a Kirchhoff [7, 121, 131, 189, 211, 214, 370] surface. In this integral approach, the associated surface integral formulation is solved for the radiated sound field in the domain beyond the boundary using known values of the acoustic field on the surface. The advantage of the Kirchhoff approach is that it is straightforward to write down and relatively efficient to compute. Lyrintzis [212] provides details on the use of the Kirchhoff integral method for sound propagation. Furthermore, Kirchhoff surfaces can be either stationary or moving [114, 115].
The Ffowcs-Williams-Hawkings (FW-H) equation is a similar approach [45, 49, 119, 167, 200, 338, 364]. The principal difference between this and the Kirchhoff approach is that the FW-H formulation is derived from the governing equations directly, rather than a general linear wave equation as in the case of Kirchhoff. In fact, it may be considered a particular implementation of Lighthill's acoustic analogy. In this sense, FW-H may be considered to be an acoustic analogy itself although, in its most basic form, requires only a surface integral rather than the volume integrals typical of other acoustic analogies.
One particular advantage of the FW-H representation is its ability to propagate non-linear flow effects while imposing fewer restrictions on the placement of the surface. It is possible to define the bounding surface such that it does not completely encompass

all the source terms. In this case, the integral formulation is known as the porous (or permeable) formulation [36, 49, 131] and the volume integral reappears alongside the surface integral in the integral equation. This approach is popular for jet noise problems as the non-linear components of the turbulent jet are convected for some distance downstream and the source region would become impracticably large if the entire source region were to be surrounded by the integration surface. Furthermore, the source fluctuations would need to be accurately propagated through the source region to the surface itself. However, the porous formulation has an increased storage requirement, due to the increased data required, compared with the standard formulation. Alternatively, the surface may be left open with modifications to the formulation [121].

If a downstream boundary is used for the FW-H surface, it is known, in the context of jet noise problems, as the outflow disc, and is usually placed within the jet such that turbulent structures exit the source region through the disc. For simplicity, the volume integral, which would incorporate the effects of these exiting eddies on the radiated sound is neglected. This practice can be detrimental to the results: Spalart & Shur [303] and Mendez *et al.* [225] examine the effects of different configurations of the FW-H procedure on the radiated field. The porous surface concept has also been used to extend the Kirchhoff approach by Pilon & Lyrintzis [254].

The use of these surface integral techniques for propagation reduces the size of the source region and hence the expense in performing a source calculation on an extensive region. In particular, the FW-H method allows the surface to be placed within non-linear regions of flow which allows the source region to be reduced further still. However, in order for the volume integral to vanish, both methods require accurate acoustic information to be available on the surface itself with accurate predictions only possible if this information is complete and precise [161]. The tools available to perform this source region propagation are usually the same numerical methods used for the hydrodynamic calculation and hence are susceptible to numerical error (see Section 2.1.2). Hence, the positioning of the surface as well as the quality of the source computation impacts the accuracy of the boundary data and hence the accuracy of the surface integral propagation behaviour. Singer *et al.* [296] remark that the further away the surface is placed the more time (and distance) the dispersion and

dissipation errors of the source scheme have to degrade the source information, and hence a tighter surface is better.

Finally, the difficulty of generating accurate information from the source region on the artificial surface is more pronounced for the FW-H approach than with the Kirchhoff method. Specifically, the FW-H integrals require a greater amount of accurate source information than the Kirchhoff approach (more than 3 variables including one in time compared with the 2 variables of the Kirchhoff method) [315]. A more generalised approach to using Kirchhoff or FW-H, which can obviate the need for a rotating surface, is to use a frequency domain boundary integral propagation step as used by Yang *et al.* [359].

2.1.4.1.2 Volume Integral Techniques Another possibility in the propagation region is the use of an appropriate acoustic analogy. As alluded to in Section 2.1.4.1, these may be solved using the integral approach. Many acoustic analogies rely on setting the boundary conditions of the general integral equation such that the surface integral vanishes. The integral equation governing the observed sound simplifies to just a volume integral over the source region. Numerous examples of their use are available [17, 18, 21, 30, 68, 69, 89, 132, 147, 172, 177, 187, 189, 199, 214, 215, 235, 263, 267, 270, 276, 281, 294, 311, 319, 340, 344, 345, 349, 352]. Although the increase in dimensionality of the integration may be seen as a disadvantage when compared with surface integral techniques, source calculations using the acoustic analogy may not require the same degree of discretisation of the source region necessary for accurate integral method surface data, making them cheaper.

As with all hybrid schemes, however, a degree of interpolation is necessary to pass data between the source region and propagation region which can be a source of inaccuracy [177]. Furthermore, all integral methods discussed here rely on a Green's function (the kernel of the integral) for their evaluation. The availability of this function is a limitation of the approach and is responsible in many cases for the restriction of the propagation region to one of free-space (see Chapter 3). We aim to directly address this restriction with this research. Other issues with the use of acoustic analogy approaches have been discussed already in Section 2.1.3.

2.1.4.2 Other Hybrid Variations

A less common approach is to combine the source computation with another numerical scheme [33, 112, 113, 181, 202, 214, 256, 325, 343]. Such a numerical-numerical scheme is an exception to the numerical-analytical definition of hybrid methods used here. The advantage of coupling two numerical schemes is the ability of such schemes to be applied within complex geometries is retained. Furthermore, the flow in the two separate regions may differ and hence different numerical methods may be appropriate. However, for really complex geometries, an unstructured mesh is required whose generation may be computationally expensive and a challenge to implement [33]. Here, Birkefeld & Munz [33] use a DRP-based DNS code for the source region coupled to a Discontinuous Galerkin Method based on the Linearised Euler Equations (LEE) for the propagation. The coupling between the two meshes and associated methods is relatively complex. Despite this, the overall accuracy of the coupled schemes is at least as good as the schemes in isolation. Quantification of the increased computational workload, however, is not reported.

More complex hybrid schemes have been known to make use of the LEE as the governing equations in a mid-field region in order to reduce the computational load of LES or DNS in the source region. A traditional acoustic analogy is still used for the far-field propagation [214]. Mincu & Manoha [228] use an implementation that is more complex with multiple codes interfacing with one another across two sub-domain boundaries. In their case, performing the scattering calculation as an additional step adds further complexity and time to the overall calculation. Given these disadvantages and subsequent advances in computing resources for DNS or LES calculations, time will tell whether such tri-domain acoustic computations will be phased out. However, in a review focussed on aerofoil noise prediction [325], such methods are still included as a typical configuration.

One disadvantage of hybrid schemes highlighted by Sandberg and Jones [273] in their justification for choosing an exclusively numerical approach, is that the use of a multi-domain, multi-technique method can exclude acoustic feedback loops between the radiated sound and the source. Therefore, the type of schemes used and the location of the interface must take into account such behaviour. Bailly *et al.* [19] and previously Singer *et al.* [295] provide more detail on the use of hybrid schemes.

2.1.5 Other Methods

Other methods are available which offer improvements for specific noise-generating flows. One of a number of approaches designed to improve modelling of turbulent sources is Proper Orthogonal Decomposition (POD) [65, 120, 140, 272]. This approach allows partial modelling (reduced order modelling) of turbulent sources by considering the most energetic modes radiated by coherent structures in the turbulent field. These modes may then be simply extrapolated to an observer location. Decomposition of DNS source data, coupled with Galerkin projection of governing fluid equations onto the modes extracted using the POD procedure, has grown in popularity since 2000. These methods show promising signs in matching up to experiment over short time evolution but not necessarily over a longer period [272] for noise generation in a shear layer. In the results of Rowley *et al.* [272], the long-time inaccuracies are attributed not to a lack of instability modes considered, but the failure to account for the spreading of the shear layer due to the growth of the oscillations themselves. In order to improve the coverage of the POD modes, Colonius and Freund [65, 120] have performed further studies which attempt to determine an optimum set of modes to consider in order to accurately represent the bulk of the noise radiated.

In addition, the use of Parabolised Stability Equations (PSE) to model a turbulent noise source in terms of the radiation from large-scale instability wave structures has been studied [140, 267]. The work of Rodriguez *et al.* [267], in particular, demonstrates that when a PSE model is used as the source within an acoustic analogy, the radiation computed is in good agreement with experimental measurements and DNS reference solutions. However, the use of parabolic equations are limited by being able to march forward in time only. This results in reflections not being considered which for many problems can be a significant source of error [13]. More detail on the PSE approach is given by Colonius *et al.* [70] and we discuss jet noise applications of PSE in Section 2.1.7.

There are a number of situations for which simplification of the acoustic problem to one satisfying an acoustic potential function allows a number of alternative methods to be used. One such method also involves the use of a Green's function and is known as the Green's function discretisation method. It is a low-cost method which constructs derivatives of the acoustic potential from a superposition of particular wave-equation

solutions known as free-space Green's functions. These assembled functions are used as shape functions to interpolate nodal values over a grid. The specific assumption made for the duct problem studied by Casalino *et al.* [52], is that although the duct is varying longitudinally, the local flow is considered uniform and acoustic fluctuations may be expressed in terms of a velocity potential. Errors are several orders of magnitude higher than many advanced numerical schemes but still of the order 10^{-2} and required only 3 points per wavelength to resolve the waves. In addition, excellent dispersion characteristics are maintained – both benefits due to the use of the Green's function basis.

The Green's function discretisation includes the fundamental solution of the problem as part of an existing numerical method. It is a special case of the broad class of 'physics-based methods'. Physics-based methods are advantageous in that they include some aspect of the underlying physics of the problem in the application of the numerical method. For example, if the solution to a problem is expected to represent a physical wave, the approximate solution may be expressed in terms of an expansion of a wave-like solution such as a Bessel [208] or Fourier series rather than a series of generic polynomials. Luostari *et al.* [208] use a Bessel series basis as part of a FEM formulation. Despite being slightly more expensive, the inclusion of the Bessel series basis significantly increases the robustness of the method by countering ill-conditioning of the constituent matrices. The work of Singh *et al.* [297] illustrates how the inclusion of a Green's function may contribute to improving the robustness and accuracy of an existing method.

Gabard *et al.* [122] discuss the potential of three physics-based methods available for aero-acoustics. In particular they consider the Green's function discretisation method, the Partition of Unity FEM (PUFEM) and the wave-based discontinuous Galerkin method (DGM). The PUFEM is an extended FEM commonly used in fracture mechanics, which includes enrichment functions to more accurately represent the local physics in a domain and is a cheaper alternative to refining the mesh. The set of physics-based DGMs (the Boundary Element Method may be considered an example of a DGM – see Chapter 6), use wave-based interpolation functions within elements (plane waves, Bessel functions, Hankel functions for instance), to provide more accurate interpolation of the solution. As a result, fewer elements are required for a given

accuracy. Due to the reduction in points per wavelength of physics-based methods, the overall cost of noise calculations is reduced. However, the constituent matrices are often poorly conditioned which requires a careful choice of solution procedure.

Recently, Hahn and Negrut [142] examined the potential of Smoothed Particle Hydrodynamics (SPH) for acoustic applications. Meshless methods easily deal with inhomogeneous media and moving complex boundaries, two things traditionally challenging for mesh-based methods. Furthermore, non-linear behaviour such as resonances, can be captured without modification unlike many linear acoustic methods based on, for example, linear Acoustic Perturbation Equations or LEE. The results of the study show that there is notable sensitivity to both smoothing length and boundary condition quality; the former causing non-physical dissipation. The latter are responsible for inducing a non-physical noise into the results which worsens over the time period. Despite these obvious drawbacks, their results indicate that qualitative studies of short duration are viable.

Finally, there are methods concerned more with 'auralisation' of the sound field rather than specific aero-acoustic details. The process of auralisation is a process which aims to generate audio which mimics the experience of the observer listening to sound in a particular acoustic space. Uses could include virtual reality applications such as computer games. Since the sources are provided as input signals, such methods are of limited use for investigation in physical mechanisms of sound generation. However, they may be used as a rapid, albeit crude, means of propagation and scattering. The most common method is that of Adaptive Rectangular Decomposition (ARD) [258] which breaks the propagation space into a number of rectangles within which eigenfunction expansion solutions are known analytically. When executed numerically on Graphics Processing Units (GPUs), using impedance boundary conditions on sponge-covered walls (see Section 2.1.6), the method is described as "the fastest time-domain solver for modelling the room acoustics of large, complex 3D scenes" [222]. This technique results in little dispersive error compared with Finite Difference approaches and uses a reasonably coarse grid. ARD may be considered a suitable algorithm for the rapid computation of low-fidelity solutions if desired.

2.1.6 Boundary Conditions

One of the significant difficulties mentioned earlier in applying discrete numerical procedures to acoustic problems is the control of the solution behaviour at the boundaries. For many acoustic problems, the computational domain often contains one or more infinite boundaries. For many methods, it is, therefore, necessary to truncate the domain at a suitable, finite location and define an artificial boundary along with an artificial boundary condition. This boundary condition must behave such that it allows outgoing waves to pass out of the domain without reflection (and, if appropriate, incoming waves to enter). Such boundary conditions are termed non-reflecting boundary conditions (NRBCs).

For problems of practical interest it often impossible to define and/or implement an exact NRBC; even the most precise analytical representations require some degree of approximation during implementation – usually the truncation of an infinite series [178]. Hence, a number of different NRBCs have been developed since the field of CAA began in the 1950s [130] with a view of balancing the accuracy of the boundary condition with the cost of implementation. Successful implementation of NRBCs for acoustic problems is subject to ongoing research and remains an unsolved problem. In hybrid schemes, it is an issue particularly relevant to the calculation of source behaviour, a task often performed using numerical methods within a sub-domain bound by an artificial boundary. Assuming the Green's function is found using one of the methods of Chapters 5 to 7, accurate source behaviour is still required to be able to compute the observed sound field. Hence, it is necessary to discuss the available NRBCs in more detail.

Of course, the specification of an artificial boundary could be avoided altogether; the problem could be transformed entirely from an infinite domain to a finite domain using some kind of mapping. However, Grosch & Orszag [136] show that this approach is only useful for a class of problems where the solution either tends rapidly to zero or a constant as infinity is approached. If the solution oscillates at infinity, as is the case for many wave problems, the technique exhibits large errors.

In addition to NRBCs, other boundary conditions are also necessary for acoustic problems including impedance conditions and inflow/outflow conditions. We discuss all types in this section.

Broadly speaking NRBCs fall into the following categories with some categories only appropriate for certain solution methods:

1. Characteristic & Expansion-based
2. Boundary Integral Formulations
3. Infinite Element Methods
4. Absorbing Layer Methods (also called sponge layers or buffer zones)

2.1.6.1 Characteristic & Expansion-based

In this section, prescriptive means of representing a non-reflecting boundary condition are explored. First, there are the characteristic boundary conditions of Thompson [326] as used by a number of authors [153, 188, 203, 272, 273]. These boundary conditions are developed through the method of characteristics. Considering the waves as characteristics allows incoming and outgoing waves to be treated separately. In order to allow outgoing waves to leave the domain without reflection, the incoming wave characteristic may be set equal to zero. Hence, Thompson uses the premise that the amplitude of the incoming waves must be constant in time, and applies this condition to the incoming characteristic. This is another way of saying that there are no incoming waves as if there were, they would be time dependent. Of course, the restriction of this boundary condition is that if a problem requires an incoming wave, as in scattering problems, this condition cannot incorporate it. Thompson develops the boundary conditions in this way in both one and two dimensions and they are implemented by rewriting the governing equations in characteristic form.

Expansion-based methods of developing NRBCs rely on knowledge of the form of the exact solution on or beyond the artificial boundary. This presents a practical disadvantage as this information is not always available *a priori*. These boundary conditions may be developed by considering asymptotic forms of this solution, perturbations about the solution, or by considering integral formulations on the boundary. Where these boundary conditions differ from those we discuss in the next two sub-sections is in their implementation. Here we consider boundary conditions which are represented as one or more differential equations and directly incorporated into the global numerical scheme, be it FDM or FEM or something else.

How the boundary condition is to be implemented numerically often has a significant bearing on their effectiveness. Two main types of numerical implementation exist: local and non-local. Local boundary conditions couple each boundary node to a small number of its neighbours. These conditions are significantly cheaper to implement than the non-local conditions but rarely achieve comparable accuracy, although local boundary conditions of high order have recently been developed [130, 337]. Non-local boundary conditions are capable of remarkable accuracy although couple every node on the truncation boundary. This non-locality applies in both space and time for time-dependent problems and storage requirements may become prohibitively large. Despite the apparent expense of non-local boundary conditions, there are a number of applications where they are affordable as we discuss below. Local approximations are often developed from non-local boundary conditions in order to circumvent the practical difficulties of their implementation. For example, Barucq *et al.* [20], make use of the exponential decay of higher-order modes to develop accurate local approximations, in prolate-spheroidal coordinates, to the non-local Dirichlet-to-Neumann operator (see below).

One of earliest attempts of developing NRBCs was that of Engquist and Majda [107]. Specifically designed for finite difference applications, the authors first develop the underlying non-local representations and then subsequently develop local approximations such that small errors in the initial boundary data do not give large errors in the solution and the resulting difference scheme remains stable. These conditions are generated from a sequence of pseudo-differential operators with the first in the sequence, being of lowest order, achieving the poorest performance with a large number of spurious reflections of outgoing waves. As the order increases, the boundary conditions become more computationally demanding but more accurate. One recurring problem with the Engquist and Majda conditions is the restriction that the wave to be transmitted must be normal to the boundary with grazing incidence waves generating large reflections. They therefore require the transverse wave number to be much smaller than the normal wave number, which is not always practical.

Subsequently, an improved sequence of boundary conditions for wave problems was proposed Bayliss and Turkel [22, 23]. Similar, but improved conditions in polar coordinates were also suggested by Grote and Keller [138]. These conditions also use a

sequence of boundary operators which are used to annihilate unwanted terms on the boundary. The higher the order of the boundary condition used, the more terms are annihilated and the better the exact boundary condition is approximated.

The boundary conditions used by Colonius *et al.* [66] based on the work of Giles [128] are some of the more common boundary conditions used as well as those accompanying the original DRP derivation [293]. In the former case, the original boundary conditions are developed by considering Fourier decomposition of the solution on the boundary. Appropriate coefficients are set to zero in order to exclude incoming waves from the solution at the boundary. This representation is exact for the case of linear waves. Due to the impracticalities of implementing this original form, Giles proceeds to develop local approximations.

Exact boundary conditions for wave problems were also developed by Ting and Miksis [328] who considered the Kirchhoff formula (an integral formula – see below) on a spherical boundary surrounding a scatterer. Although an exact boundary condition initially, in order to minimise the time history required for its evaluation (typical of hyperbolic problems), the condition was modified to be local in time. The exact boundary conditions of Ting and Miksis were seen to exhibit a long-time instability and were improved by Teng [324]. A similar approach is presented by Givoli [129] for exterior scattering problems solved using FEM. This time, the non-local space component of the boundary condition is generated using a Dirichlet-to-Neumann map [178]. This type of approach has been pursued for different problems by others [137] and has been seen to be highly accurate where it has been implemented.

Non-local boundary conditions based on the Dirichlet-to-Neumann (DtN) operator can be developed by considering a known solution in the region beyond the artificial boundary. Often, this region is considered to be one of free-space containing no sources such that only the homogeneous governing differential equation applies. The solution is usually known analytically for these cases and may indeed be expressed as an infinite series of eigenfunctions, depending on the differential equation. Differentiation of this solution produces an expression for the solution in terms of its normal derivative at the boundary. This expression defines the DtN operator. Since the solution in the computational domain reduces to the homogeneous solution beyond the artificial boundary, the DtN operator can be used to match the two solutions at the artificial boundary,

thus providing the additional boundary conditions required to close the system. There are a number of classes of problem for which the region beyond the artificial boundary is not free-space. For these problems, the geometry beyond the artificial boundary may still be one within which the solution is known analytically [146] and hence an analytical DtN operator may still be constructed. For the Helmholtz equation, the DtN operator is available in a number of coordinate systems [138]. It is typically represented in terms of Fourier integrals although She and Lu [290] represent the DtN boundary condition as a fictitious source distribution (similar to the method of images described in Section 3.3.1 but with sources of arbitrary location and magnitude).

Although the DtN operator is exact, it is often an infinite series representation and practically must be truncated when used as part of numerical methods. The truncation of the series can result in non-uniqueness [178] and also problems at the artificial boundary with essentially eigenfunctions not included in the truncated series being set equal to zero [246]. For wave problems, this is a particular issue as spurious reflections are generated for these eigenfunctions (modes). Harari *et al.* [146] provide guidance on the minimum number of terms to be retained in the expansion to minimise these effects. Specifically, all propagating modes must be retained. They also provide an alternative solution in the form of the modified DtN formulation [138] which improves convergence of the series and automatically addresses the issues with truncation. Where the number of terms retained is large, the boundary can be placed very close to (or indeed in) complex regions, such as a scattered wave field, which minimises the overall size of the computational domain.

Most DtN applications are associated with Finite Difference (FD) or Finite Element (FE) procedures [173, 246], with the form of DtN being amenable to incorporation into variational formulations. However, as observed in [178], the non-local nature of the boundary condition removes the favourable sparse nature of the FEM stiffness matrices, increasing the overall cost of the method. More advanced applications of DtN consider multiple truncation boundaries with the DtN condition allowing both the necessary incoming waves from the other sub-domain as well as the outgoing waves from its own [139]. NRBCs may also be used in setting up matching conditions for sub-domain algorithms [106] such as the Schwarz Alternating Method (SAM) used with

both FEM-BEM coupling and multi-domain Sinc methods (see Chapter 7). A comparison between non-local and local boundary conditions is performed by Deakin and Rasmussen [84], who demonstrate both the increase in accuracy and computational demand for non-local conditions over local approximations.

2.1.6.2 Boundary Integral Formulations

For problems featuring a closed infinite domain boundary (an exterior problem) a boundary integral method may be used to solve the problem in the domain by considering only the internal boundary and hence a NRBC is not needed. However, for problems featuring one or more infinite boundary sections or when using a domain method, NRBCs are required and may be represented as integral equations to be solved along with the domain equations. These boundary conditions may be included by considering the solution at the closed boundary at infinity. If an incoming wave is present, this may be incorporated through the simple addition of the incident quantity to the formulation [354]. Alternatively, a hybrid approach may be used which uses a boundary integral formulation as a boundary condition but coupled to a domain method. Examples of such problems use a combination of FEM and BEM in a hybrid procedure [165, 207, 288, 369] to allow accurate specification of a truncation boundary for the FEM. The hybrid approach utilises the strengths of both of the methods but, due to the expensive of applying FEM to a large domain, would be an expensive treatment of acoustic problems. A review of FEM-BEM and FEM-DtN coupling can be found in [124].

For the application of boundary methods to semi-infinite problems, the DtN operator may be incorporated as part of a BEM to close the domain and define an interior problem [135]. The inclusion of the DtN operator in this way, shares similarities with the natural boundary integral formulation [360, 361] which when used for exterior problems, may be easily coupled to FEM for the interior problem. Furthermore, it can be used to reduce the hyper-singularity of some boundary integral formulations [244]. The development of boundary methods for the calculation of Green's functions, and the use of DtN NRBCs to close a domain, is discussed in more detail in Chapter 6.

2.1.6.3 Infinite Element Methods

Another approach used to treat semi-infinite problems is to use infinite boundary elements [27] for BEM or the FEM analogue of infinite domain elements [26, 368], which may be interpreted as regular finite elements which include far-field enrichment functions [122]. These elements are usually of linear order or higher where one of the nodes is placed at infinity and special shape functions interpolate the variation of a parameter over the semi-infinite element. These shape functions decay in the infinite direction based on a user-specified function associated with a known or expected solution. The principal weakness of these conditions is that the correct specification of the decay function relies on knowledge of a solution *a priori* which may or may not be known. For wave problems, this decay function is usually a wave function which allows for incoming waves as well as the decay of outgoing waves [365].

2.1.6.4 Absorbing Layer Methods

Throughout the literature on direct computation of acoustic flows using FD schemes, boundary conditions are consistently selected from either sponge layers or exit-zone grid-stretching regions, or a combination of the two [2, 7, 49, 50, 66, 68, 69, 72, 172, 177, 181, 190, 200, 202, 203, 258, 259, 271, 273, 323, 329, 338]. Sponge-layers (also known as buffer-zones) are designed to damp out physical or non-physical waves crossing the truncation boundary by implementing artificial damping in that region. These are often used in combination with grid-stretching which involves gradually coarsening the grid through the sponge-layer to deliberately lose resolution of the waves such that they vanish as the grid becomes unable to support them. The Perfectly Matched Layer (PML) [28] is a particular type of absorbing boundary condition useful for where the region beyond the boundary is free-space [177, 222, 258, 323]. Designed to replace previous matched layer attempts, the PML has no dependency on the direction of approaching waves. The region precisely matches the acoustic medium at the boundary to prevent reflections at this location. It then varies its properties throughout the layer such that the acoustic radiation which passes into the layer is damped out. The disadvantage of many of the sponge-type boundary conditions is the complexity of implementation. The benefits of sponge layers is highlighted in [171].

2.1.6.5 Other Boundary Conditions

Other necessary boundary conditions include wall/impedance boundaries common in room or underwater acoustics [216, 258, 308] and may also be the source of spurious wave reflections and the introduction of a non-physical, numerical boundary layer [317]. For realistic acoustic problems, internal walls are unlikely to be perfectly acoustically rigid or flexible but instead are characterised by an impedance. An example of a common impedance condition is that of Myers [13, 52]. Redon *et al.* [264] provide an application of both a DtN NRBC as well as the Myers impedance condition for realistic duct acoustics. However, current impedance models are not universally valid, with Roche *et al.* [266] demonstrating their breakdown when incident sound levels are of large amplitude. This is principally due to the linearised nature of current impedance models which fail to capture the non-linear acoustic-flow interactions which are of increased importance for high-amplitude acoustic waves. A simple and novel means or representing internal walls of finite impedance is the Impedance Mismatch Method (IMM) of Chung & Morris [62]. Finally, of specific importance in jet noise calculations, are inflow boundary conditions which can accommodate entrainment [7, 36] or the start of the jet itself if the nozzle is not included in the internal geometry. For the latter case, the boundary condition needs to be capable of representing jet-nozzle interaction effects, something which, specifically where directivity effects are concerned, has been highlighted as a short-coming of earlier attempts [7, 172]. A review of boundary conditions for infinite domains may be found in [336].

2.1.7 Applications of CAA

Owing to an increase in available computing resources, applications of even the most computationally demanding CAA codes are becoming more common. However, to date, many demanding CAA calculations (such as those involving DNS) have only been applied to solve so-called 'model problems' – in other words computation of the sound field generated by isolated fluid structures in space [77]. Problems of higher complexity not only require more powerful processors to ensure execution time remains practical, but they also require increased data storage and memory as the number of mesh nodes and the density of information increases. However, CAA applied to model

problems provides us with not only the predicted noise of the studied flow feature but also, through the computed flow field, an understanding of the behaviour of a variety of often complex hydrodynamic flow features. This latter benefit not only allows validation of the numerical calculations against experimental or theoretical work but also potentially provides an insight into the physics of combinations of model problems.

Typically model CAA studies involve vortical flows, for example the scattering due to an isolated vortex or vortex-pair interaction [72, 188, 229] which is compared to the original analytical work on vortex sound by both Möhring [226] and Powell [255]. These articles contribute to the understanding of more complex vortical flows such as the turbulent jet, an application we discuss in more detail below. Another common class of problem is the study of vortex shedding from a sharp edge [215, 345] or the interaction of a shed vortex with a body [211]. The former cases cited compare their results to the analytical conclusions of Ffowcs-Williams & Hall [118] on the structure of the radiated sound and the role of amplification of the sharp edge. This class of model problem is particularly well-suited to analysis using Green's functions as Ffowcs-Williams & Hall demonstrate. This model problem is relevant when considering the more realistic application of aerofoil self-noise (see below). The generation of noise due to the presence of a single shockwave within a flow [53, 203] presents additional challenges to CAA codes but incorporates noise sources of particular importance for fans and supersonic jets.

The study of model problems, for which analytical solutions do not exist, using highly resolved numerical schemes may also provide a high-fidelity solution containing information difficult to obtain from experiment. DNS results have been recorded as benchmark solutions which may not have an analytical expression, thus extending the database of solutions with which new code may be validated. A typical example is that of jet noise, see the introduction of Lo *et al.* [200] and references therein. Furthermore, DNS has been used to identify the source of behaviours for scenarios where analytical models are either difficult to accurately construct or the effects of the simplifications are unknown: for example, the resonance of a ducted jet [329], and the behaviour of micro-cavity absorption [50]. The latter case concludes that the features neglected by the analytical model are of little importance, with the DNS results interpreted as a means of validating the analytical approach. This highlights the potential danger of

using analytical solutions as a means to validate code as many analytical solutions were derived under a number of assumptions to simplify the mathematics. In cases where the CAA code being applied aims to resolve the exact governing equations of the fluid (as in DNS), these assumptions may not be met and the analytical solution becomes unsuitable as a benchmark. Due to the diverse nature of different CAA codes, and the lack of a solution of high-enough accuracy, many of the same problems have been recycled, particularly in the case of jet noise where the precise mechanisms of radiation have been under debate for some time (see below).

2.1.7.1 More Realistic Applications

Since 2000, there have been attempts to apply CAA codes (particularly those based on DNS) to more complicated situations, potentially ones which can be considered to represent more realistic scenarios such as noise in ducts, engine intakes and fans [4, 228, 237, 266, 320, 321, 323, 340, 364, 370], and the coupling involved in resonant cavities [131, 249, 271] and combustion [311]. Astley [13] provides a recent review of available methods and their application to studies concerning the components of a turbo-fan engine. Furthermore, largely driven by the introduction of the jet engine and 'super-jumbo' aircraft, there continues to be a large number of CAA studies which focus exclusively on jet noise of heated and unheated jets at both sub- and supersonic Mach numbers [7, 17, 18, 30, 38, 172, 181, 187, 254, 259, 263, 319, 338, 343]. Boundary layer [50, 237, 270, 345] and mixing layer noise [19, 66–69] are also well-studied due to their role in airframe noise which is of particular concern during aircraft approach.

2.1.7.1.1 Aerofoil Noise Aerofoil noise is a dominant source for wind turbines [248] and, in light of advances in the noise reduction of jet engines, is now considered to be a significant contributor to the overall noise of aircraft on approach. The source of this noise is attributed to the unsteady flow past complicated airframe components such as high-lift devices and landing gear. In order to contribute to the understanding of the former, the 1989 report by Brooks *et al.* [47] presents 5 identified mechanisms of aerofoil self-noise – the noise due to interaction between an aerofoil and its own boundary layer or wake [273]. These mechanisms are identified as:

- Boundary layer turbulence passing over the trailing edge

- Stalled aerofoil flow (including separated boundary layer noise)
- Vortex shedding (due to laminar boundary layer instabilities)
- Vortex shedding due to trailing edge bluntness
- Turbulent vortex flow at the tips convected donwstream (tip vortices)

Of these 5 mechanisms, the first 4 involve interaction with the aerofoil trailing edge and are hence termed trailing edge sources. From the work of Ffowcs-Williams & Hall [118], it is accepted that the scattering effect of the trailing edge causes significant amplification of the sound and hence there are a number of numerical and analytical studies involved in testing noise reduction strategies including the use of brushes [150] and serrations [273]. Analytical representations of the acoustic source associated with the convection of turbulence over the trailing edge of an aerofoil is typically based on the linear theory of Amiet [5, 6], improved by Christophe *et al.* [61] to include near-field scattering effects. Amiet's original theory [5] computes the unsteady body force of the aerofoil based on the classical formulation of Curle [81] and idealises the geometry to that of a flat plate. Amiet [6] then extends the theory to account for the convected turbulence component of the noise and concludes that this contribution is small for a typical trailing edge but is likely to be more significant for sharper edges or trailing edge flaps. For this reason, for aerofoils of large to infinite span, the agreement between this theory and experiment for a body of turbulence, unmodified as it passes over the trailing edge, is reasonably good. Hence, it has remained a popular choice for the prediction of trailing edge noise and related problems [282]. In addition to Amiet's approach, other approaches have been considered including an analysis based on the compact Green's function [161] (see Section 5.1) and an acoustic analogy by Howe [156]. This analysis was performed both for a flat plate and a simple rounded trailing edge. Despite attempts to analytically model trailing edge sources in particular, the real problem includes a contribution from a number of sources which many analytical models will struggle to incorporate entirely. Furthermore, sources of noise in addition to the 5 outlined by Brooks *et al.* [47] have been identified in experiments and DNS studies (see Sandberg & Jones [273] and references therein).

Hybrid schemes can offer an effective means of examining different configurations of

such problems. A relatively recent hybrid study on a slat-wing configuration by Singer *et al.* [296] uses a combination of RANS and the porous FW-H method to compute the radiated sound. Such simulations are significantly cheaper than the experimental equivalent, which is shown by Oerlemans *et al.* [248] to be a significant undertaking for wind turbine applications in particular.

2.1.7.1.2 Sub-/Super-sonic Jet Noise By far the largest category of CAA studies is that of jet noise. Since the introduction of Lighthill's analogy, there have been a large number of investigations which have developed alternative analogies through reformulation of Lighthill's original expression as well as new theories to describe the generation and propagation of jet noise: specifically to take into account the interaction of acoustic radiation with the non-uniform hydrodynamic flow obscured in Lighthill's source term. The mechanisms of jet noise are still not understood precisely from first principles and whilst in general it is accepted that sound is generated by both large-scale and small-scale structures within the turbulent jet, the mechanisms of radiation and which of the two sources dominates remains a subject of debate. The large-scale pairing of vortices in isolation, originally studied as a model problem, was one of the original models of jet noise challenged by Bridges & Hussain in 1992 [46]. Descriptions currently available range from Lilley's acoustic analogy for turbulent shear flows [196] to Tam's 2-source model [319], challenged by Morris and Farassat [235]. There are a number of studies which model the source using wave-packets [54, 70, 262, 267] where the growth and decay of instability waves within the jet align well with measured Mach wave radiation in supersonic jets. This idea agrees with the earlier suggestions that this radiation is caused by the supersonic convection of turbulent eddies [17, 21, 117, 253]. In addition, the temperature of the jet is also known to affect the decay of the radiation with some numerical experiments specifically demonstrating this behaviour [7, 225].
Noise associated with shock systems in supersonic jets may be broadly considered to be a combination of discrete tones (screech tones) and broadband shock associated noise. Attempts to model the latter analytically were made by Harper-Bourne and Fisher [149] with results in good agreement with experimental data for the particular jet configuration of interest. Numerical CAA techniques have been applied including the use of DRP [153], where, as expected, due to the abruptness of the shock, convergence

of the method is slowed by the increasingly small time steps. Andrè *et al.* [8] present experimental measurements on the effects of nozzle slots on the radiated shock noise which highlights a Mach number dependence on their noise reduction effectiveness.

2.1.7.2 Far-Field Scattering

It may be noticed that, for all the applications mentioned above, the radiated (far-field) sound is considered to be in free-space (i.e. in a region of space unobstructed by surfaces capable of scattering the acoustic waves). This free-space simplification cannot be universally applied in reality, particularly in confined geometries, or geometries which remain complex into the far field. Current practices are unable, in any reasonable amount of time, to compute the scattered sound field in these cases. This is due to the fact that the scattering effects of any geometry, currently must be computed by a CFD-type numerical scheme, such as those used in the the source region part of a hybrid calculation. Therefore, in many cases, the domain of numerical schemes is extended to include the features of the problem responsible for the scattering.
Alternatively, numerical-numerical hybrid schemes can be used where a more appropriate integral-based method can treat the complex geometry as well as the complex flow. For example, currently the study of wing-slat combinations is important in the context of airframe noise, see for example [32]. In this paper, the authors deal with the complex geometry of the problem by using RANS on a small source region and then incorporate a discontinuous Galerkin solver for the far-field which now includes the scattering contribution of the wing and part of the slat. However, the execution is still relatively expensive, with the meshing of the propagation domain still a requirement. Boundary-integral or source-volume-integral techniques cannot currently be employed to propagate the sound for this type of problem due to the lack of a suitable integral kernel to incorporate the scattering effects. The means of achieving this would be to construct a Green's function which satisfies the boundary conditions of the propagation geometry, specifically those on arbitrary scattering surfaces or at flow features. In this way, the Green's function takes into account the scattering behaviour of a specific geometry and may be used as a suitable integral kernel to compute the propagation using a single integration. This project can directly address the current issues associated with obtaining these Green's functions by providing an efficient and robust means

of numerically computing them (in 2D initially). These numerical Green's functions may then be used as part of existing integral solution methods to allow application of hybrid CAA codes to a greater variety of situations. The expensive CFD-type numerical methods may then be restricted to a concentrated source region, with an integral approach being used to propagate the sound to the observer. In the next chapter we examine the role of Green's functions in more detail.

Chapter 3

Green's Functions in Acoustics

The scattering of acoustic waves in engineering problems is one of crucial importance for many applications from fluid mechanics to seismology. The presence of solid boundaries in an acoustic flow is known to affect the waves through scattering and amplification effects. The theory of Curle [81] captures the fundamental reflections from surfaces by means of representing the surface as a distribution of additional sources in the flow. Furthermore, the analytical study by Ffowcs-Williams & Hall [118] demonstrates a coupling between acoustic disturbances and the surface not included in the representation of Curle. Finally, the use of MAE by Crighton & Leppington [78] for a turbulent source, and then Crighton [75] for a moving vortex, demonstrates clearly the amplification effects of sharp edges and scattering bodies. The former study in particular revises Lighthill's free-space eighth power law estimate [194] to one involving the sixth and third powers of velocity due to the change in nature of the source from the quadrupole of Lighthill to the more efficient dipole form. In this chapter, we discuss how scattering effects may be incorporated precisely while propagating sound sources through use of Green's functions.

All acoustic analogies, as inhomogeneous differential equations, can be solved using an integral method. As described in Section 2.1.4, this approach initially yields an integral equation expressing the acoustic field variable in terms of a volume integral and a source integral. A particular configuration of this general case causes the surface integral to vanish and the solution may be expressed as the volume convolution between a specialised function (kernel) known as a Green's function and the inhomogeneous term (source term). This Green's function satisfies a special form of the

differential equation of interest, usually referred to as the 'Green's function form' or 'singular form', whose source term is a Dirac delta function. Physically, this singular form of the differential equation governs the field produced by an idealised unit point source. The Green's function is actually a function belonging to the broader class of 'fundamental solutions' of the original differential equation. This Green's function not only satisfies the Green's function form of the differential equation, but also a given set of boundary conditions. Therefore, for a given acoustic analogy, any number of Green's functions exist depending on the boundary conditions chosen. These boundary conditions do not necessarily need to be equivalent to the corresponding boundary conditions of the original problem. When these boundary conditions are the same as the original differential equation describing the physical acoustic problem, the resulting Green's function is termed the *exact* Green's function. However, this terminology can cause confusion as although the Green's function is exact in the sense that it is *exactly* equal to the boundary conditions of the physical problem, in a calculation the function itself may be represented approximately. For example, if the exact Green's function is represented by an infinite series, practically we truncate the series in the numerical calculation. In this sense we use an approximate representation of the exact Green's function.

Physically, for the wave equation subject to the radiation condition, this Green's function solution may be interpreted as the outgoing wave solution of the problem for an impulsive point source located at a specific position. The integral representation may be derived by applying integration to both the original differential equation as well as the Green's function form and then combining them using Green's second theorem. This method of solution gives the acoustic analogy and other integral representations a significant advantage over exclusively numerical approaches: In terms of execution time, the far-field sound data may be computed from a single integration of the source data and the Green's function (see the appendix of [76] for example). Furthermore, the use of the Green's function precludes the need to mesh the propagation domain and avoids numerical approximation of the solution behaviour on and inside the domain boundary. The use of this technique remains efficient, even for singular source behaviour, when combined with accelerated convolution methods (see Beylkin *et al.* [31] and references therein). However, for general geometries, this advantage only exists if

the Green's function itself can be constructed – a task often requiring significant skill. Methods of solving integral equations (and hence differential equations) using Green's functions may be considered to be a fundamental part of the mathematics of differential equations. The method has existed for many years and has been put to good use in a wide variety of fields although may not have been referred to by name. However, the versatility of the general theory is rarely exploited with popular methods using readily available Green's functions rather than developing new ones. The fundamental solutions used in the Boundary Element Method for instance are in fact equivalent to the free-space Green's function, though this link is seldom made explicitly.

In terms of acoustic problems, the power of the Green's function approach is its ability to separate out the source and propagation effects. Therefore, the singular form of the differential equation may be solved to obtain a description of the scattering of a particular geometry regardless of the nature of the sources. Knowledge of the Green's function therefore can give preliminary details about a particular problem before expensive prediction methods are then employed for a given source configuration. In general, the scattering of waves within arbitrary geometries may, subsequently, be easily incorporated into the acoustic field solution for a given source, something which even the latest numerical methods struggle to achieve. Although Colonius's 2010 paper [70] criticises acoustic analogies for lacking a universal source representation, it does recognise that even new numerical approaches in the near-field have difficulties in including the role of complex geometries in source models, particularly the inclusion of nozzle geometry for jet flows [172] – something the Green's function is capable of doing in a precise manner.

3.1 Green's Function and Hybrid Schemes

Current hybrid CAA schemes may be extended beyond the scenarios for which the propagation region is free of any boundaries responsible for scattering of acoustic radiation. The presence of scattering boundaries would not be problematic for the Green's function solution method if the Green's function for the problem can be found either analytically or numerically. Furthermore, after computation of the Green's function for a particular geometry, the hybrid scheme may be executed numerous times for

a variety of flows without the need to re-compute the Green's function. This is a significant advantage over the use of exclusively numerical approaches which may require costly re-meshing for each new simulation. This highlights the versatility of the Green's function insomuch as the Green's function itself is not dependent on the source of the differential equation but merely the operator and boundary conditions. A number of Green's functions exist in closed analytical form for acoustic radiation problems where there are no boundaries to scatter the sound between the source and the observer. Such Green's functions are called free-space Green's functions and are used extensively in the propagation step of current hybrid schemes. However, there are few exact Green's functions available in analytical form for problems involving scattering boundaries, noted by, amongst others, Kaltenbacher *et al.* [177]. This is due to the unique properties of the Green's function which lead to their construction being a highly complex, and in many cases intractable, mathematical procedure. Furthermore, the Green's function approach to solution requires knowledge of the source terms. Realistic sources are unlikely to be represented analytically but as discussed in Section 2.1.4, numerical methods are readily available for the specification of source data, hence the only requirement is the specification of the Green's function. Despite the work of Howe [163] and others on Green's function derivation for specific problems where the free-space Green's function is unsuitable (see [311] and later references on Green's function construction), the catalogue of analytical Green's functions remains difficult to populate and currently no robust method exists for the numerical specification of the Green's function. This research establishes a portfolio of robust methods to this end.

3.2 Acoustic Application of Green's Functions

Since the use of Green's functions belongs to the general theory of differential equations, it can be applied to a range of problems. There are many analytical studies which use Green's functions for the solution of different governing equations in a variety of geometries (including free-space) [76, 115, 157, 159, 169, 174, 205, 226, 247, 253, 308, 310, 332, 348]. These applications include the use of the BEM, which relies on

relatively simple analytical expressions for the free-space Green's function as a fundamental solution to the equation being solved. In terms of aero-acoustic problems we usually require the Green's function for the wave equation or the reduced wave equation (Helmholtz equation), with or without a mean flow. Many scattering problems for which Green's functions are given analytically usually involve only simple geometries such as the scattering by a cylinder [157, 170, 234, 366]. As is clear from the work of Morris [234], the need to find the exact Green's function for the geometry can be avoided if the incident and scattered fields are treated separately and then matched at the boundary of the simple shape to form the appropriate boundary condition. In such cases, only the free-space Green's function is needed for the two separate fields. However, there are limitations to the extent to which such analytical matching techniques can be applied (see below). Green's functions are not necessarily restricted to Green's function integral approaches but have been used as a basis (each Green's function centred at a mesh node) for the construction of shape functions for a low-cost domain method known as the Green's function discretisation technique [52] (see also Page 41 in this document).

3.3 Methods of Construction

There is only a small amount of literature available concerned with the theory and application of Green's functions as remarked by a number of authors [110, 186]. Methods of constructing Green's functions, when consulting this limited literature, are found to be largely problem-specific [93]. However, a set of standard mathematical tools may contribute to the construction, such as Fourier transforms for wave problems and Laplace transforms for time-dependent problems. However, a common obstacle in such cases is computing the inverse transform [192]. For more details on possible mathematical tools see [88] and references therein.

Given the lack of a universal method this research explores three methods which we select in Chapter 4. As the Green's function depends only on the geometry and its boundary conditions, it may be computed during a pre-processing step and stored once for a given acoustic geometry. As such, once it is known for a particular geometrical configuration, the same Green's function can be used time and time again

with a variety of source flows [339, 347], reducing the time taken to conduct a set of geometrically similar studies. Existing CFD-based methods of noise prediction used in many design processes do not have this capability with a re-meshing of both source and propagation domains generally required for a change in the flow field within or around a component.

3.3.1 Analytical Green's Functions

Although there are no universal methods of constructing Green's functions there are a number of situations, where exact Green's functions, which apply in a domain with boundaries, may be defined analytically. A number of these may be computed from integral representations [110, 111]. Also, one advantage of knowing the free-space form of the Green's function analytically is that simple boundary configurations (such as the infinite half plane) can be represented quite easily as a superposition of two free-space forms where one of the Green's functions represents an 'image source'. The image source method of Green's function representation is very common for room or rectangular cavity acoustics [3, 168, 251, 308] where the boundaries tend to be flat surfaces, perpendicular to one-another. The Green's function represented using the image source method in cases with two or more parallel boundaries is generally an infinite series due to the repeated reflections required [242]. Practically, the series must be truncated in order to evaluate the Green's function numerically. However, the convergence of this particular infinite series representation is often very poor, precluding its use without modified evaluation procedures as discussed below.

Multi-pole expansions of analytical representations can have important computational advantages, particularly when applied to boundary integral methods [60] (see Chapter 6). The modification of boundary integral methods using such expansions of analytical Green's functions allows boundary methods to remain competitive, even when compared with existing fast solvers for wave problems such as those based on the Fast-Fourier Transform (FFT).

3.3.2 Series Representations

The lack of computer-friendly forms of a lot of series-based Green's functions has been the motivation behind much research since the late 1990s. Melnikov and Melnikov [224], in particular, present a means of addressing the issues surrounding the computability of the typical double-Fourier series representation for the Helmholtz equation in a rectangle. Lattice sum representations of Green's functions for periodic domains are similar in form to an image source infinite series but, as shown by Dienstfrey *et al.* [86], can be evaluated more quickly and more accurately than their image source counterparts. Accuracy close to floating point precision can be achieved. However, they are often hampered by conditional or slow convergence [168, 197, 198, 233]. There are a number of other techniques available to either mitigate or circumvent the problems posed by the evaluation of infinite series. Practically, the series cannot be evaluated numerically in its entirety; hence a degree of approximation is introduced by truncation of the series. The number of terms required to achieve an acceptable accuracy can still be prohibitively large. Fortunately there are means to accelerate the convergence of such infinite series: Ewald's method is a particularly common approach which is highly effective at improving the convergence of these expressions [168, 175, 233, 251, 274, 275]. This technique splits the existing series representation of the Green's function into two parts using an arbitrary splitting parameter. Integration may then take place over the two parts both of which exhibit exponential convergence. Huang and Jiang [168] show convincingly that when compared with a modal expansion of the Green's function, far fewer terms are needed by the split series of Ewald's transformation than by the single modal expansion. A discussion of suitable parameter selection may be found in Arens *et al.* [12]. The likelihood of producing a robust algorithm capable of constructing an exact image source representation of the Green's function for arbitrary geometries is remote, although the approach may indeed be more suitable that most others for geometries with parallel sides.

3.3.3 Problem-Specific Construction Techniques

In order to facilitate many of the more *ad hoc* construction procedures, assumptions can be introduced (or properties evoked) which reduce the complexity of the problem

but still allow an exact Green's function for the new problem to be found. Green's functions satisfy a number of properties [186]. In the spatial sense, the Green's function is a function of both the position of a 'source' and an 'observer' (interpreted in an acoustic context). One key property is that of symmetry, known physically as reciprocity; the observer and source locations of the Green's function are interchangeable. Hence, the computation of the Green's function can be simplified by considering the positions exchanged. This concept, in some cases, greatly simplifies the construction of the Green's function [163]. Some problems involving differential operators which are not self-adjoint (e.g. the convected wave operator) can be modified to allow use of the concept of reciprocity. Recently both Alonso & Burdisso [4] and Tam *et al.* [315] have made use of the adjoint problem and the associated Green's function known as the adjoint Green's function. Of course, if the differential operator were self-adjoint, the Green's function and the adjoint Green's function would be equivalent. Other modifications include the 'surface Green's function', which functions in the same way as the usual Green's function but with the source function being distributed over the surface surrounding the source region rather than being distributed as points within it [216].

It may be possible to make assumptions about the physical domain to simplify the problem for which the Green's function is desired, for instance by allowing some imposition of quasi-periodicity [175, 184, 185, 198, 233]. One particular class of problem pertinent to acoustics are those which consider the scattering by a compact body or geometrical feature [157, 161]. We discuss this class of problem in more detail in Section 5.1. Alternatively, the domain or equation may be transformed or modified under assumptions to simplify calculation [152, 176, 236, 367].

Although it seems a viable procedure to simply transform the governing wave operator into something more manageable such as the conformally invariant Laplacian operator, there are a number of issues associated with attempting to transform operators. For example, the introduction of a further spatial dependence as remarked by the review of Meinke [223]. Hong & Goodrich [152] successfully apply a transformation under the condition that the boundary curves are altered only by a small amount such that the kernel of boundary integrals remains small. The application of transmutation (the mapping of one equation onto another) by Gilbert *et al.* [127] is a similar

approach. It removes some of the difficulties of using the Parametrix method [123], used previously to construct approximations to Green's functions by generating an approximately equivalent pseudo-inverse differential operator. Exact representations are rarely obtained using such methods and the number of situations for which the resulting Green's functions are accurate are limited by the restrictions imposed by the validity of the transformations involved.

Embree & Trefethen [105] use the novel approach of numerical conformal mapping as a means of facilitating Green's function calculation, albeit it for the simpler case of Laplace's equation. They define an algorithm which can be used to find the Green's function for the 2D Laplace equation within a geometry characterised by a number of bodies which sit symmetrically on a horizontal line through the domain. However, the algorithm uses a bespoke sequence of conformal maps and is largely inextensible to a broader range of geometries. The Green's functions developed in this project are far more general than this attempt.

3.3.4 Other Methods of Construction

There a number of less popular methods for Green's function computation which have generally been applied to Laplace's equation in the context of potential problems. By their very nature, Green's functions are problem specific and hence the functions can in fact be constructed without the need for a standardised method, as long as the result satisfies the properties of the Green's function and meets the needs of the integral method to be used. For example, the use of the Liènard-Wiechert potential coupled with a bespoke parametric method [57] or super-lattice construction [16].

There is also the possibility of reconstructing Green's functions from measured field data, sometimes referred to as 'Green's function extraction' [302]. See also Colombi *et al.* [64] and references therein. This approach is useful when the Green's function for a previously designed geometry is required. Since experimental measurements are required, the use of the Green's function is these cases would be more retrospective than predictive.

3.4 Green's Functions in other contexts

Due to obvious similarities, the wave equation in many areas of physics can be solved using Green's functions. Of particular interest are the methods used in other research fields to arrive at a Green's function for a given situation whether analytically or numerically. Early field computation using integral techniques in the context of electromagnetic waves can be traced back to the work of Garabedian [123] and beyond – the obvious difference between this realm and the that of acoustic waves being the transverse nature of waves in the former and the potential for polarisation. Luo *et al.* [206] have recently proposed a boundary integral technique for electromagnetic scattering which utilises a suitable Green's function for the problem. Furthermore, Torabi *et al.* [330] use a novel means of constructing the Green's function for a dielectric medium. The technique decomposes the domain and builds the global Green's function from local analytical representations which is shown to form part of a numerical solution method both accurate and quick. In part this is due to requiring no numerical integration.

Similarly, Green's function-based scattered field calculations can be found in electrical and electronic engineering [141, 155]. Due to the equivalence of (inverse) differential operators and matrices, the former citation makes use of a particular form of Green's function called the 'dyadic Green's function'. The dyadic Green's function takes into account the directivity the source points and is specifically necessary when dealing with vector sources and vector fields. It is, therefore, regarded as a 'higher-dimensional' Green's function in the same way a tensor is 'higher-dimensional' vector. This dyadic Green's function is also used by a number of other authors is similar contexts [251, 339]. Gysen *et al.* [141] use conformal mapping (see Section 5.2.1) to transform the governing equation, which in this case is Poisson's equation. The problem considered is one subject to periodic boundary conditions, a necessary restriction for the success of the method.

A more unusual Green's function application is that of Treeby & Cox [332] who derive a Green's function for a wave equation incorporating power-law absorption (representative of the absorbing behaviour of biological tissue). This is a similar application to the development of the Green's function for a linearly inhomogeneous medium by Li

et al. [193].

Another common research field in which acoustic waves reside is not just fluid mechanics (including waves in both air and water) but also solid mechanics. Specifically, field calculation using the Green's function method and Green's function calculation itself is commonplace in many recent papers in the fields of seismology and geophysics [42, 154, 183, 341, 347]. Of particular interest is how a Green's function can account for the changes in impedance of layered ('stratified') solid media. Integral methods are a popular choice in these fields due to their efficiency when performing calculations on semi-infinite or infinite domains. The calculation of both analytical and numerical Green's functions are performed using more bespoke methods such as the Discrete Wave-number Method (DWM) developed by Bouchon [41]. This method constructs a Green's function from consideration of analytical solutions of varying wave-number, something typical of wave propagation through the Earth's crust. This could be adapted for inclusion in an aero-acoustic context, if stratified media are encountered.

Green's functions may also be found in many shallow-water scenarios where they are an ideal mechanism for taking into account the reflection and absorption of the seabed [116, 125–127, 201, 274, 275]. The boundary conditions found in these problems tend to share many similarities with aero-acoustic boundary conditions, particularly the description of impedance characteristics. Finally, the Green's function is not limited by any particular coordinate system and has been derived in prolate spheroid coordinates for studies on acquifers by Antangana [14].

Chapter 4

Choice of Numerical Methods

In this chapter, we present the rationale behind the decision to select the three methods which are the focus of this research. As discussed in the previous two chapters, there are numerous characteristics of acoustic problems which preclude the use of traditional methods of solution for differential equations. Specifically we recall:

1. The domain may be very large compared with the acoustic wavelength;
2. The domain boundaries may be of a complex geometry and feature a variety of acoustic boundary conditions;
3. The wavelengths of interest can vary significantly up to a factor of 1000.

The aim of this work is to assess three methods for their potential to provide a robust and accurate means of numerically computing the Green's function for an acoustic boundary value problem both in an arbitrarily complex geometry and for an arbitrary flow field. Many acoustic problems are represented by the wave equation or a variation of the wave equation. A large number of acoustic problems are time-harmonic and hence the solution of the wave equation may be facilitated in the frequency domain. Removing the time-dependence of the problem makes the problem more amenable to solution while being only an inverse Fourier transform away from the original time-dependent form. For the purposes of this research an adequate assessment of the chosen methods is possible by considering the time-independent form; the solution of the time-dependent wave equation is unnecessary. Hence, for simplicity, we solve the Helmholtz equation governing the velocity potential $\hat{\phi}$ of a monochromatic wave

of frequency ω produced by source $\hat{q}$ within an arbitrary geometry, subject to some condition on the boundary.

$$\left(\nabla^2 + k^2\right)\hat{\phi}\left(\mathbf{x},\omega\right) = \hat{q}\left(\mathbf{x},\omega\right) \tag{4.1}$$

Equation (4.1) may be solved by transforming it into an integral equation. If the source is considered to be distributed over a local region, with the position of the individual point sources given by $\mathbf{y}$, our integral equation is defined:

$$\hat{\phi}\left(\mathbf{x},\omega\right) = \int \hat{G}\left(\mathbf{x},\mathbf{y},\omega\right)\hat{q}\left(\mathbf{y},\omega\right)\mathrm{d}^3\mathbf{y} \tag{4.2}$$

The function $\hat{G}\left(\mathbf{x},\mathbf{y},\omega\right)$ is a fundamental solution of the singular form of the governing differential equation (Eqn. (4.3)) which also satisfies all the same boundary conditions and hence is an exact Green's function. Physically the Green's function may be interpreted as an outgoing wave produced by an impulsive unit point source at $\mathbf{y}$, observed at $\mathbf{x}$.

$$\left(\nabla^2 + k^2\right)\hat{G}\left(\mathbf{x},\mathbf{y},\omega\right) = \delta\left(\mathbf{x}-\mathbf{y}\right) \tag{4.3}$$

In the absence of physical boundaries we may consider this wave to propagate in free-space with solution in 3D

$$\hat{G}\left(\mathbf{x},\mathbf{y},\omega\right) = \frac{e^{-ik|\mathbf{x}-\mathbf{y}|}}{4\pi\left|\mathbf{x}-\mathbf{y}\right|} \tag{4.4}$$

However, as we introduce walls and bodies into the domain, the Green's function should either satisfy the boundary conditions on these additional surfaces or else additional terms are required to completely define the solution. We therefore wish to solve Eqn. (4.3) subject to arbitrary boundary conditions while considering the unique characteristics of acoustic problems identified at the beginning of this section. Additionally, we may justify a number of practical restrictions on our choice of methods:

- Any method requiring a domain mesh is likely to be too expensive as we expect to apply the technique to large domains, hence semi-analytical or boundary methods are expected to be more suitable.

  - If we wish to incorporate our numerical Green's function method as a pre-processing technique before applying a hybrid CAA scheme, the time taken to perform this step should be significantly less than if we had extended the source region to incorporate the geometrical complexity. The exception would be if the chosen domain method converged rapidly such that only a very small number of mesh points were needed to accurately represent the solution.

- We require a method which is capable of either satisfying the boundary conditions exactly by utilising analytical solutions, or approximating the boundary conditions accurately without contaminating the domain solution.

  - Many of the numerical studies cited earlier, which principally use numerical domain methods, rely on complicated boundary treatment to ensure the solution is free from errors generated by poor quality boundary conditions. By making use of integral representations or canonical solutions, boundary conditions may be incorporated semi-analytically. As discussed in Section 2.1.6, such boundary conditions significantly improve the robustness of the numerical methods used to find the solution in the domain interior.

- The method must be robust for a wide range of geometries

  - Either the method must be sufficiently general to be applicable to a range of geometries, or it must be possible to cheaply and accurately superimpose or couple instances of the method to construct the solution within the more complex geometry.

Domain methods based on traditional finite difference approximations would not be appropriate for this task due to needing to mesh the whole domain and use an expensive discretisation scheme to resolve all the acoustic disturbances. Even parallel methods like LBM, although cheaper than finite-difference-based methods, are unlikely to achieve the level of accuracy required throughout a potentially large propagation domain. However, boundary methods are often physics-based which allows

accurate representation of boundary conditions and domain behaviour while offering a reduction in mesh extent and a versatility when it comes to complex boundary geometries. Due to this, and the additional benefits discussed in Chapter 6, we consider the Boundary Element Method (BEM) as one of the options. Sometimes, the acoustic problem of interest may satisfy certain physical conditions which can cause difficulties for boundary methods as we later discuss. In such circumstances it is prudent to consider alternative methods.

The subject of aero-acoustics is grounded in a significant amount of analytical theory. We therefore consider the uses of a particular part of this theory in Chapter 5, where we construct an approximation to the Green's function for a class of geometries where the scattering object is small with respect to the wavelength of interest (i.e. compact). The boundary conditions on the surface of the scattering geometry are satisfied exactly by the analytical part of the procedure and for the described class of acoustic problems, the approximation is known to be highly accurate. Where the underlying assumptions are met, the method is notably more efficient than the BEM.

Finally, we also consider the potential of emerging techniques. We consider in Chapter 7 a flexible, physics-based Galerkin method. This method uses a Sinc function basis set for the representation of the solution. Essentially, this Sinc basis is a set of scaled and translated spherical Bessel functions – the first spherical Bessel function $j_1(r)$ to be precise. This function decays with $1/r$ and would be a sensible choice for modelling physical problems with similar decay behaviour. The approach is similar to using a wavelet basis with the difference being the compactness of the basis functions. The exponential convergence of the method as well as its avoidance of numerical integration offset the computational disadvantage of needing to seed nodes in the domain itself.

Having validated and assessed the selected methods in Chapters 5 to 7, we reason in Chapter 8 that the method deemed most suitable depends strongly on the class of geometry to which it is to be applied. Indeed, maximum versatility is achieved when all three methods are considered as a portfolio and using suitable guidance, the most appropriate method is selected.

Chapter 5

Compact Green's Function Method

In this chapter, we investigate the first of the three methods discussed in the previous chapter. Since analytical representations of exact Green's functions are often difficult to obtain [93], methods of constructing approximate Green's functions are often employed to increase the number of Green's functions available for use. These approximation procedures usually involved an asymptotic expansion of either a length or frequency variable to simplify the mathematics [56]. We establish here a numerical means of constructing a specific approximation to the Green's function useful for a range of acoustic problems. The approximation requires the computation of a correction to an appropriate analytical Green's function.

First, we present a brief outline of the approach to approximate the Green's function under the conditions used by Howe [163]. We then develop a numerical implementation for the calculation of this approximate Green's function and apply it to two simple geometries for which analytical solutions are known as a comparison. The effects of the key parameters of the method on both accuracy and computation time are discussed and improved variations on the method suggested. Finally, we discuss the extension of the method to 3D problems and calculate the compact Green's function for a baffle of two different thicknesses within a channel. This latter example demonstrates the ability of the method to be applied to more realistic geometries.

5.1 The Compact Green's Function

The compact Green's function, developed by Howe [157], is a good approximation to the exact Green's function for rigid bodies under a number of assumptions. These assumptions are interpreted generally as:

1. The observer must be located many wavelengths away from any scattering feature in the domain (in the far-field),

2. The source must be close to a scattering feature of the geometry (within the largest dimension of the feature),

3. The largest dimension of the scattering feature must be significantly smaller than the wavelength of the sound under consideration (compact scatterer).

For many realistic cases, these assumptions are not particularly restrictive and hence Howe and others have produced and applied several examples over the last 3 decades of such approximate Green's functions [75, 157, 160, 162, 221, 226, 247]. In all cases an analytical expression has been produced but at the cost of significant mathematical effort. Many of the known compact Green's functions may be found in [163]. It should also be noted that, although Howe coined the phrase 'compact Green's function', far field forms of Green's functions have been used before by Ffowcs-Williams & Hall in their 1970 paper [118] based on an exact form of the Green's function derived as early as 1915 (see references therein). Compact Green's functions and the analytical solution method of MAE are related by their inclusion of asymptotic assumptions. The applicability of the two are compared in a review by Zheng *et al.* [366]. Zheng concludes, by application to classical acoustic problems that, as expected, the two methods agree in the far-field but not in the near-field which corroborates the known inflexibility of observer position in the case of the compact Green's function (the first assumption in the list above).

For situations where the boundary conditions allow it, truncated expansions of eigenfunctions are a means of obtaining an approximation to the Green's function [126, 275]. Although exact as an infinite series, for the purposes of numerical evaluation, truncated series representations are required. Also known as modal solutions, the traditional eigenfunction expansion method is seen to converge very slowly when compared

with image source methods which utilise Ewald's transformation discussed earlier. Finally, there is work of Garabedian [123] which uses the Parametrix Method to construct a parametrix which can be seen as being an approximation to the fundamental solution (Green's function) of a particular differential equation. The structure of the parametrix is a series approximation to the Green's function (also interpreted as the kernel of the inverse differential operator) consisting of differential operators of increasing order multiplied by coefficients. Such series approaches are reminiscent of the methods of the construction of local boundary operators for non-reflecting boundary conditions (see Section 2.1.6).

In this project, the choice of methods for the computation of the Green's function is partially motivated by the need for rapidity. In order for the calculation of the Green's function to be a viable pre-processing step in a hybrid scheme, it must take less time to complete than the simple extension of the source region to incorporate the scattering. Furthermore, the resources required to perform the calculation in terms of available memory must not exceed those required by the most demanding part of the existing scheme. To this end, in this chapter, we examine a semi-analytical procedure which requires only a minimal boundary mesh for computation. An expensive domain mesh, which is invariably large in size if it is to enclose all scattering geometry up to the observer, is not required.

5.2 Constructing the Compact Green's Functions

In a typical acoustic problem it is necessary to consider the effect on far-field sound observed at observer location $\mathbf{x}$ due to the positioning of a scattering body, with largest dimension l, near to the sound source at source location $\mathbf{y}$. The influence of a solid body adjacent to a source has been shown by Curle [81] to be equivalent to a monopole and dipole distribution over the body surface. The compact Green's function [163] includes a *first order approximation* for the net effect of these additional source distributions. We outline briefly below the procedure for constructing the compact Green's function. For more details see Howe [163]. Initially the origin is taken to be inside the body and we assume that the source is located within one characteristic dimension of the body $|\mathbf{y}| \sim l$. The Green's function for scattering problems where the scatterer is in a region

of free-space is considered to consist of the free-space Green's function (Eqn. (4.4)) plus a correction $\hat{G}'$ accounting for the scattering of this body. Note at this point that construction of the compact Green's function for other 'starting' geometries would require a different analytical form. Although analytical representations of acoustic Green's functions are not numerous, many real problems may still be treated with those which are available. Using the principle of reciprocity, the free-space Green's function $\hat{G}_0$ and its correction $\hat{G}'$ are stated as:

$$\begin{aligned}\hat{G}(\mathbf{y},\mathbf{x},\omega) &= \hat{G}_0(\mathbf{y},\mathbf{x},\omega) + \hat{G}'(\mathbf{y},\mathbf{x},\omega) \\ &= \frac{-e^{ik|\mathbf{x}-\mathbf{y}|}}{4\pi\,|\mathbf{x}-\mathbf{y}|} + \hat{G}'(\mathbf{y},\mathbf{x},\omega)\end{aligned}$$

The observer (source in the reciprocal problem) is then removed to the far field and the far-field assumptions $|\mathbf{x}-\mathbf{y}| \approx |\mathbf{x}| - |\mathbf{y}|\cos\theta$ and $\frac{1}{|\mathbf{x}-\mathbf{y}|} \approx \frac{1}{|\mathbf{x}|}$, defined by application of the Taylor expansion in $|\mathbf{y}|$ about the origin, are applied. In Howe [163], all terms in the expansion involving distances to powers greater than 1 are not printed explicitly, disguising the truncation error. We retain them here to illustrate the role of the compact assumptions. Thus, introducing this Taylor expansion into the free-space Green's function we obtain:

$$\begin{aligned}\hat{G}_0(\mathbf{x},\mathbf{y},\omega) &= \frac{e^{ik|\mathbf{x}-\mathbf{y}|}}{|\mathbf{x}-\mathbf{y}|} \\ &= \frac{-e^{ik|\mathbf{x}|}}{|\mathbf{x}|}\Bigg[1 - ik\,|\mathbf{y}|\cos\theta - \frac{1}{2}\,|\mathbf{y}|^2 k^2\cos^2\theta \\ &+ \frac{1}{|\mathbf{x}|}\left(|\mathbf{y}|\cos\theta - |\mathbf{y}|^2\, ik\cos^2\theta + \frac{1}{2}\,|\mathbf{y}|^2\, ik\sin^2\theta\right) \\ &+ \frac{1}{|\mathbf{x}|^2}\left(|\mathbf{y}|^2\cos^2\theta - \frac{1}{2}\,|\mathbf{y}|^2\sin^2\theta\right) \\ &+ \dots\Bigg]\end{aligned}$$

Howe then introduces the correction for the presence of the body by a function $\phi(\mathbf{y})$ which is given by $\hat{G}' = -U_j\phi_j + \mathcal{O}(kl)^2$ where $\phi_j \to 0$ with $|\mathbf{y}|$ and $U_j = \frac{e^{ik|\mathbf{x}|}}{4\pi|\mathbf{x}|}\frac{ikx_j}{|\mathbf{x}|}$, the latter being a constant for a given *source* position in the reciprocal problem $|\mathbf{x}|$. The complete Green's function is given by

$$\begin{aligned}\hat{G} &= c + U_j(y_j - \phi_j) + \frac{e^{ik|\mathbf{x}|}}{4\pi\,|\mathbf{x}|}\left[\frac{1}{2}\,|\mathbf{y}|^2\,k^2\cos^2\theta\right] + \dots \\ &= c + U_j(y_j - \phi_j) + \left[V_j y_j^2 + W y_1 y_2\right] + \dots \end{aligned} \tag{5.1}$$

where the constants are defined by

$$\begin{aligned} c &= \frac{-e^{ik|\mathbf{x}|}}{4\pi\,|\mathbf{x}|} \\ U_j &= \frac{e^{ik|\mathbf{x}|}ikx_j}{4\pi\,|\mathbf{x}|^2} \\ V_j &= \frac{e^{ik|\mathbf{x}|}k^2x_j^2}{4\pi\,|\mathbf{x}|^3} \\ W &= \frac{e^{ik|\mathbf{x}|}k^2x_1x_2}{4\pi\,|\mathbf{x}|^3} \end{aligned}$$

The correction to the free-space Green's function in this instance may be made accurate up to derivatives of first order – sometimes referred to as dipole order. This allows confident use of the derivative of this Green's function as would be required when dealing with dipole sources (see Section 5.6). In order to achieve this, the terms in square brackets in Eqn. (5.1) must vanish. The required restrictions define a class of compact problems and are seen to consist of [163]:

i. The observer is considered to be located in the far-field $|\mathbf{x}| \to \infty$, or $\frac{x}{\lambda} \gg 1$.

ii. The source is to be located a distance of no more than l from of the body $|\mathbf{y}| \sim \mathcal{O}(l)$;

iii. The largest dimension of the adjacent body is considered to be significantly smaller than the wavelength of the sound (i.e. the body is acoustically compact) $\lambda \gg l$;

which is the mathematical analogue of the earlier physical list, in which case, the Green's function Eqn. (5.1) reduces to the *compact* Green's function Eqn. (5.2), the above assumptions constituting a scattering body which is *compact* with respect to the wavelength of the sound under consideration.

$$\hat{G}(\mathbf{x}, \mathbf{y}, \omega) \approx \frac{e^{-ik|\mathbf{x}|}}{4\pi\,|\mathbf{x}|}\left(1 - \frac{ikx_jY_j}{|\mathbf{x}|}\right) \tag{5.2}$$

Y_j is the j-th component of the Kirchhoff vector $\mathbf{Y}$. Physically, this field is not a wave field but is interpreted as the potential of a uniform, *unit potential flow* corrected for the presence of the scattering geometry. In the far-field (near the reciprocal problem source and away from the scattering body), the Kirchhoff vector components decay such that the free-space form of the Green's function is recovered.

5.2.1 Potential Flow Solutions

For a given wave number k, source and observer location, $\mathbf{x}$ and $\mathbf{y}$ respectively, the compact Green's function for a scatterer in free-space may easily be evaluated from Eqn. (5.2) once the components of the Kirchhoff vector have been found. The definition of the Kirchhoff vector requires us to seek potential flow solutions around or within the problem geometry. Each component of the Kirchhoff vector typically will depend on the coordinates of the source $\mathbf{y}$. These potential flow solutions may be constructed by considering one or more 2D potential flow problems in the complex plane $z = y_1 + iy_2$ where the solution is represented by complex potential $\Phi = \phi + i\psi$, where ϕ represents the potential function and ψ the stream function. Physically, this complex potential has encoded within it, the 2D velocity field of an irrotational, incompressible flow in the geometry. The effect on an initially uniform flow in a particular direction due to the geometry is represented by the velocity potential field. The Kirchhoff vector component is therefore extracted from this field data as $\phi = \Re\{\Phi\}$.

The solution of Laplace's equation in anything other than simple geometries is usually made possible by the application of conformal mapping. An arbitrary physical domain may be transformed to a much more simple computational domain in which the potential flow solution is known analytically. Due to the conformal invariance of the Laplacian operator the inverse transformation then allows the potential flow in the original domain to be evaluated. Although many conformal maps may be described analytically [see 280, Appendix A-2], a more robust method is needed to transform more general geometries. The Schwarz-Christoffel mapping technique may be used to determine the mapping in more general cases: The boundary of the physical domain is discretised into straight line segments connected at n vertices. For the chosen computational domain the conformal map f maps any point $\zeta \in \mathbb{C}$ to its image $z \in \mathbb{C}$ and the computational pre-vertices a_k to the physical vertices n. Of use to us here

is the transformation from an arbitrary domain to a computational infinite half-plane defined by Eqn. (5.3) [90], where K is a scaling constant and α_k is the interior angle of the k-th physical vertex.

$$\frac{\mathrm{d}z}{\mathrm{d}\zeta} = K \sum_{k=1}^{n-1} (\zeta - \alpha_k)^{\alpha_k - 1} \tag{5.3}$$

The conformal mapping function f may be found by using by numerical integration to solve the integral of Eqn. (5.3)

$$f = A + K \int_0^{\zeta} \sum_{k=1}^{n-1} (\zeta - a_k)^{\alpha_k - 1} \mathrm{d}\zeta \tag{5.4}$$

where the complex constant A provides translation. Conformal mapping has been used extensively thus for a wide range of problems [91, 141, 250, 252, 304]. Rather than developing a numerical implementation to compute the mappings required in this work, we make use of the readily available Schwarz-Christoffel Toolbox for MATLAB [see 90, Appendix: Using the SC Toolbox]. The capabilities of this toolbox include the solution of mappings from a range of computational domains including the infinite strip which we later show can provide increased robustness for certain classes of geometries.

5.3 Application to 2D Problems

In this section we validate the proposed method by configuring and solving for the required potential flow to construct the Kirchhoff vector for two types of model problems. These geometries are chosen as the potential flow problems have analytical solutions with which we compare our results. We consider first the case of a uniform cylinder in an infinite medium whose dimensions remain unchanged in one of the three directions. Another useful problem for which the compact Green's function may be constructed, albeit derived from a different starting point than Eqn. (4.4), is that of the scattering by a backward-facing step in a channel. The compact Green's function for this problem is expected to be constructed from the correction of the Green's function for two pipes of different height, matched at the step [94]. For simplicity at this stage, this problem is treated as being wholly 2D although the axi-symmetry of a 3D pipe would result in the same problem being solved in any case. As well as

these problems having analytical compact Green's functions for comparison, they are also selected due to their practical relevance: The first problem is an exterior problem involving the scattering by rigid bodies in free-space. Using symmetry, we may solve this as a semi-cylindrical protrusion from a virtual wall described by any line of symmetry through the cylinder centre. The second is an interior problem representing a simple two-dimensional area change in a duct or pipe, a geometry known to produce important scattering effects since sharp corners are known to be an important source of noise amplification [75, 78, 118]. The diversity in the two test problems allows us to ensure versatility of the method is retained during development. Since in both cases we are only a substitution away from obtaining the compact Green's function, it is reasonable to compare the evaluation of the potential function as a means of assessing the accuracy of the method.
The algorithm is as follows:

- Identify a suitable analytical Green's function for correction and then the Kirchhoff vector components.
- For each Kirchhoff vector component,
  - Configure the geometry.
  - Select the mapping.
  - Compute the mapping numerically.
  - Specify the grid points in the computational domain.
  - Evaluate the complex potential model in the computational domain.
  - Transform the grid points and their associated complex potential the physical domain using the numerical mapping.
- Substitute the Kirchhoff vector components into the compact Green's function to evaluate.

Variations on this algorithm are possible. If the grid is specified in the physical domain; useful if the observer or source grid point placement requires more control; the grid points are first mapped using the inverse transformation to the computational domain then the complex potential evaluated. Furthermore, whether the grid represents

source or observer locations is also flexible depending on what results are required. The 2D examples below identify some important influences on the accuracy and robustness of the method. In order to use the Schwarz-Christoffel procedure, a suitable computational domain needs to be selected to which we may transform the physical geometry. The level of discretisation required to achieve accurate potential flow behaviour over curved surfaces, such as we have with the cylinder example, is shown to be an important consideration. The backward-facing step example is used to illustrate the role this decision plays in the overall accuracy and robustness of the procedure; we show that when mapping from the upper half-plane the computational potential model is singular and the mapping very sensitive to error. These initial results are then improved by changing the mapping to one from an infinite strip where the computational model is a simple uniform flow.

5.3.1 Circular Cylinder of Infinite Length

The interaction of acoustic waves with a single or array of circular cylinders is a canonical problem [152, 234] and one whose potential flow solution may be described analytically. We therefore use this model problem as one of two problems which aim to validate the results of this chapter.

We require the computation of two Kirchhoff vector components (although from the symmetry of the geometry, these components are identical). We have, therefore, two potential problems to solve. The use of the rotational symmetry of the problem to study only half-cylinders has two benefits: First, by specifying an infinite vertex, we turn an unbounded domain into a bounded domain which allows the use of a half-plane mapping; secondly, we reduce the number of vertices used to compute the map, reducing execution time. Specific to this problem is the application of the mapping technique to a curved surface. Although the mathematics behind the analytical procedure of mapping circular arcs exists [34], the functionality is not yet available in the toolbox. Rather than introducing the functionality ourselves, we opt to approximate the cylinder surface by a number of straight-line segments. The physical and computational geometries are defined as in Fig. 5.1. The complex potential in the computational domain is represented analytically by uniform flow past the upper half-plane $U'\zeta_1$. This complex potential, evaluated over a uniform grid, is transformed back

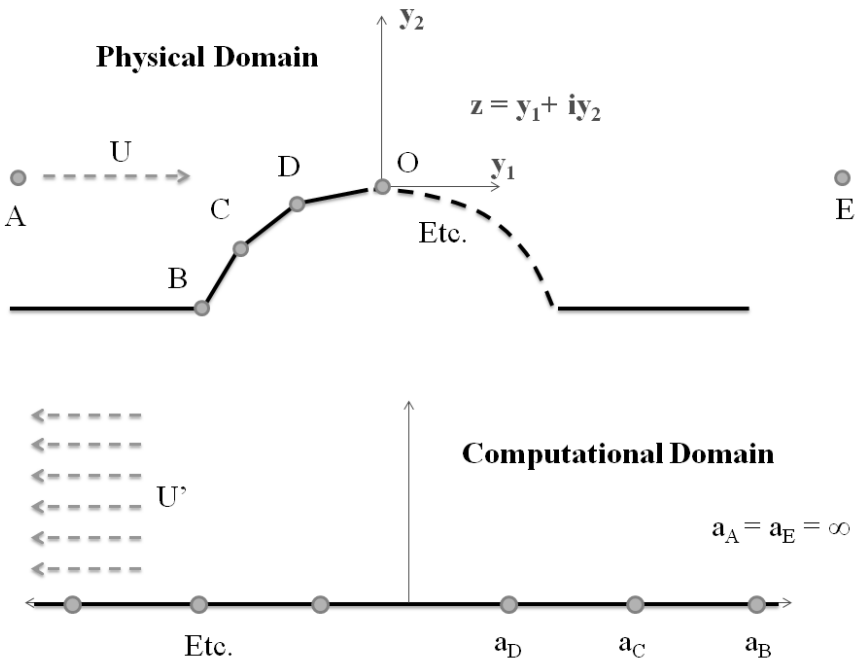

Figure 5.1: Circular cylinder problem in both the untransformed and transformed domains.

to the physical domain to obtain the Kirchhoff vector component. The computation of the second Kirchhoff vector component uses a procedure and geometry identical to the first but considers the potential flow solution in the y_2 direction. Note that although a circular cylinder has identical Kirchhoff vector components Y_1 and Y_2, this would not be the case for asymmetric geometries.

A significant difficulty in using the half-plane map in this instance is the correct specification of the computational flow velocity U'. By observing how a uniform grid in the computational domain is rescaled under forward mapping and considering continuity of the flow we arrive at an appropriate value. Improvements in the choice of this value are discussed in Section 5.4. The analytical solution to the potential flow round a cylinder of radius a_0, in polar coordinates, with origin at the centre of the circle, is given by [327]

$$\Phi(r,\theta) = U\left(r + \frac{a_0^3}{2r^2}\right)\cos\theta \tag{5.5}$$

where in our case, by definition of the Kirchhoff vector, the free-stream speed $U = 1$. Results for the absolute error in the potential function for the first Kirchhoff vector component evaluated over the mapped grid points are shown in Fig. 5.2. The results

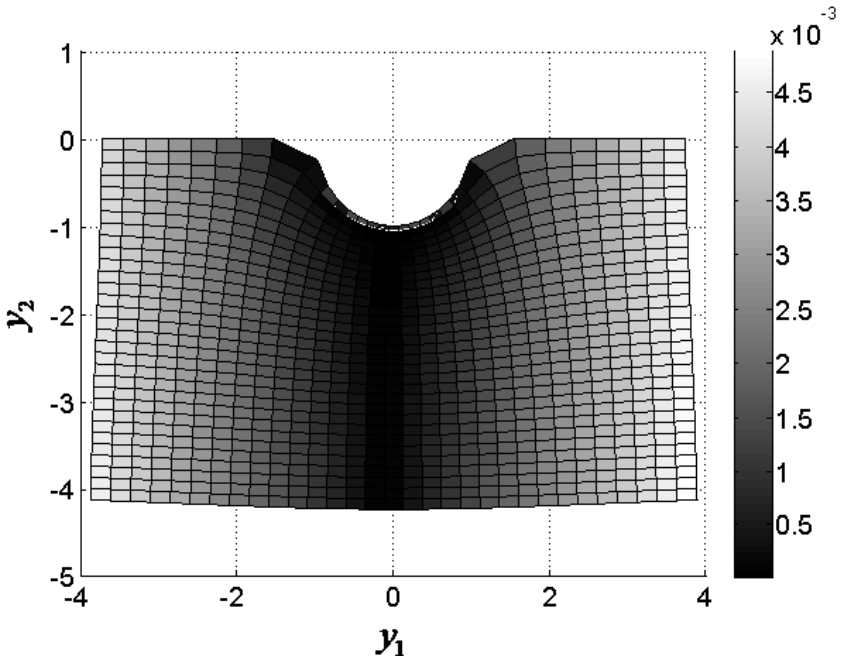

Figure 5.2: Absolute Error of potential function for half a circular cylinder.

indicate that the solution is most accurately represented near $y_1 = 0$ and deteriorates away from this value suggesting a dependence on its magnitude. This behaviour is studied further in Section 5.4.2.

5.3.2 Backward-Facing Step in a Channel of Infinite Width

For the backward-facing step problem, as the channel is rigid, sound is only observed within the channel itself. Therefore, we have an additional constraint on our far-field location in that it must be within the upper and lower walls of the channel $0 < x_1 < h$. The far-field location is hence considered to be downstream $x_2 \to \infty$ and it is concluded that the Green's function will only require correction in the stream-wise y_1-direction. The Kirchhoff vector component Y_1 is to be found with the other component $Y_2 = y_2$. We define the physical problem and its geometry transformed to the upper half-plane as in Fig. 5.3. Note that the dummy vertex A is not necessary if Eqn. (5.4) excludes one of the infinite vertices, but is included here for completeness. In the computational domain we model the transformed potential flow analytically as a sink of strength q at the prevertex location corresponding to the infinite downstream vertex E:

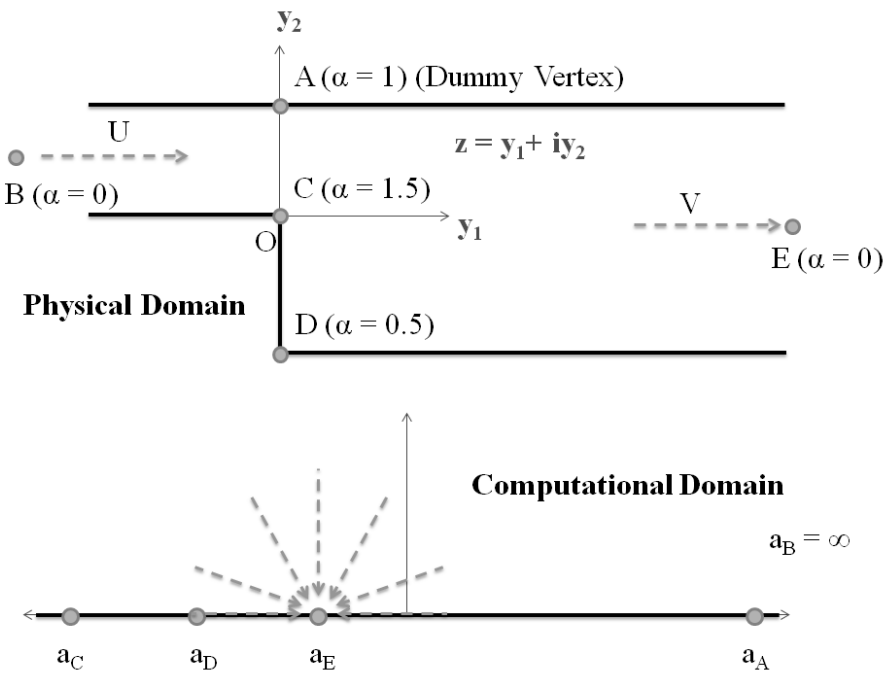

Figure 5.3: Backward-facing step problem in both the untransformed and transformed domains.

$$\begin{aligned}\Phi(\zeta) &= \phi + i\psi \\ &= -\frac{q}{\pi}\log(\zeta + 0.3333)\end{aligned}$$

The transformation of this complex potential to the physical domain using inversion of the mapping function:

$$f^{-1}(z) = \zeta$$

gives us

$$\Phi(z) = -\frac{q}{\pi}\log\left(f^{-1}(z) + 0.3333\right)$$

The analytical solution of the potential flow for a backward-facing step is given parametrically by Milne-Thomson [227].

Table 5.1: Details of the numerical mapping for the backward-facing step from the half-plane (4 sig. fig.)

Vertex Label	Vertex Location w_n	Prevertex Location a_k	Angle α_k
A	i	1.000	1
B	$-\infty$	∞	0
C	0	-1.000	1.5
D	$-i$	-0.4999	0.5
E	∞	-0.3333	0
$K = -0.3182 + (5.846 \times 10^{-17})\, i$			

$$\Phi(\zeta) = -\frac{q}{\pi}\log(\zeta) \tag{5.6a}$$

$$\zeta = \frac{4 - t^2}{1 - t^2} \tag{5.6b}$$

$$z = \frac{2}{\pi}\left[\log\left(\frac{1+t}{1-t}\right) - \frac{1}{2}\log\left(\frac{2+t}{2-t}\right)\right] - i \tag{5.6c}$$

This corresponds to a complex potential representing a source at the computational origin, which is in keeping with the slightly different half-plane map used to derive the analytical solution – the solution to our mapping is given in Table 5.1.

Figure 5.4 shows the variation in absolute error over the mapped computational uniform grid minus a constant of integration which contaminates the result. Compared to the cylinder problem the overall error is lower, which suggests the approximation of the curved surface using straight-line segments could be important. We discuss this suggestion in Section 5.4. The abrupt change in the error over the physical grid in Fig. 5.4 is likely an accumulation of small numerical errors in the mapping with the associated grid distortion difficult to control when specifying the grid initially in the computational domain. One means of tempering this would be to specify the grid in the physical domain first although this would require additional inverse mapping of the points which is not only a less accurate procedure (see later discussion) but also more time consuming.

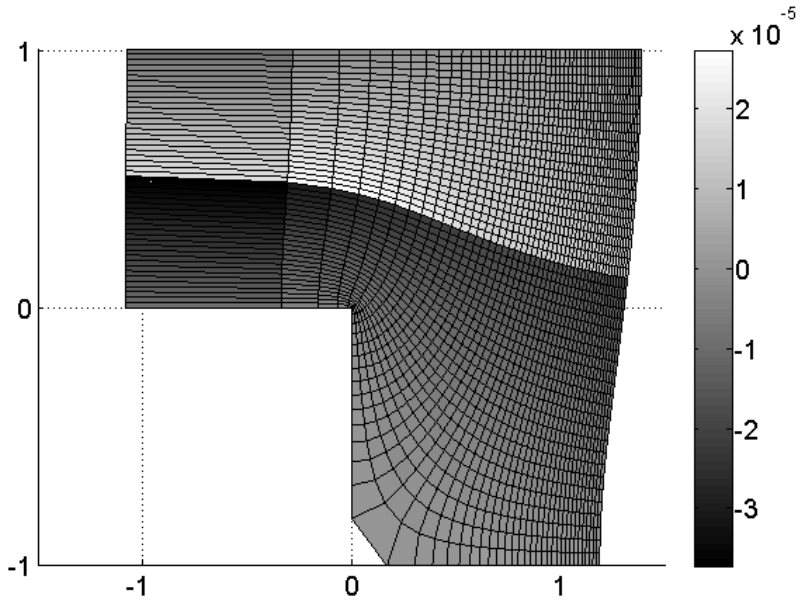

Figure 5.4: Absolute error variation in the potential for the backward-facing step. Note: The numerical results are shown minus a constant of integration

5.4 Influence of Grid and Map Configuration

As can be seen from Fig. 5.2 and Fig. 5.4, the decision to map from the upper half-plane reveals some interesting problems which limit the accuracy of the method. If this method is to be useful in practical acoustic calculations we need to ensure that the error in the potential field (and hence in the Green's function) is lower than the magnitude of the acoustic fluctuation itself (usually $\mathcal{O}(10^{-4})$). We outline here the sources of error and, where possible, determine a means of control or avoidance.

5.4.1 Backward-facing Step

In this problem, the error variation over the domain may be attributed to a number of sources:

i. Error due to the constant of integration we show here to be characterised by the translation of the origin under the transformation.

ii. Errors in evaluating the complex potential and mapping due to imprecision of the numerical mapping of the vertices.

iii. Floating point errors and limitations in the accuracy of numerical integration used in computing the mapping.

iv. Errors due to the sensitivity of singular complex potential models to inaccuracies.

We can determine the significance of the first two sources of error analytically by constructing the simple Schwarz-Christoffel transformation mapping points from the upper half-plane to a 2D channel with uniform potential flow. A 2D straight-sided channel with uniform flow is mapped numerically with details shown in Table 5.2.

Table 5.2: Details of the numerical mapping for a simple channel with unit flow from the half-plane (4 sig. fig.)

Vertex Label	Vertex Location w_n	Prevertex Location a_k	Angle α_k
A	$-\infty$	∞	0
B	$-i$	-1.000	1
C	∞	$a_C = 2.552 \times 10^{-5}$	0
D	i	1.000	1
$K = -0.6366 + (7.796 \times 10^{-17})\, i$			

The channel has a non-singular complex potential in the physical domain:

$$\Phi(z) = Uz \tag{5.7}$$

If we model the complex potential as a sink located at prevertex a_C of strength $q = 2U$ (from consideration of continuity) then we have a similar model to the backward-facing step problem, specifically:

$$\Phi(\zeta) = -\frac{q}{\pi} \log(\zeta - a_C) \tag{5.8}$$

In order to determine the sources of error, we derive the Schwarz-Christoffel transformation by hand using the same fixed degrees of freedom and complex potential model Eqn. (5.8) as the numerical mapping. The resulting analytical expression may then be used to compare map data to those provided by the numerical implementation. The forward mapping function generated by the solution of Eqn. (5.4) is given by:

$$f(\zeta) = A + K \log(\zeta - a_C) \tag{5.9}$$

By substituting in the required mappings in order to mimic the details of Table 5.2 we get:

$$K = \frac{-2i}{\log\left(\frac{a_C+1}{a_C-1}\right)} \tag{5.10}$$

In order to find A we may substitute in one of the known mappings from the numerical mapping data giving:

$$A = i + \frac{2i}{\log\left(\frac{a_C+1}{a_C-1}\right)} \log\left(1 - a_C\right) \tag{5.11}$$

We can now write general expressions for the forward and inverse mapping functions as

$$z = i + K \log\left(\frac{\zeta - a_C}{1 - a_C}\right) \tag{5.12}$$

$$\zeta = (1 - a_C)\, e^{K^{-1}(z-i)} + a_C \tag{5.13}$$

where K is defined in Eqn. (5.10). We also examine the derivative of the complex potential – in other words the velocity distribution $w(u, v)$, where u and v are the 2D velocity components in the x_1 and x_2 respectively. Using the exact mapping Eqn. (5.12) we have:

$$\begin{aligned} \frac{\partial \Phi}{\partial z} &= w(u, v) \\ &= u - iv \\ &= \frac{\partial \Phi}{\partial \zeta} \cdot \frac{\partial \zeta}{\partial z} \\ &= -\frac{2}{\pi} \frac{1}{\zeta - a_C} \cdot \frac{(\zeta - a_C)}{K} \\ &= -\frac{2}{\pi} \frac{1}{K} \end{aligned} \tag{5.14}$$

We see from the above analysis that the error in the mapping indeed consists of two parts: one part due to the imprecision associated with mapping the vertices and another (blanket) error which comes about due to the constant of integration of the mapping function A. From Eqn. (5.11), this constant of integration is clearly

dependent on the placement of the origin and hence its value must be corrected. Furthermore, the error arising due to imprecision of vertex mapping gives rise to a variation in error in the complex potential. Expressing the error in the complex potential as ϵ the total error in the potential field in terms of the position of origin prevertex a_C is given by

$$\begin{aligned}\epsilon &= \Phi_\zeta - \Phi_z \\ &= Uz - \frac{-2U}{\pi}\log\left[(1-a_C)e^{K^{-1}(z-i)}\right] \\ &= z\left(1+\frac{2}{\pi K}\right) + \frac{2}{\pi}\log(1-a_C) - \frac{2i}{\pi K} \\ &= g(z) - \frac{2}{\pi K}A\end{aligned}$$

If $a_C = 0$, then the mapping of the prevertex a_C may be considered precise and then only the second component of the error remains due to the constant of integration. Specifically where $\epsilon = i = A|_{a_C=0}$. This additional error component can be removed through the conformal invariance of the Laplacian operator, which states [334]:

$$\Delta_\zeta \Phi_\zeta = |f'(\zeta)|^2 \Delta_z \Phi_z \tag{5.15}$$

where each complex potential model Φ is a valid solution to Laplace's equation in its own domain. These complex potentials are not necessarily unique since any constant could be added, which provides translation of the field. Since this constant would disappear with differentiation, the complex potentials would still satisfy Laplace's equation and Eqn. (5.15). We may therefore conclude that when using the half-plane map in this way, the origin in the physical domain must be chosen such that the constant of integration of the map A vanishes. In practice, we would not know the physical complex potential to allow us to accurately calculate the constant or the appropriate location of the origin; hence Green's functions computed using mapping from the half-plane is impracticable to general geometries with simple (monopole) acoustic sources. However, for dipole (or quadrupole) sources of sound, the *derivative* of the compact Green's function could be utilised. The constant of integration would have no influence in this case since differentiation will remove it and use of the half-plane map again becomes viable.

The third source of error, concerning the floating point errors in the numerical integration, is seen to be insignificant when compared with the fourth source of error – error due to the sensitivity to singularities in the complex potential. Furthermore, it is possible to circumvent the fourth source of error in such a way that the first source of error concerning the constant of integration is also automatically eradicated. We construct the mapping for the same 2D channel with uniform potential flow as before but map from an infinite strip of unit height in ($\zeta = \eta + i\xi$), where the complex potential is given by a uniform flow along the strip. With regards to the sensitivity of the solution to the singularities in the complex potential, the significance here is that the complex potential in the computational domain is not singular, as was the case for the upper half-plane, so any imprecision in the mapping is less likely to be magnified by the singularity.

In the physical domain we have complex potential

$$\Phi(z) = Uz \tag{5.16}$$

and in the computational domain

$$\Phi(\zeta) = U'\zeta \tag{5.17}$$

If we allow the complex potential in the computational domain to take into account both the new speed of the flow U' to maintain continuity *and* the relocation of the origin we may equate the two potentials without knowing the constant of integration *a priori* using Eqn. (5.18), where L is the translation of the origin represented in the ζ-domain.

$$\Phi(\zeta) = U'(\zeta - L) \tag{5.18}$$

We show this by comparing again to the hand-worked solution, this time computed using the equation for the Schwarz-Christoffel transformation from an infinite, straight-sided strip Eqn. (5.19) [90] where the n vertices considered exclude those infinite vertices at the strip ends.

$$f(z) = A + K \int \prod_{k=1}^{n} \left[\sinh \frac{\pi}{2}(\zeta - a_k)\right]^{\alpha_k - 1} \mathrm{d}\zeta \tag{5.19}$$

In the physical z-domain the origin is in the centre of a 2D strip (channel) of height 2 units and in the computational ζ-domain the origin is located on the centre of the lower boundary of a channel of height 1 unit. The resulting mapping function from solution of Eqn. (5.19) is $f(\zeta) = A + K\zeta$. The values of A and K can be found by considering the mapping of points on the upper and lower boundaries of the channel ($\zeta = i$ when $z = i$ and $\zeta = 0$ when $z = -i$) which gives $A = -i$ and $K = 2$. We can then determine the origin relocation parameter L using the inverse mapping function $f^{-1}(0) = \frac{1}{2}i$. This relocation of the origin is simply a translation of the potential field in this domain.

We note that we can equate the complex potentials exactly

$$\begin{aligned}\epsilon &= \Phi(\zeta) - \Phi(z) \\ &= Uz - 2U(\zeta - L) \\ &= Uz - 2U\left[\frac{1}{2}(z+i) - \frac{1}{2}i\right] \\ &= 0\end{aligned}$$

where L is the known translation of the origin in the computational domain. This mapping function is quite clearly unaffected by the issues of origin relocation which plagued the half-plane map. This time, the mapping function is corrected by the translation of the flow field to account for the translation of the origin. The maximum relative error using the infinite strip map is dramatically reduced to 5.75×10^{-10}. Note that this technique of adding a translation of the flow field to account for origin relocation may not be applied to the complex potential for the upper half-plane due to the non-linear nature of the computational complex potential. Specifically, by modifying Eqn. (5.8) to read

$$\Phi(\zeta) = -\frac{2}{\pi}\log(\zeta - L - a_C) \tag{5.20}$$

where L is the translational constant defined as before by $f^{-1}(0)$ we can substitute for ζ using Eqn. (5.13) to get:

$$\Phi(\zeta) = \frac{-2}{\pi}\log\left[(1-a_C)e^{-K^{-1}(z-i)} + a_C - a_C - (1-a_C)e^{K^{-1}(-i)} - a_C\right]$$

Since we are concerned only with the error associated with the constant of integration we let $a_C \to 0$ so $K^{-1} \to \frac{-\pi}{2}$ to simplify the mathematics giving

$$\begin{aligned}\Phi(\zeta) &= \frac{-2}{\pi}\log\left[e^{-\frac{\pi}{2}(z-i)} - e^{\frac{\pi}{2}i}\right] \\ &= \frac{-2}{\pi}\log\left[e^{\frac{\pi}{2}i}\left(e^{\frac{\pi}{2}z} - 1\right)\right] \\ &= -i - \frac{2}{\pi}\log\left(e^{-\frac{\pi}{2}z} - 1\right) \end{aligned} \tag{5.21}$$

At $z = 0$ we expect $\Phi = 0$ since in the physical domain $\Phi|_{z=0} = Uz|_{z=0} = 0$. However substituting $z = 0$ in Eqn. (5.21) we get $\Phi = -i + \infty \neq 0$. This demonstrates that a simple translation of the coordinates in the complex potential will not suffice in this case due to the non-linear nature of the complex potential function. The use of a computational domain where a linear complex potential function applies allows us to incorporate origin translation simply with just the addition of the quantity L, addressing the principal source of error in the earlier half-plane calculations.

By incorporating the understanding described above, we re-solve the backward-facing step problem to demonstrate the magnitude of the improvements. The same analytical expressions for the complex potential in the physical domain (z-plane) are used as before (Eqn. (5.6)) but this time we map from the infinite strip representing the complex potential in the computational domain as per Eqn. (5.18). For a 30×30 grid, execution time was approximately 0.53 seconds with a maximum relative error over the grid of 9.1×10^{-9}. The variation in the relative error over the grid is shown by the surface in Fig. 5.5. The upstream increase in error may be explained by the stretching of the grid in this region. The grid is distorted thus due to the fact that it is computed by a uniformly spaced grid in the computational domain used to generate the analytical solution. In practice, where no analytical solution exists, the grid would be designed with the physical plane in mind and hence would ideally use a custom spacing.

5.4.2 Circular Cylinder

The complex potential computed for this problem, whose error is shown in Fig. 5.2, varies roughly as expected but absolute values still lack precision. Two possible sources of error, specific to this class of problem are identified:

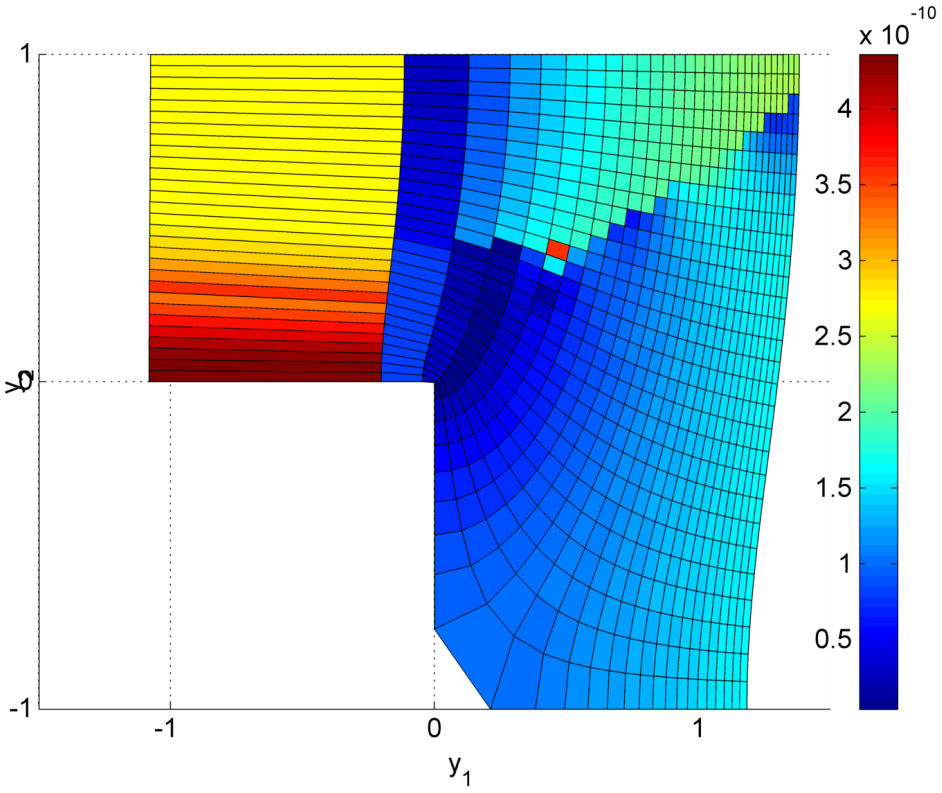

Figure 5.5: Absolute Error variation over a 30×30 grid using a strip map

i. The incorrect specification of the velocity U' in the complex potential model in the computational domain

ii. The inaccuracies associated with approximating the curved surface by a series of straight lines.

Due to the unbounded nature of the half-plane domain, we cannot simple use continuity considerations to establish a suitable computational flow velocity. This is a disadvantage when choosing to use a half-plane mapping procedure for finding the potential flow solution for exterior problems. Investigation shows that in order to achieve suitable accuracy, this velocity must be correct to a large number of decimal places. Even errors of the order 10^{-5} in U' may lead to an increase in the average error over the grid by an order of magnitude. A dramatic improvement in error over the whole grid may, therefore, be observed when an improved computational velocity is used (Fig. 5.6). Note that the lack of symmetry of this absolute error map is not due to the values but due to how the rendering takes place. It is clear from inspection of the mesh data that the error is indeed symmetrical. In Fig. 5.6, the highest error values are now found near the cylinder surface, likely driven by

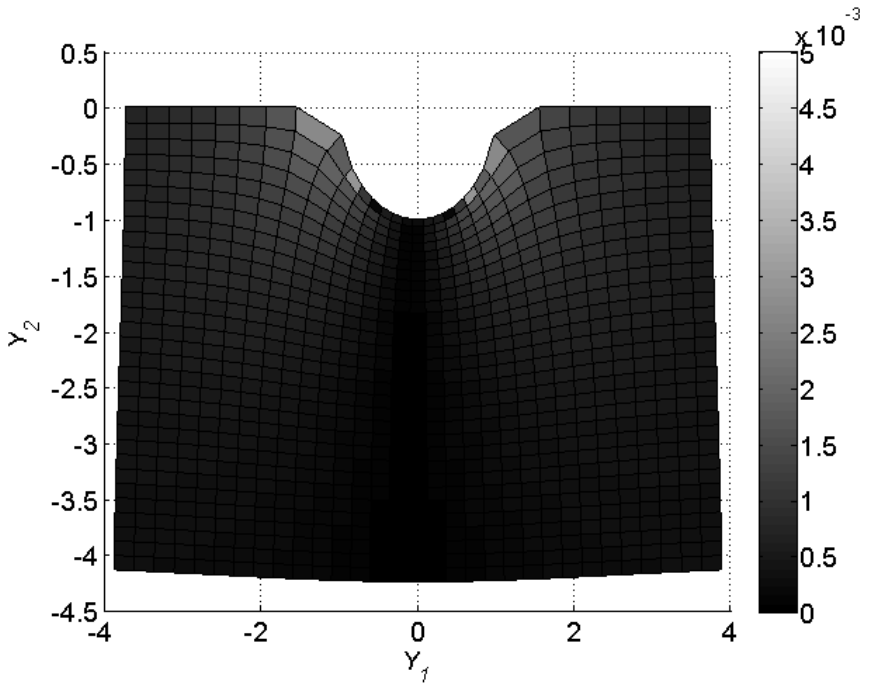

Figure 5.6: Absolute Error variation for improved potential flow solution for circular half-cylinder. The same colour scale has been used as for Fig. 5.2 to illustrate the decrease in error more effectively.

the approximation of the curved surface by straight-line segments. Furthermore, the error remains higher by approximately half an order of magnitude where the geometry changes more suddenly. Here the transformed grid is most distorted and hence will be more sensitive to inaccuracies in the mapping procedure when used to evaluate the potential. One way to circumvent this source of error would be to specify the grid in the physical domain first such that it fits the geometry more closely.

Furthermore, the minimum error over the grid actually forms a "radial band" such that the cylinder surface and the minimum error radial band are concentric. Any error in the specification of U' not only increases the error over the whole grid but also moves the radial band. In testing, this movement was seen to be very sensitive to small changes in U'. Just how sensitive is illustrated by Fig. 5.7 where we have plotted the location of the band against selected values of U'. Figure 5.7 demonstrates a singular behaviour. This type of behaviour is highly undesirable to the practitioner with errors in the specification of U' of $\mathcal{O}(10^{-5})$ capable of causing dramatic changes in the average error and location of the minimum error over the domain surrounding the scatterer. We consider the use of the strip map in Section 5.4.2.1 as a means of addressing the issue.

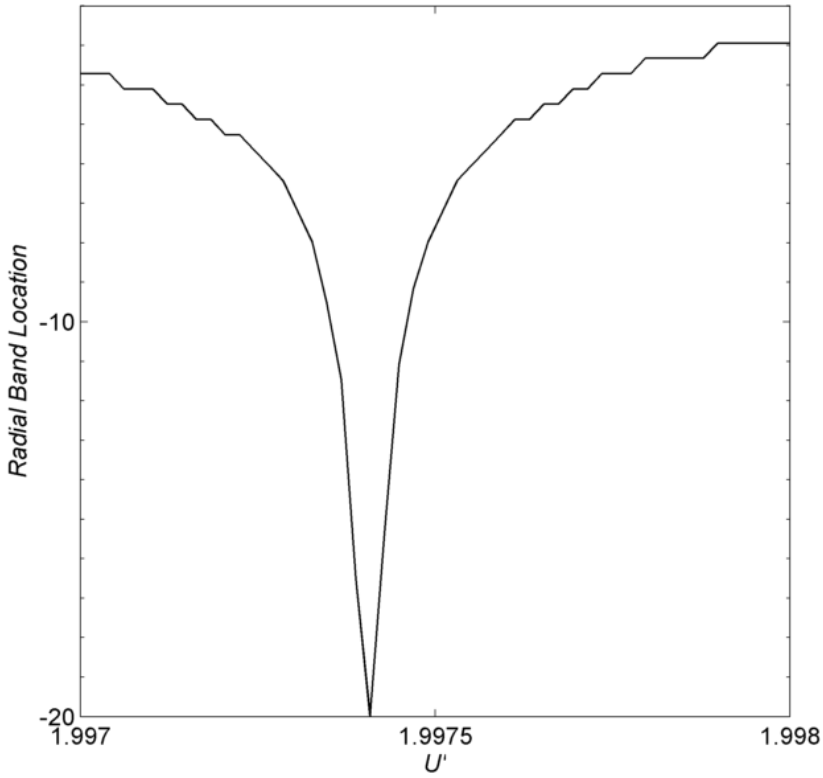

Figure 5.7: The vertical axis indicates at which radial value the minimisation is largest. These results were obtained from a grid with largest radius equal to 20.

With regards to the second item in the above list, increasing the number of straight-line segments used to represent the curved surface benefits the results in two ways. First, the abrupt changes, or "spikes", in the potential function near to the approximated surface of the cylinder are minimised. The practical implications of this are significant as scattering effects are more pronounced near to surfaces and can only be captured accurately with the accurate evaluation of the compact Green's function in these regions. Second, the error further away from the surface is reduced as the equi-potential and stream lines tend quicker to the appropriate curvature. An increase in the number of straight-line segments used to approximate the arc is the simplest solution to use although does impact the time taken to compute the map, as illustrated later. Figure 5.8a and Fig. 5.8b show how the absolute error map changes as the polygon vertex is increased. The computational velocity U' used in each case is only correct to 5 decimal places. In Fig. 5.8a the error on the surface of the cylinder due to insufficient vertex density dominates. Close to the surface the scattering behaviour is often important and hence errors of this nature are undesirable. However, the error reduces dramatically in these regions by an order of magnitude when we increase the

vertex density by a factor of 10 (Fig. 5.8b).

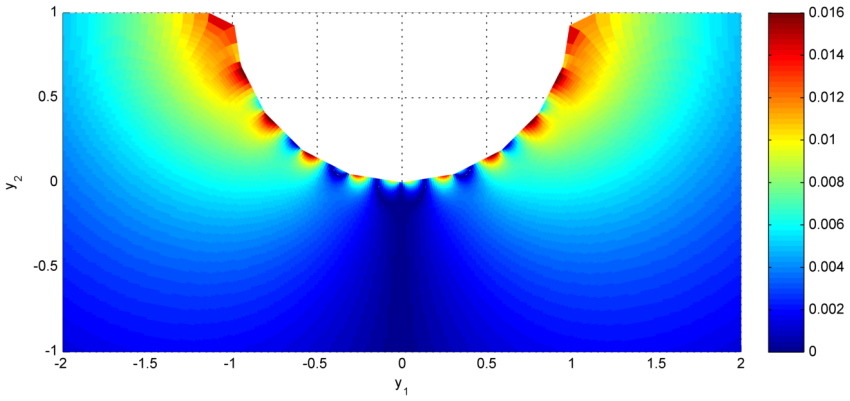

(a) Computational Velocity $U' = 1.98648$, Polygon Vertices = 20, Grid Points = 100,000

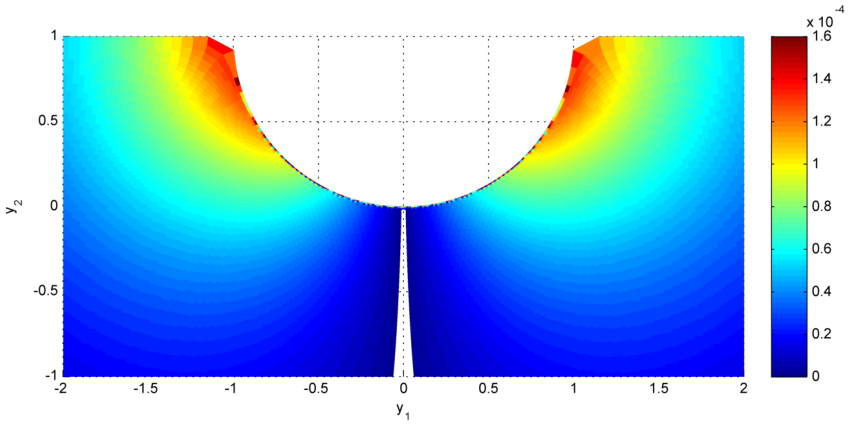

(b) Computational Velocity $U' = 1.99986$, Polygon Vertices = 200, Grid Points = 100,000

Figure 5.8: Variation in absolute error with changes in vertex density.

Just how accurately we need to represent an arc using straight lines before we can be assured of reasonable accuracy is directly related to how accurately the value of π can be calculated for each of the polygons specified. For a computationally cheap 1,000 point grid we evaluate a forward map for a range of polygon vertex densities. The variation in *relative* error is given in Fig. 5.9.

The variation in the error, shown in Fig. 5.9, is compared to how accurately the value of π can be calculated for a given polygon used to approximate a circle. If we derive a general expression for π calculated by considering a unit diameter, n-sided polygon as an approximation for a circle, we can obtain a variation in the error by increasing the number of sides of the polygon. *Note: that there are two possible expressions – either the polygon faces, or the polygon vertices, can lie on the circle being approximated. These two values actually provide the error bounds of the approximation. For the*

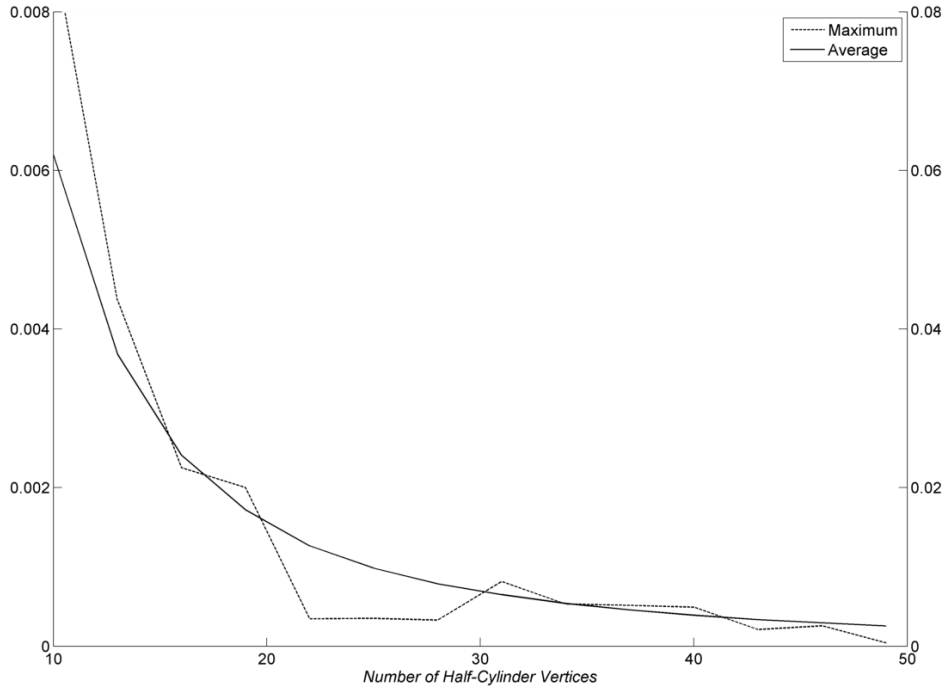

Figure 5.9: Maximum (right-hand scale) and Average (left-hand scale) relative error with polygon vertex density

comparison here we use the average of these two values. The variation in relative error (Fig. 5.10) exactly mimics the variation in average error in Fig. 5.9. Therefore, this may be used as a suitable rule of thumb for judging the number of polygon vertices to use.

One source of error which can also be significant, especially under transformations, is that of the impact of floating point errors; expressions with singularities will be particularly sensitive to errors in the vicinity of the singularity as mentioned in the previous section. The effect of refining the grid or changing the boundary representation for the cylinder may, therefore, have an effect on both the numerical and the analytical solutions since by the analytical representation of the Kirchhoff vector component Y_1 for a circular cylinder (Eqn. (5.22)) we approach a singularity as we approach the cylinder.

$$\phi = y_1 \left(1 + \frac{1}{r^2}\right) \tag{5.22}$$

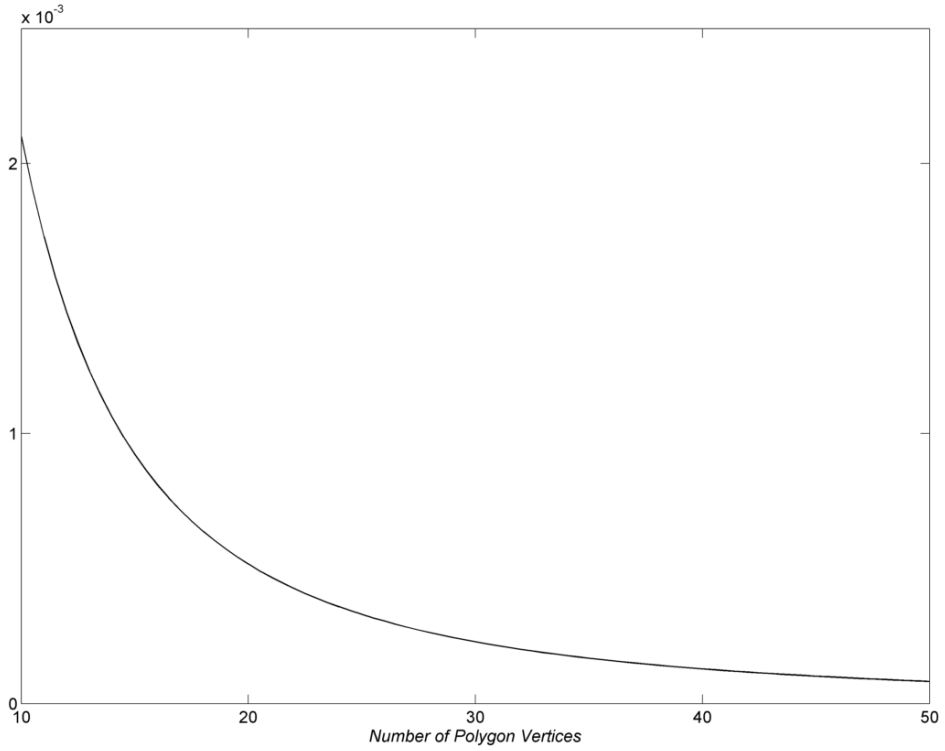

Figure 5.10: Relative error of estimation of π for polygons of increasing number of vertices

5.4.2.1 Cylinder using a Strip Map

In Section 5.4.1 we presented a means of circumventing a number of issues which arise when using a half-plane map as the computational domain. In the case of the backward-facing step, the use of an infinite strip for the computational domain allowed the use of non-singular complex potential model and allowed for correction of the mapping for arbitrary origin placement by simply adding a linear function to the complex potential.

Use of the half-plane map for the circular cylinder problem required the manual specification of the computational velocity in order to evaluate the complex potential. Continuity could not be used due to the unbounded nature of the computational domain and hence specifying this quantity accurately was difficult. Furthermore, the solution was highly sensitive to inaccuracies in this value. We demonstrate now that it is possible, using the strip map, to improve the procedure for computing the potential flow solution around the cylinder. In order to implement the new transformation, in the physical domain we require the addition of a non-physical wall parallel to the line of symmetry. The main advantage gained by taking this approach is that in the

imaginary direction (perpendicular to the flow direction) the fixed upper wall in both the physical and computational domains allows us to understand any scaling of the flow geometry through continuity and account for it using a constant scaling factor rather than the highly sensitive, variable factor required for the half-plane map, discussed in detail in the previous section. However, as this wall is non-physical, it must be placed sufficiently far away from the cylinder surface that its influence on the flow, which would exist in the absence of the wall, is negligible.

It is useful to ascertain just how far away the non-physical wall must be placed given the cylinder diameter. We consider the transformation in Fig. 5.11. As illustrated by Figs. 5.8a and 5.8b, the number of vertices used to approximate the curved cylinder surface is an important source of error. In order to reduce the source of error in the calculation to those related to the non-physical wall placement only, the half-cylinder surface is approximated by 50 vertices, giving a maximum relative error, according to Fig. 5.9, of the order 1%. This ensures that any error in the field is given principally by the placement of the non-physical wall. As was the case with the backward-facing step problem, we have a dummy vertex located on the non-physical wall (labelled Z in Fig. 5.11). The vertical placement of this vertex is dictated by specifying the channel width h. We consider a range of values $2 \leq h/r_0 \leq 20$, where r_0 is the cylinder radius. This range is sufficient to show the trend. We fix the observer grid arbitrarily $-10 \leq x_1/r_0 \leq 10$ where at the grid edges the disturbance of the flow due to the presence of the cylinder is suitably small such that all of the most dramatic behaviour is captured. In the vertical direction we fix the grid at the nearest location the non-physical wall is placed $h/r_0 = 2$.

Figure 5.12 confirms that the error in the calculation decreases as the non-physical wall is moved further away from the cylinder surface with values of $h/r_0 = 20$ giving average absolute errors of 10^{-3} and relative errors less than 1%. When compared with the improved half-plane procedure (Fig. 5.6) we may conclude that the use of the strip map allows potential flow solutions to be computed with an accuracy comparable to, or better than, the half-plane map but with the significant practical advantage of using a computational velocity deduced from continuity rather than empirically. Finally, we note that the execution time does not depend on the wall placement as the number of boundary nodes used to describe the polygon in the physical domain does not change

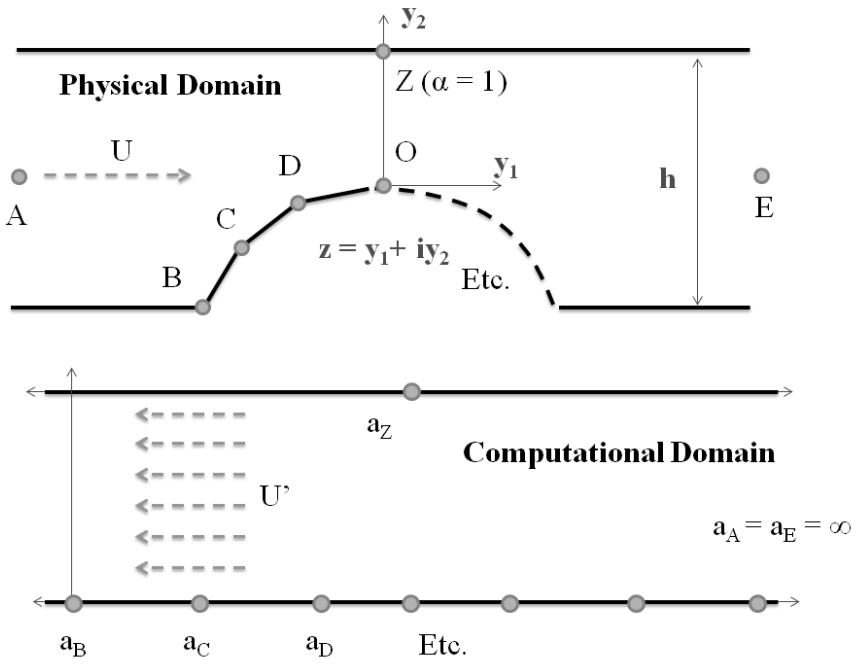

Figure 5.11: Circular cylinder problem in both the physical and computational strip domain.

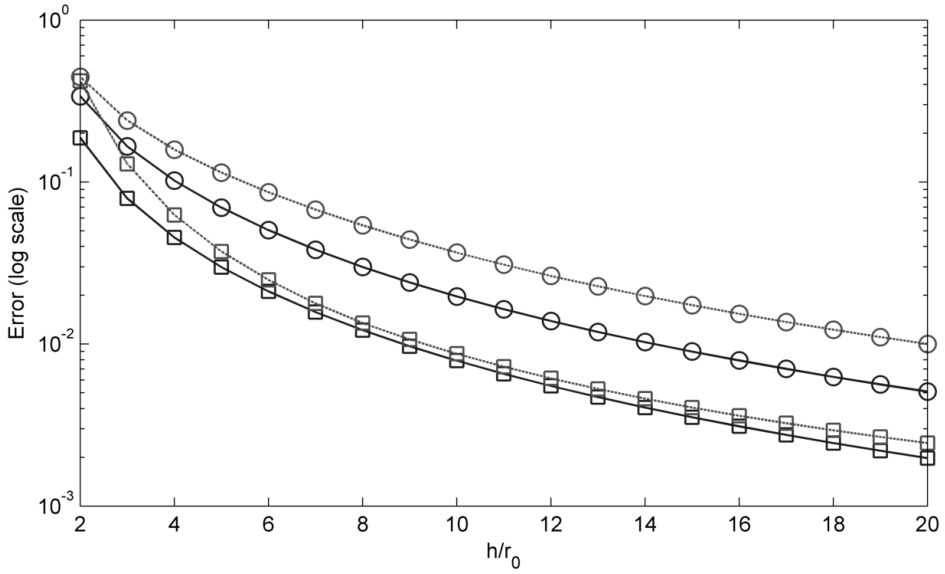

Figure 5.12: Average (solid) and maximum (dashed) Absolute Error (circle) and Relative Error (square) in the numerical velocity potential around the circular half-cylinder computed using a strip map.

with wall placement and the time taken to execute the algorithm is independent of polygon side length. It is therefore conceivable to place the wall at a distance away far in excess of what is necessary to ensure any error due to the wall placement is eradicated in a practical sense.

5.4.3 Execution Time

One of the motivations of using hybrid schemes for acoustic calculations is the benefit of a reduction in execution time of the code compared with exclusively numerical schemes. The effects of polygon vertex and grid density on the time taken to complete the two phases of the numerical method is therefore important. The time taken to construct the mapping function, is expected to increase with the number of vertices used to define the mapping. However, it will also be affected by the aspect ratio of the geometry and issues of vertex crowding [164, 250]. We do not present any investigation into the impact of these two issues here as a modification to the mapping formulation may be implemented to mitigate the effect [335]. Instead, we choose a geometry free of these features for the test. In the second phase of the computation, the computed mapping is evaluated to transform the analytical solution back to the physical domain at a number of grid points. The number of grid points is specified by the user. Due to the semi-analytical nature of the method, the number of grid points does not affect the accuracy of the result, but only serve as points at which the compact Green's function should be known. The precise number of points chosen depends on how the Green's function computed is to be subsequently used but could range from a single point to a dense grid depending on the context. The simulations were performed on a PC using the Intel Core i7 870 CPU and the results of Fig. 5.13 confirm a linear relationship with map evaluation time but a non-linear relationship with map construction time. Where the observer grid is large, the latter time becomes a negligible component of the overall computation time for all but very complex geometries.

It is important to note that the method may specify the grid in either the computational domain or the physical domain. In the latter case, the grid points must be mapped using the inverse transformation to the computational domain (grid inversion). The evaluation of this inverse transformation is an iterative procedure [90] and

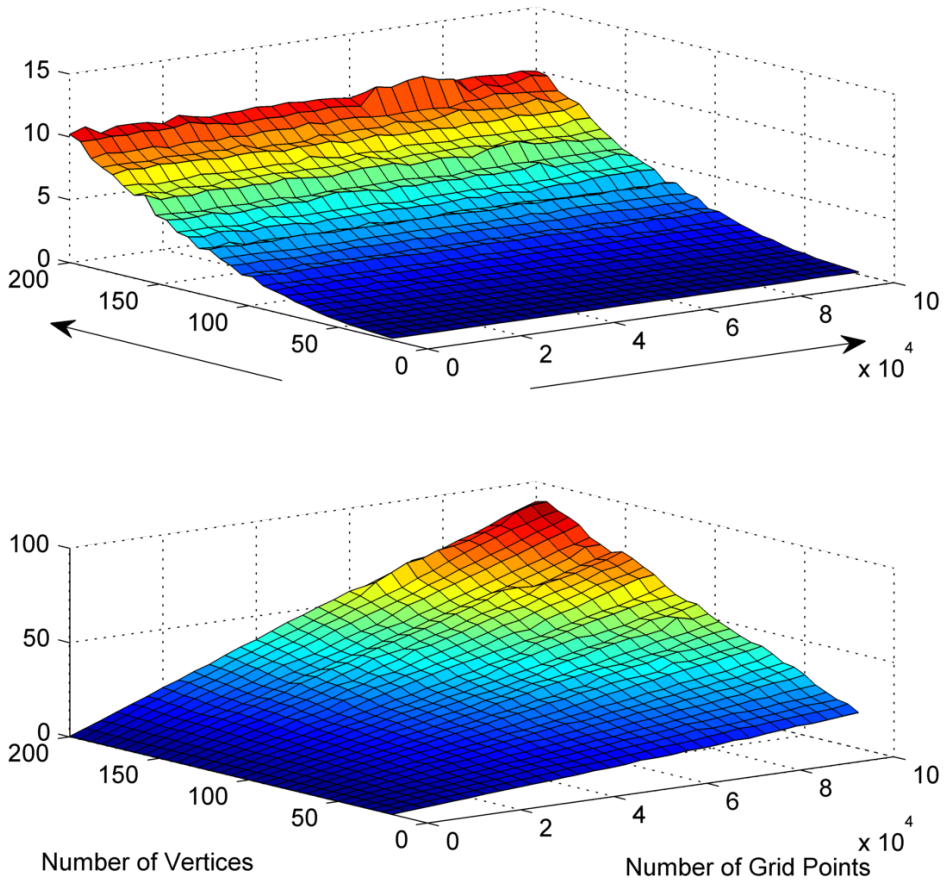

Figure 5.13: The computation time (in seconds) required for construction of the mapping function (top) and evaluation of the mapping function over the grid points (bottom)

poor conditioning of physical grid points can result in a large number of iterations being required for convergence. The advantage of using grid inversion, however, is that grid point distribution may be performed to effectively capture the features of the geometry. The time taken to invert the half-plane map was recorded for 50 different grid sizes consisting of computational points ranging from 2,500 to 1,000,000 in number. The inversion of the maps in these cases gives the approximately linear variation in execution time we saw in Fig. 5.13 but with some spread. The apparent spread of the results in Fig. 5.14 about the straight line is easily explained from knowledge of the inversion process: In order to invert a Schwarz-Christoffel map, Newton-Raphson iteration may be used, beginning with an initial guess obtained from the solution of a Ordinary Differential Equation, in order to obtain a converged solution to the inverted map. Currently, this is the most robust method available for map inversion. Hence, the performance of this procedure is dependent on the conditioning of the forward map at the computational points. As the grid sizes increase we can see a significant impact of the convergence rate of this iterative procedure on the recorded execution time, with the additional time required for convergence at problematic points increasing the overall execution time by around 40% for a relatively insignificant increase in the number of points. Likewise, increases in grid points by the same increment may also see a decrease in execution time by a similar factor.

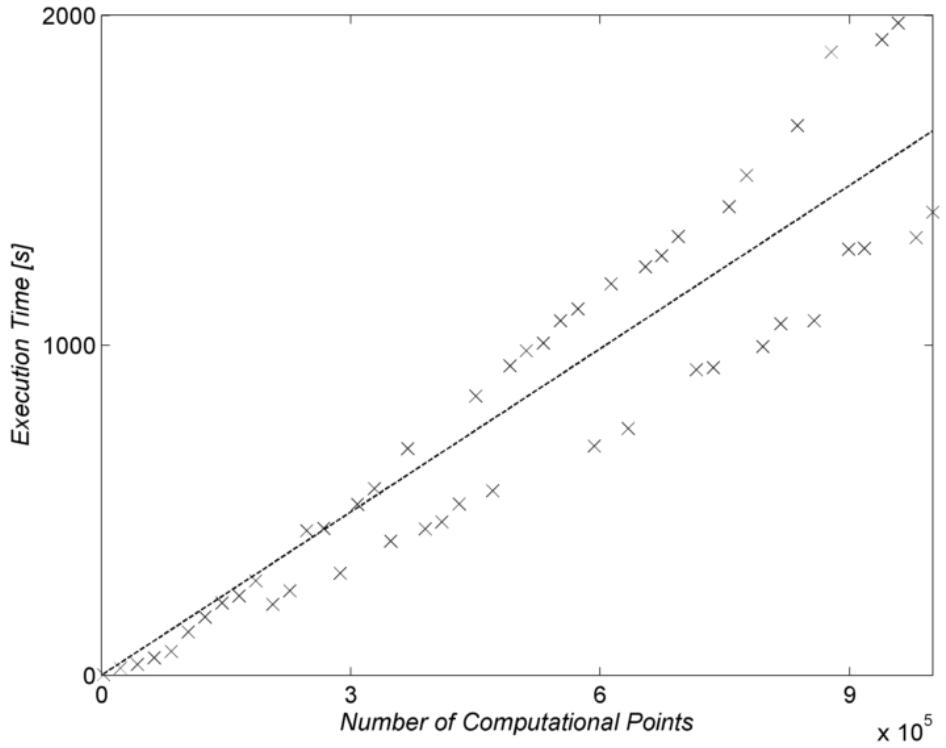

Figure 5.14: Variation of computation time involving map inversion with number of grid points. The upper and lower bounds relate to the convergence ability of the iterative process used to invert the map. The linear plot is selected arbitrarily for illustration of the trend.

5.5 Application to 3D Problems

Although we have thus far studied only 2D applications, the inherent two-dimensionality of the method does not preclude treatment of three-dimensional problems. We demonstrate 3D capability now by describing the computation of the compact Green's function for a 3D projection from a rigid half-plane, specifically a hemispherical bump. This problem is selected not for its realism but as a means of validating this approach to 3D Green's function evaluation. A realistic example would then simply be an extension of this problem where the hemisphere may assume a suitable shape and the conformal mapping re-solved for the new geometry.

The observer is assumed in the far-field as usual and the source within one characteristic dimension of the projection, within which the origin is contained (the restriction on the origin location is not strictly necessary for validity). Considering the reciprocal problem, the analytical solution may be constructed from the Green's function for a rigid half plane (the sum of two free-space Green's functions Eqn. (4.4), one for the real source at $\mathbf{x}$ and one for its image at $\bar{\mathbf{x}}$)

$$\hat{G}(\mathbf{x},\mathbf{y},\omega) = \frac{e^{ik|\mathbf{x}-\mathbf{y}|}}{4\pi\,|\mathbf{x}-\mathbf{y}|} + \frac{e^{ik|\bar{\mathbf{x}}-\mathbf{y}|}}{4\pi\,|\bar{\mathbf{x}}-\mathbf{y}|}$$

plus a first order correction for the presence of the bump. The Green's function is then

$$\hat{G}(\mathbf{x},\mathbf{y},\omega) \approx \frac{e^{ik|\mathbf{x}-\mathbf{Y}|}}{4\pi\,|\mathbf{x}-\mathbf{Y}|} + \frac{e^{ik|\bar{\mathbf{x}}-\mathbf{Y}|}}{4\pi\,|\bar{\mathbf{x}}-\mathbf{Y}|} \tag{5.23}$$

where the Kirchhoff vector components $Y_2 = y_2$ and Y_1 and Y_3 are the potential flow solutions Eqn. (5.22). Note that the Kirchhoff vector components Y_i are functions of the local radius of the hemisphere $a(y_j)$ where y_j refers to one of the components of the source location and $i \neq j$. This radius is the radius of the hemisphere obtained at the intersection of the 3D geometry with a 2D plane intersecting with the source point but normal to the unit vector in the y_j direction as in Fig. 5.15. Given that, if $|\mathbf{y}| > a$, the scattered field would vanish. We therefore specify the principal dimension l in this example to be equal to a. For a given source position $\mathbf{y}$, we compute the Kirchhoff vector components by solving the two individual potential flow problems equivalent to Fig. 5.1. We specify the source position in spherical coordinates $\bar{\mathbf{y}} = (r,\theta,\phi)$ with origin coincident with the centre of the hemisphere base as $\bar{\mathbf{y}} = [1.1a \quad 0 \quad \pi/4]^T$. If we convert these into Cartesian coordinates we see that this problem is no different from that of the circular cylinder studied in 2D earlier. All that is required is that we solve two complex 2D problems with coordinates $z = y_a + iy_b$ with the radius of the hemisphere a function of coordinate y_c with $c \neq a \neq b$ but $\{a,b,c\} \in \{1,2,3\}$. Having computed the potential flow solutions and hence the Kirchhoff vector components, the compact Green's function may be evaluated using Eqn. (5.23).

Note, that in order to compute the compact Green's function for 3D geometries in free-space using Eqn. (5.2), (including model geometries like a sphere, ellipsoid, or prolate or oblate spheroid), all three Kirchhoff vector components would need to be computed from the *three* corresponding potential flow problems. In this case, all that is required is a third application of the method described in this chapter for the extra potential flow problem.

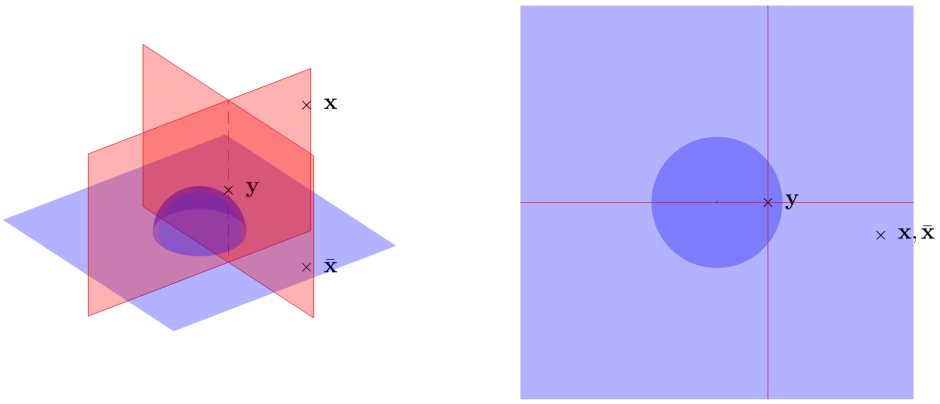

Figure 5.15: Identification of the two potential problems to be solved to obtain the Kirchhoff vector components for the 3D problem of a hemispherical projection from a rigid half-plane. The source is located at $\mathbf{y}$ and the observer and its 'image' are at $\mathbf{x}$ and $\bar{\mathbf{x}}$ respectively. These latter two locations are illustrative purposes only and will be allowed to vary whereas the source positions stays fixed. In practice, varying the source for a fixed observer position is also a useful activity to provide data on how the source position affects a particular observer location.

5.6 Compact Green's Function for a Throttle

Another class of realistic problems, for which a 2D Green's function is particularly useful, are those 3D problems dominated by 2D effects. One of the earliest observations of the (then inexplicable) damping of acoustic waves through vortex shedding was made by Borth in 1916 [40]. Similar mean-flow acoustic problems have been successfully analysed using 2D Green's functions [94] due to the relative insignificance of 3D effects. Sharp edges within the vicinity of a sound source are known to be also an important means of noise amplification [118, 156]. This effect is confined to dipole (or higher multipole) sources which depend on the derivatives of the Green's function. We consider here a 2D throttle mechanism in a duct where the baffle is set at a 45 degree angle. Unlike previous applications in this chapter, we fix the observer position and vary the source position. This allows us to investigate how the position of the source affects a particular value of the Green's function in the observer field. The exploitation of the symmetry of the compact Green's function in this way is particularly useful when studying the scattering effects of particular geometrical features. We compute approximations to the derivatives using a second-order finite difference scheme over the point-evaluated Green's functions. Two baffles of different thickness (tip radii) are considered. The resulting variations in Green's function illustrate the scattering and amplification effects due to both source position and baffle tip radius. The two

numerical experiments with their potential flow solutions are shown in Fig. 5.16.

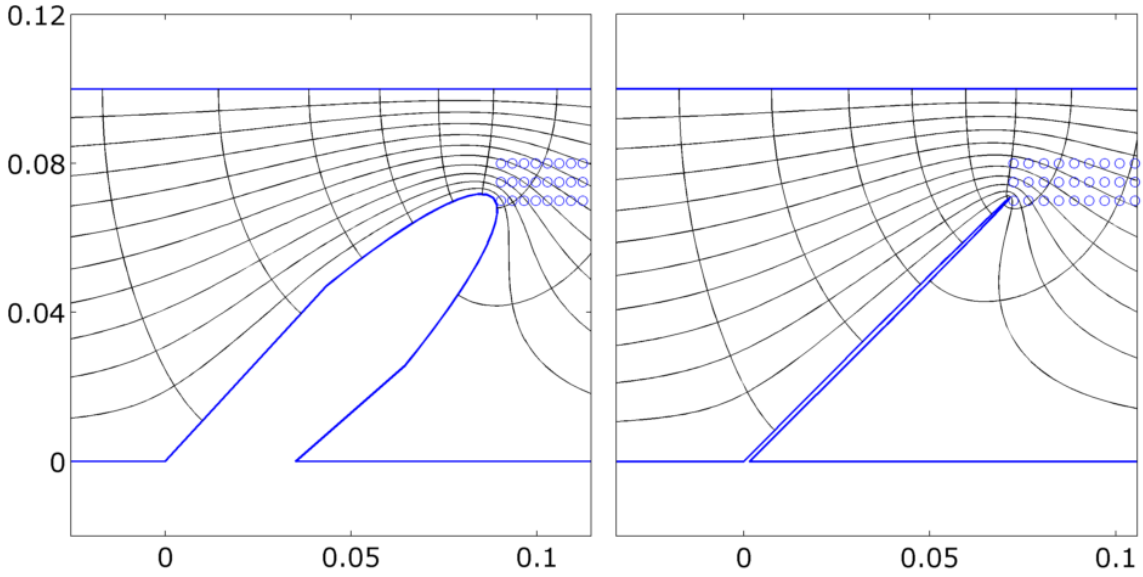

Figure 5.16: Two baffle geometries analysed with the array of source positions shown as circles. Note that the two horizontal-axis scales are slightly different for clarity but the spacing of the source locations is identical in both cases.

The calculation uses the semi-analytical method described earlier in this chapter. Both geometries are mapped from the straight-sided channel, as in the validation cases, in which we define uniform potential flow. The baffle tip is defined by half an ellipse whose line is approximated by 30 straight-line segments. This number is chosen to allow accurate description of the curved tip of the baffle without crowding the region with vertices. Crowding not only increases the time taken to solve the mapping but also can lead to instability in the mapping procedure as the spacing of the x-coordinates of the vertices at the tip of the baffle tends to floating point. The crowding of vertices has been controlled in our implementation by specifying the distribution of the x-coordinates of the ellipse with polynomial rather than linear spacing. The height of the duct is chosen to be 100mm and hence we choose a frequency of 1kHz for our sound source which is placed at locations adjacent to the baffle tip at a number of points within the limit of validity of the underlying theory. The observer point is chosen 25 wavelengths away from the source on the duct centreline. All parameters have been specified in order to comply with the three assumptions in Section 5.2. The derivative of the Green's function with respect to the source y_2-coordinate is shown in Fig. 5.17 where the vertical position of the source locations correspond to the middle of the three rows of sources shown in Fig. 5.16.

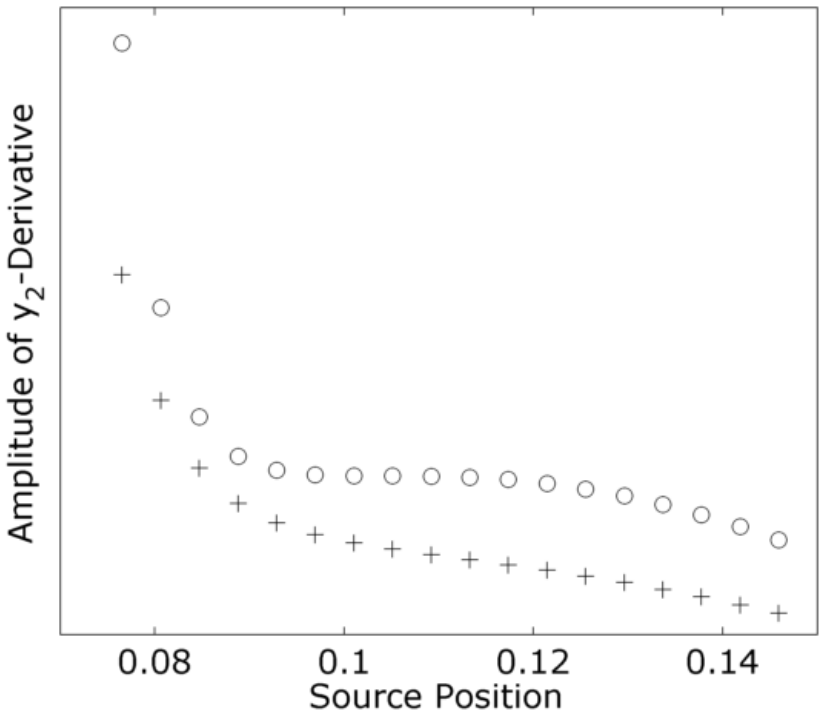

Figure 5.17: Variation of the magnitude of the gradient of the Green's function with source position two baffle geometries. The circles correspond to the thinner baffle.

The variation in the derivative of the Green's function is as expected with sources in close proximity of the baffle being amplified more than those further away. The variation also illustrates the tendency to singular behaviour for an infinitely sharp corner. Finally, the sharper-tipped baffle is shown to amplify the derivative of the Green's function more than the round-tipped baffle, which agrees with the amplification behaviour suggested by the work of Ffowcs-Williams & Hall [118].

5.7 Summary

In order to extend the use of hybrid acoustic prediction schemes to consider propagation within geometries of arbitrary boundary we have developed a method capable of computing a Green's function which represents the scattering effects of arbitrary 2D rigid boundaries. We have shown that for a number of scenarios where we have a near field source and a far-field observer adjacent to a compact body, the specific approximation to the Green's function (known as the compact Green's function) for the Helmholtz equation can be computed semi-analytically. This Green's function may then be passed to an acoustic analogy for solution of the far-field sound, or used with

a range of source values to investigate the amplification and scattering of geometrical features. The calculation of the compact Green's function using the semi-analytical method presented centres on the construction of one or more potential flow solutions within the geometry of interest. The method uses an existing software package to transform a more complex physical domain into a simplified computational domain where potential flow solutions may be easily represented analytically and evaluated over a grid of points. We have validated the results against two 2D benchmark problems, described its extension to 3D problems and demonstrated its use in studying the behaviour of a more arbitrary geometrical feature (a baffle).

Geometries featuring curved boundaries have been treated by approximating the curved boundary as a series of straight boundary segments. In order to achieve a high degree of accuracy in these cases, a large number of approximating segments is required with computation time scaling linearly. If the appropriate computational domain is chosen for the transformation, we have shown that non-singular expressions for the potential flow in the transformed domain may be used with only a simple modification to account for translation of the origin if necessary. Furthermore, the parameters for the potential flow solution in this domain may be deduced from simply considering continuity. Any other sources of error have been identified and mitigated to ensure the robustness of the procedure.

For the test problems considered, computation time using MATLAB is acceptable and the method achieves relative errors of less than 1% or better. Additional functionality may be implemented to increase the versatility of the numerical conformal mapping procedure and allow application of the method presented in this chapter to an even wider range of geometries.

Chapter 6

Boundary Element Method

The need for demanding computational resource for noise prediction arises due to the discretisation of the usually extensive region between source and observer. If the observer is located a large distance from the source, the cost of performing acoustic propagation through this meshed region becomes prohibitive. As we wish to perform Green's function computation as a relatively inexpensive precursor to a hybrid calculation, it is sensible to consider the use of boundary integral techniques to evaluate the Green's function. This chapter examines the use of the Boundary Element Method (BEM) for the numerical calculation of Green's functions. Specifically we focus on a particularly useful class of 2D problems – acoustic scattering in a channel with or without geometrical obstructions [147, 163]. Such problems are typically dominated by 2D effects and their role in sound attenuation has been observed for some time [40]. Although the treatment in this chapter is limited to 2D problems, the principles are easily extended to 3 dimensions.

The typical version of the direct BEM formulation used in this chapter, requires a closed boundary on which either the solution variable or its normal derivative is known on every segment of the boundary. For the semi-infinite class of domains we examine in this chapter, such a specification is not readily available. We could transform the geometry such that it becomes finite but this procedure has proven to be of little use when the solution is oscillatory in the far-field [136]. Instead, we truncate the channel in both the upstream and downstream directions, then specify a non-reflecting boundary condition (NRBC) on these boundaries which simultaneously closes the BEM system mathematically. For the best performance, this boundary condition ought to

be based on an exact representation [84, 137, 139, 146, 178, 324, 328]. However, many exact representations are only available for relatively simple boundaries and are usually non-local in nature since they couple degrees of freedom on the boundary. This latter property can make numerical implementation expensive for large-scale problems [336] and local approximations to these exact boundary conditions, devised using discretised pseudo-differential operators [107] or the method of asymptotic expansions [22, 23], have developed as an alternative. However, for certain problems this claim has been refuted through efficient inclusion and evaluation of non-local boundary conditions [178, 246]. One reason for the additional expense in computing non-local boundary conditions is due to the computation of a large number of integrals. We show in this chapter that the inclusion of a non-local boundary condition in the constant element, direct BEM avoids the additional numerical integration entirely, and thus allows an accurate truncation of the BEM domain at little cost.

6.1 Introduction to Boundary Methods

The concept of surface integral methods has been discussed already in terms of the Kirchhoff and FW-H methods. These two methods are examples of how a boundary value problem can be reduced to a boundary integral equation (BIE). This reduction is achieved through application of integration to the original governing differential equation followed by the substitution of the boundary conditions. This latter step yields boundary integral terms as well as the volume integral terms of the equation. Given a suitable fundamental solution, the volume integral can be made to vanish and what remains is a BIE which is usually computationally easier to solve than the original BVP. Specifically, the fundamental solution must satisfy the homogeneous equation everywhere in the domain. Details on this common form of boundary reduction can be found in many textbooks on boundary methods, for example by Brebbia & Dominguez [44]. Fundamental solutions for many differential operators are known analytically and therefore BIEs are a popular method of solving differential equations in extensive, complicated geometries in a wide range of fields [74, 166, 362].

6.1.1 Boundary Element Method

Where the solution procedure of the BIE formulations cannot be carried out analytically, we may turn to the Boundary Element Method (BEM). This method attempts to solve a particular BIE through discretisation of the boundary into elements over which nodal values of the set of boundary conditions in terms of the solution variable and its normal derivative are known, and their variation over the element approximated. BEM is a well established technique with many open source implementations available, see for example the code of Kirkup [179]. The textbooks of Brebbia & Dominguez [44] and Ang [9] provide further information on the theory and practice of the BEM.

6.1.2 Issues with Implementing BEM

Many problems treatable with BEM are also treatable with the Finite Element Method (FEM). The difference between these two is principally that the latter requires discretisation of the problem domain. In the case of acoustic problems, this domain may be extensive, particularly for an observer in the far-field. Use of traditional domain techniques is not only expensive but also encounters many of the problems associated with CFD schemes (see earlier). Some advantages of using BEM are discussed by Zienkiewicz *et al.* [369] and are included in the following list:

1. Infinite regions are straightforward to analyse with the BEM.
2. Singularities can be incorporated in BEM formulations.
3. Surface integrals are required for simple sources instead of volume integrals (can be computationally less demanding due to the reduction in dimensionality).
4. Large regions can be analysed without the computational cost associated with domain discretisation.

Since the Green's function contains a singularity at the source position, the second advantage is of particular value to this research. The BEM has been used to compute the Green's function before by Rokhlin [268, 269]. However, BEM does provide a number of challenges in its implementation. First, BEM is not ideally suited to analysing thin structures: near-singular behaviour is observed when the structure folds back

on itself [59]. Cheng *et al.* [59] give the example of thin projections in a recessed pipe. They suggest the use of multi-domain BEM as one way to alleviate this problem. This involves defining sub-domains and coupling separate BEM problems in each sub-domain using matching conditions at the boundaries. Also, in cases where the boundary geometry changes abruptly or boundary data exhibits singular behaviour, the BEM can be slow to converge to the expected solution [218]. Marin *et al.* [218] present a modified BEM formulation which greatly improves the accuracy without the need for mesh refinement near a boundary singularity. Furthermore, Zienkiewicz *et al.* [369] highlight the following drawbacks to using the BEM over the FEM:

1. The FEM can handle more complicated equations as an analytical fundamental solution is not needed like in the BEM.

2. Discretisation is localised making the matrix system banded unlike the full matrices of the BEM.

3. Nodal parameters are physical quantities where it is not necessarily the case for the BEM – (this is only true for indirect BEM formulations).

The boundary conditions developed in this chapter also produce full matrices so the second disadvantage is not as pronounced. Furthermore, the context and implementation selected render the other two irrelevant. The remaining issues of implementation in BEM relate primarily, but not exclusively, to the integration involved in the solution process and efficient solution of the resulting system of equations. The work of Rokhlin [268, 269] and also Bebendorf [24] suggest improved solution methods which involve the construction of a degenerate kernel (finite sums of separable functions to approximate the operation described by the coefficient matrix), or low-rank matrix approximations of blocks of the original coefficient matrix. In both cases, the approximations can lead to redefined systems which are better conditioned or sparser in nature than the original. Rokhlin in particular suggests fast solvers for the system generated by the indirect BEM which reduces the scaling of computation time on the system size. Grasedyck [134] also suggests an algorithm capable of reducing the storage requirements.

With regards to the integrals, due to the use of the fundamental solution (a Green's

function) they inevitably involve integrands which contain singularities over the range of the integration. Their computation is, therefore, one issue which has received particular attention, with recommendations available for many scenarios by Hall [144]. These solutions consist of:

1. Row-Sum Elimination (each row of matrices must sum to unity hence the diagonal element can be found from the off-diagonal elements [44]).
2. Exact Integration over simply boundaries (analytical representations [309]).
3. Specialised Gaussian quadrature schemes.
4. Singularity cancelling transformations (smoothing or cancellation of the singularity).
5. Singularity subtracting methods.

In many cases, the integrals may be computed using standard numerical methods such as Gaussian quadrature and there are numerous textbooks which set out the variety of methods available (see for example Davis & Rabinowitz [83]) for different classes of integrands. However, in the field of BEM the use of available methods is not always standard since the nature of the integrand differs with governing equation and order of the elements. In some cases of BEM even generally robust numerical integration schemes have historically performed poorly with the need for additional transformations which aim to weaken the singularity such as the transformation of Sato *et al.* [277]. In the relevant case of the Helmholtz equation, analytical solutions have been shown to exist for some of the typically encountered singular integrals involving Hankel functions [309] which, being exact, eradicate the source of error completely. Where the derivative of the solution is required in the domain, the standard BIE used with the BEM can be differentiated. This results in integrals with hyper-singular kernels [244, 333, 339, 361]. The issues of numerical integration are, therefore, more pronounced with these formulations. A recent numerical implementation of the hyper-singular formulation [265] is shown to work well for the benchmark problems presented. For specific situations of nearly singular integrals, methods such as that proposed by Elliot & Johnston [104] may be used at the expense of complicating the

implementation of the overall code.

Finally, an issue specific to the solution of the Helmholtz equation is the non-uniqueness of the solution at particular frequencies when solving the exterior problem. Numerical solution of the Kirchhoff-Helmholtz Integral equation fails to obtain a unique solution at certain frequencies for exterior acoustic problems. The characteristic frequencies of the exterior Neumann problem are found to be equal to the eigenfrequencies of the interior Dirichlet problem. Since the solution of the interior Dirichlet problem has eigenfrequencies which indicate a resonance, and these are shared by the exterior Neumann problem which has no physical resonances, then non-physical resonances are established in the exterior problem solution. The use of a special formulation known as the Combined Helmholtz Integral Equation Formulation (CHIEF), proposed by Schenck [279], is a method of addressing the issue. It combines the exterior and interior Helmholtz integral formulations. For the exterior problem this adds a small number of additional equations to the exterior problem system. The additional equation requires the interior problem to be satisfied as well as the exterior problem for specific interior points known as CHIEF points. The selection of these CHIEF points must be done carefully otherwise, if one is chosen on a nodal point of the field inside the surface, then no constraint is applied and a non-zero field inside the surface may still exist. Choosing appropriate points is more difficult at higher frequencies. One way of overcoming this is to choose more CHIEF points than necessary in the hope that most of them will be suitable points. The resulting over-determined system of equations can be solved in a least squares sense although this procedure was criticised for being a complicated and inefficient way of treating the problem by Buick *et al.* [51]. A review by Zaman [362] provides details of the range of boundary formulations most useful for acoustic scattering problems. A more general discussion of the issues prevalent to BEM can be found by Treeby & Pan [333] along with a summary of proposed resolutions.

6.1.3 Hybrid BEM/BIE Schemes

A novel method pioneered by Epstein & Bliss [108] is that of a hybrid BEM formulation which uses both the numerical BEM procedure as well as analytical source representations where possible. The analytical near-field constructs consist of building-block

aerodynamic features. These are constructed using a typical panel method (also called 'singularity methods') of early aerodynamics. A far-field numerical solution is then computed with the matching between the two cancelling their effects in the other's region of the field. The approach is known as Analytical Numerical Matching (ANM) and has shown success in the introductory papers on the subject [108, 109]. Due to the use of a panel method to model the boundary behaviour, its use for arbitrary scattering devices or complicated sources is restricted and Epstein & Bliss recognising the large number of limitations of using singularity methods. In general, the smoothing feature of the panel method must be chosen to maintain accuracy in the transition zone between the two solutions which is shown to be non-trivial.

Other hybrid BEM methods include the shallow water code of Grilli *et al.* [135] where BEM solutions can be matched to solutions expressed as eigenfunction expansions in the far-field where the geometry is more regular. This latter method is useful at capturing the important effects efficiently by applying the most expensive method only where it is needed but it may be regarded as being reasonably limited to a class of problems where the matching is viable. A recent review by Chandler-Wilde *et al.* [55] examines the development and use of these so-called hybrid-BIE methods. More recently there has been a move to use asymptotic expansions as opposed to eigenfunction expansions for hybrid methods which allows matching to take place in far-field regions where the solution in terms of an eigenfunction expansion may be unknown. Such uses of far-field solutions are more akin to their use as boundary conditions than as hybrid methods.

6.2 Green's Function for the Helmholtz Equation

Time-harmonic acoustic problems, in the absence of a mean flow, may be represented by a Helmholtz Boundary Value Problem (BVP) of the form

$$(\nabla^2 + k^2)\hat{\phi}(\mathbf{x},\omega) = -\hat{q}(\mathbf{x},\omega) \qquad \text{in} \quad \Omega \tag{6.1a}$$

$$\hat{\phi}(\mathbf{x},\omega) = a(\omega) \qquad \text{on} \quad \Gamma_1 \tag{6.1b}$$

$$\frac{\partial\hat{\phi}}{\partial n}(\mathbf{x},\omega) = b(\omega) \qquad \text{on} \quad \Gamma_2 \tag{6.1c}$$

In the most general case we assume the source term to be a function of spatially compact support

$$\text{supp}\,[\hat{q}(\mathbf{x},\omega)] = \mathbf{y} \in S$$

where S represents the source region. One method of developing an analytical solution to this BVP is to transform the differential equation into an integral equation in which we can substitute the boundary conditions (Eqn. (6.2)). These boundary conditions are incorporated in the Green's function $\hat{G}(\mathbf{x},\mathbf{y},\omega)$. This is the solution to the singular form of the original differential equation Eqn. (6.3) and satisfies the original boundary conditions. Physically, it may be interpreted as an outgoing wave produced by an impulsive unit point source at $\mathbf{y}$.

$$\hat{\phi}(\mathbf{x},\omega) = \int_{-\infty}^{\infty} \hat{G}(\mathbf{x},\mathbf{y},\omega)\hat{q}(\mathbf{y},\omega)\mathrm{d}^3\mathbf{y} \tag{6.2}$$

$$(\nabla^2 + k^2)\hat{G}(\mathbf{x},\mathbf{y},\omega) = \delta(\mathbf{x}-\mathbf{y}) \tag{6.3}$$

In the absence of boundary conditions we may consider this wave to propagate in free-space and hence we often use the free-space Green's function, readily available in analytical form. However, the introduction of boundaries and hence associated boundary conditions complicate matters as an analytical representation of $\hat{G}$ is difficult to construct. In the remainder of this chapter we show that the BEM can be a robust and accurate means of numerically computing Green's functions within arbitrary geometries. We now develop a robust BEM formulation suitable for solving a class of two-dimensional Helmholtz BVPs, which may be applied in finite, semi-infinite, or infinite geometries.

6.3 Direct Collocation Boundary Element Formulation

When analysing problems on infinite domains, the Boundary Element Method (BEM) offers a number of advantages over the Finite Element Method (FEM) [362, 369] as discussed earlier: First, the discretisation is limited to the boundary and not the entire

domain which serves to reduce storage requirements in particular for large domains. Second, for many problems the BEM requires only the calculation of surface integrals as opposed to volume integrals. Third, the use of a fundamental solution (free-space Green's function) in the BEM formulation automatically satisfies the radiation condition for acoustic problems without any additional constraints on the BVP. Finally, BEM is also capable of solving exterior flow problems (infinite domain problems) without the need for domain truncation since only the closed finite domain needs to be discretised. Solution of the same problem using FEM would require a non-reflecting boundary to be specified between the finite boundary and infinity to close the problem. However, the matrices which comprise BEM are full as opposed to the sparse matrices of FEM. This is due to the slow decay of the free-space Green's function used as part of the formulation [269] which may reduce the efficiency of the matrix algorithms. This may explain the continued interest in the development on NRBCs for FEM. A number of different BEM formulations exists depending on the type of boundary reduction procedure used. The direct formulation is arguably the simplest to derive and implement with many introductory texts on the subject of BEM focussing on this formulation in particular [44]. For those problems where a single BEM application is unsuitable, for example, when the domain folds back on itself [59] or very thin structures where more boundary elements would be required than domain elements [365], multiple applications (sub-structuring) or even the coupling of BEM and FEM is seen to be a useful means of calculation [124, 165, 369].

We first present the direct BIE representation of the general BVP Eqn. (6.4) where, for convenience, we have dropped the hat notation. The derivative of the solution ϕ with respect to the outward normal is represented by the symbol ψ. This considers a BVP where the boundary is closed and comprises three different types of boundary characterised by the information known on the particular boundary segment: Γ_1-type (type 1) boundaries contain known values of ϕ, Γ_2-type (type 2) boundaries contain known values of ψ. We also consider an extension to this problem where we also have Γ_3-type (type 3) boundaries which are truncation boundaries and hence contain no known information (Fig. 6.1).

The traditional formulation of the BEM, based on Eqn. (6.4), is soluble while some information about the solution is known at each node on the boundary. We then

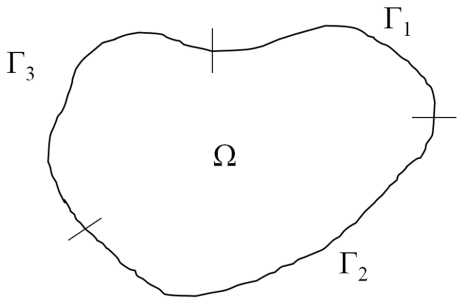

Figure 6.1: General 2D BVP geometry with the boundary segmented into those of type 1, type 2 and type 3.

extend the formulation to include boundary nodes where no information is known. In the following section, we close this under-determined system through inclusion of an approximation to a global NRBC.

Considering for the moment the case where all segments of the boundary may be classified as either type 1 or type 2, application of the weighted residual method produces the usual BIE (Eqn. (6.4)) where ϕ^* and ψ^* represent the free-space Green's function and its normal derivative for the homogeneous differential equation in free-space [44]. The double overbar signifies a known quantity.

$$c\phi + \int_{\Gamma_2} \phi\psi^* \mathrm{d}\Gamma + \int_{\Gamma_1} \bar{\bar{\phi}}\psi^* \mathrm{d}\Gamma = \int_{\Gamma_2} \bar{\bar{\psi}}\phi^* \mathrm{d}\Gamma + \int_{\Gamma_1} \psi\phi^* \mathrm{d}\Gamma \tag{6.4}$$

This statement is discretised into elements. The variation of the solution and its normal derivative over each element is considered to be constant and the nodes are located at the centre of each element. Constant elements are the simplest type of boundary element available and have been selected in this case to facilitate an easier incorporation of the Dirichlet-to-Neumann boundary condition as will become clear later on. The principle of collocation is to force the residual error at the nodal locations to zero. This is achieved by centring the fundamental solution at each node on the boundary in turn. The discretised equations will therefore apply for each fundamental solution location and we generate a system of equations to be solved for the unknown values ϕ and ψ on the boundary. For the i-th fundamental solution position we have the following discretised BIE

$$c_i\phi_i + \sum_{j=1}^{N} \left(\int_{\Gamma_j} \psi_j^* \mathrm{d}\Gamma \right) \phi_j = \sum_{j=1}^{N} \left(\int_{\Gamma_j} \phi_j^* \mathrm{d}\Gamma \right) \psi_j \tag{6.5}$$

which we represent in matrix form as

$$\mathbf{H}\vec{\phi} = \mathbf{G}\vec{\psi} \tag{6.6}$$

This formulation is soluble since type 1 and type 2 boundaries specify either ϕ or ψ at each node of the boundary, resulting in only a single unknown per element.
If we now introduce a segment of type 3 boundary as part of the problem consisting of K elements, the system becomes under-determined. One means of addressing this is to eliminate one set of unknowns through the introduction of additional equations which relate the two unknowns for each element on the type 3 boundary. In this case we end up with a system whose i-th component is

$$c_i\phi_i + \sum_{j=1}^{N}\left(\int_{\Gamma_j}\psi_j^*\mathrm{d}\Gamma\right)\phi_j = \sum_{j=1}^{N-K}\left(\int_{\Gamma_j}\phi_j^*\mathrm{d}\Gamma\right)\psi_j + \sum_{j=1}^{K}\left(\int_{\Gamma_j}\phi_j^*\mathrm{d}\Gamma\right)\psi_j \tag{6.7}$$

Now for all values of $j \in K$ we have two unknowns. What we require therefore, is to eliminate the unknown values ψ_j by using an equation which maps values of $\psi_j \mapsto \phi_j$ for $j \in K$. We call this mapping a DtN map or DtN operator.

6.4 Dirichlet-to-Neumann Operator

In order to fully determine the system of equations in the previous BEM formulation Eqn. (6.7), we require an additional set of equations which relate ϕ to ψ on the artificial boundary. Global NRBCs based on the Dirichlet-to-Neumann (DtN) operator [178] meet the requirements; using the DtN operator, the solution ϕ may be mapped to its normal derivative ψ. If applied at every node on the artificial boundary, enough additional equations are generated to close Eqn. (6.7). The DtN operator is constructed by considering the solution to the homogeneous BVP in the region beyond the truncation boundary, be that upstream or downstream. Knowledge of an analytical general solution in this region, evaluated on the truncation boundary is therefore equivalent to the solution of the interior problem on the same boundary as away from the source point (or source region if source is distributed) the two BVPs should be equivalent. The construction of the DtN operator requires knowledge of a specific homogeneous solution characterized by the type of geometry beyond the truncation boundary. It is,

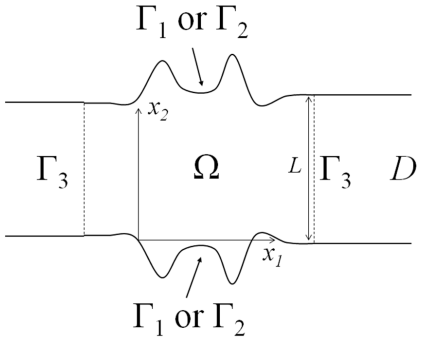

Figure 6.2: An arbitrary 2D waveguide which is assumed to be a parallel-sided 2D waveguide beyond truncation boundaries denoted Γ_3

therefore, necessary to restrict ourselves in this chapter to a subset of the general class of problem in which the domains beyond the truncation boundaries are those of rectangular channels or ducts (Fig. 6.2) [146]. Examples of DtN construction on a range of other exterior domains, in different coordinate systems, in domain decomposition methods and for different equations are available [106, 129, 137, 264], although many are still limited to regions of free-space.

The problem domain, in which the BVP defined by Eqn. (6.1) applies, is defined by Ω and the infinite analytical domain in which the homogeneous version applies D. Since we are dealing with a waveguide, it is appropriate to express the vector position $\mathbf{x}$ in terms of its scalar components $[x_1, x_2]$. We drop the frequency dependence for convenience from the propagating wave number $\gamma_n \equiv \gamma_n(\omega)$ in the following derivation. The solution to the problem in D subject to rigid-wall boundary conditions on the upper and lower walls is, therefore, given by the function $\phi(x_1, x_2)$ which, using separation of variables, may be represented by an eigenfunction expansion (Fourier series representation) in the cross-duct direction multiplied by a general outgoing wave function centred on the truncation boundary at $\tilde{x}_1$ as:

$$\begin{aligned}\phi(x_1, x_2) &= \phi_1(x_1)\phi_2(x_2) \\ &= \left[a_0 + \sum_{n=1}^{\infty} a_n \cos\left(\frac{n\pi x_2}{L}\right)\right] e^{\pm i\gamma_n |x_1 - \tilde{x}_1|} \end{aligned} \tag{6.8a}$$

Where the coefficients are the usual Euler formulae for the cross-duct Fourier series

$$a_0 = \frac{1}{L}\int_0^L \phi_2(x_2)\mathrm{d}x_2 \tag{6.8b}$$

$$a_n = \frac{2}{L}\int_0^L \phi_2(x_2)\cos\left(\frac{n\pi x_2}{L}\right)\mathrm{d}x_2 \tag{6.8c}$$

We can differentiate this with respect to the outward normal to the truncation boundary to get an expression for ψ as:

$$\begin{aligned}\frac{\partial\phi}{\partial x_1}(x_1,x_2) &\equiv \psi(x_1,x_2)\\ &= \pm i\gamma_0 a_0 e^{i\gamma_0|x_1-\tilde{x}_1|} \pm i\sum_{n=1}^{\infty}\gamma_n a_n \cos\left(\frac{n\pi x_2}{L}\right)e^{\pm i\gamma_n|x_1-\tilde{x}_1|}\end{aligned} \tag{6.9}$$

This relationship may then be used as the definition of DtN operator M defined as

$$\psi(x_1,x_2) = M\left[\phi(x_1,x_2)\right]$$

Our analysis is equivalent to the 2D rigid wall expressions of Harari *et al.* [146].

It is worth noting here that the inclusion of a DtN representation as part of a BEM is not in itself novel. One particular form of boundary reduction, known as natural boundary reduction represents the BVP as an integral equation of the form $\partial\phi/\partial n = K\left[\phi\right]$ where K is termed a *natural integral operator* [360]. This operator is equivalent to a DtN operator and allows the derivative of the solution to be computed from known Dirichlet data on the boundary. Numerical implementation of this BIE is popular, particularly through incorporation in the variational formulation of the FEM [124, 207, 244, 361]. In the next section we take a similar approach but use the DtN operator we have defined as a boundary condition to close a direct BEM system. It is apparent during our derivation that the implementation is straight forward, only if we use constant boundary elements.

6.5 BEM Implementation

The DtN boundary condition (Eqn. (6.9)) is exact. However, we should note that practical implementation requires us to truncate the infinite series and hence this exactness is lost. The waves absent from the truncated series essentially have a boundary

condition $\partial/\partial n = 0$ which not only generates reflections on the boundary for these modes but also can cause issues of non-uniqueness [138]. One solution is to ensure the number of terms in the DtN condition is large enough to include all modes required for the solution to the problem to be unique. However, as pointed out in [137], particularly for higher-dimensional problems and problems involving high frequency propagation, the series representation may contain a large number of terms, many of which are included to ensure uniqueness rather than to improve the accuracy by any appreciable amount. Their modified DtN formulation which imposes the radiation condition on these missing modes instead, is a more practical alternative.

Wave-guide problems afford a certain degree of simplification of the issue of uniqueness and reflection caused by truncation of the DtN series. In a wave-guide, the propagating modes are restricted based on the relationship between frequency and duct geometry. Since the boundary condition $\partial/\partial n = 0$ is exact for the cut-off modes, Harari *et al.* [146] and others [246] have shown that we only require at least the propagating modes in the boundary condition expansion in order for a unique solution to be guaranteed. Our truncation boundaries are placed far enough from the source to ensure all evanescent modes have decayed to amplitudes lower than the error of the boundary element scheme by the truncation boundary. We justify this quantitatively in Section 6.8.1. Therefore, the standard DtN containing a relatively few number of terms is sufficient for both uniqueness and accuracy.

To incorporate the DtN relationship into the boundary element formulation we introduce the discrete representation of the solution on the truncation boundary into the DtN operator. We label the values of ϕ_j over the outlet $j \in K$ ϕ_k. The manipulation of the coefficient integrals then uses the fact that since we have used constant (discontinuous) boundary elements, the values of ϕ_k are constant over each element on the truncation boundary. The values of ϕ_k may be brought outside the integrals with the remaining integral simple to compute analytically.

$$\begin{aligned} a_0 &= \frac{1}{L}\int_0^L \phi_2(x_2)\mathrm{d}x_2 \\ &= \frac{1}{L}\sum_k \int_k \frac{\phi_k}{e^{\pm i\gamma_n|x_1-\tilde{x}_1|}}\mathrm{d}x_2 \end{aligned}$$

As the variation of ϕ over the element k is constant, the whole of the integrand may be brought outside the integral and the remaining integral is simply l_k

$$= \frac{1}{L}\sum_k \frac{\phi_k}{e^{\pm i\gamma_n|x_1-\tilde{x}_1|}} l_k$$

where l_k is the length of the k-th element. Similarly the other integral becomes:

$$\begin{aligned} a_n &= \frac{2}{L}\int_0^L \phi_2(x_2)\cos\left(\frac{n\pi x_2}{L}\right)\mathrm{d}x_2 \\ &= \frac{2}{L}\sum_k \frac{\phi_k}{e^{\pm i\gamma_n|x_1-\tilde{x}_1|}}\frac{L}{n\pi}\Delta_{nk} \end{aligned}$$

where $\Delta_{nk} = \left[\sin\left(\frac{n\pi b_k}{L}\right) - \sin\left(\frac{n\pi a_k}{L}\right)\right]$ in which $[a_k, b_k]$ are the coordinates of the end-points of the k-th element in the x_2-direction. We may now substitute for the ϕ_k values on the truncation boundary and rearrange the system which results in a reduction in the elements of $\mathbf{G}\vec{\psi}$ and a correction of the elements of $\mathbf{H}$. The modifications are summarised as

$$h_{ij} \mapsto h_{ij} - \sum_k g_{ik}\delta_{jk} \tag{6.10a}$$

$$\delta_{jk} = \alpha_j + \sum_n \beta_{nj}\Psi_{nk} \tag{6.10b}$$

$$\alpha_j = \frac{ikl_j}{L} \tag{6.10c}$$

$$\beta_{nj} = \frac{2i\gamma_n}{\pi}\frac{\Delta_{nj}}{n} \tag{6.10d}$$

$$\Psi_{nk} = \cos\left(\frac{n\pi\,(x_2)_k}{L}\right) \tag{6.10e}$$

$$\Delta_{nj} = \left[\sin\left(\frac{n\pi b_j}{L}\right) - \sin\left(\frac{n\pi a_j}{L}\right)\right] \tag{6.10f}$$

The substitution of Eqn. (6.10) into Eqn. (6.7) fully determines the system which can now be solved for all the missing values on the type 1 and type 2 boundaries and the ϕ values on the type 3 boundary. The corresponding values of ψ on the type 3 boundary may then be found from the discretised equation

$$\psi_i = \pm\frac{ik}{L}\sum_k \phi_k l_k \pm \frac{2i}{\pi}\sum_k\left[\left(\sum_k \frac{\phi_k\delta_{nk}}{n}\right)\gamma_n\cos\left(\frac{n\pi\gamma_i}{L}\right)\right] \tag{6.11}$$

In the context of the discussion given in Section 2.1.6, we note that this boundary condition is non-local in the sense that it couples all the unknowns on the truncation boundary. Due to the already full nature of the BEM matrix as well as the lack of numerical integration for constant boundary elements, this non-locality in space does not degrade the performance of the overall method. The implementation procedure may be repeated for an arbitrary number of separate truncation boundaries n and is of the form

$$c_i\phi_i + \sum_{j=1}^{N}\left(\int_{\Gamma_j}\psi_j^*\mathrm{d}\Gamma\right)\phi_j = \sum_{j=1}^{N-(K_l+\ldots+K_n)}\left(\int_{\Gamma_j}\phi_j^*\mathrm{d}\Gamma\right)\psi_j + \sum_{j=1}^{K_l}\left(\int_{\Gamma_j}\phi_j^*\mathrm{d}\Gamma\right)\psi_j + \ldots + \sum_{j=1}^{K_n}\left(\int_{\Gamma_j}\phi_j^*\mathrm{d}\Gamma\right)\psi_j \quad (6.12)$$

where $l \in \{1, 2, \ldots, n\}$.

6.6 Results

Having established an extended BEM to approximate solutions to BVPs in finite, semi-infinite or infinite domains, in this section we determine how the number of terms in the DtN map affects the accuracy and execution time and whether they are affected by any notable interactions between the choice of number of terms, mesh density and frequency. The mesh density may assist in filtering out unsupported reflected modes from the boundary condition but may also fail to allow unsupported transmitted modes through the boundary, which would contaminate the solution. We first present the output from a number of tests which aim to demonstrate the nature of the BEM code for a problem without non-reflecting boundaries. We consider the case of plane waves in a 2D rigid channel. We then introduce the DtN non-reflecting boundary condition formulated earlier into the method by considering the computation of Green's functions within domains bound by more than one non-reflecting boundary. The application of the DtN condition on such boundaries allows the calculation of arbitrary 2D acoustic Green's functions, without previous limitations on boundary locations. We present and analyse the effects of changing the mesh density, DtN expansion terms and frequency on the accuracy and execution time for each case.

6.7 1D Waves in a Rigid Channel

We first consider a problem without type-3 boundaries in order to establish the performance of the BEM implementation without inclusion of the DtN modification. This is a useful means of both validating the unmodified code and allowing us to later distinguish error generated by the boundary conditions from typical errors in the rest of the code. We consider the very low frequency model problem of Wrobel [353]. In this example, the Helmholtz equation is assumed to govern the variation of solution $u(x, y)$ in a square domain of size $L \times L$. The boundaries corresponding to $x = 0, L$ are type 1 boundaries with values of $u = \hat{u}$ and $u = 0$ assigned respectively. The other two boundaries corresponding to $y = 0, L$ are type 2 boundaries on which normal derivative $u' = 0$ (acoustically rigid). This problem physically models an acoustic flow in a open, rigid-walled channel of length L driven in the positive x-direction.

For simplicity, at this stage, we consider only 1D solutions of the problem. The 1D solution may be obtained by considering the 1D component of the higher-dimensional case. The 2D solution consists of a modal summation with components of the form $u_m(x, y) = [A_m e^{-i\gamma_m x} + B_m e^{i\gamma_m x}] \cos(\frac{m\pi y}{L})$. The wave number of the m-th mode in the x-direction γ_m is governed by the dispersion relation

$$k^2 - \left(\frac{m\pi}{L}\right)^2 = \gamma_m^2 \tag{6.13}$$

From the boundary conditions, the modal coefficients A_m and B_m are determined as

$$A_m = \frac{\hat{u} e^{i\gamma_m L}}{2i \sin(\gamma_m L)} \tag{6.14}$$

$$B_m = \hat{u} \left[1 - \frac{e^{i\gamma_m L}}{2i \sin(\gamma_m L)}\right] \tag{6.15}$$

The plane wave solution is, therefore, obtained by setting $m = 0$. In order to ensure this is physically correct, we only consider those frequencies for which no higher-order modes are cut-on. This condition is determined from Eqn. (6.13) as being $f < \frac{c}{2L}$. The plane wave analytical solution is therefore simply

$$u_0(x) = \left[A_0 e^{-i\gamma_0 x} + B_0 e^{i\gamma_0 x}\right] \tag{6.16}$$

Comparisons of particular interest are how the relative error and execution time vary with both the frequency and the mesh density. The relative error is computed by dividing the absolute error by the root mean square value of the plane wave. We select a domain size of $L = 6$ to ensure mesh densities remain manageable, giving us a cut-on frequency for the first higher-order mode at about 28 Hz. We therefore consider a frequency range of 10 - 30 Hz to compare to the plane wave solution. Of course, these frequencies are largely inaudible, but the intention of this section is to validate the unmodified BEM code, not to provide a useful physical solution. In order to keep the results well-spaced when plotting, we consider a wide range of mesh densities from $n = 5$ to $n = 60$ where n is the number of elements per unit length of side.

First we present the results illustrating the variation in both the mean relative error over the 2D grid and execution time (Figs. 6.3a and 6.3b) with frequency for 3 different mesh densities. As might be expected the error increases with frequency as the gradients of the solution in the domain increase and errors in the boundary integrals become increasingly inflated. The observable jump in the error beyond a frequency of 28 Hz may be explained by recalling that this frequency signals the cutting-on of the first higher-order mode, not represented by the analytical solution used as our benchmark for comparison. The BEM solution will contain the effects of this first-order mode which makes the analytical plane wave solution unsuitable for comparison. In Fig. 6.3b we see that execution time also increases with frequency. It is the evaluation of the Bessel functions which dominates the overall execution time of the code and the increased time is a consequence of passing a larger argument to the Bessel function evaluation routine. This trend in execution time may be reversed by the use of multi-threading. Indeed, the execution of the code on a later release of MATLAB, uses the multi-threading capability to do just that.

To summarise the effects of mesh density, we plot the mesh density as the independent variable and execution time and relative error as the dependent variables (Figs. 6.4a and 6.4b). Lower frequencies clearly have the advantage of both lower error and lower execution time. Reasons for both these observations have been stated above. We note that for a frequency of 5 Hz, a relative error of the order 10^{-4} is achieved using a mesh density of $n = 10$. If the frequency is made 6 times larger, the mesh density must increase by more than a factor of 6 to achieve the same accuracy. The

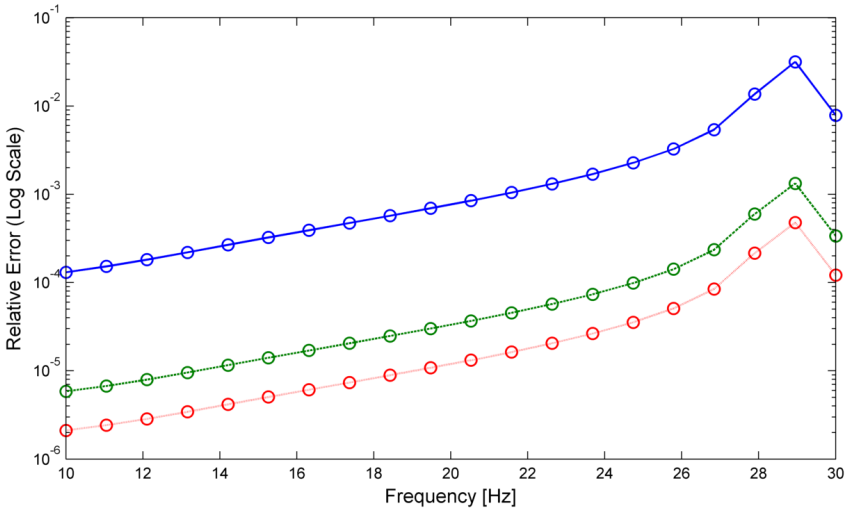

(a) Relative Error

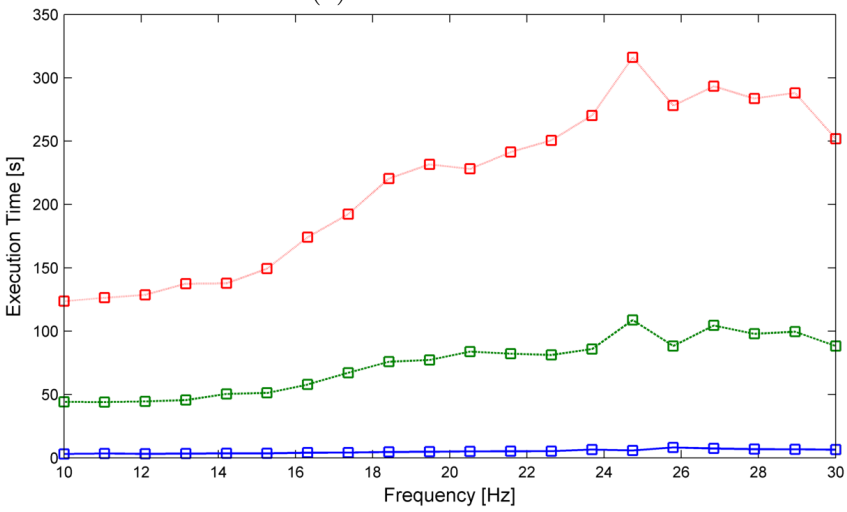

(b) Execution Time

Figure 6.3: Variation in Execution Time (bottom) and Relative Error (top) with frequency for 3 different mesh densities. Solid blue line $n = 5$; dashed green line $n = 33$, dotted red line $n = 60$.

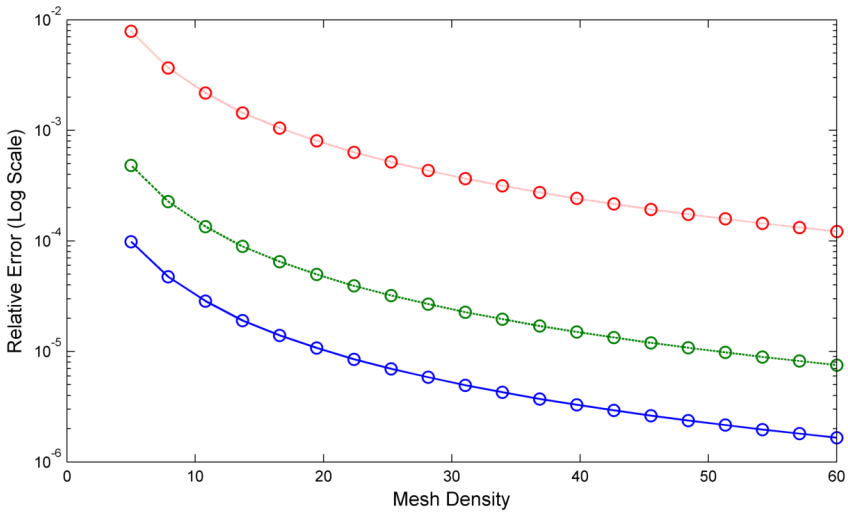

(a) Relative Error

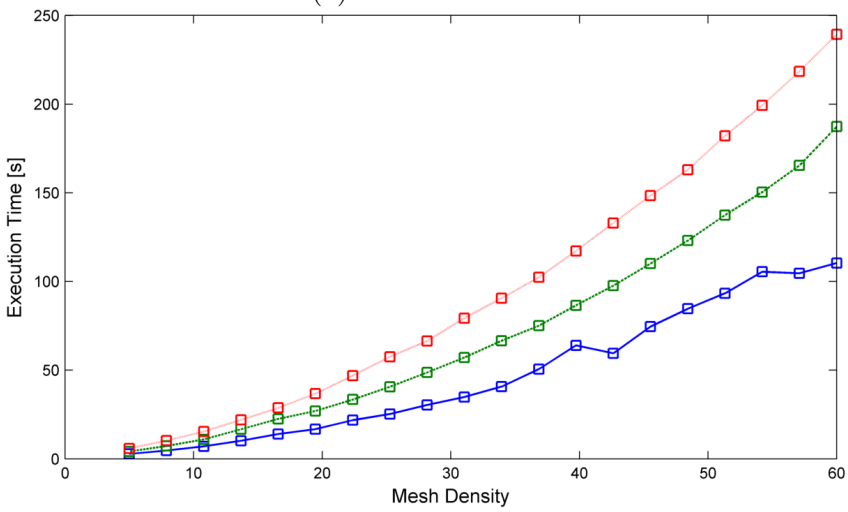

(b) Execution Time

Figure 6.4: Variation in Execution Time (bottom) and Relative Error (top) with mesh density for 3 different frequencies. Solid blue line $f = 5$ Hz; dashed green line $f = 17.5$ Hz, dotted red line $f = 30$ Hz.

asymptotes of the error variations also vary non-linearly with frequency suggesting that errors associated with resolution of the waves do not manifest themselves in a linear way.

6.8 2D Green's Function for a Rigid Channel

We now introduce the DtN condition into the BEM formulation. This functionality allows us to compute solutions for problems featuring transparent boundaries. In this chapter we wish to compute 2D acoustic Green's functions which satisfy the 2D form of Eqn. (6.3) along with appropriate boundary conditions. Our first example

is an extension of the previous problem: we consider the Green's function for an acoustically rigid channel of width d. As before, the geometry beyond the problem domain is assumed to continue to be that of an acoustically rigid, straight-walled channel. The analytical solution to this problem for a source position (ξ, η), observer position (x, y) and origin located on the lower surface of the channel is given by [198]

$$G(X, y, \eta) = -\frac{1}{2} \sum_{m=0}^{\infty} \epsilon_m \frac{e^{-\gamma_{2m}|X|/d}}{\gamma_{2m}} \cos \frac{m\pi y}{d} \cos \frac{m\pi \eta}{d}$$

where

$$\gamma_m = -i \left(k^2 d^2 - \frac{m^2 \pi^2}{4} \right)^{0.5}$$

and

$$\epsilon_m = \begin{cases} 1 & \text{if } m = 0 \\ 2 & \text{otherwise} \end{cases}$$

and

$$X = x - \xi$$

This solution is evaluated using 5000 terms of the infinite series which gives an accuracy of at least 5 significant figures [198]. Errors will, therefore, be of the same order of magnitude as the threshold of hearing (2×10^{-5}). Although we choose to vary the mesh density n, the number of terms in the DtN expansion M and the frequency f for a channel of arbitrary width $d = 1$, we could have chosen to vary the placement of the downstream and upstream boundaries. This parameter influences both the number of elements on the top and bottom of the channel (and hence mesh density n) as well as the number of terms required in the DtN expansion M: The further away from the source the boundary is place, the more elements are needed to mesh the upper and lower surfaces and hence, for a given n, the execution time of the code will increase. Likewise, as the source will generate higher-order modes, it is expected that placement of the artificial boundary in the near-field will require a larger M to maintain a given accuracy as even the cut-off higher-order modes may not have decayed sufficiently for any reflections from the artificial boundary to be negligible.

These additional terms will also increase execution time. We choose to fix the location of the boundaries arbitrarily at $x = \pm 3d$. We examine later the implications of such boundary placement on evanescent modes in the channel.

6.8.1 Range Selections

For our numerical experiments we select the audible frequency range from $f = 20$ to 20,000 Hz. We stipulate a required absolute accuracy corresponding the threshold of hearing (of the order 10^{-5}). In reality, for noise calculations, this need not be so stringent as audible error noise even an order of magnitude greater would likely be quiet enough to not attract attention. However, where there are instabilities, they may be excited by any amplitude of acoustic wave as they set up feedback loops or other forms of radiation [273, 312]. If our numerical Green's functions were used in such cases, the low amplitude numerical error may impact the solution behaviour significantly. In order to determine a range of mesh density selections n which will resolve the waves at frequency f and achieve the desired accuracy, we recall that by using a constant element BEM formulation we approximate the exact behaviour of waves on the boundary by a piecewise constant function. In order to relate the mesh density to the absolute error in the function we first integrate both the exact and the numerical functions and then use the exact integral to back-fit a wave whose amplitude is such that the integral of this new wave is equal to the integral of the approximating function. The absolute error between the exact amplitude and this new amplitude will then be used as a measure of the quality of the approximation for the given mesh density. The variation in this absolute error with the number of elements used to approximate the half sine wave is shown in Fig. 6.5.

Ideally, as the purpose of computing acoustic Green's functions is to use them in acoustic calculations, we require the maximum error be that of the threshold of hearing. However, it is clear from Fig. 6.5 that the number of elements required to achieve this would become impractical since, from Fig. 6.5, we would need the number of elements per wavelength $e = 2 \times 200 = 400$. In fact, for source wavelength λ_f, our mesh density $n = 400/\lambda_f$ must range from 24 to 23,256 elements per metre to fully resolve all source frequencies in the axial direction. Our standard BEM implementation, therefore, would require multiple double-precision matrices of size 23256^2 each. This would

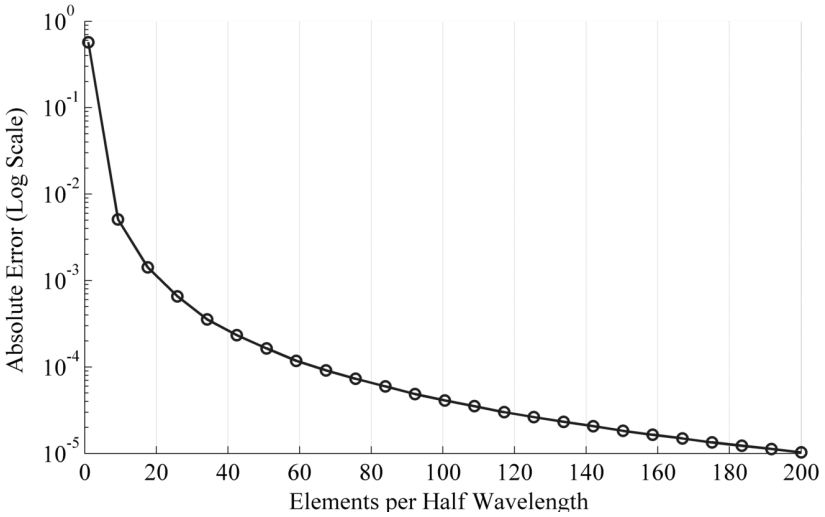

Figure 6.5: Absolute error in the amplitude against the number of elements per half wavelength.

require memory of the order 10^2GB, computational resources not widely available. A more modest target would be $e = 8$ which achieves an absolute error in the amplitude of the order 10^{-2}, a relative error of less than 10%. Furthermore, this selection adheres to the 8 'point per wavelength' rule suggested by Tam [313] for the approximation of acoustic waves. Therefore, we choose to vary the mesh from $n = 10$ to $n = 500$ to ensure a mixture of good and poor resolution across the range of source frequencies. This upper limit has the added benefit of being able to resolve all the propagating waves at the highest frequency f.

The choice of DtN terms in the expansion on the truncation boundary should allow us to investigate results for both resolved and unresolved DtN waves. We choose to vary the number of DtN terms in the expansion from $M = 10$ to 250, where the upper limit is beyond the resolution capabilities of the mesh. As discussed earlier, the exclusion of propagating modes in the DtN series at the artificial boundary results in essentially setting a boundary condition equal to zero for those modes. Unwanted reflections are thus inevitable if either the DtN expansion does not support the appropriate number of propagating modes or the boundary is close enough to the source that the cut-off higher-order modes have not sufficiently decayed. This latter situation is only expected at lower frequencies for our chosen boundary position. We can justify this expectation by considering the decay of the first cut-off mode (also the slowest mode to decay). The wavenumber of the first cut-off mode at a given frequency is given by the dispersion relation Eqn. (6.13) with L replaced by $d = 1$. At the highest frequency of 20,000

Hz we have

$$m > \left\lfloor \sqrt{\frac{d^2k^2}{\pi^2}} \right\rfloor$$
$$m \Rightarrow 117$$

At the lowest frequency we see that only the plane wave propagates and all higher-order modes are cut-off. We desire the pressure of the cut-off modes to have decayed to less than the minimum audible pressure (2×10^{-5}) by the boundaries. Therefore, we determine the distance from a source at $x = 0$ that we must place the boundary x_w by stipulating that the pressure of the higher-order mode, normalised by the pressure at the source $x = 0$, be of the order of 10^{-5}. The sound pressure level (SPL) in decibels, for the first cut-off mode at $f = 20,000$ Hz, may be found by considering the ratio between the SPL at $x = 0$ and $x = x_w$ giving

$$\begin{aligned} SPL_{x=x_w} &= \log_{10}\left(e^{i\gamma_{117}x_w}\right) \\ &= -5 \end{aligned}$$

This gives a wall placement of $0.28L$. For the lowest frequency of $f = 20$ we get $x_w = 3.69L$.

For clarity we define several parameters whose values allow us to determine to what degree the boundary mesh is capable of resolving the source and the waves corresponding to the highest frequency wave in the DtN expansion dictated by the M-th mode. The wavelength of the source is termed λ_f and the wavelength of the M-th mode in the DtN expansion λ_M. For our mesh density value range of $n = 10 - 500$ points per unit length, using the 8 point per wavelength minimum guide, we have a wavelength resolution range of $\lambda_n = 0.8 - 0.016$. We thus define the DtN mode resolution parameter $\bar{M}(M, n)$ as

$$\bar{M}(M, n) = \frac{\lambda_M(M)}{\lambda_n(n)} \tag{6.17}$$

and the source frequency resolution parameter $\bar{f}$

$$\bar{f}(f, n) = \frac{\lambda_f(f)}{\lambda_n(n)} \tag{6.18}$$

Obviously, when these parameters are greater than unity, the mesh represents all the waves in the DtN boundary condition and the source waves respectively using at least 8 points per wavelength. We define a similar parameter $\bar{M}_c(M, n, f)$ which replaces λ_M in the above with the wavelength of the last propagating mode $\lambda_c(M, f)$ determined by

$$m = \left\lfloor \frac{dk}{\pi} \right\rfloor$$
$$\lambda_c(M, f) = \frac{2d}{m}$$

where the dependence on M is implicit based on whether enough modes are available in the expansion to allow all propagating modes to be represented. In all cases tested, after computing the boundary values, the code proceeds to evaluate the solution over a line of 120 points. All error values are mean values over this grid. This is considered a fairer representation of the accuracy of the calculation than considering the maximum error as errors near the singularity and near boundaries are expected to be larger than elsewhere in the domain. Since these regions occupy only a small percentage of the overall region of interest their error values in isolation are not a suitable measure.

6.8.2 Accuracy variation with Frequency

We start by examining the variation in RMS relative error with frequency for different combinations of M and n. Errors can arise from several sources:

1. The poor resolution of the source waves at all boundaries;
2. The lack of terms in the DtN boundary condition;
3. The poor resolution of the DtN waves at the artificial boundary;
4. The poor performance of internal point valuation by the BEM when the point is near the singularities in the fundamental solution at the boundary.

Figures 6.6a to 6.6c show the variation in error over the range of f and M for 3 values of n. As can be seen, a sudden jump in error is evident as an increase in frequency

cuts-on higher-order modes not capable of being represented by the boundary conditions of lower M. This behaviour is consistent with the results of Harari *et al.* [146] and others who state that accuracy of the DtN condition is ensured by including all the propagating modes in the expansion. This source of error is the most significant. For the higher values of n, the error ramps up with source frequency f rather than jumps. This suggests that the exclusion of propagating modes is more detrimental at the lower resolutions. If the frequency is increased further, there comes a point beyond which further exclusion of modes has no dramatic effect, with a relatively uniform increase in error attributed to the increasingly poor resolution of higher frequency waves. Likewise, the inclusion of increasing numbers of evanescent modes also has little effect on the accuracy, even at low frequencies. This is due to the rapid decay of such modes and the placement of our downstream boundary such that the magnitude of these waves are negligible. In fact, the inclusion of large numbers of evanescent modes in the boundary representation can result in singular behaviour [92].

In contrast, the inclusion of propagating modes into the DtN expansion at the lowest mesh resolution has little effect on the error variation with frequency. The value of $\bar{f} \ll 1$ for all but the first frequency and this poor resolution is the principal source of error for coarse meshes with inclusion of propagating modes having little benefit if they are poorly resolved. Therefore, we can conclude that if resolution is adequate, the principal source of error with frequency relates to the inclusion of propagating modes in the DtN expansion, with poor resolution of the waves in the field responsible for a more general increase in error with frequency.

6.8.3 Execution Time variation with Frequency

From Fig. 6.7 we see that, as was the case with the 1D rigid channel example studied earlier (Fig. 6.3b), the execution time using MATLAB R2013a on an Intel Core i7 870 CPU decreases with frequency due to the increased efficiency of Bessel function evaluation for larger and larger arguments. There is little variation in the execution time over the range of values of M selected. However, further studies (see later) have shown that when M becomes very large, the execution time is significantly increased due to the number of column swapping operations required to set up the system.

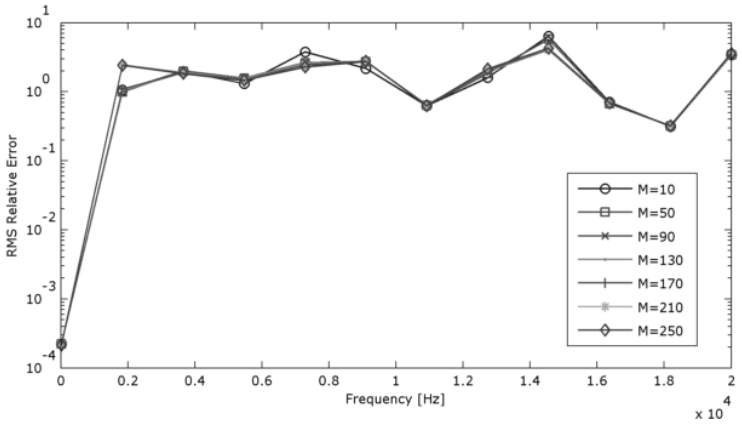

(a) Mesh Density $n = 10$

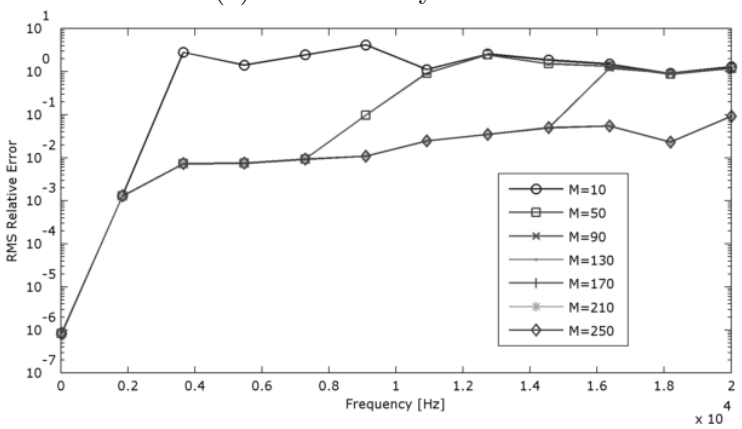

(b) Mesh Density $n = 255$

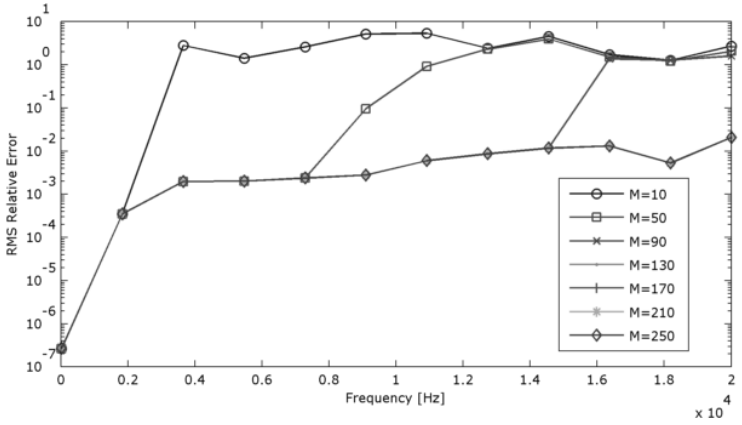

(c) Mesh Density $n = 500$

Figure 6.6: Variation in RMS relative error with frequency f and terms in the DtN boundary expansion M for selected mesh densities n.

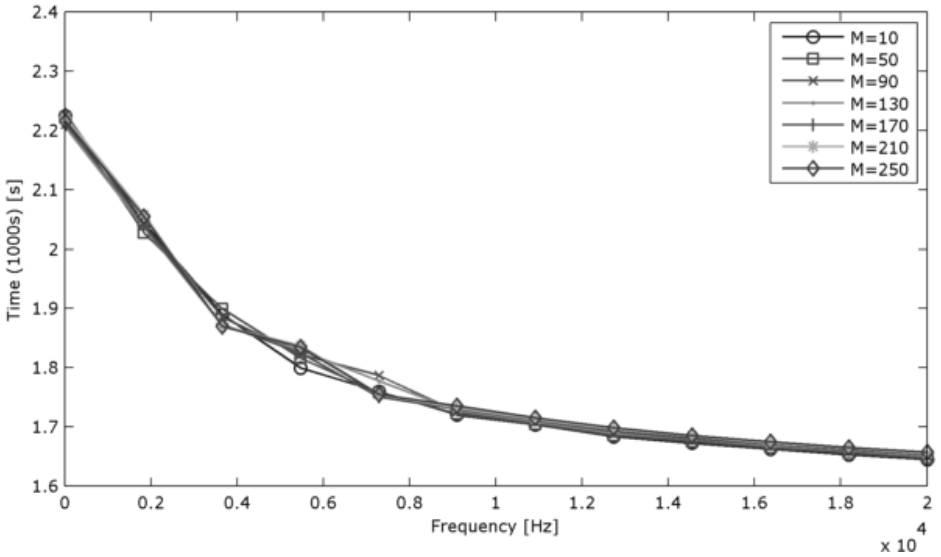

Figure 6.7: Variation in execution time with frequency f for $n = 500$.

6.8.4 Accuracy variation with Mesh Density

In general, the error decreases with mesh density. This behaviour is strongly influenced by the inclusion of enough terms in the DtN expansion such that M is large enough to allow all propagating cross-channel modes to be represented. However, there are some instances, where for a given combination of f and M a 'spike' is observed in the error at $n = 90$. Such behaviour is visible in Fig. 6.8b and Fig. 6.8c but not at lower frequencies.

One possible reason for this could be the known phenomenon that the inclusion of an increased number of evanescent modes in the solution forces systems to be near-singular [92]. Such behaviour would be amplified through matrix inversion as part of the solution of the linear system. As can be seen from Figs. 6.8b to 6.8c, these error 'spikes' may be avoided by selecting either a higher (or lower) value for M.

6.8.5 Execution Time variation with Mesh Density

As can be seen in Fig. 6.9, the value of M has little effect on the execution time. As before, we can assert that this is only true for relatively small values of M (suitable for our application). For larger values, it was found that the extra time needed to compute the DtN boundary condition influences execution time at least as much as the mesh density. The reduction in execution time with frequency is also observable. The rapid increase in execution time with mesh density means that between the last

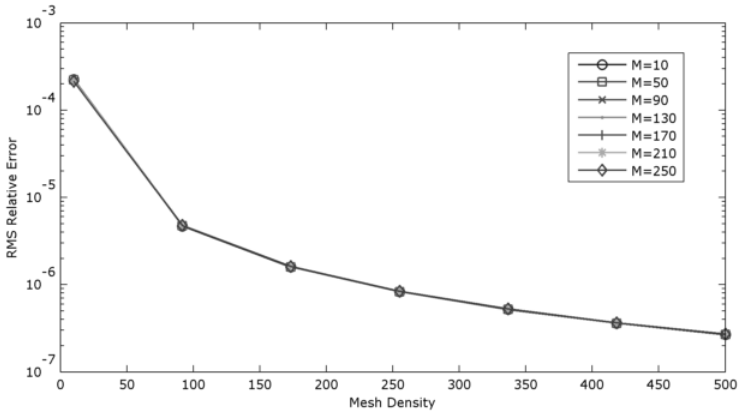

(a) Frequency $f = 20$ Hz, $\bar{f}(n) = [0.022, 0.20, 0.37, 0.55, 0.72, 0.90, 1.1] \times 10^3$

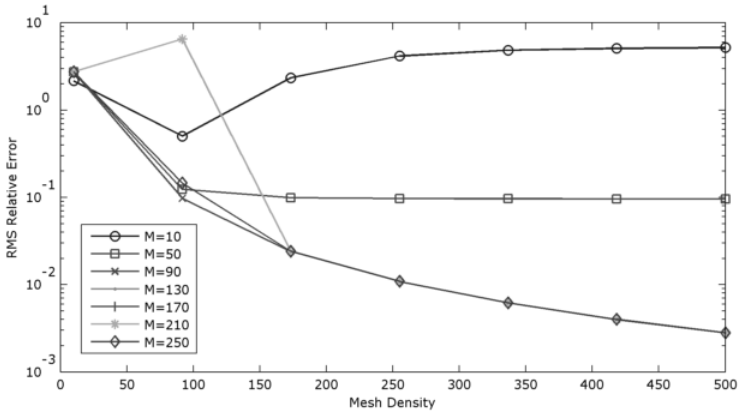

(b) Frequency $f = 9.1$ kHz, $\bar{f}(n) = [0.047, 0.43, 0.82, 1.2, 1.6, 2.0, 2.4]$

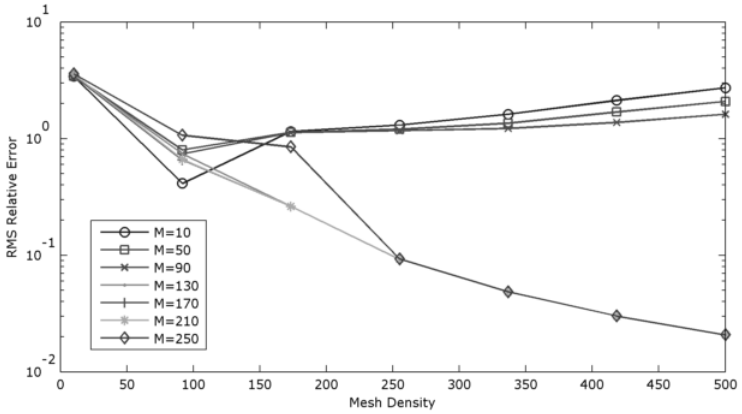

(c) Frequency $f = 20$ kHz, $\bar{f}(n) = [0.022, 0.20, 0.37, 0.55, 0.72, 0.90, 1.1]$

Figure 6.8: Variation in RMS relative error with mesh density n and terms in the DtN boundary expansion M for selected frequencies f.

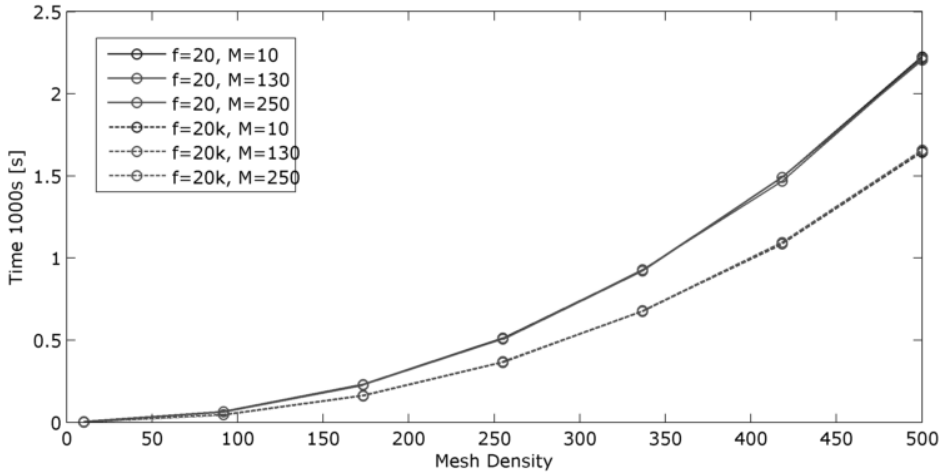

Figure 6.9: Variation in execution time with mesh density for $f = 20$ Hz and $f = 20$ kHz for range of M

two mesh densities considered, execution time increases by half as much again for a gain in accuracy of just 0.5% at the highest frequency. At the lower frequencies the increase in accuracy is even less as the solution has almost converged to a relative RMS error of the order 10^{-4}%.

6.8.6 Influence of Cross-Channel Mesh Density

Earlier, we suggested that the resolution of the waves in the boundary condition may be an important consideration when using the DtN boundary condition for BEM calculations. However, the influence of the resolution of the boundary condition is impossible to study in isolation as the cross-channel mesh density also affects the resolution of the solution itself: we cannot fix the mesh describing the solution and vary the mesh describing the boundary condition as they are implemented on the same set of nodes. Instead, we fix the axial mesh density at $n = 500$ and vary the cross-channel mesh density over the same range as used for earlier tests. We examine the error again over our line of 120 points down the centreline of the channel. Figures 6.10a to 6.10b, show little deviation from the variation in error in Figs. 6.6a to 6.6b where the mesh density on all the walls is changed. The resolution of the end walls must, therefore, be instrumental in reducing the overall error of the grid; despite the fact that the grid is perpendicular to these boundary segments.

If we consider the variation of error with the mesh density in the cross-channel direction and compare Figs. 6.11a to 6.11c to Figs. 6.8a to 6.8c we see that at the lowest

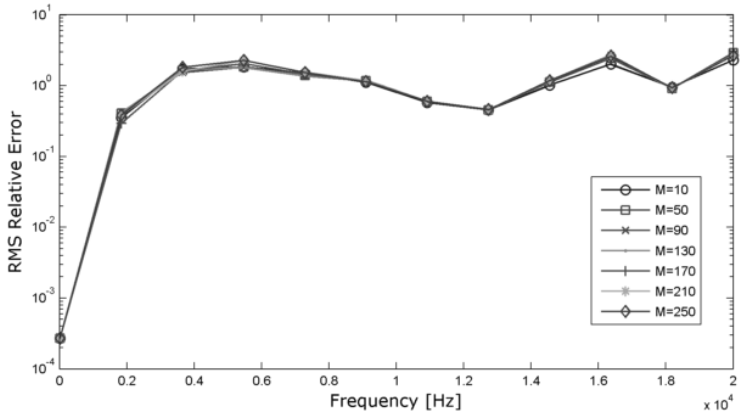

(a) Mesh Density $n = 10$

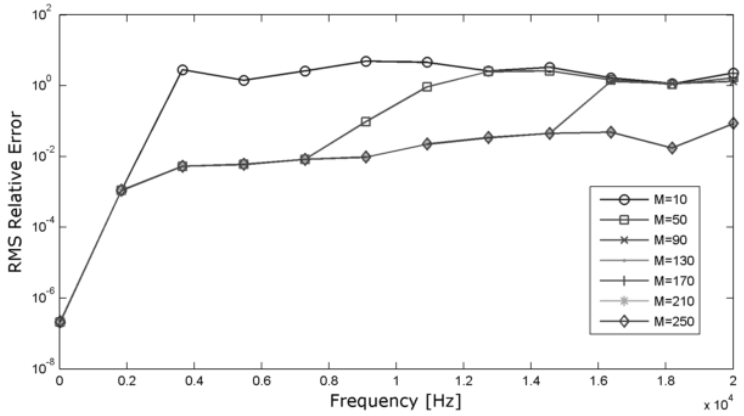

(b) Mesh Density $n = 255$

Figure 6.10: Variation in RMS relative error with frequency f and terms in the DtN boundary expansion M for selected cross-channel mesh densities n.

frequency tested, the resolution in the cross-channel direction has little effect on the error. Furthermore, a lower resolution actually gives a reduction in error. This apparent contradiction may be explained by considering that at the lowest frequency the only propagating wave is the plane wave whose amplitude is constant across the channel. Hence a lower mesh resolution will poorly describe any deviation from this constant behaviour and the representation will actually represent the physical solution more closely. Of course, there comes a point where, when computing the solution at internal points, the number of nodes on the boundary matters and the fewer the nodes, the less accurately an internal point can be computed: This is why at very low mesh densities the error dramatically increases. At the other two frequencies selected, we are seeing an order of magnitude improvement across all mesh densities due to the use of the maximum mesh density on the upper and lower surfaces. However, the variation is now strongly dependent on the cross-channel mesh.

The results in this section support the analytical analysis of [146] in suggesting that accuracy of the DtN condition is assured as long as all propagating modes are included in the expansion. This assurance may be made more accurate by adding the qualification that in such cases the artificial boundary must be positioned such that all higher-order modes have decayed to negligible levels. Otherwise, it is expected that a number of evanescent modes must be also included to maintain accuracy. This expectation is not tested here as, for most cases of practical interest, the truncation boundaries may be placed far enough away to ensure the decay of higher-order modes, while incurring little additional cost of meshing the extended boundary. However, the inclusion of an increasing number of evanescent modes is not a guarantee of increased accuracy due to their potential for causing near-singular behaviour in system matrices, as discussed earlier.

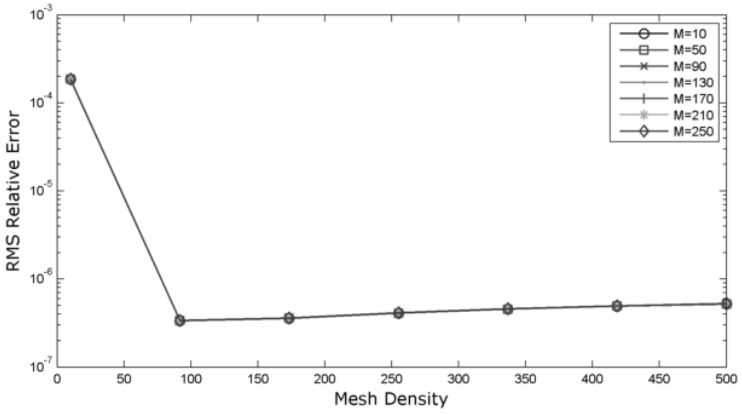

(a) Frequency $f = 20$ Hz

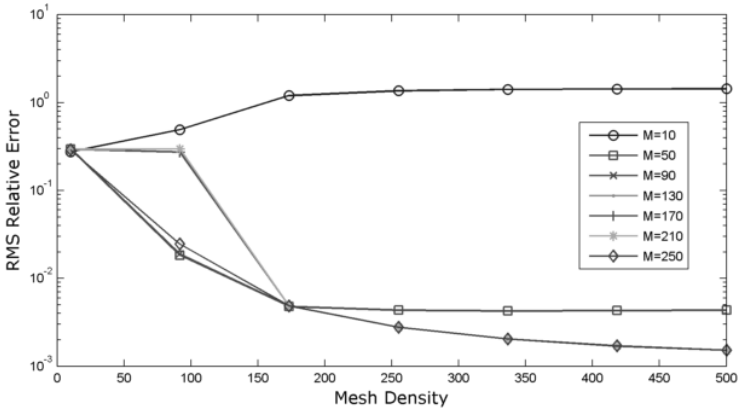

(b) Frequency $f = 9.1$ kHz

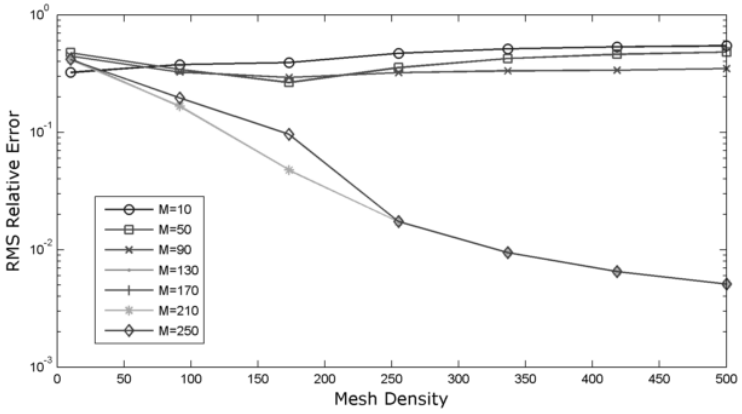

(c) Frequency $f = 20$ kHz

Figure 6.11: Variation in RMS relative error with mesh density n and terms in the DtN boundary expansion M for selected frequencies f.

6.9 Throttle

So far we have considered model problems as a means of investigating the accuracy of the BEM implementation. In one final application, we demonstrate its use applied to a more realistic problem. Of interest in gas turbine noise is the study of scattering in ducts and channels by protrusions. One specific example could be the scattering of waves generated by vortex shedding from a single stator blade in a duct. Borth [40] recognised the (then inexplicable) generation and scattering of acoustic waves by a throttle. This problem is one of a broader class of 3D acoustic problem typically dominated by 2D effects and was studied using the compact approach in Section 5.6. The baffle is approximated by an ellipse which is simple to implement numerical. Furthermore, the mesh generation routine automatically seeds more mesh points near the end of the ellipse such that the mesh density increases quadratically towards the tip. This latter property allows automatic refinement of the mesh near to the acoustically important region at the baffle tip. For a source positioned less than a wavelength away at $(0.1, 0.08)$ (with the baffle tip at $(\sqrt{2}/20, \sqrt{2}/20)$), for a mesh density of $n = 300$, expansion size of $M = 250$ and a frequency of 2500 Hz to provide easy visualisation we get the Green's function Fig. 6.12.

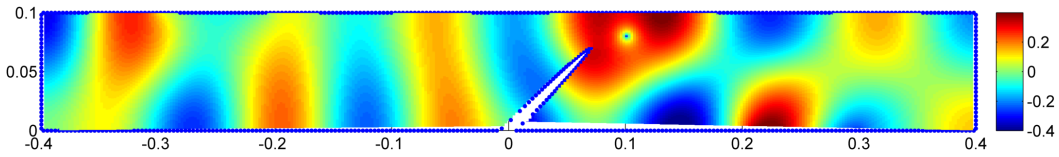

Figure 6.12: 2D Green's Function for the upper half of a throttle with the blue dots representing the element centres.

The darker regions of Fig. 6.12 indicate large amplitudes and the lighter regions smaller amplitudes for a particular instance of time. We see that the baffle provides a degree of shielding to the left of the domain with the strongest variation in amplitude occurring to the right of the source. This behaviour is expected as the acute angle of the baffle strongly reflects and amplifies sound in the same way a corner of a room would. This example demonstrates the utility of Green's functions as qualitative tools too with crucial regions of scattering revealed by visualising the computed field. When coupled to an acoustic propagation routine which uses integral methods, the numerical Green's function shown here contains all the information necessary to accurate account

for the scattering of the baffle.

6.10 2D Green's Functions with other boundaries

Although our DtN boundary condition has been formulated assuming a rigid, straight-sided waveguide beyond the truncation boundaries, the modified BEM code can still be useful when applied without further modification to other classes of problem. Consider the case of the Green's function for an infinite half-plane. The region beyond the transparent boundary is not a rigid waveguide but a region of free space, or free-space bound on one side by a rigid wall. A circular boundary is perhaps more suitable with the DtN condition re-derived for this new boundary – a full Fourier series in cylindrical coordinates would be a sensible choice. However, practically this would involve the discretisation of a curved boundary into a number of straight segments, a practise expected to introduce more error (see Section 5.4). The analytical solution is given by a combination of two free-space Green's functions, each one centred equi-distance from the rigid wall. If the origin is coincident with the location of the real source and the wall is distance d from the real source, the analytical solution in Cartesian system (x, y) is given by

$$G(r_1, r_2, \omega) = \frac{i}{4} H_0^{(2)}(k(\omega) r_1) + \frac{i}{4} H_0^{(2)}(k(\omega) r_2) \tag{6.19}$$

where $r_1 = \sqrt{x^2 + y^2}$ and $r_2 = \sqrt{x^2 + (y + 2d)^2}$. Using a square boundary and the same formulation as before we find that, despite the limitations of our boundary condition, qualitatively, the results agree very well. Figure 6.13 shows the comparison for $n = 100, f = 1000, M = 10,000$ which achieves a mean error, relative to the RMS value, of 5.7%. By simply inspecting the resulting Green's function, regions of significant scattering in the geometry may be identified. In addition, the results are obtained rapidly, especially for the selection $n = 100$. We conclude, therefore, that the formulation here may be applied without modification to a wider class of problems to rapidly obtain useful qualitative results. It should be noted that we consider here the case of scattering by a rigid plane (type 2 boundary) to allow comparison to a simple analytical representation. However, the BEM code developed in this chapter may be easily modified to account for flexible (type 1) or mixed (Robin – which we term type

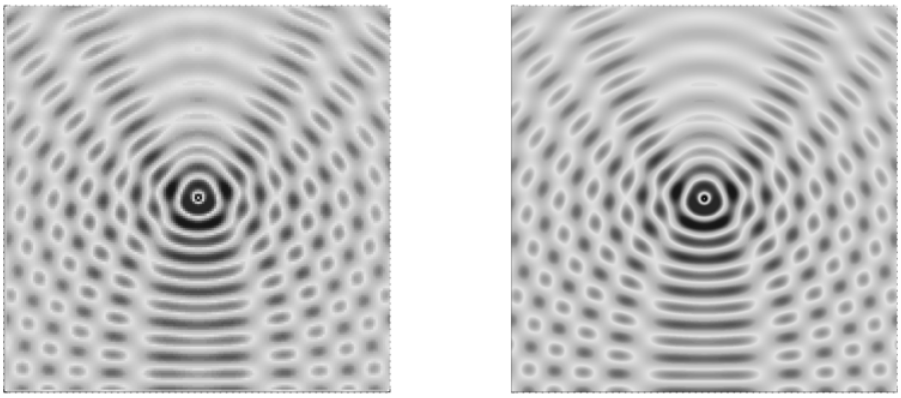

Figure 6.13: Qualitative comparison between BEM (left) and analytical (right) evaluations of the 2D Green's function for the Helmholtz equation for a source located above an infinite half-plane (bottom edge of image)

4) boundaries. Furthermore, we may also change the geometry of the plane to more reflect a more realistic ground geometry if desired.

6.11 Summary

In this chapter we have shown that the BEM is a suitable means of accurately computing an acoustic Green's function for 2D geometries, including a range of semi-infinite geometries. This calculation is accomplished through the solution of the singular form of the governing BVP including the boundary conditions associated with the original problem. Where artificial (transparent or non-reflecting) boundary conditions are required to close the originally semi-infinite domain, we have circumvented the potential under-determination of the system of boundary equations by utilising a Dirichlet-to-Neumann operator to provide the necessary additional equations. The use of constant elements for the BEM greatly simplifies the implementation by avoiding the need for additional numerical integration of the DtN expansion. Multi-threading has also been used to increase efficiency at higher frequencies. The validation exercises compare the numerical results with analytical solutions. Excellent agreement is achieved with relative errors of less than 1%. The new formulation has been successfully applied to a broader class of problems to rapidly obtain qualitative results which provide an indication of regions of significant scattering in a particular geometry by inspection. The DtN boundary condition may be extended to other geometries by simply changing

the form of the series solution used to construct the DtN operator, with the implementation largely unchanged.

Chapter 7

Sinc-Galerkin Method

In Chapters 5 and 6, we presented two methods for the numerical evaluation of the Green's function for the Helmholtz equation. The compact Green's function provides a good approximation for the class of acoustic problems where the scatterer is compact with respect to the acoustic wavelength and either the observer or source is in the acoustic far-field. The method is rapid and accurate. In Chapter 6 we explored the use of the Boundary Element Method (BEM) for the evaluation of the Green's function for more general two-dimensional geometries, introducing a new NRBC implementation to enhance versatility. Again accurate results were obtained. However, although the BEM was seen to be more versatile in that it may be applied to a wider variety of problems, it is also significantly more demanding computationally and takes longer to execute. For this reason we develop another method which aims to achieve comparable accuracy to the other two methods, be applicable to a wider range of problems than the compact Green's function but be cheaper to execute than the BEM. The method selected in Chapter 4 is a Galerkin method based on the basis set of sinc functions. As with previous methods, we develop the method such that it is suitable for our purpose and validate it against available analytical solutions.

7.1 Sinc Methods

The set of sinc numerical methods represent the function of interest as an expansion of translated sinc functions. For the Paley-Wiener class of functions (see Lund and Bowers [204] for their properties), this infinite series representation is exact and called the

Whittaker-Cardinal function. The representation was initially presented by Whittaker [350] but more recently has been developed into a practical spatial/spectral method for the solution of elliptic and parabolic linear and non-linear differential equations by Stenger [305]. This is facilitated by using the sinc expansion to approximate functions not of the Paley-Wiener class. This approximate representation then forms the basis of associated numerical methods. Stenger demonstrates that for appropriately selected discretisation parameters, the unique properties of the sinc basis ensure exponential convergence of the sinc series representation.

In one dimension, the sinc basis functions exist along the whole real line ($x \in \mathbb{R}$), centred at uniformly distributed sinc nodes. This infinite interval, and the functions within the space, may be transformed to any semi-infinite or finite interval through the specification of appropriate 1D conformal maps. This allows functions on an arbitrary 1D interval, as well as their integrals and derivatives, to be approximated using a transformed expansion of sinc functions centred at the transformed nodal locations in the interval. For many practical problems, such as the ones presented in this chapter, the solution in the domain is assumed unknown. The sinc expansion may be then used in collocation [240, 241, 261, 355, 356], Galerkin [98, 220] or highest derivative [299] procedures to find the unknown coefficients. The collocation method is generally chosen over the Galerkin method for problems with variable coefficients as the resulting implementation is a more efficient means of achieving a given accuracy [355, 356]. However, the Galerkin procedure is more flexible as it lends itself to basis modification and extension without the stringent smoothness requirements of the collocation method [230]. This is particualrly useful when considering a variety of boundary condtiions and so is used in this chapter. A rigorous mathematical summary of the sinc method formulae can be found in Lund and Bowers [204] and Stenger [306], although key formulae will be stated as appropriate throughout the chapter.

7.1.0.1 Advantages of the Sinc-Galerkin Method

An important practical advantage of using spectral-like methods over other numerical methods such as the boundary element method (BEM) is that once the coefficients have been found, the evaluation of points within and on the domain boundaries requires only the evaluation and assembly of the series components. We compare our

sinc implementation to a typical BEM implementation in Section 8.2, where the issue of re-evaluating coefficient matrices for every internal point is seen to significantly impact execution time.

The principal advantage of the Sinc-Galerkin method over Galerkin methods with different basis functions is the ability to achieve exponential convergence of the series solution. Exponential convergence offers a practical advantage, over other numerical approaches, of using a fewer number of functions and nodal points to accurately represent the function of interest [241]. The single exponential convergence of early sinc implementations may by improved upon by using a double exponential conformal mapping [245, 307, 355, 356]. This exponentially convergent behaviour has been established for a number of problems in the literature, even for those featuring a boundary singularity [97, 98, 210, 220, 300]. However, the method has not been applied in earnest to a BVP featuring a domain singularity. The conditions governing exponential convergence are violated when the solution is not smooth throughout the domain interior and, as demonstrated in the brief example of Morlet *et al.* [232], convergence in this case is degraded. We present here an application of the Sinc-Galerkin method to construct a Green's function – a problem characterised by a domain singularity at the source point. We investigate the possibility that even degraded convergence of an exponentially convergent method may still achieve practically useful results.

Additional advantages of the Sinc-Galerkin approach when compared with alternative numerical methods include [43]:

1. Problems in semi-infinite and infinite domains may be solved without the need for artificial boundaries and non-reflecting boundary conditions which are always inexact and can be complicated to implement;

2. Sinc methods do not require numerical integration in order to compute the component matrices, just point evaluations, which require significantly less computational effort;

3. The error of the approximation is not dependent on any derivatives hence it is capable of approximating singular solutions without such amplification of errors;

4. The exponential convergence rate is maintained even for problems with boundary singularities [220];

5. Time-dependent problems may be expressed as a linear system rather than a system of ODEs typical of many Galerkin procedures [220];

6. The weight function in the Galerkin procedure can be selected to ensure a symmetric matrix system which can increase solution efficiency [219].

However, unlike the Finite Element Method (FEM) and the Finite Difference Method (FDM), the ensuing matrices are full which precludes the use of efficient sparse solvers. This disadvantage only partially offsets the significant benefit of the exponential convergence rate of the sinc series [219, 220] equivalent to $\mathcal{O}(e^{-k\sqrt{N}})$ where $k > 1$ and the number of basis functions used to construct the approximate solution is $2N + 1$. In addition, the matrix systems, although not banded, consist of Toeplitz matrices and, for linear problems, the form of the resulting matrix equation is that of the Sylvester equation [301]. This particular equation may be solved using a number of established techniques; two of the most common being described by Lund and Bowers [204] (detailed in Section 7.5), with efficient solvers available, for handling the special structure of the constituent matrices.

7.1.0.2 Applications of the Sinc-Galerkin Method

The merits of the Sinc-Galerkin method have led to its application to both 1D and higher-dimensional problems subject to homogeneous Dirichlet [43, 85, 97–102, 182, 191, 209, 210, 219, 220, 230, 238, 240, 241, 245, 283, 284, 300, 301, 358, 363] and inhomogeneous Dirichlet boundary conditions [98, 182, 219, 238, 245, 260, 261, 292, 300, 301]. Included in the previous citations are examples of both linear and non-linear problems for a variety of differential operators, including singular boundary value problems, known to cause stability issues in many traditional numerical methods (in particular see [101]). The solution of non-linear problems often uses Newton iteration applied to the matrix system [102]. More recently, there has been applications of sinc methods for the inverse problem – reconstruction of an unknown source [301].
The wave equation and the Helmholtz equation, previously treated by McArthur, Bowers and Lund [220] (wave equation) and [43] (Helmholtz as a general elliptic equation), are of particular interest in acoustics and will be the focus of this chapter. The use of sinc methods with Dirichlet conditions is relatively straight-forward since the sinc

function satisfies the homogeneous Dirichlet condition automatically at the edges of the interval. A simple change of variable is all that is required for the conversion of the problem with inhomogeneous conditions to the problem with homogeneous conditions as discussed later. However, when the boundary conditions are Neumann conditions (or mixed conditions involving both the solution and its derivative), the sinc basis must be modified to ensure the derivative of the individual basis functions exist at the endpoints of the interval, since ordinarily the derivative of the sinc function is undefined here. These modified functions, however, although defined at the boundary, still do not satisfy the boundary conditions. Therefore, the basis may be extended by including additional basis functions to interpolate the boundary conditions [204]. Such functions are typically Hermite polynomials. Many examples of the modification [143, 182, 241, 301] and the extension [85, 143, 182, 209, 210, 230, 241, 301] of the basis to treat a variety of BVPs exist. However, Mueller and Shores [238] suggest a means of treating the convection-diffusion equation subject to mixed boundary conditions without the need to differentiate the coefficients. Their motivation for developing this alternative approach is that basis extension using polynomial functions often hampers implementation. Their approach considers the variational form of the Galerkin weighted residual statement and the problem is transformed by including a decaying function to ensure that the transformed problem may be represented by an unmodifed and unextended sinc basis.

One apparent absentee from the literature is that of the Sinc-Galerkin formulation for the Helmholtz equation on a rectangle subject to Neumann or mixed conditions on the boundary. The physical significance of these problems in acoustics are those subject to rigid wall or impedance boundary conditions. We present one possible formulation in Section 7.7. Since this problem is a 'pure Neumann problem', it is expected that the compatibility condition must also be satisfied to ensure that the solution to the problem remains unique; the boundary conditions not being sufficient to uniquely define the solution: any constant may be added to one solution to produce another equally as valid. Another variation on the traditional boundary treatment is proposed by Wu *et al.* [355] in 1D and then also in 2D [356]. In principle, these approaches are the same as using the Hermite polynomials to extend the basis, using a bicubically-blended Coons patch in 2D to interpolate the boundary conditions. The differences are only

in terms of the terminology and details of the implementation.

Sinc methods, like wavelet methods [15], are limited in their direct application to rectangular or rectangular parallelepiped infinite, semi-infinite or finite geometries. This is ideal for treating problems with periodic boundary conditions. Attempts to extend Sinc-Galerkin and similar procedures to more complex geometries or operators either transform the problem as recommended by McArthur *et al.* [220] or use a sub-domain ('building-block') approach [210]. The former relies on the conformal invariance of the operator to allow the results to be transformed back to the original problem [358]. Unfortunately, not every operator of interest satisfies this criterion. The latter divides the domain into 'patches' [210] on which individual sinc problems are solved. Matching conditions at the patch boundaries are used to relate the individual sub-problems to each other. Overlapping methods are similar to patching methods but where the sub-domains overlap one another [209, 210]. The simultaneous solution of the sub-domain problems, proposed by Lybeck & Bowers [210], may demand significant memory requirements, depending on the number of sub-domains and the size of the basis used within each sub-domain. To avoid memory overruns, alternating algorithms may be used, such as the Schwarz-Alternating Method [231], which effectively handle the coupling on the shared boundary by solving iteratively over the collected sub-domains [209]. Due to the matching conditions for the patching method being more cumbersome to implement [210], the overlapping method is generally preferred. Furthermore, by increasing the overlapping region, the convergence rate of alternating algorithms used to solve the coupled sub-domain matrix systems may be increased.

Care is required when using domain decomposition to ensure that the basis functions in each domain are capable of being matched at the boundary. As discussed earlier, the sinc approximation cannot be differentiated at the domain boundary which not only introduces difficulties when considering boundary value problems featuring Neumann boundary conditions but also can complicate the construction of matching conditions for patching methods [210]. In lieu of modifying the basis to ensure the derivative remains defined (see Section 7.7), Lybeck & Bowers [210] use finite difference approximations to compute the matching conditions of the patching method under the assurance of Morlet *et al.* [232] that the exponential convergence of the method remains in tact. The inclusion of finite difference approximations at the boundary has

also been used by Narasimhan *et al.* [241], as an alternative to modifying the basis, to allow for Neumann boundary conditions. Contrary to the work of Morlet *et al.* [232], Wu *et al.* [355] claim that the inclusion of finite difference solutions will limit the accuracy of sinc methods and propose an alternative boundary treatment to increase the rate of convergence. The proposed treatment closely resembles the basis extension method discussed earlier.

7.2 Green's Function for the Helmholtz Equation

As we have seen in the previous two chapters, time-harmonic acoustic problems, in the absence of a mean flow, may be represented by a Helmholtz boundary value problem (BVP). We initially consider the Dirichlet BVP of the form

$$(\nabla^2 + k^2)u(\mathbf{x},\omega) = f(\mathbf{x},\omega) \qquad \text{in} \quad \Omega \tag{7.1a}$$

$$u(\mathbf{x},\omega) = q(\mathbf{x},\omega) \qquad \text{on} \quad \partial S \tag{7.1b}$$

where $\mathbf{x}$ represents the spatial coordinate and ω the frequency of the wave under consideration. This BVP physically describes an acoustic source f radiating sound at a given frequency ω into the domain where the resulting acoustic fluctuations are governed by the linear wave equation and are equal to q on the domain boundary. We assume the source term to be a function of spatially compact support

$$\text{supp}\,[f(\mathbf{x},\omega)] = \mathbf{y} \in \Omega_S$$

where $\Omega_S \in \Omega$ represents a sub-domain of the overall domain Ω we define as being the 'source region', within which the spatial coordinate is denoted by $\mathbf{y}$. Physically, this is the region within which the acoustic sources may be considered to be located. We develop the analytical solution to this BVP by transforming the differential equation into an integral equation in which we can substitute the boundary conditions. These boundary conditions are incorporated in the integral kernel through the Green's function $\hat{G}(\mathbf{x},\mathbf{y},\omega)$, which is dependent on both the position of the observer $\mathbf{x}$ and the source $\mathbf{y}$. This function physically represents the outgoing wave produced by an impulsive unit point source at $\mathbf{y}$ subject to the same boundary conditions as the original

problem. It is the solution to the singular form of the original BVP, where our point source is described by the Dirac delta function Eqn. (7.2).

$$(\nabla^2 + k^2)\hat{G}(\mathbf{x}, \mathbf{y}, \omega) = \delta(\mathbf{x} - \mathbf{y}) \qquad \text{in} \quad \Omega \tag{7.2a}$$

$$\hat{G}(\mathbf{x}, \mathbf{y}, \omega) = q(\mathbf{x}, \mathbf{y}, \omega) \qquad \text{on} \quad \partial S \tag{7.2b}$$

Solution of this BVP yields the exact Green's function for Eqn. (7.1). In the remainder of this chapter we show that the Sinc-Galerkin method can be a robust and accurate means of numerically computing Green's functions for homogeneous Dirichlet Helmholtz BVPs within a particular class of geometries.

We have chosen to solve the 2D Helmholtz equation rather than a higher-dimensional version or indeed the time-dependent wave equation for simplicity although the Sinc-Galerkin may be easily extended to higher dimensions with little effort. As alluded to earlier, a typical use of the resulting Green's function would be to integrate it with an acoustic source term as part of an acoustic analogy. Accurate descriptions of acoustic sources are usually based on the frequency content as producing an explicitly time-dependent source description, necessary for the solution of the wave equation, from either computational or experimental data or using a mathematical model can be difficult, especially for real sources which may consist of random behaviour [349]. However, we note that if we wished to compute a Green's function for the wave equation rather than the Helmholtz equation, the Sinc-Galerkin method has the advantage of being able to treat the time variable in the same way as the space variables; a conformal map is used to map the time functions to the interval $[0, \infty]$. Hence, the method may be applied just as easily to the wave equation as the Helmholtz equation without the need for a complicated time-stepping algorithm or solution of a system of ODEs in time [220]. This makes the solution of time-dependent problems both quick and stable.

7.3 1D Sinc Approximations

We start by presenting the key formulae associated with sinc numerical methods before extending them to cover our particular application. The one-dimensional sinc series

for a function $f(x)$ on the real line $x \in \mathbb{R}$ may be defined for node spacing $h > 0$ and integer values of k as

$$C(f,h)(x) \equiv \sum_{-\infty}^{\infty} f(kh)\text{sinc}\left(\frac{x-kh}{h}\right) \tag{7.3}$$

where

$$\text{sinc}(z) \equiv \frac{\sin(\pi z)}{\pi z}$$

This series converges for the Paley-Wiener class of complex functions [305] in which case C is called the *cardinal function* of f. Since $\text{sinc}\left(\frac{x-kh}{h}\right) = 1$ when $x = kh$, the cardinal function can be used to interpolate f at the collocation points $\{nh\}_{n=-\infty}^{\infty}$. Although this cardinal function representation is exact for Paley-Wiener functions, we may also use the series to accurately approximate functions outside this class. Furthermore, we truncate Eqn. (7.3) in practice such that $-M \leq k \leq N$. In these circumstances, the 1D sinc interpolation formula for f is stated as [204]

$$f(x) \approx \sum_{k=-M}^{N} f(kh)\text{sinc}\left(\frac{x-kh}{h}\right) \tag{7.4}$$

Integration of the series representation Eqn. (7.3) over all space $-\infty < x < \infty$, followed by a truncation of the resulting series, defines the 1D quadrature rule

$$\int_{-\infty}^{\infty} f(x)\text{d}x \approx h \sum_{k=-M}^{N} f(kh) \tag{7.5}$$

When using these approximate formulae, it is important to select the parameters which relate M and N to h such that the approximation converges. It is possible to select parameters such that the error decays exponentially. Accurate approximations may then be achieved using a relatively small number of terms in the series. This is a particular strength of sinc series representations over similar representations such as Fourier series. The mathematical rules for parameter selection are established for a number of problems in [204], although in all cases, knowledge of the solution behaviour at the endpoint of the interval is required. In practice, such information is rarely available and hence a set of 'general' selections are made when performing our calculations which are detailed later.

For many boundary value problems, the domain boundaries are finite, and Eqn. (7.4)

may be mapped from $x \in \mathbb{R}$ to $x' \in [a, b]$ the conformal mapping function $\phi : x \mapsto x'$ defined by

$$\phi(x) = \ln\left(\frac{x-a}{b-x}\right) \tag{7.6}$$

If the inverse mapping function is defined by $\psi(x') = \phi^{-1}(x')$ then we have the new interpolation formula for the interval $[a, b]$ as

$$f(x) \approx \sum_{k=-M}^{N} f \circ \psi(kh)\,[S(k,h) \circ \phi(x)] \tag{7.7}$$

as well as the new quadrature formulation

$$\int_a^b f(x)\mathrm{d}x \approx h \sum_{k=-M}^{N} \frac{f}{\phi'} \circ \psi(kh) \tag{7.8}$$

where we have introduced a shorthand notation for a translated sinc function defined by

$$S(k,h)(z) \equiv \mathrm{sinc}\left(\frac{z-kh}{h}\right) \tag{7.9}$$

Fig. 7.1 shows the basis functions $k = -1, 0, 1$ on the interval $[0, 2]$ as an example of the translation and mapping of the basis set. For clarity we have not plotted the curves immediately near the end points. Had we done so, their rapid decay to zero would be evident.

Finally, as differential equations contain derivatives we also state the following [182]

$$\delta_{jk}^{(n)} \equiv h^n \frac{\mathrm{d}^n}{\mathrm{d}\phi^n}\,[S(j,h) \circ \phi(x)]\Big|_{x=x_k} \qquad n = 0, 1, 2, \ldots \tag{7.10}$$

where $x_k = \phi^{-1}(kh) = \psi(kh)$. Specifically for the context of this work we note the values of $\delta_{jk}^{(0)}$, $\delta_{jk}^{(1)}$ and $\delta_{jk}^{(2)}$ by observing $\phi(x_k)|_{x=x_k} = \phi\left(\phi^{-1}(kh)\right) \equiv x|_{x=kh}$ and

$$\frac{\mathrm{d}^n}{\mathrm{d}\phi^n}\,[S(j,h) \circ \phi(x)]\Big|_{x=x_k} = \frac{\mathrm{d}^n}{\mathrm{d}x^n}\left[\mathrm{sinc}\left(\frac{x-jh}{h}\right)\right]\Big|_{x=kh}$$

giving us

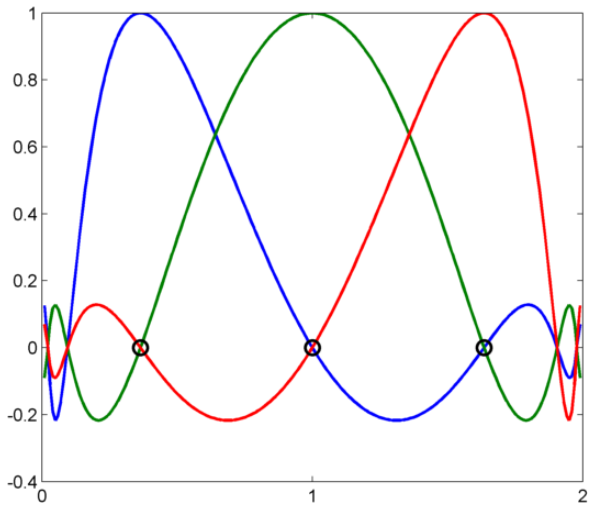

Figure 7.1: 3 Sinc Basis Functions (shifted to their centring points (circles) and transformed to interval (0,2). The blue curve is $k = -1$, the green $k = 0$ and the red $k = 1$.)

$$\delta_{jk}^{(0)} \equiv [S(j,h) \circ \phi(x)]|_{x=x_k} = \begin{cases} 1 & j = k \\ 0 & j \neq k \end{cases} \tag{7.11a}$$

$$\delta_{jk}^{(1)} \equiv h\frac{\mathrm{d}}{\mathrm{d}\phi}\left[S(j,h) \circ \phi(x)\right]\Big|_{x=x_k} = \begin{cases} 0 & j = k \\ \frac{(-1)^{k-j}}{k-j} & j \neq k \end{cases} \tag{7.11b}$$

$$\delta_{jk}^{(2)} \equiv h^2\frac{\mathrm{d}^2}{\mathrm{d}\phi^2}\left[S(j,h) \circ \phi(x)\right]\Big|_{x=x_k} = \begin{cases} -\frac{\pi^2}{3} & j = k \\ \frac{-2(-1)^{k-j}}{(k-j)^2} & j \neq k \end{cases} \tag{7.11c}$$

Next we introduce the Sinc-Galerkin procedure for a two-dimensional Helmholtz BVP and show the simple extension of the formulae presented in this section to two dimensions.

7.4 2D Sinc-Galerkin for the Helmholtz Equation

The 2D Sinc-Galerkin method for a homogeneous Dirichlet BVP may be derived by considering the Helmholtz equation on a rectangle $(a,b)\times(c,d)$ subject to homogeneous Dirichlet conditions on the edges Eqn. (7.12).

$$(\nabla^2 + k^2)u(x,y) = -f(x,y) \qquad (x,y) \in \Omega = (a,b) \times (c,d) \tag{7.12a}$$

$$u(x,y) = 0 \qquad (x,y) \in \partial S \tag{7.12b}$$

Alternatively, as the problem is separable, we could write the original BVP as two ordinary BVPs: the corresponding BVPs in x for a given y_k and in y for a given x_j. The advantage of this latter approach is that the simple discretisation schemes established for 1D operators [43, 191, 220] may be used to build the higher-dimensional solution. If boundary conditions are inhomogeneous, a simple change of variable [204] may be used to transform the BVP from one with inhomogeneous Dirichlet boundary conditions to one with homogeneous conditions, as in [301], thus. Consider the general problem

$$-v''(x) + p(x)v'(x) + q(x)v(x) = f(x) \quad x \in (a,b)$$

$$a_0 v(a) = a_2$$

$$b_0 v(b) = b_2$$

Using the linear function

$$l(x) = Ax + B$$

with coefficients defined by

$$A = \frac{b_0 a_2 - a_0 b_2}{D}$$

$$B = \frac{a_0 b_2 a - b_0 a_2 b}{D}$$

$$D = a_0 b_0 (a - b) \neq 0$$

Finally $u(x) = v(x) - l(x)$ and $\bar{f}(x) = f(x) - \mathcal{L}[l(x)]$ where $\mathcal{L}$ is the original differential operator giving

$$-u''(x) + p(x)u'(x) + q(x)u(x) = \bar{f}(x) \quad x \in (a,b)$$

$$a_0 u(a) = 0$$

$$b_0 u(b) = 0$$

As we are considering only the homogeneous Dirichlet problem in this chapter we may treat the problem directly. Extending Eqn. (7.8) to two dimensions we may approximate the solution to Eqn. (7.12) as a sinc series

$$u_A(x,y) = \sum_{j=-M_x}^{N_x} \sum_{k=-M_y}^{N_y} u_{jk} S_{jk}(x,y) \tag{7.13}$$

In this case, the coefficients at the nodal points of each sinc function in the basis set are unknown since the solution itself is unknown. These unknown are represented by the coefficients u_{jk}. The basis functions $\{S_{jk}(x,y)\}$ use the shorthand of Eqn. (7.9) are defined

$$S_{jk}(x,y) = [S(j,h_x) \circ \phi_x(x)]\,[S(k,h_y) \circ \phi_y(y)] \tag{7.14}$$

The required mapping function for the x-direction is given by

$$\phi_x(x) = \ln \frac{x-a}{b-x}$$

which maps (a,b) to $(-\infty,\infty)$ and for the y direction

$$\phi_y(y) = \ln \frac{y-c}{d-y}$$

which maps (c,d) to $(-\infty,\infty)$. We initiate the Galerkin method by considering the orthogonalisation of the residual $R = -(\nabla^2 + k^2)u_A - f$ with respect to the original basis set of functions Eqn. (7.14)

$$\left\langle \left(-(\nabla^2 + k^2)u_A - f\right), S_{pq} \right\rangle = 0$$

The inner products are defined by

$$\langle h, g \rangle = \iint_\Omega h(x,y) g(x,y) w(x) v(y) \mathrm{d}x\mathrm{d}y$$

where $w(x)v(y)$ is a weight function. Green's second identity

$$\iint_\Omega \left(g\nabla^2 h - h\nabla^2 g\right) \mathrm{d}x\mathrm{d}y = \int_{\partial S} \left(g\frac{\partial h}{\partial n} - h\frac{\partial g}{\partial n}\right) \mathrm{d}\Gamma$$

can be used to swap the derivative operations from the solution to the basis functions for which the derivatives are known (Eqn. (7.10)). We therefore get, for a constant wave number, the equivalent integral equation

$$-\iint_{\Omega} u_A \nabla^2 g \mathrm{d}x\mathrm{d}y + B_T - k^2 \iint_{\Omega} u_A g \mathrm{d}x\mathrm{d}y = \iint_{\Omega} f g \mathrm{d}x\mathrm{d}y$$

where B_T is the boundary integral. As a means of keeping the notation compact we have used g to represent the weights and basis functions such that

$$\begin{aligned} g &\equiv g(x,y) \\ &= g_x(x) g_y(y) \\ &= \left[S(p,h_x) \circ \phi_x(x)\right] w(x) \left[S(q,h_y) \circ \phi_y(y)\right] v(y) \end{aligned}$$

We continue by expanding the 2D Laplacian operator in the first term in the integral equation and assume the weight vw is selected to cause B_T to vanish. A suitable choice of weight function to achieve this is $w(x)v(x) = 1/\sqrt{\phi_x'(x)\phi_y'(y)}$. The purpose of the weighting function can be to [85, 300]:

1. Simplify the discrete system;
2. Introduce special symmetric structure to reduce computational cost [243];
3. Reduce the truncation error of the infinite series;
4. Force boundary terms to zero (necessary assumption during the application of quadrature);
5. Allow the approximation to match physical solutions more closely thus reducing overall errors due to coefficient inaccuracies;
6. Allow the direct analysis of problems on semi-infinite and infinite domains [240];

For a more detailed discussion of appropriate weighting functions see [97]. Our weighted residual statement is, therefore:

$$-\iint_{\Omega} u_A g_y g_x'' \mathrm{d}x\mathrm{d}y - \iint_{\Omega} u_A g_x g_y'' \mathrm{d}x\mathrm{d}y - k^2 \iint_{\Omega} u_A g \mathrm{d}x\mathrm{d}y = \iint_{\Omega} f g \mathrm{d}x\mathrm{d}y \qquad (7.15)$$

The weighted residual statement is then discretised by substituting the approximation for u_A and applying the 2D quadrature rule

$$\iint z(x,y)\mathrm{d}x\mathrm{d}y \approx h_x h_y \sum_{j=-M_x}^{N_x} \sum_{k=-M_y}^{N_y} \frac{z(x_j,y_k)}{\phi'_x(x_j)\phi'_y(y_k)}$$

which is equivalent to Eqn. (7.8) extended to two dimensions where $z(x,y)$ is an arbitrary 2D function and the nodal points are represented by combinations of (x_j, y_k). A special case of the quadrature rule useful for our analysis, for given values of p and q, is [182]

$$\iint G(x,y)\left[S(p,h_x)\circ\phi_x(x)\right]\left[S(q,h_y)\circ\phi_y(y)\right]\mathrm{d}x\mathrm{d}y \approx h_x h_y \frac{G(x_p,y_q)}{\phi'_x(x_p)\phi'_y(y_q)} \tag{7.16}$$

where implicitly the known results of $\delta_{pj}^{(0)}$ and $\delta_{qk}^{(0)}$ from Eqn. (7.11) have been used. The product rule is used on the weighted residual statement (Eqn. (7.15)) to expand the derivatives in the inner products. Specifically we note that

$$\begin{aligned} g''_x(x) &= \left[\left[S(p,h_x)\circ\phi_x(x)\right]w(x)\right]'' \\ &= \left[S'w + w'S\right]' \\ &= \left[S''w + S'w' + w''S + w'S'\right] \\ &= \left[S''w + w''S + 2S'w'\right] \end{aligned}$$

but $S' = \tilde{S}'\phi'_x$ where $\tilde{S}'$ is viewed as a function of ϕ_x. Therefore applying the product rule again $S'' = \tilde{S}'\phi''_x + \tilde{S}''\left(\phi'_x\right)^2$ gives us

$$= \left[\tilde{S}''\left(\phi'_x\right)^2 w + \tilde{S}'\left(w\phi''_x + 2w'\phi'_x\right) + Sw''\right] \tag{7.17}$$

and likewise for $g''_y(y)$. Application of the quadrature rule to the discretised weighted residual statement gives us the following discretised equation for a given combination of basis functions

$$\frac{v}{\phi'_y}(y_q)\sum_{j=-M_x}^{N_x}\left[-\frac{1}{h_x^2}\delta_{pj}^{(2)}\phi'_x w-\frac{1}{h_x}\delta_{pj}^{(1)}\left(\frac{\phi''_x}{\phi'_x}w+2w'\right)-\delta_{pj}^{(0)}\frac{w''}{\phi'_x}\right](x_j)u_{jq}$$
$$+\frac{w}{\phi'_x}(x_p)\sum_{k=-M_y}^{N_y}\left[-\frac{1}{h_y^2}\delta_{qk}^{(2)}\phi'_y v-\frac{1}{h_y}\delta_{qk}^{(1)}\left(\frac{\phi''_y}{\phi'_y}v+2v'\right)-\delta_{qk}^{(0)}\frac{v''}{\phi'_y}\right](y_k)u_{pk}$$
$$-k^2\frac{vw}{\phi'_x\phi'_y}(x_p,y_q)u_{pq}=\frac{fvw}{\phi'_x\phi'_y}(x_p,y_q) \quad (7.18)$$

Allowing p and q to vary over their range of values we generate a system of equations which after some slight rearrangement can be expressed as

$$\mathbf{D}(\phi'_x)\tilde{\mathbf{A}}(w)\mathbf{D}(\phi'_x)\mathbf{V}+\mathbf{V}\left[\mathbf{D}(\phi'_y)\tilde{\mathbf{A}}(v)\mathbf{D}(\phi'_y)\right]^T-k^2\mathbf{V}=\mathbf{G}$$

where $\mathbf{D}$ represents a diagonal matrix and

$$\begin{aligned}\tilde{\mathbf{A}}(\omega)&=-\frac{1}{h^2}\mathbf{I}^{(2)}-\frac{1}{h}\mathbf{I}^{(1)}\mathbf{D}\left(\frac{\phi''}{(\phi')^2}+\frac{2\omega'}{\phi'\omega}\right)-\mathbf{D}\left(\frac{\omega''}{(\phi')^2\omega}\right)\\ \mathbf{V}&=\mathbf{D}(w)\mathbf{U}\mathbf{D}(v)\\ \mathbf{G}&=\mathbf{D}(w)\mathbf{F}\mathbf{D}(v)\end{aligned} \quad (7.19)$$

where ω can be either v or w and the elements of the matrices $\mathbf{I}^{(n)}$ are evaluated using Eqn. (7.11). Using the definitions $\mathbf{D}(\phi'_x)\tilde{\mathbf{A}}(w)\mathbf{D}(\phi'_x)=\mathbf{A}_x$ and $\mathbf{D}(\phi'_y)\tilde{\mathbf{A}}(v)\mathbf{D}(\phi'_y)=\mathbf{A}_y$ we represent this system as a generalised Sylvester equation

$$\begin{aligned}\mathbf{A}_x\mathbf{V}+\mathbf{V}\mathbf{A}_y^T-k^2\mathbf{V}&=\mathbf{G}\\ \Rightarrow(\mathbf{A}_x-k^2\mathbf{I}_{m_x})\mathbf{V}+\mathbf{V}\mathbf{A}_y^T&=\mathbf{G}\end{aligned} \quad (7.20)$$

$\mathbf{I}_{m_x}$ is here an identity matrix of size $m_x \times m_x$, where m_x refers to the size of the x-basis.

7.5 Solution Method

The two most common solution methods for this system are presented in [204] and comprise:

1. Rewriting the system as a large sparse linear system by concatenating the vectors and matrices of the current system.

2. Assuming $\mathbf{A}_x - k^2\mathbf{I}_{m_x}$ and $\mathbf{A}_y^T$ are diagonalisable (depends on the choice of weight function and order of the problem), factorising to construct $\mathbf{V}$ and hence $\mathbf{U}$.

Solution using the former method begins by concatenating the components of the left hand side of Eqn. (7.20) such that a single linear system is produced. This procedure is described by the following theorem [182].

Theorem 7.5.1 *For unknown matrix* $\mathbf{U}$*, let there be a series of linear systems*

$$\mathbf{A}_1\mathbf{U}\mathbf{B}_1 + \ldots + \mathbf{A}_n\mathbf{U}\mathbf{B}_n = \mathbf{G}$$

where the dimensions of the matrices $\mathbf{A}_i$ *and* $\mathbf{B}_i$ *are* $m_x \times m_x$ *and* $m_y \times m_y$ *respectively and therefore both* $\mathbf{U}$ *and* $\mathbf{G}$ *are* $m_x \times m_y$*. This is equivalent to*

$$\mathbf{C}\mathrm{co}(\mathbf{U}) = \mathrm{co}(\mathbf{G})$$

where

$$\mathbf{C} \equiv \mathbf{B}_1^T \otimes \mathbf{A}_1 + \ldots + \mathbf{B}_n^T \otimes \mathbf{A}$$

and the concatenation operator co( ) *is defined formally in the appendix of [204].*

We may thus rewrite the system Eqn. (7.20) in this form with

$$\mathbf{C} = \mathbf{I}_{m_y} \otimes \left(\mathbf{A}_x - k^2\mathbf{I}_{m_x}\right) + \mathbf{A}_y \otimes \mathbf{I}_{m_x}$$

Also,

$$\begin{aligned}\mathrm{co}\mathbf{V} &\equiv \mathrm{co}\left(\mathbf{D}(w)\mathbf{U}\mathbf{D}(v)\right)\\ &= \left[\mathbf{D}(v) \otimes \mathbf{D}(w)\right]\mathrm{co}(\mathbf{U})\\ &= \mathbf{D}_{vw}\mathrm{co}(\mathbf{U})\end{aligned}$$

and hence

$$\mathrm{co}(\mathbf{G}) = \mathbf{D}_{vw}\mathrm{co}(\mathbf{F})$$

The Gauss-Jordan elimination method may be applied to increase computational efficiency, exploiting the special structure of the resulting linear system [219, 220]. Furthermore, as discussed earlier, certain choices of weighting function enable the constituent matrices to be symmetric. In this case, it is possible to dramatically reduce the number of operations required to solve the system from $\mathcal{O}(n^3)$ to $\mathcal{O}(n \log n)$, for a 1D system of dimension n, and from $\mathcal{O}(n_x^3 + n_x n_y)$ (or $\mathcal{O}(n_y^3 + n_y n_x)$) to $\mathcal{O}(n_x n_y)$, for a 2D system of dimensions $n_x \times n_y$, by applying appropriate pre-conditioners as illustrated by Ng [243].

The alternative procedure for solving Eqn. (7.20) is valid assuming we have chosen a weight function which enables $\mathbf{A}_x - k^2\mathbf{I}_{m_x}$ and $\mathbf{A}_y^T$ to be diagonalised. If this is true, then, from classical results, there exists matrices $\mathbf{P}$ and $\mathbf{Q}$ which satisfy

$$\mathbf{P}^{-1}(\mathbf{A}_x - k^2\mathbf{I}_{m_x})\mathbf{P} = \mathbf{\Lambda}_x$$
$$\mathbf{Q}^{-1}\mathbf{A}_y^T\mathbf{Q} = \mathbf{\Lambda}_y$$

where $\mathbf{\Lambda}_{x,y}$ is a diagonal matrix of the eigenvalues of $\mathbf{A}_x - k^2\mathbf{I}_{m_x}, \mathbf{A}_y^T$ and matrices $\mathbf{P}$ and $\mathbf{Q}$ have columns corresponding to the associated eigenvectors. This allows us to rewrite the system

$$\mathbf{\Lambda}_x\mathbf{W} + \mathbf{W}\mathbf{\Lambda}_y = \mathbf{H}$$

where

$$\mathbf{W} = \mathbf{P}^{-1}\mathbf{V}\mathbf{Q}$$
$$\mathbf{H} = \mathbf{P}^{-1}\mathbf{G}\mathbf{Q}$$

If the spectrum of the matrices are denoted

$$\sigma(\mathbf{A}_x - k^2\mathbf{I}_{m_x}) = \{(\lambda_x)_i\}_{i=-M_x}^{N_x}$$
$$\sigma(\mathbf{A}_y) = \{(\lambda_y)_j\}_{j=-M_y}^{N_y}$$

then the components of the unknown matrix $\mathbf{W}$ are given by

$$w_{ij} = \frac{h_{ij}}{(\lambda_x)_i + (\lambda_y)_j}$$

where h_{ij} refers to the elements of $\mathbf{H}$. Therefore the unknown values of the coefficients stored in $\mathbf{U}$ may be recovered from

$$\mathbf{U} = \mathbf{D}\left(\frac{1}{v}\right)\mathbf{P}\mathbf{W}\mathbf{Q}^{-1}\mathbf{D}\left(\frac{1}{w}\right)$$

where we could also have written $\mathbf{D}\left(\frac{1}{v}\right) \equiv \mathbf{D}^{-1}(v)$ and $\mathbf{D}\left(\frac{1}{w}\right) \equiv \mathbf{D}^{-1}(w)$. In order to implement the method, it is necessary to find $\mathbf{P}$, $\mathbf{Q}$, $\mathbf{\Lambda}_x$ and $\mathbf{\Lambda}_y$.

Of the two methods, the former method requires no presumption of the properties of the matrices and is a more tractable approach when the PDE has non-constant coefficients or contains operators and terms of low order [220]. Furthermore, using the former method of solution, the unknowns in $\mathbf{V}$ are treated as a vector which lends itself to parallel computing systems. The former method is, therefore, selected over the latter. One obvious disadvantage of the approach is the amount of memory required to store the large matrices involved. This can put restrictions on the chosen basis size, and hence approximation accuracy.

7.5.1 Parameter Selection

The optimum choice of M_x and N_x depends on the behaviour of the solution at the boundaries of the interval. Suitable choices enhance the convergence rates of the method as the theorems in Lund & Bowers [204] illustrate. However, for practical problems, the solution is likely to be unknown and hence we use the advice of Mueller and Shores [238] to make selections they describe as being 'safe' in most cases. Specifically, Mueller and Shores recommend

$$N = \left\lceil \left| \frac{\alpha}{\beta} M + 1 \right| \right\rceil$$

and also

$$h = \sqrt{\frac{\pi d}{\alpha M}}$$

and also choose $\alpha = \beta = 1$. In addition, we use the choice of $d = \pi/4$, considered as 'conservative' by Mueller and Shores.

7.5.2 Removal of the Singularity

At this point it is worth recalling that the exponential convergence of the Sinc-Galerkin method is only maintained if the problem has *at worst regular singular points at the boundary* [305]. By introducing a singular source within the domain, we violate the conditions for exponential convergence of the sinc series. However, one way to proceed could be to remove the singularity from the solution and then apply the Sinc-Galerkin procedure to the non-singular problem, rather than tackling the problem directly. This would require knowledge of the nature of the singularity in advance, which may not be available. If, however, we assume the singularity to be of a logarithmic nature we may write the solution to Eqn. (7.1) as

$$u(x,y) = \ln v(x,y) + \bar{u}(x,y)$$

where $\bar{u}$ represents the non-singular part of the solution to be expressed as a sinc expansion. The equation to solve is then

$$\begin{aligned} \mathcal{L}\bar{u} &= -(f + \mathcal{L}\ln v) \\ &\equiv \bar{f} \end{aligned}$$

where $\mathcal{L}$ is the Helmholtz operator in the case studied here. Alternatively, we could use classical results to construct the singularity. For example, the known expansion for a corner singularity is used in Marin *et al.* [218]. Such a procedure is not the focus of this work as we wish to examine how we may directly apply the Sinc-Galerkin procedure to problems whose solutions contain unknown domain singularities.

7.6 Numerical Validation

We now apply the 2D Sinc-Galerkin formulation established in the previous section to compute Green's functions within a rectangular patch subject to homogeneous Dirichlet-type boundary conditions ($g = 0$ in Eqn. (7.1)). Although we choose to compute Green's functions for the Helmholtz equation, the formulation presented here may also be used for Laplace's equation by simply setting the wave number $k = 0$. As discussed in Chapter 3, the use of the Green's function to solve realistic boundary

value problems is a fast and accurate alternative to common numerical schemes such as FEM or finite differences provided the Green's function can be found. Traditionally, the solution of many acoustic BVPs would have been undertaken using an acoustic analogy [81, 226, 247]. However, the lack of available Green's functions for more general geometries restricts its present use. Choosing the domain to be a patch we allow the present formulation to be included in a more complicated patching or overlapping algorithm [209, 210]. Such algorithms allow the method to be applied to a wider class of geometries. Through the selection of appropriate conformal maps, it is also possible to apply the Sinc-Galerkin method to semi-infinite and infinite rectangular geometries. In these cases the Sinc-Galerkin method does not require artificial boundaries or non-reflecting boundary conditions as would be necessary for use of the FEM for the same problem, which can be particularly useful. We provide the analytical solutions for both the examples below which we use as a means of assessing the accuracy of our results. These examples demonstrate that the Sinc-Galerkin method may be used to numerically evaluate Green's functions with accuracy. The extension of the present formulation to 3D is straightforward [204] but is not performed here to ensure the results are clearly understood. As a means of examining convergence, we vary the mesh density uniformly up to a maximum of 3 times the lowest mesh density in order to show the trend. All computations are performed using MATLAB on an Intel Core i7 870 CPU.

7.6.1 Source Specification

In order to configure the Sinc-Galerkin method for our problem, we must specify a suitable source function f. As we are considering the BVP defined by Eqn. (7.2), along with homogeneous boundary conditions, the source function is equal to the Dirac delta function centred at (y_1, y_2). A suitable numerical approximation to the delta function would be required for many numerical methods, usually by considering the well-known limits of a Gaussian function [23, 234] or a Lorentzian function. Moreover, Tornberg and Björn [331] present an analysis of a variety of regularisation techniques for a delta function with compact support. However, as we use a Galerkin weighted residual technique, the application of a numerical quadrature to evaluate the source term inner product is not strictly necessary. The source term is a delta function which

is an integrable singular function. Therefore we exploit the sifting property to express the source inner product analytically avoiding any potential error introduced by an approximation. Using the coordinate definition of the previous section and denoting the source location in the rectangle by (x_0, y_0) we have

$$\begin{aligned}\langle f, S_{pq}\rangle &= \iint_{\Omega} \delta(x-x_0)\delta(y-y_0)\left[S(p,h_x)\circ\phi_x(x)\right]\left[S(q,h_y)\circ\phi_y(y)\right]\mathrm{d}x\mathrm{d}y \\ &= S_{pq}vw(x_0,y_0)\end{aligned}$$

In order to incorporate this into Eqn. (7.18) we need to manipulate this further; in moving from Eqn. (7.18) to Eqn. (7.20) we have divided both sides by $h_x h_y$, multiplied through by $\phi'_x\phi'_y(x_p, y_q)$ and then, due to the definition of $\mathbf{G}$, multiplied through by $vw(x_p, y_q)$. Therefore, we incorporate the inverse of these operations in the definition of f in Eqn. (7.18) giving us a source function defined by

$$f_{pq}(x_0,y_0,x_p,y_q) \equiv \frac{1}{h_x h_y}\left[S_{pq}vw\right](x_0,y_0)\left[\frac{vw}{\phi'_x\phi'_y}\right](x_p,y_q) \tag{7.21}$$

7.6.2 Green's Function for the 2D Helmholtz equation

We consider the Green's function for the Helmholtz equation in a rectangle subject to homogeneous Dirichlet boundary conditions on the walls (Eqn. (7.2) with $g = 0$). The analytical solution to the problem may be constructed using a double Fourier sine transform method thus [285]: Starting with

$$\left(\nabla^2 + k^2\right)u(x,y) = -f(x,y)$$

and letting

$$f(x,y) = f_0 F(x,y)$$

gives

$$\left(\nabla^2 + k^2\right)u(x,y) = -f_0 F(x,y)$$

Given the boundary conditions we may apply double Fourier sine transforms to both sides by multiplying by $\sin\left(\frac{n\pi x}{a}\right)\sin\left(\frac{m\pi y}{b}\right)$ and integrating over the rectangle

$$\int_0^a\int_0^b \left[\nabla^2 u(x,y) + k^2 u(x,y)\right] \sin\left(\frac{n\pi x}{a}\right) \sin\left(\frac{m\pi y}{b}\right) \mathrm{d}y\mathrm{d}x$$

$$= -f_0 \int_0^a\int_0^b F(x,y) \sin\left(\frac{n\pi x}{a}\right) \sin\left(\frac{m\pi y}{b}\right) \mathrm{d}y\mathrm{d}x$$

Integrating the left hand side by parts term by term and applying the boundary conditions gives

$$-\frac{n^2\pi^2}{a^2} \int_0^a\int_0^b u(x,y) \sin\left(\frac{n\pi x}{a}\right) \sin\left(\frac{m\pi y}{b}\right) \mathrm{d}y\mathrm{d}x$$

$$-\frac{m^2\pi^2}{b^2} \int_0^a\int_0^b u(x,y) \sin\left(\frac{n\pi x}{a}\right) \sin\left(\frac{m\pi y}{b}\right) \mathrm{d}y\mathrm{d}x$$

$$+k^2 \int_0^a\int_0^b u(x,y) \sin\left(\frac{n\pi x}{a}\right) \sin\left(\frac{m\pi y}{b}\right) \mathrm{d}y\mathrm{d}x$$

Factorising and rearranging gives

$$\int_0^a\int_0^b u(x,y) \sin\left(\frac{n\pi x}{a}\right) \sin\left(\frac{m\pi y}{b}\right) \mathrm{d}y\mathrm{d}x = \frac{f_0 \int_0^a\int_0^b F(x,y) \sin\left(\frac{n\pi x}{a}\right) \sin\left(\frac{m\pi y}{b}\right) \mathrm{d}y\mathrm{d}x}{\pi^2\left(\frac{n^2}{a^2} + \frac{m^2}{b^2}\right) - k^2}$$

In order to obtain an expression for u on the left hand side, we next take the inverse transform which gives for a general source F and $(\eta, \xi) \in (0 \le x \le a, 0 \le y \le b)$

$$u(x,y) = \frac{4f_0}{ab} \sum_{n=1}^{\infty}\sum_{m=1}^{\infty} \left\{ \frac{\sin\left(\frac{n\pi x}{a}\right) \sin\left(\frac{m\pi y}{b}\right)}{\pi^2\left(\frac{n^2}{a^2} + \frac{m^2}{b^2}\right) - k^2} \int_0^a\int_0^b F(\eta,\xi) \sin\left(\frac{n\pi\eta}{a}\right) \sin\left(\frac{m\pi\xi}{b}\right) \mathrm{d}\xi\mathrm{d}\eta \right\}$$

For the Green's function we substitute $F(\eta,\xi) = \delta(\eta - \eta_0)\delta(\xi - \xi_0)$ and evaluate the integral to give the following analytical Green's function

$$u(x,y) = \frac{4f_0}{ab} \sum_{n=1}^{\infty}\sum_{m=1}^{\infty} \left[\frac{\sin\left(\frac{n\pi x}{a}\right) \sin\left(\frac{m\pi y}{b}\right) \sin\left(\frac{n\pi\eta_0}{a}\right) \sin\left(\frac{m\pi\xi_0}{b}\right)}{\pi^2\left(\frac{n^2}{a^2} + \frac{m^2}{b^2}\right) - k^2} \right] \tag{7.22}$$

Equation (7.22) describes the outgoing wave of wave-number k, produced by a point source of strength f_0, located at (η_0, ξ_0), observed at (x, y) subject to pressure release boundary conditions $(u = 0)$ on the boundaries of a rectangle of dimensions $a \times b$.

7.6.3 Centred Source

We now look at applying the 2D Sinc-Galerkin method developed earlier to solve the BVP whose solution is given by Eqn. (7.22). We consider first the case where the source is located at the centre of the rectangle. The number of terms used in the sinc expansion (size of the basis) in both the x and y-directions are the same (as the expected solution is symmetric) and equal to 8 uniformly spaced values between $M = 12$ and $M = 36$. This range allows us to increase the mesh density by up to a factor of 3. We also vary the frequency (and hence the wave number k). We test 4 frequencies in the range 20 Hz to 2000 Hz. The lower limit is the lowest audible frequency and the upper limit chosen so that the plots do not contain too many high order modes making them difficult to read. The analytical solution Eqn. (7.22) is evaluated at each of the four frequencies truncating the series after 50 terms, by which time the series has suitably converged. The Sinc-Galerkin results for an expansion of $2M+1 = 65$ (32 sinc functions either side of the centre plus a single function at the centre) is compared to the analytical solution at the tested frequencies in Fig. 7.2. All plots use the same colour scale.

Figure 7.2 illustrates that the analytical solution behaves as expected: the homogeneous Dirichlet boundary conditions are met as the solutions tends to zero on all boundary edges. In fact, every one of the sinc functions in the basis set decay to zero at the edge of the domain which ensures this boundary condition is satisfied by the composite solution. The characteristic singularity of the Green's function at the centre of the point source is also visible. As the frequency is increased the higher harmonics of the allowable modes appear which is expected to put increased demands on the ability of the numerical schemes to resolve the solution. By comparing the Sinc-Galerkin solution to the analytical solution, we see that the singularity is only captured up to a point, with the precision of the sinc-based approximation in the immediate vicinity of the source point being lost. This is the principle source of error when using the Sinc-Galerkin to solve our class of BVP. This may be attributed to the uneven distribution of sinc mesh points: our source is located in the centre of the region under consideration. This coincides with the region most sparsely populated with mesh nodes. Therefore, it is expected that steep gradients are difficult to represent in this region. In addition, the peak of the sinc function has a value of unity and hence to capture a

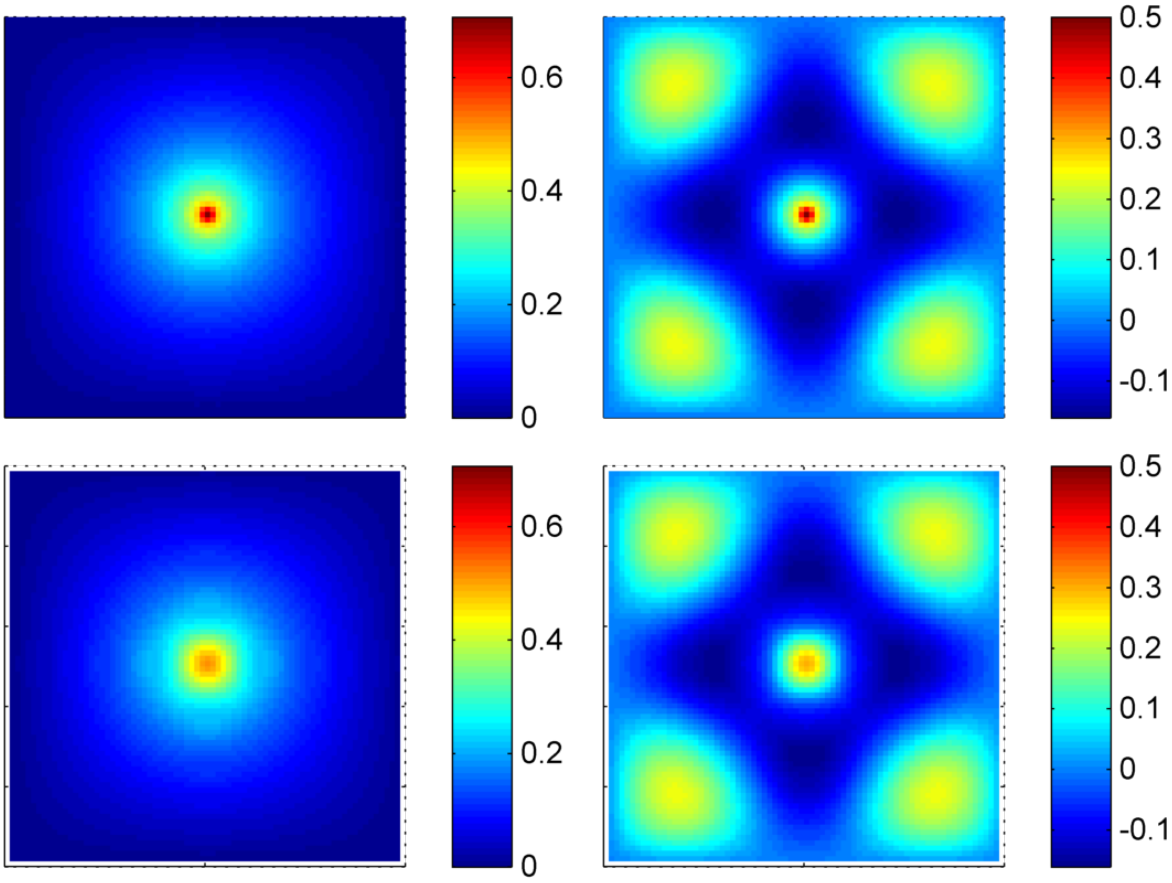

(a) f=20 (left column) and f=680 (right column)

singularity requires a relatively large coefficient which would impact the contribution of this function over the whole of the domain. The resulting behaviour is, therefore, a trade-off between overall accuracy and the ability to capture the singularity. If the method were included as part of a domain decomposition approach to the problem, the sub-domain boundaries could be defined such that the singularity is situated on the boundary. In this case, the exponential convergence of the method could be restored. We present the relative error and the execution time for all frequencies tested (Fig. 7.3a (log scale) and Fig. 7.3b). For most of the mesh densities tested, the Sinc-Galerkin method performs reasonably well with the mean relative error remaining less than 15%. Initially, for the highest frequency, the method performs poorly. This is due to the basis being of insufficient size to ensure the expansion converges to a suitable degree as to accurately represent the field – a trait common to spectral/spatial methods with a finite set of basis functions. As the number of terms in the expansion is increased, the error begins to reduce. Although at the highest mesh density tested the relative error is still large, it is driven by a combination of localised error in the vicinity of the

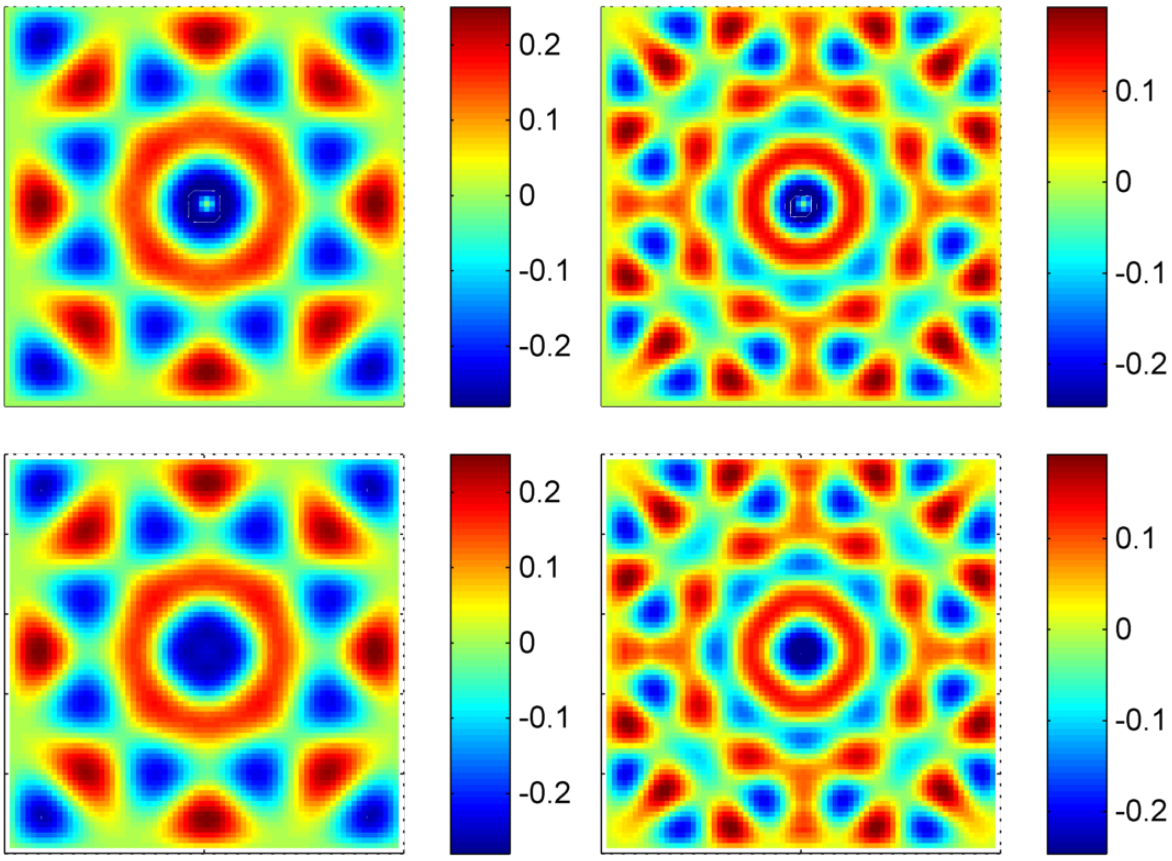

(b) f=1340 (left column) and f=2000 (right column)

Figure 7.2: Results for the analytical expression Eqn. (7.22) (top row) and Sinc-Galerkin M=32 (bottom row) for a source centred in the unit square

singularity, specifically at the 'tip', and small errors in regions where the analytical representation is near zero resulting in large relative errors. Figure 7.2 supports this assertion as qualitatively the results agree well.

Despite the presence of a domain singularity, in the main, the lines are roughly linear which suggests an exponential variation (logarithmic scale). Figure 7.3a also indicates the limit of exponential convergence based on the error at the lowest mesh density. This limit is computed from setting the error equal to

$$A(f)e^{-\sqrt{N}} \tag{7.23}$$

equivalent to setting $k = 1$ in the expression given in Section 7.1.0.1. The constant $A(f)$ is frequency dependent and is chosen such that the curves coincide at the lowest mesh density. The convergence is generally uneven with mesh density and varies with frequency, with the lowest frequency converging less than exponentially with mesh density. However, in the case of the higher frequencies, it converges at worst with the exponential convergence limit and in some cases exceeds this. We conclude that the exponential convergence of the method can still be achieved but the decay is significantly slower than other studies whose solutions do not contain a singularity. This is expected as spectral methods generally only guarantee rapid convergence when the functions being represented are smooth without strong singularities or discontinuities. Convergence rates may be improved by implementing the double exponential transformation ([245, 307, 356]).

7.6.4 Near-Boundary Source

For sources near to the boundary, many boundary integral techniques fail due to the proximity of the singularity to the collocation points. The steep gradients of the exact solution exacerbates the role of small errors in integration. It is of interest, therefore, to examine the case of a near-boundary source. With the Sinc-Galerkin method, we effectively locate the singularity in a region of the domain with a denser sinc node distribution. This distribution is a result of the non-linear conformal transformation of the evenly-spaced sinc nodes along the real line. We expect to see an improvement in the Sinc-Galerkin's ability to capture the singularity. We repeat the same tests as in the previous section but locate the source with an x-coordinate corresponding to

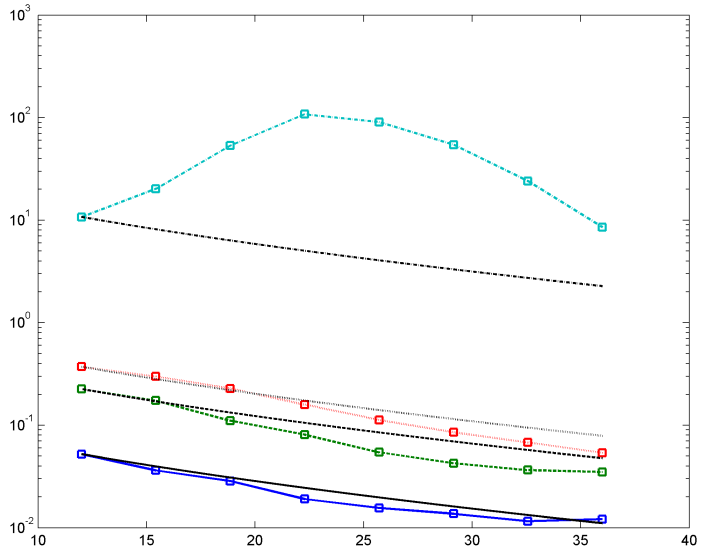

(a) f=20 (solid blue), f=680 (dashed green), f=1340 (dotted red), f=2000 (dot-dash cyan)

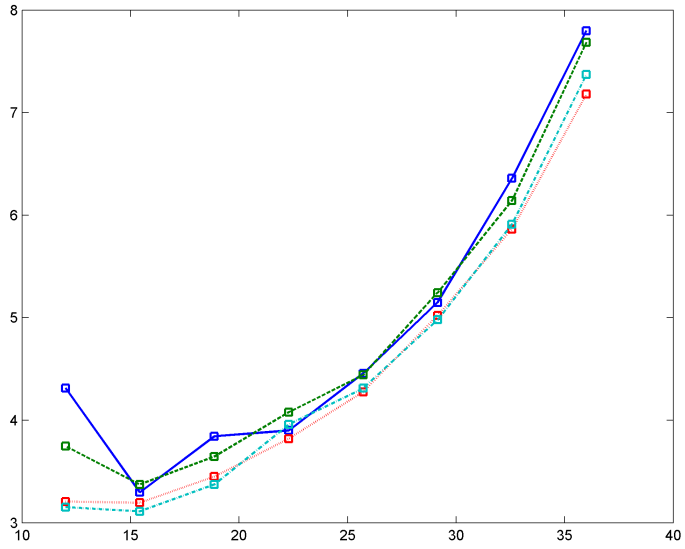

(b) f=20 (solid blue), f=680 (dashed green), f=1340 (dotted red), f=2000 (dot-dash cyan)

Figure 7.3: Relative error (top) and execution time in seconds (bottom) for Sinc-Galerkin for $M = 12$ to $M = 36$ (horizontal axis) for a centred source. The limit of exponential behaviour according to Eqn. (7.23) is shown in black for each frequency.

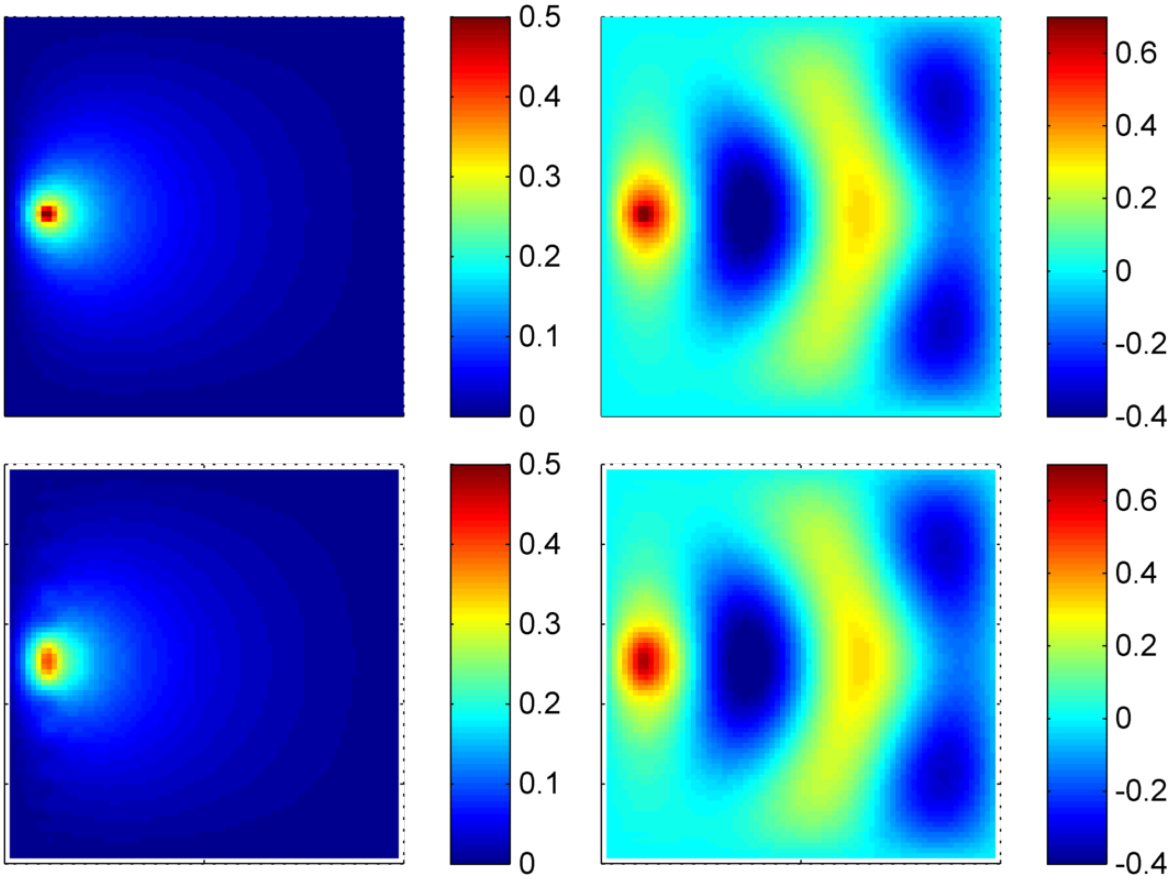

(a) f=20 (left column) and f=680 (right column)

$x/W = 0.1$ where $W = 1$ is the domain width. As before, we plot the surfaces for a Sinc-Galerkin expansion of $2M+1 = 65$ and compare to the analytical solution, again evaluated using 50 terms of the expansion Eqn. (7.22). We also plot the relative error and the execution time in all cases (Fig. 7.5a and Fig. 7.5b).

The analytical solution, plotted in Fig. 7.4, again illustrates the expected behaviour including the singularity located nearer the boundary. The inclusion of higher-order modes and spreading of the acoustic wave is visible at $f > 680$ Hz. Although the Sinc-Galerkin results indicate that the decay of the solution is well-represented away from the singularity, again the immediate vicinity of the singularity is not captured in its entirety. Singularities in the Green's function are often interpreted as representing regions of significant sound pressure (potentially due to scattering) and the loss of resolution could be viewed as a significant drawback of the method. However, as we see from Fig. 7.4, the tendency of the solution to develop into a singularity remains clear despite the point itself being lost. Therefore, the implications of the loss in fidelity may not be as severe as first appears. However, this suggestion should be

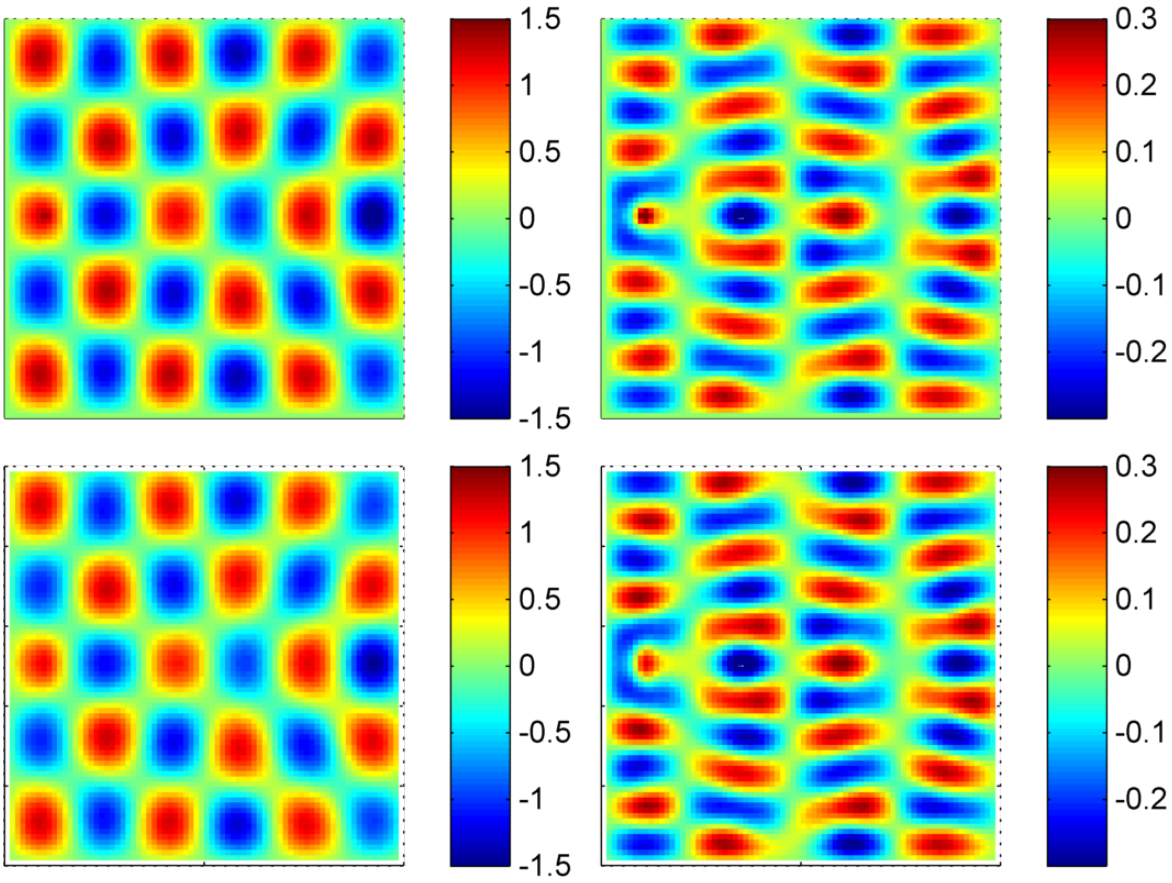

(b) f=1340 (left column) and f=2000 (right column)

Figure 7.4: Results the analytical expression Eqn. (7.22) (top row) and Sinc-Galerkin M=32 (bottom row) for a source near the boundary of the unit square

investigated further as part of future work by linking the Green's function computed using the Sinc-Galerkin method to an acoustic analogy to explore the implications of errors in singular regions on the observed sound field.

When comparing Fig. 7.5a to Fig. 7.3a, the error now increases with frequency across the whole range tested unlike for the centred source with an increase in the overall error of the order $10^{-0.5}$. The Sinc-Galerkin generally converges exponentially again (straight line on the logarithmic graph) and convergence remains relatively quick regardless of frequency. The exception is the highest frequency tested where the convergence is less predictable. The behaviour is, however, not entirely unexpected: more terms are required for the expansion to represent the rapid changes in the solution at the highest frequency. Clearly, there is a minimum number of terms required before the cancellation between the high frequency modes begins to aid accuracy rather than exacerbate inaccuracies. This may explain the 'hump' in convergence observable in the figure. Overall, both Fig. 7.5b and Fig. 7.3b show little sensitivity to source location. This indicates that the source location selected here is insufficiently close to the boundary as to cause any notable computational difficulties. Moving the source closer to the boundary, therefore, has little effect on both the overall error, execution time and the convergence of the Sinc-Galerkin method.

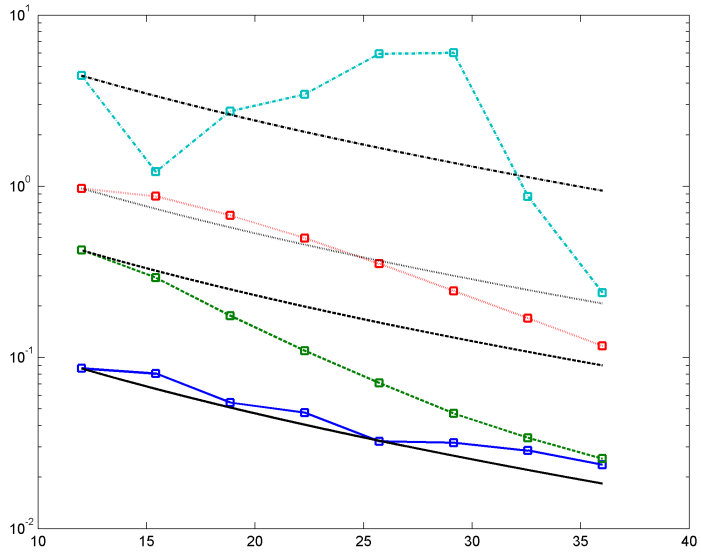

(a) f=20 (solid blue), f=680 (dashed green), f=1340 (dotted red), f=2000 (dot-dash cyan)

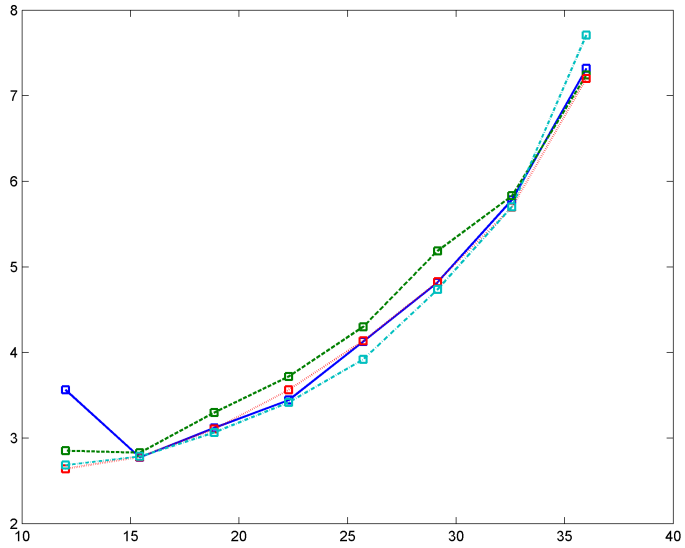

(b) f=20 (solid blue), f=680 (dashed green), f=1340 (dotted red), f=2000 (dot-dash cyan)

Figure 7.5: Relative error (top) and execution time in seconds (bottom) for Sinc-Galerkin for $M = 12$ to $M = 36$ (horizontal axis) for a near-boundary source. The limit of exponential behaviour according to Eqn. (7.23) is shown in black for each frequency.

7.7 2D Sinc-Galerkin for the Helmholtz Equation with Neumann Boundary Conditions

Our analysis has focused up to this point on the Dirichlet formulation. For a number of other useful acoustic problems, boundary conditions involve the spatial derivative of the solution. This derivative condition is commonly referred to as the Neumann boundary condition. In order to apply the Sinc-Galerkin method to problems featuring such boundary conditions, we introduce here a suitable discretisation of the problem, guided by the work of Lund and Bowers [204].

7.7.1 Formulation

Two modifications are required to our basis in order to allow their application to the latter BVP. First, since by definition, 1D sinc functions satisfy homogeneous Dirichlet conditions at the ends of the interval, they are incapable of representing a non-zero boundary solution. The first modification is to extend the basis to include functions which represent the solution in the vicinity of the boundary. For simplicity, the modification are initially applied to the 1D BVP

$$\begin{aligned} \mathcal{L}\left[u(x)\right] = -u''(x) + p(x)u'(x) + q(x)u(x) = f(x) \qquad & x \in [a,b] \\ a_0 u(a) - a_1 u'(a) = 0 & \\ b_0 u(b) + b_1 u'(b) = 0 & \end{aligned}$$

The values of a_0, a_1, b_0, b_1 are positive and if $a_1 = 0$ then $b_1 \neq 0$ and *vice versa* [204]. The basis may be extended by two additional functions $w_a(x)$ and $w_b(x)$ giving approximate solution

$$u_A(x) = u_{-M-1} w_a(x) + \left(\sum_{k=-M}^{N} u_k \xi_k(x) \right) + u_{N+1} w_b(x)$$

where $\xi_k(x)$ are, for now, the usual shifted sinc function basis components Eqn. (7.14). The boundary functions w_a and w_b are interpolating Hermite functions of order 3 which interpolate the boundary conditions given in the problem definition as

$$w_a(x) = a_0\frac{(x-a)(b-x)^2}{(b-a)^2} + a_1\frac{(2x+b-3a)(b-x)^2}{(b-a)^3}$$
$$w_b(x) = b_1\frac{(-2x+3b-a)(x-a)^2}{(b-a)^3} + b_0\frac{(b-x)(x-a)^2}{(b-a)^2}$$

The second modification is to divide the sinc functions in the basis by ϕ' to ensure that the derivative of each basis function is defined at the boundary, which will in turn ensure that the solution remains defined in these regions. Consider then the Helmholtz BVP with homogeneous Neumann conditions on a square domain defined as

$$\begin{aligned}(\nabla^2 + k^2)u(x,y) &= -f(x,y) \qquad && (x,y) \in \Omega = (a,b)\times(c,d)\\ \frac{\mathrm{d}u}{\mathrm{d}n} &= 0 && (x,y) \in \Gamma\end{aligned}$$

The approximate solution defined in terms of the modified and extended basis is given by

$$u_A(x,y) = \sum_{k=-M_y-1}^{N_y+1}\sum_{j=-M_x-1}^{N_x+1} u_{jk}\xi_j(x)\zeta_k(y)$$

where

$$\xi_j(x) = \begin{cases} w_0(x) & j = -M_x - 1\\ \frac{S(j,h_x)\circ\phi_x(x)}{\phi_x'(x)} \equiv \tilde{S}_j & j = -M_x,\ldots,N_x\\ w_1(x) & j = N_x+1\end{cases}$$

and

$$\zeta_k(y) = \begin{cases} w_2(y) & k = -M_y - 1\\ \frac{S(k,h_y)\circ\phi_y(y)}{\phi_y'(y)} \equiv \tilde{S}_k & k = -M_y,\ldots,N_y\\ w_3(y) & k = N_y+1\end{cases}$$

The ensuing method now is based on the following modified inner product orthogonalisation which is not a true Galerkin procedure but a Petrov-Galerkin procedure since the basis functions used for the orthogonalisation are a different set to the base used to represent the approximate solution. In fact, we now orthogonalise the residual with respect to the unmodified basis set

$$S_{pq} \equiv [S(p,h_x)\circ\phi_x(x)]\,[S(q,h_y)\circ\phi_y(y)]$$

for $-M_x-1 \leq p \leq N_x+1$ and $-M_y-1 \leq q \leq N_y+1$. We follow the convention [182] and split up the approximate solution. Our problem produces 9 sub-sets defined thus

$$\begin{aligned}
u_A(x,y) = {} & u_{(-M_x-1)(-M_y-1)}w_0(x)w_2(y) + \sum_{j=-M_x}^{N_x} u_{j(-M_y-1)}\tilde{S}_j(x)w_2(y) \\
& + u_{(N_x+1)(-M_y-1)}w_1(x)w_2(y) + \sum_{k=-M_y}^{N_y} u_{(-M_x-1)k}w_0(x)\tilde{S}_k(y) \\
& + \sum_{k=-M_y}^{N_y}\sum_{j=-M_x}^{N_x} u_{jk}\tilde{S}_j(x)\tilde{S}_k(y) + \sum_{k=-M_y}^{N_y} u_{(N_x+1)k}w_1(x)\tilde{S}_k(y) \\
& + u_{(-M_x-1)(N_y+1)}w_0(x)w_3(y) + \sum_{j=-M_x}^{N_x} u_{j(N_t+1)}\tilde{S}_j(x)w_3(y) \\
& + u_{(N_x+1)(N_y+1)}w_1(x)w_3(y)
\end{aligned}$$

$$\begin{aligned}
\equiv {} & u_{A1}(x,y) + u_{A2}(x,y) + u_{A3}(x,y) + u_{A4}(x,y) + u_{A5}(x,y) \\
& + u_{A6}(x,y) + u_{A7}(x,y) + u_{A8}(x,y) + u_{A9}(x,y)
\end{aligned}$$

We see that u_{A5} is equivalent to the approximation using for the associated Dirichlet problem (Eqn. (7.13)) with the additional terms arising due to the boundary conditions. We now look at each inner product of the residual and the unmodified basis set in turn and throughout make use of the quadrature rule (Eqn. (7.16)) and the delta notation of Eqn. (7.11) and we also note that our operator $\mathcal{L} \equiv \left(\frac{\partial^2}{\partial x^2} + \frac{\partial^2}{\partial y^2} + k^2\right)$. First we start with the inner product featuring u_{A_1} where the weighting function is given by $w(x)v(y)$.

$$\begin{aligned}
\langle \mathcal{L}[u_{A1}], S_p(x)S_q(y)\rangle = u_{(-M_x-1)(-M_y-1)} \Bigg\{ & \iint w_0''(x)w_2(y)S_p(x)S_q(y)w(x)v(y)\mathrm{d}x\mathrm{d}y \\
& + \iint w_0(x)w_2''(y)S_p(x)S_q(y)w(x)v(y)\mathrm{d}x\mathrm{d}y \\
& + k^2 \iint w_0(x)w_2(y)S_p(x)S_q(y)w(x)v(y)\mathrm{d}x\mathrm{d}y \Bigg\}
\end{aligned}$$

There is no need for any application of Green's second identity or integration parts, we can just apply the quadrature rule directly giving us

$$\langle \mathcal{L}[u_{A1}], S_p(x)S_q(y)\rangle \approx h_x h_y \left[\frac{w_0''w}{\phi_x'}(x_p)\frac{w_2 v}{\phi_y'}(y_q)u_{(-M_x-1)(-M_y-1)} + \frac{w_0 w}{\phi_x'}(x_p)\frac{w_2'' v}{\phi_y'}(y_q)u_{(-M_x-1)(-M_y-1)} + k^2\frac{w_0 w}{\phi_x'}(x_p)\frac{w_2 v}{\phi_y'}(y_q)u_{(-M_x-1)(-M_y-1)}\right]$$

Since u_{A3}, u_{A7} and u_{A9} are very similar we can immediately write down their inner product approximations

$$\langle \mathcal{L}[u_{A3}], S_p(x)S_q(y)\rangle \approx h_x h_y \left[\frac{w_1''w}{\phi_x'}(x_p)\frac{w_2 v}{\phi_y'}(y_q)u_{(N_x+1)(-M_y-1)} + \frac{w_1 w}{\phi_x'}(x_p)\frac{w_2'' v}{\phi_y'}(y_q)u_{(N_x+1)(-M_y-1)} + k^2\frac{w_1 w}{\phi_x'}(x_p)\frac{w_2 v}{\phi_y'}(y_q)u_{(N_x+1)(-M_y-1)}\right]$$

$$\langle \mathcal{L}[u_{A7}], S_p(x)S_q(y)\rangle \approx h_x h_y \left[\frac{w_0''w}{\phi_x'}(x_p)\frac{w_3 v}{\phi_y'}(y_q)u_{(-M_x-1)(N_y+1)} + \frac{w_0 w}{\phi_x'}(x_p)\frac{w_3'' v}{\phi_y'}(y_q)u_{(-M_x-1)(N_y+1)} + k^2\frac{w_0 w}{\phi_x'}(x_p)\frac{w_3 v}{\phi_y'}(y_q)u_{(-M_x-1)(N_y+1)}\right]$$

$$\langle \mathcal{L}[u_{A9}], S_p(x)S_q(y)\rangle \approx h_x h_y \left[\frac{w_1''w}{\phi_x'}(x_p)\frac{w_3 v}{\phi_y'}(y_q)u_{(N_x+1)(N_y+1)} + \frac{w_1 w}{\phi_x'}(x_p)\frac{w_3'' v}{\phi_y'}(y_q)u_{(N_x+1)(N_y+1)} + k^2\frac{w_1 w}{\phi_x'}(x_p)\frac{w_3 v}{\phi_y'}(y_q)u_{(N_x+1)(N_y+1)}\right]$$

Now we consider the inner product associated with u_{A2} which is

$$\langle \mathcal{L}[u_{A2}], S_p(x)S_q(y)\rangle = \sum_{j=-M_x}^{N_x} u_{j(-M_y-1)} \left\{ \iint \tilde{S}_j''(x)w_2(y)S_p(x)S_q(y)w(x)v(y)\mathrm{d}x\mathrm{d}y + \iint \tilde{S}_j(x)w_2''(y)S_p(x)S_q(y)w(x)v(y)\mathrm{d}x\mathrm{d}y + k^2\iint \tilde{S}_j(x)w_2(y)S_p(x)S_q(y)w(x)v(y)\mathrm{d}x\mathrm{d}y\right\}$$

This time, before we apply quadrature, we need to apply Green's second identity to the first inner product to transfer the derivative onto the sinc basis. Implicitly in the

process we assume the weighting functions will be selected to ensure the boundary terms vanish. The first integral becomes

$$\iint \tilde{S}_j''(x)w_2(y)S_p(x)S_q(y)w(x)v(y)\mathrm{d}x\mathrm{d}y \mapsto - \iint \tilde{S}_j(x)w_2(y)S_q(y)v(y)\left[S_p(x)w(x)\right]''\mathrm{d}x\mathrm{d}y$$

We use the product definition of Eqn. (7.17) to arrive at the final approximation.

$$\begin{aligned}\langle \mathcal{L}[u_{A2}], S_p(x)S_q(y)\rangle \approx h_x h_y \sum_{j=-M_x}^{N_x} u_{j(-M_y-1)} \Bigg\{ & \frac{w}{[\phi_x']^2}(x_j)\delta_{pj}^{(0)}\frac{w_2''v}{\phi_y'}(y_q) \\ & + k^2\frac{w}{[\phi_x']^2}(x_j)\delta_{pj}^{(0)}\frac{w_2 v}{\phi_y'}(y_q) \\ & - \frac{1}{[\phi_x']^2}\left[\frac{\delta_{pj}^{(2)}}{h_x^2}[\phi_x']^2 w + \frac{\delta_{pj}^{(1)}}{h_x}\left(w\phi_x'' + 2w'\phi_x'\right) + \delta_{pj}^{(0)}w''\right](x_j)\frac{w_2 v}{\phi_y'}(y_q)\Bigg\}\end{aligned}$$

It should be noted that the definition of $\tilde{S}_j \equiv S_j/\phi_x'$ has been substituted to ensure the delta definitions could be used. This accounts for one of the ϕ_x''s appearing in the denominator of the first part of the approximation where the second, which makes the denominator a square, is due to the quadrature definition. We may immediately write down the expression for u_{A8}

$$\begin{aligned}\langle \mathcal{L}[u_{A8}], S_p(x)S_q(y)\rangle \approx h_x h_y \sum_{j=-M_x}^{N_x} u_{j(N_y+1)} \Bigg\{ & \frac{w}{[\phi_x']^2}(x_j)\delta_{pj}^{(0)}\frac{w_3''v}{\phi_y'}(y_q) \\ & + k^2\frac{w}{[\phi_x']^2}(x_j)\delta_{pj}^{(0)}\frac{w_3 v}{\phi_y'}(y_q) \\ & - \frac{1}{[\phi_x']^2}\left[\frac{\delta_{pj}^{(2)}}{h_x^2}[\phi_x']^2 w + \frac{\delta_{pj}^{(1)}}{h_x}\left(w\phi_x'' + 2w'\phi_x'\right) + \delta_{pj}^{(0)}w''\right](x_j)\frac{w_3 v}{\phi_y'}(y_q)\Bigg\}\end{aligned}$$

For u_{A4} and u_{A6} we have a similar analysis

$$\begin{aligned}\langle \mathcal{L}[u_{A4}], S_p(x)S_q(y)\rangle = \sum_{k=-M_y}^{N_y} u_{(-M_y-1)k} \Bigg\{ & \iint w_0''(x)\tilde{S}_k(y)S_p(x)S_q(y)w(x)v(y)\mathrm{d}x\mathrm{d}y \\ & + \iint w_0(x)\tilde{S}_k''(y)S_p(x)S_q(y)w(x)v(y)\mathrm{d}x\mathrm{d}y \\ & + k^2\iint w_0(x)\tilde{S}_k(y)S_p(x)S_q(y)w(x)v(y)\mathrm{d}x\mathrm{d}y\Bigg\}\end{aligned}$$

As before, we apply Green's second identity to transfer the derivative operations to the basis. However, this time, we apply it to the second inner product. The second integral becomes

$$\iint w_0(x)\tilde{S}_k''(y)S_p(x)S_q(y)w(x)v(y)\mathrm{d}x\mathrm{d}y \mapsto - \iint w_0(x)\tilde{S}_k(y)S_p(x)w(x)\left[S_q(y)v(y)\right]''\mathrm{d}x\mathrm{d}y$$

We use the product definition of Eqn. (7.17) again to arrive at the final approximation.

$$\begin{aligned}\langle \mathcal{L}[u_{A4}], S_p(x)S_q(y)\rangle \approx h_x h_y \sum_{k=-M_y}^{N_y} u_{(-M_x-1)k} \Bigg\{ &\frac{w_0''w}{\phi_x'}(x_p)\frac{v}{[\phi_y']^2}(y_k)\delta_{qk}^{(0)} \\ &- \frac{1}{[\phi_y']^2}\left[\frac{\delta_{qk}^{(2)}}{h_y^2}[\phi_y']^2 v + \frac{\delta_{qk}^{(1)}}{h_y}\left(v\phi_y'' + 2v'\phi_y'\right) + \delta_{qk}^{(0)}v''\right](y_k)\frac{w_0 w}{\phi_x'}(x_p) \\ &+ k^2\frac{w_0 w}{\phi_x'}(x_p)\frac{v}{[\phi_y']^2}(y_k)\delta_{qk}^{(0)}\Bigg\}\end{aligned}$$

Immediately we find u_{A6} to be

$$\begin{aligned}\langle \mathcal{L}[u_{A6}], S_p(x)S_q(y)\rangle \approx h_x h_y \sum_{k=-M_y}^{N_y} u_{(N_x+1)k} \Bigg\{ &\frac{w_1''w}{\phi_x'}(x_p)\frac{v}{[\phi_y']^2}(y_k)\delta_{qk}^{(0)} \\ &- \frac{1}{[\phi_y']^2}\left[\frac{\delta_{qk}^{(2)}}{h_y^2}[\phi_y']^2 v + \frac{\delta_{qk}^{(1)}}{h_y}\left(v\phi_y'' + 2v'\phi_y'\right) + \delta_{qk}^{(0)}v''\right](y_k)\frac{w_1 w}{\phi_x'}(x_p) \\ &+ k^2\frac{w_1 w}{\phi_x'}(x_p)\frac{v}{[\phi_y']^2}(y_k)\delta_{qk}^{(0)}\Bigg\}\end{aligned}$$

We then have the formulation for u_{A5} which is

$$\begin{aligned}\langle \mathcal{L}[u_{A5}], S_p(x)S_q(y)\rangle = \sum_{k=-M_y}^{N_y}\sum_{j=-M_x}^{N_x} u_{jk}\Bigg\{ &\iint \tilde{S}_j(x)\tilde{S}_k''(y)S_p(x)S_q(y)w(x)v(y)\mathrm{d}x\mathrm{d}y \\ &+ \iint \tilde{S}_j''(x)\tilde{S}_k(y)S_p(x)S_q(y)w(x)v(y)\mathrm{d}x\mathrm{d}y \\ &+ k^2\iint \tilde{S}_j(x)\tilde{S}_k(y)S_p(x)S_q(y)w(x)v(y)\mathrm{d}x\mathrm{d}y\Bigg\}\end{aligned}$$

Using Green's second identity on the first and second integrals this time we get

$$\tilde{S}_j(x)\tilde{S}_k''(y)S_p(x)S_q(y)w(x)v(y)\mathrm{d}x\mathrm{d}y \mapsto$$
$$-\iint \tilde{S}_j(x)\tilde{S}_k(y)S_p(x)w(x)\left[S_q(y)v(y)\right]''\mathrm{d}x\mathrm{d}y$$

and

$$\tilde{S}_j''(x)\tilde{S}_k(y)S_p(x)S_q(y)w(x)v(y)\mathrm{d}x\mathrm{d}y \mapsto$$
$$-\iint \tilde{S}_j(x)\tilde{S}_k(y)S_q(y)v(y)\left[S_p(x)w(x)\right]''\mathrm{d}x\mathrm{d}y$$

Hence using the quadrature rule and the usual product rule substitution, we get

$$\begin{aligned}\langle \mathcal{L}[u_{A5}], S_p(x)S_q(y)\rangle \approx h_x h_y \sum_{k=-M_y}^{N_y}\sum_{j=-M_x}^{N_x} u_{jk}\Bigg\{ &\frac{\tilde{v}}{\phi_y'}(y_k)\delta_{qk}^{(0)}\times \\ &\left[-\frac{1}{h_x^2}\delta_{pj}^{(2)}\phi_x'\tilde{w} - \frac{1}{h_x}\delta_{pj}^{(1)}\left(\frac{\phi_x''}{\phi_x'}\tilde{w} + 2\tilde{w}'\right) - \delta_{pj}^{(0)}\frac{\tilde{w}''}{\phi_x'}\right](x_j) \\ + \frac{\tilde{w}}{\phi_x'}(x_j)\delta_{pj}^{(0)}&\left[-\frac{1}{h_y^2}\delta_{qk}^{(2)}\phi_y'\tilde{v} - \frac{1}{h_y}\delta_{qk}^{(1)}\left(\frac{\phi_y''}{\phi_y'}\tilde{v} + 2\tilde{v}'\right) - \delta_{qk}^{(0)}\frac{\tilde{v}''}{\phi_y'}\right](y_k) \\ &-k^2\frac{\tilde{v}\tilde{w}}{\phi_x'\phi_y'}(x_j,y_k)\delta_{pj}^{(0)}\delta_{qk}^{(0)}\Bigg\}\end{aligned}$$

Inclusion of the usual tilde notation (signifying division by the derivative of the map) as well as the replacement of all the $\delta^{(0)}$ with the appropriate value of coefficient u, is performed to show the similarity to the Dirichlet formulation (Eqn. (7.18)). In particular, note the definitions of the derivatives

$$\tilde{v}' = \frac{v'}{\phi'} \neq \left(\frac{v}{\phi'}\right)'$$
$$\tilde{v}'' = \frac{v''}{\phi'} \neq \left(\frac{v}{\phi'}\right)''$$

The fact that the Neumann formulation bears a resemblance to the Dirichlet formulation makes implementation easier as existing Dirichlet code may be used as a basis. Finally, the source function inner product is given by

$$\begin{aligned}\langle f(x,y), S_p(x)S_q(y)\rangle &= \iint f(x,y)S_p(x)S_q(y)w(x)v(y)\mathrm{d}x\mathrm{d}y \\ &\approx h_x h_y \frac{fwv}{\phi_x'\phi_y'}(x_p,y_q)\end{aligned}$$

7.7.2 Modified Solution Method

The aim now is to assemble these individual discretised formulations into matrix systems of the form $\mathbf{A}_1\mathbf{U}\mathbf{B}_1+\ldots+\mathbf{A}_n\mathbf{U}\mathbf{B}_n$. These systems can then be combined to form the generalised Sylvester equation $\mathbf{AUB}+\mathbf{CUD}=\mathbf{F}$ which we have seen before. If the number of basis functions in the unmodified set with which we are orthogonalising is given by $m_x \times m_y$ then we can say $p \in m_x$ and $q \in m_y$. With the original modified and extended basis, we can identify the basis without the additional extending boundary functions by $n_x = m_x - 2$ and $n_y = m_y - 2$. Therefore $j \in n_x$ and $k \in n_y$.
First, we consider the sub-systems assembled from the inner products involving the components u_{A1}, u_{A3}, u_{A7} and u_{A9} which are all of the form

$$\mathbf{AUB}+\mathbf{\Gamma U\Delta}+k^2\mathbf{\Gamma UB}$$

where $\mathbf{U}$ is a $m_x \times m_y$ matrix of coefficients and the remaining matrices are block matrices. The block matrices in this system are defined in Table 7.1.
The sub-systems assembled from the inner products involving u_{A2} and u_{A8} are all of the form

$$\tilde{\mathbf{H}}\mathbf{UB}+\mathbf{\Gamma U\Delta}+k^2\mathbf{\Gamma UB}$$

The block matrices in this system are defined in Table 7.2.
The sub-systems assembled from the inner products involving u_{A4} and u_{A6} are of the form

$$\mathbf{\Delta U\Gamma}+\mathbf{BU}\tilde{\mathbf{H}}+k^2\mathbf{BU\Gamma}$$

with the block matrices defined in Table 7.3.
Finally, the sub-system which forms from the u_{A5} inner product is of the form

$$\tilde{\mathbf{H}}\mathbf{UB}+\mathbf{\Gamma U}\tilde{\mathbf{Z}}+k^2\mathbf{\Gamma UB}$$

where the block matrices are defined in Table 7.4. We may now use Theorem 7.5.1 to find the coefficients contained within the matrix $\mathbf{U}$.

The structure of the final matrix system is similar to that of the Dirichlet formulation. The 'core' of the matrices are identical the matrices describing the Dirichlet

Table 7.1: Block Matrices for Sub-System Type 1

	u_{A1}	u_{A3}	u_{A7}	u_{A9}
$A(m_x \times m_x)$	$\left[\ \alpha \mid \mathbf{0}\ \right]$ $\alpha = w_0'' w/\phi_x'(x_p)$	$\left[\ \mathbf{0} \mid \alpha\ \right]$ $\alpha = w_1'' w/\phi_x'(x_p)$	$\left[\ \alpha \mid \mathbf{0}\ \right]$ $\alpha = w_0'' w/\phi_x'(x_p)$	$\left[\ \mathbf{0} \mid \alpha\ \right]$ $\alpha = w_1'' w/\phi_x'(x_p)$
$B(m_y \times m_y)$	$\left[\frac{\beta}{\mathbf{0}}\right]$ $\beta = w_2 v/\phi_y'(y_q)$	$\left[\frac{\beta}{\mathbf{0}}\right]$ $\beta = w_2 v/\phi_y'(y_q)$	$\left[\frac{\mathbf{0}}{\beta}\right]$ $\beta = w_3 v/\phi_y'(y_q)$	$\left[\frac{\mathbf{0}}{\beta}\right]$ $\beta = w_3 v/\phi_y'(y_q)$
$\Gamma(m_x \times m_x)$	$\left[\ \gamma \mid \mathbf{0}\ \right]$ $\gamma = w_0 w/\phi_x'(x_p)$	$\left[\ \gamma \mid \mathbf{0}\ \right]$ $\gamma = w_1 w/\phi_x'(x_p)$	$\left[\ \mathbf{0} \mid \gamma\ \right]$ $\gamma = w_0 w/\phi_x'(x_p)$	$\left[\ \mathbf{0} \mid \gamma\ \right]$ $\gamma = w_1 w/\phi_x'(x_p)$
$\Delta(m_y \times m_y)$	$\left[\frac{\delta}{\mathbf{0}}\right]$ $\delta = w_2'' v/\phi_y'(y_q)$	$\left[\frac{\mathbf{0}}{\delta}\right]$ $\delta = w_2'' v/\phi_y'(y_q)$	$\left[\frac{\delta}{\mathbf{0}}\right]$ $\delta = w_3'' v/\phi_y'(y_q)$	$\left[\frac{\mathbf{0}}{\delta}\right]$ $\delta = w_3'' v/\phi_y'(y_q)$

Table 7.2: Block Matrices for Sub-System Type 2

	u_{A2}	u_{A8}
$\tilde{H}(m_x \times m_x)$	$\left[\ \mathbf{0}\ \middle\vert\ \tilde{\eta}\ \middle\vert\ \mathbf{0}\ \right]$ $\tilde{\eta} = \mathbf{HA}$	$\left[\ \mathbf{0}\ \middle\vert\ \tilde{\eta}\ \middle\vert\ \mathbf{0}\ \right]$ $\tilde{\eta} = \mathbf{HA}$
$H(m_x \times n_x)$	η $\eta =$ $\left(\frac{\delta_{pj}^{(2)}}{h_x^2}[\phi_x']^2 w + \frac{\delta_{pj}^{(1)}}{h_x}(w\phi_x'' + 2w'\phi_x') + \delta_{pj}^{(0)} w''\right)(x_j)$	η $\eta =$ $\left(\frac{\delta_{pj}^{(2)}}{h_x^2}[\phi_x']^2 w + \frac{\delta_{pj}^{(1)}}{h_x}(w\phi_x'' + 2w'\phi_x') + \delta_{pj}^{(0)} w''\right)(x_j)$
$A(n_x \times n_x)$	$\mathrm{diag}[\alpha]$ $\alpha = -1/[\phi_x']^2(x_j)$	$\mathrm{diag}[\alpha]$ $\alpha = -1/[\phi_x']^2(x_j)$
$B(m_y \times m_y)$	$\left[\frac{\beta}{\mathbf{0}}\right]$ $\beta = w_2 v/\phi_y'(y_q)$	$\left[\frac{\mathbf{0}}{\beta}\right]$ $\beta = w_3 v/\phi_y'(y_q)$
$\Gamma(m_x \times m_x)$	$\left[\ \mathbf{0}\ \middle\vert\ \frac{\mathbf{0}}{\mathrm{diag}[\gamma]}\ \middle\vert\ \mathbf{0}\ \right]$ $\gamma = w/[\phi_x']^2(x_j)$	$\left[\ \mathbf{0}\ \middle\vert\ \frac{\mathbf{0}}{\mathrm{diag}[\gamma]}\ \middle\vert\ \mathbf{0}\ \right]$ $\gamma = w/[\phi_x']^2(x_j)$
$\Delta(m_y \times m_y)$	$\left[\frac{\delta}{\mathbf{0}}\right]$ $\delta = w_2'' v/\phi_y'(y_q)$	$\left[\frac{\mathbf{0}}{\delta}\right]$ $\delta = w_3'' v/\phi_y'(y_q)$

Table 7.3: Block Matrices for Sub-System Type 3

	u_{A4}	u_{A6}
$\tilde{H}(m_y \times m_y)$	$\left[\begin{array}{c} \mathbf{0} \\ \hline \tilde{\eta} \\ \hline \mathbf{0} \end{array}\right]$ $\tilde{\eta} = (\mathbf{HA})^T$	$\left[\begin{array}{c} \mathbf{0} \\ \hline \tilde{\eta} \\ \hline \mathbf{0} \end{array}\right]$ $\tilde{\eta} = (\mathbf{HA})^T$
$H(m_y \times n_y)$	η $\eta = \left(\frac{\delta^{(2)}_{qk}}{h_y^2}[\phi'_y]^2 v + \frac{\delta^{(1)}_{qk}}{h_y}(v\phi''_y + 2v'\phi'_y) + \delta^{(0)}_{qk} v''\right)(y_k)$	η $\eta = \left(\frac{\delta^{(2)}_{qk}}{h_y^2}[\phi'_y]^2 v + \frac{\delta^{(1)}_{qk}}{h_y}(v\phi''_y + 2v'\phi'_y) + \delta^{(0)}_{qk} v''\right)(y_k)$
$A(n_y \times n_y)$	$\mathrm{diag}[\alpha]$ $\alpha = -1/[\phi'_y]^2(y_k)$	$\mathrm{diag}[\alpha]$ $\alpha = -1/[\phi'_y]^2(y_k)$
$B(m_x \times m_x)$	$\left[\begin{array}{c\|c} \beta & \mathbf{0} \end{array}\right]$ $\beta = w_0 w/\phi'_x(x_p)$	$\left[\begin{array}{c\|c} \mathbf{0} & \beta \end{array}\right]$ $\beta = w_1 w/\phi'_x(x_p)$
$\Gamma(m_y \times m_y)$	$\left[\begin{array}{c\|c\|c} \mathbf{0} & \begin{array}{c} \mathbf{0} \\ \hline \mathrm{diag}[\gamma] \\ \hline \mathbf{0} \end{array} & \mathbf{0} \end{array}\right]$ $\gamma = v/[\phi'_y]^2(y_k)$	$\left[\begin{array}{c\|c\|c} \mathbf{0} & \begin{array}{c} \mathbf{0} \\ \hline \mathrm{diag}[\gamma] \\ \hline \mathbf{0} \end{array} & \mathbf{0} \end{array}\right]$ $\gamma = v/[\phi'_y]^2(y_k)$
$\Delta(m_x \times m_x)$	$\left[\begin{array}{c\|c} \delta & \mathbf{0} \end{array}\right]$ $\delta = w''_0 w/\phi'_x(x_p)$	$\left[\begin{array}{c\|c} \mathbf{0} & \delta \end{array}\right]$ $\delta = w''_1 w/\phi'_x(x_p)$

Table 7.4: Block Matrices for Sub-System Type 4

	u_{A5}	
$\tilde{H}(m_x \times m_x)$	$\left[\begin{array}{c\|c\|c} \mathbf{0} & \tilde{\eta} & \mathbf{0} \end{array}\right]$	$\tilde{\eta} = \mathbf{HA}$
$H(m_x \times n_x)$	η $\eta = \left(\frac{\delta_{pj}^{(2)}}{h_x^2}[\phi_x']^2 w + \frac{\delta_{pj}^{(1)}}{h_x}(w\phi_x'' + 2w'\phi_x') + \delta_{pj}^{(0)} w''\right)(x_j)$	
$A(n_x \times n_x)$	$\mathrm{diag}[\alpha]$	$\alpha = -1/[\phi_x']^2(x_j)$
$B(m_y \times m_y)$	$\left[\begin{array}{c\|c\|c} \mathbf{0} & \begin{array}{c}\mathbf{0}\\ \hline \mathrm{diag}[\beta]\\ \hline \mathbf{0}\end{array} & \mathbf{0} \end{array}\right]$ $\beta = v/[\phi_y']^2(y_k)$	
$\Gamma(m_x \times m_x)$	$\left[\begin{array}{c\|c\|c} \mathbf{0} & \begin{array}{c}\mathbf{0}\\ \hline \mathrm{diag}[\gamma]\\ \hline \mathbf{0}\end{array} & \mathbf{0} \end{array}\right]$ $\gamma = w/[\phi_x']^2(x_j)$	
$\tilde{Z}(m_y \times m_y)$	$\left[\begin{array}{c}\mathbf{0}\\ \hline \tilde{\zeta}\\ \hline \mathbf{0}\end{array}\right]$ $\tilde{\zeta} = (\mathbf{Z\Delta})^T$	
$Z(m_y \times n_y)$	ζ $\zeta = \left(\frac{\delta_{qk}^{(2)}}{h_y^2}[\phi_y']^2 v + \frac{\delta_{qk}^{(1)}}{h_y}(v\phi_y'' + 2v'\phi_y') + \delta_{qk}^{(0)} v''\right)(y_k)$	
$\Delta(n_y \times n_y)$	$\mathrm{diag}[\delta]$	$\delta = -1/[\phi_y']^2(y_k)$

formulation but, in the Neumann formulation, are now bordered. These borders reflect the additional set of equations generated by the 2D interpolating boundary functions. The implementation of the Neumann formulation was not pursued as part of this project due to time constraints.

7.8 Summary

We have applied the 2D Sinc-Galerkin method to numerically evaluate the Green's function for the Helmholtz equation in a rectangular patch subject to homogeneous Dirichlet boundary conditions. The results for a range of frequencies and mesh densities have been presented and in terms of relative error and execution time. The results illustrate that increasing the basis size of the Sinc-Galerkin method by a factor of 3 results in a slower convergence than the exponential convergence characteristic of the method applied to other BVPs. However, the number of operations required to solve the Sinc-Galerkin system may be dramatically reduced in the future by applying specialist algorithms as illustrated by Ng [243]. Furthermore, the domain singularity is not completely captured in the immediate vicinity of the point itself. However, a suitable means of domain decomposition could move this singularity onto the boundary and more rapid exponential convergence of the method could be restored. Overall representation of the solution is relatively accurate, robust and quick to evaluate. As the basis size increases, the time taken to execute and storage requirements increase non-linearly however. The general efficiency of the method may be attributed to the lack of a requirement for expensive numerical integration. Furthermore, despite the domain singularity, which reduces the potency of the exponential convergence of the Sinc-Galerkin method, for most combinations of mesh density and frequency tested, the Sinc-Galerkin achieves acceptably low relative errors. Finally, the Sinc-Galerkin is insensitive to a source located near to the boundary which highlights the robustness of the method. The formulation presented may be easily extended to 3D spatial and temporal variations and a formulation for Neumann (or mixed) boundary conditions is presented.

This chapter has explored a third and final method for computing acoustic Green's functions numerically. We have shown that it is capable of complimenting the other

two methods in terms of both applicability, accuracy and speed. In the next chapter we draw the analysis of the previous three together by comparing and contrasting the methods.

Chapter 8

Comparison & Assessment of the Methods

Three methods have been used to compute approximations of the Green's function for the Helmholtz equation in a range of geometries. For the purposes of validation, all these methods have been applied to model problems with available analytical solutions. The characteristics of each method have been discussed in the respective sections of this document. In this chapter, we compare and contrast the methods studied. In addition, we devise guidelines to aid the selection of a suitable method given the characteristics of the problem.
In the following sections we review the methods in terms of

1. Accuracy
2. Execution Time
3. Computational Resources
4. Flexibility
5. Ease of Use/Implementation

In the rest of this chapter, where appropriate, we select suitable model problems to compare methods directly. Specifically, we compare the compact Green's function method applied to the backward-facing step, and the Sinc-Galerkin method applied to a rectangular patch, to the BEM. We compare and contrast the results in terms of

accuracy and execution time. We close with a summary which discusses the results of the previous chapters in a general sense and provide guidelines to the use of the three methods as a portfolio for treating a range of acoustic geometries.

8.1 Compact GF Method vs. BEM

In Chapter 5 we computed the potential flow solution through or around specific geometries. This computation obtained the Kirchhoff vector components necessary to define the compact Green's function approximation for a given acoustic problem. We performed this part of the calculation using a semi-analytical procedure involving the construction of a numerical conformal map to transform the geometry as required. Alternative means of calculating the potential flow solution are numerous although are expected to yield less accurate results and/or take longer to execute. We now demonstrate both the speed and accuracy of the semi-analytical method when compared with a typical BEM formulation using the same computational resources in each case. The BEM is chosen for comparison due to its capability for producing accurate solutions to differential equations as well as its relative ease to implement for low-order elements. Furthermore, it is a common technique used in the solution of potential problems and many open-source codes are available.

Use of the BEM allows application directly to the problem domain without transformation. However, the method relies on the construction and solution of a matrix system for each internal grid point, which is often more time consuming than the grid evaluation in the compact method. Furthermore, the solution is constructed from numerical approximations of boundary values as opposed to the analytical exactness of the compact formulation, hence numerical errors are higher. The potential flow solution (Kirchhoff vector) for the backward-facing step problem of Chapter 5 is computed in MATLAB using the direct collocation BEM with 994 uniformly distributed constant elements. This number of elements is a result of the seeding of 1000 points over the 6 sides of the polygon. The number of elements is selected arbitrarily. The inflow and outflow boundary values used are computed using conformal mapping to ensure exact matching at either end for the purposes of a fair comparison. However, in practice, these values are rarely available. The practitioner could consider 2 options:

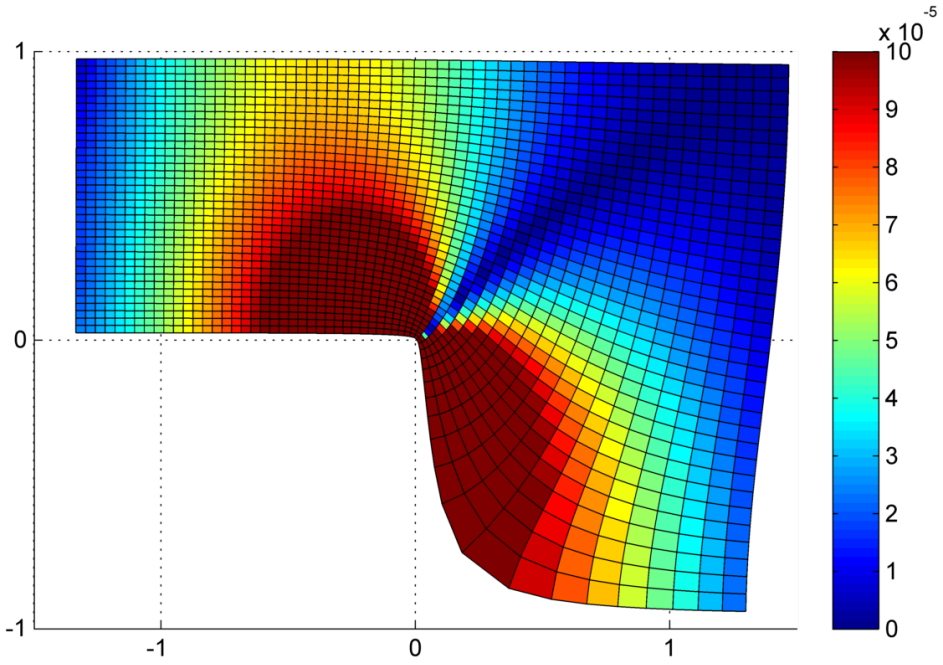

Figure 8.1: Error in the BEM solution for 994 uniformly distributed linear elements

either the upstream and downstream boundaries could be taken far away from the geometrical complexities to ensure the existence of a uniform, unit velocity profile on the boundary; or a transparent boundary condition could be specified on the truncation boundaries. Where the former is possible, the domain may become excessively large and the solution impracticable. Execution of the code took 9.3 seconds using the Intel Core i7 870 CPU – the same CPU used for the conformal mapping computations. The relative error variation over the grid when compared with the exact analytical solution is shown in Fig. 8.1.

From Fig. 8.1 the BEM sees errors near the sharp corner of the order 10^{-3}, orders of magnitude greater than elsewhere on the grid. This is a significant result as any singular behaviour may describe amplifying and scattering effects on sound sources. It is therefore essential that the Green's function be accurately computed in these regions. The inaccuracy in the BEM here is unsurprising since we know from potential flow theory that the solution around a 90 degree corner may be represented algebraically by a power law expression whose derivative tends to infinity at the apex. This singularity results in large gradients in the vicinity which results in a high sensitivity to error in discrete numerical solutions. We improved the performance of the BEM code by using a quartic polynomial to redistribute the boundary nodes and increase the concentration of elements near to the corner apex. Simulations using the modified

code of around 3000 elements took approximately 80s to execute and were capable of achieving a general accuracy over the grid of the order 10^{-7} which is still orders of magnitude away from the solution of order 10^{-9} obtained using the compact method which uses conformal mapping. More demanding simulations were not possible within the limitations of our available computing resources.

This latter experiment demonstrates another drawback of applying the BEM instead of the compact method to construct the Kirchhoff vector components; the design of the mesh is reliant on prior knowledge of singularities or regions of steep gradients within the potential flow solution. Although for the trivial case above, this information can be determined by inspection, for some geometries, the potential flow solution is likely to be more complicated. If this information is not known, the discretisation of the boundary cannot be performed in the most effective manner. In addition, the preparation of the mesh and the complexity of the code will almost certainly increase for more complex geometries due to possible iterative grid refinement and potential use of higher-order elements. Such factors will only increase the already comparatively long time spent in running a BEM simulation for these problems on desktop computers. Further optimisation of the BEM code (including parallelisation) may improve the accuracy and execution time of the BEM as discussed in Chapter 6.

The compact Green's function method far exceeds expectations for the backward-facing step problem with an accuracy of the order 10^{-9} and execution time of just 1.3s compared with an accuracy of 10^{-7} in around 80s for the Boundary Element Method. The same computational resources are used in both cases. Furthermore, BEM encounters difficulties in handling boundary singularities in the potential flow solution which limits its ability to compete with the semi-analytical method, particularly when these singular regions of the flow are not known *a priori* and hence cannot influence the meshing process.

8.2 Sinc-Galerkin vs. BEM

The second comparison repeats the solution of the Dirichlet square BVP used in Chapter 7. We compare the Sinc-Galerkin results to those computed using the direct-collocation BEM implementation, developed in Chapter 6, over a range of mesh densities. As performed in Chapter 7, we vary the mesh density from a lower to upper limit where the ratio between the largest and smallest mesh density is 3, this time for both methods. We configure a typical direct BEM implementation to use a range of 4 to 12 constant elements per unit length to solve the same problem and compare the results. We record the time taken to execute the code in both cases. All computations are performed on an Intel Core i7 870 CPU. The source configuration used in the Sinc-Galerkin method is that described by Eqn. (7.21) and the analytical solution is Eqn. (7.22) and evaluated for 50 terms.

8.2.1 Centred Source

The Sinc-Galerkin results for an expansion of $2M + 1 = 65$ and the BEM for 44 elements (12 elements per unit length) are both compared to the analytical solution at the tested frequencies in Fig. 8.2. The same colour scale is used at each frequency as before. Both numerical methods give the expected variations and accurately satisfy the boundary conditions: the BEM allows the boundary conditions to be specified precisely as an input to the method and the nature of the Sinc function itself means it decays to zero at the edge of the domain.

Although the BEM results indicate that the BEM captures the singularity more precisely than the Sinc-Galerkin method, there is evidence of a loss of definition in Fig. 8.2b at the peaks and troughs at the higher frequencies tested. Therefore, qualitatively, the Sinc-Galerkin captures the *general* behaviour of the solution with a higher degree of fidelity than the BEM, the latter demonstrating a notable resolution-driven sensitivity to frequency.

Comparing the relative error and the execution time in all cases (Fig. 8.3a (log scale) and Fig. 8.3b), the BEM sees a reduction in error with mesh density more steeply than the Sinc-Galerkin method with a 3 fold increase in the mesh density. The error is reduced to below 1% for the lowest two frequencies. When using BEM the

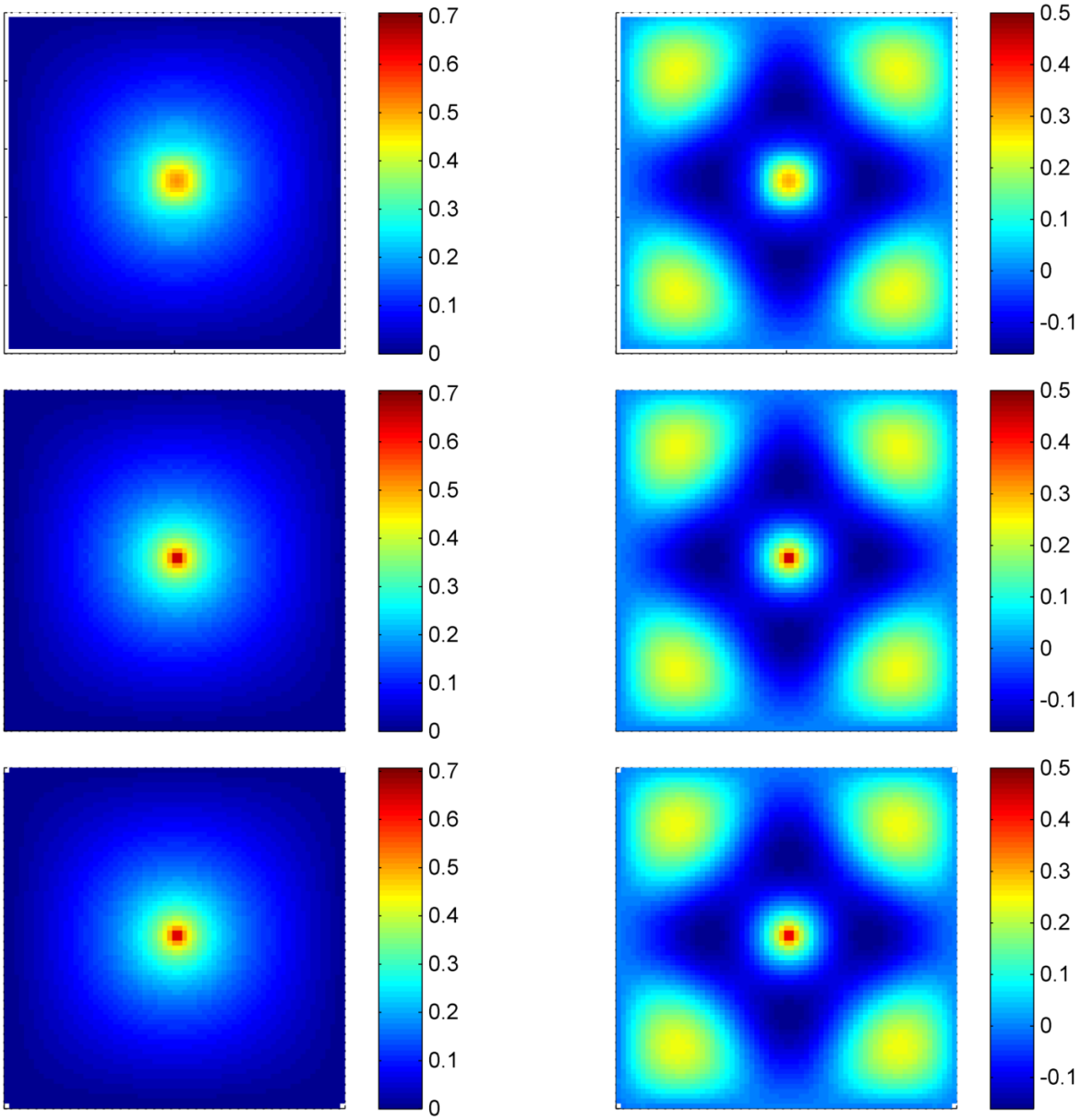

(a) f=20 (left column) and f=680 (right column)

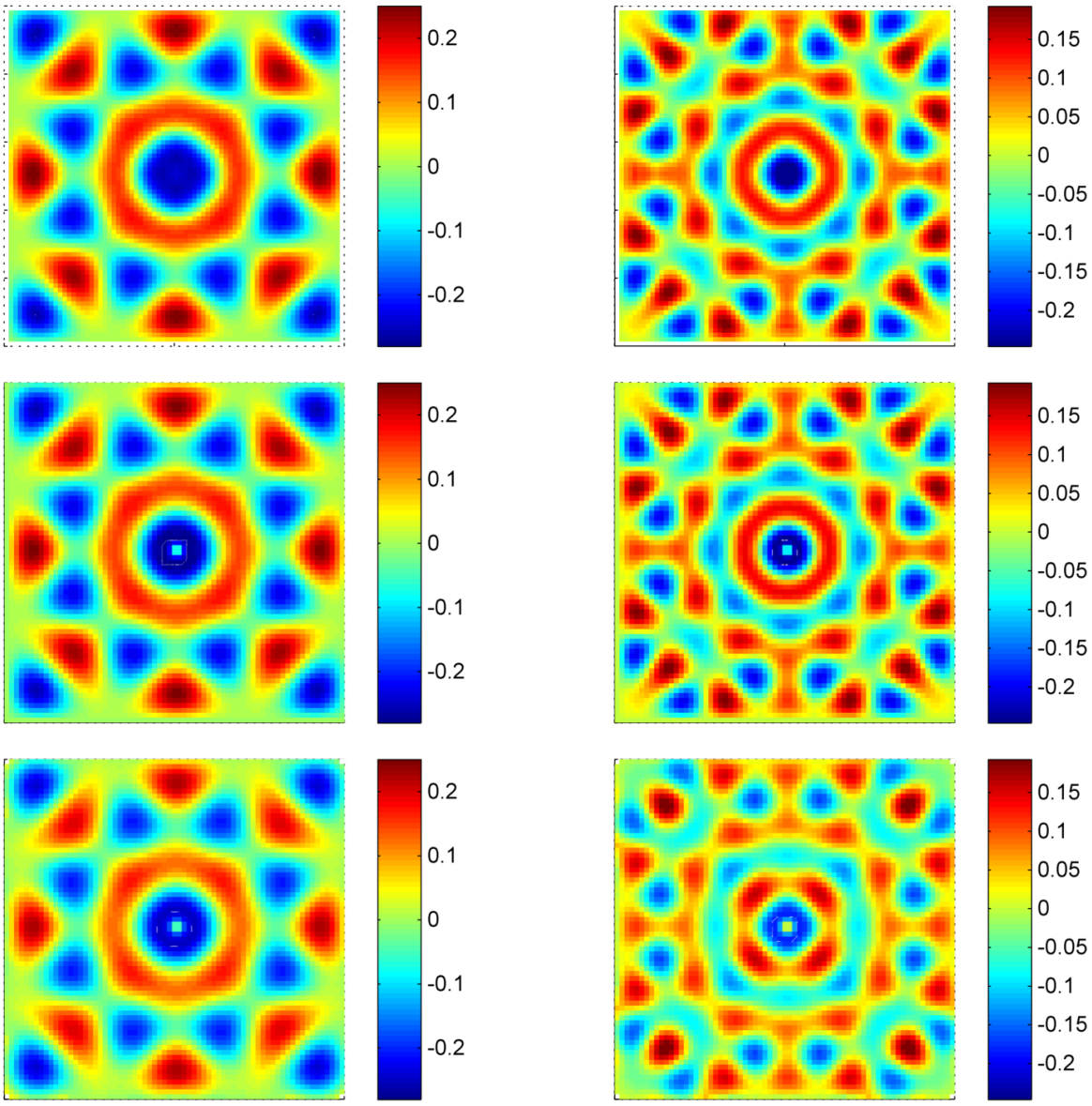

(b) f=1340 (left column) and f=2000 (right column)

Figure 8.2: Results for for the BEM n=12 (bottom row), analytical expression Eqn. (7.22) (middle row) and Sinc-Galerkin M=32 (top row) for a source centred in the unit square

largest errors are typically found near the boundary. Although a large relative error at these points is expected, as the analytical solution tends to zero in these regions, the absolute error is also larger than the Sinc-Galerkin method in these regions. Due to the nature of internal point evaluation for the BEM, singular collocation points on the boundary are close by and sensitive to numerical inaccuracies. From Fig. 8.3a, the convergence rates for both the BEM and the Sinc-Galerkin are different, with the BEM converging quicker with a trebling of the mesh density compared with the Sinc-Galerkin. As in Chapter 7, we have included the limit of exponential convergence, based on the error at the lowest mesh density, computed using Eqn. (7.23).

At the highest frequency, the relative error in the Sinc-Galerkin initially diverges with mesh density as the basis fails to support the waves. It does, however, converge again but with a relative error an order of magnitude larger than the BEM. The near 100% relative error here is driven by near zero analytical solution behaviour as explained in Chapter 7. When the *absolute* errors are used as a means of comparison (Fig. 8.4), we see that the unusual trend in the relative error is not mirrored. In Fig. 8.4, the absolute errors are lower for the lowest frequency for the BEM but relative errors are comparable at the same frequency. The errors in the singularity region where the Sinc-Galerkin fails are responsible for damaging the overall performance of the Sinc-Galerkin in this case. Also clear from Fig. 8.4 is the sensitivity of the accuracy of the BEM to frequency with the highest two frequencies producing large absolute errors compared with the Sinc-Galerkin. Given that the relative error is unreliable as a measure when the solution nears zero, the absolute error may be more useful and indicates here that the Sinc-Galerkin method is excellent at accurately representing a wider range of frequencies for a given mesh density. This adds support to a similar conclusion drawn in Chapter 7.

Despite the apparent drawbacks of the Sinc-Galerkin method when compared with the BEM, it still out performs the BEM in most of the combinations tested while still taking less time to execute (Fig. 8.3b). Specifically, at lower mesh resolutions, it can be up to 2.5 times longer to use the BEM over the Sinc-Galerkin. This is due to the simplicity of the sinc quadrature rule which avoids expensive numerical integration. As the mesh density increases, however, the time taken scales non-linearly for the Sinc-Galerkin and roughly linearly for the BEM although with an increased

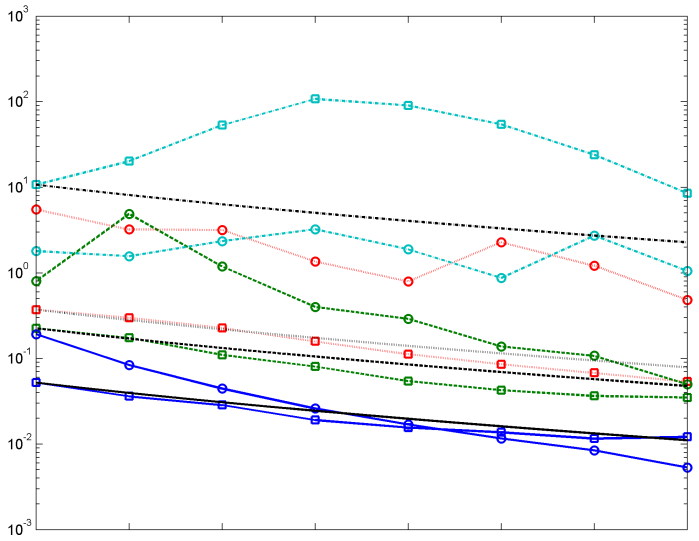

(a) f=20 (solid blue), f=680 (dashed green), f=1340 (dotted red), f=2000 (dot-dash cyan)

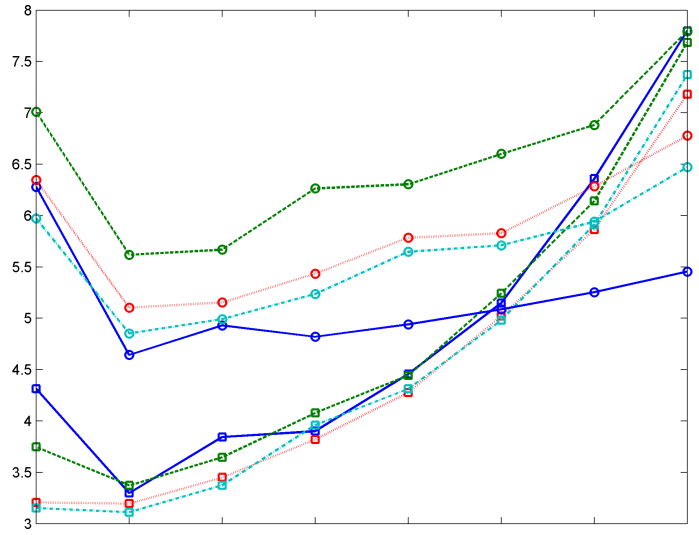

(b) f=20 (solid blue), f=680 (dashed green), f=1340 (dotted red), f=2000 (dot-dash cyan)

Figure 8.3: Relative error (top) and execution time in seconds (bottom) for Sinc-Galerkin (squares) and BEM (circles) for the range of mesh densities tested (horizontal axis) for a centred source. The corresponding black lines represent the limit of exponential convergence as computed using Eqn. (7.23).

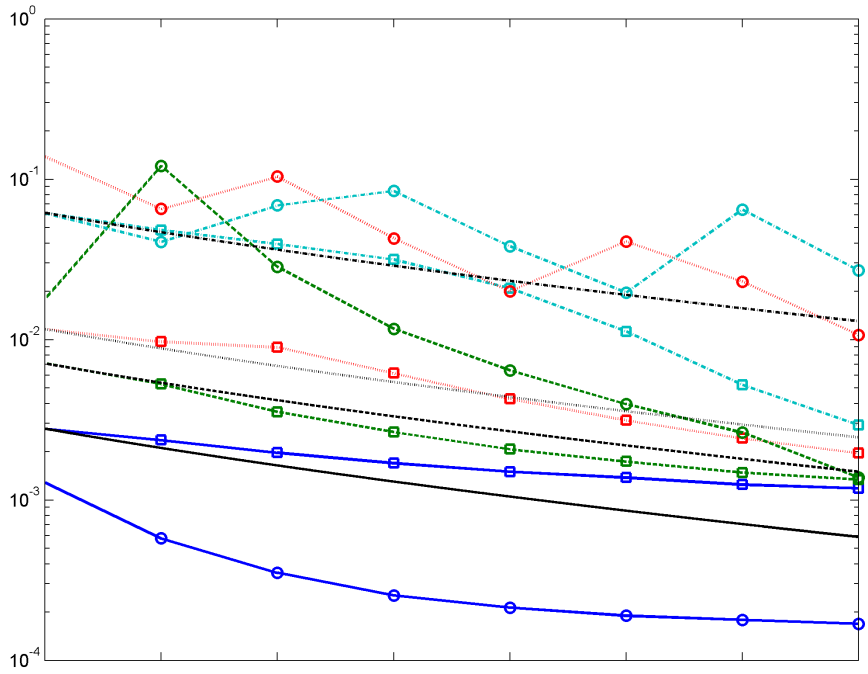

Figure 8.4: Absolute Error for a centre source for Sinc-Galerkin (squares) and BEM (circles) for f=20 (solid blue), f=680 (dashed green), f=1340 (dotted red), f=2000 (dot-dash cyan). The corresponding black lines represent the limit of exponential convergence as computed using Eqn. (7.23). The horizontal axis ticks represent an increase in the mesh density comparable in both methods.

frequency dependence. For very large Sinc-Galerkin systems, not only does the time taken to compute the Kronecker products increase but the storage also increases in an approximately quadratic sense as the dimensions of the Kronecker matrix is $(m_x m_y \times m_x m_y)$. In such cases, the alternative solution procedure discussed in Section 7.5 may be more efficient.

8.2.2 Near-Boundary Source

For completeness we also compare the near-boundary source case studies in Chapter 7. By moving the source to the boundary, a deterioration in the BEM's ability to accurately evaluate the solution without special treatment [218] is expected as the internal points approach the singular collocation nodes on the boundary elements. However, as the following results indicate, the deterioration was not as severe as predicted. We use the same setup as Chapter 7 with the source located with x-coordinate corresponding to $x/W = 0.1$ where $W = 1$ is the domain width. We plot the surfaces for a Sinc-Galerkin expansion of $2M + 1 = 65$, the BEM for 44 elements, and compare to the analytical solution evaluated using 50 terms of the expansion Eqn. (7.22). We also plot the relative error and the execution time in all cases (Fig. 8.6a and Fig. 8.6b).

Qualitatively, the BEM again captures the singularity well but struggles at the higher frequencies Fig. 8.5b. The solution is over-predicted at peaks and troughs. This is more noticeable with the near-boundary source than with the centred source, although this may be due to the overall solution being an order of magnitude greater in these regions as indicated by the colour scale. Interestingly, at a frequency of $f = 1340$ Hz (Fig. 8.5b), we see that the phase of the BEM result is incorrect by 180 degrees. Further testing over frequencies $1320 \leq f \leq 1350$ Hz show particularly poor performance by the BEM. Quantitatively, the results are highly inaccurate throughout the domain. However, it is only at $f = 1340$ Hz that we get such a noticeable qualitative error (the phase shift). At this frequency we see that the condition number of the coefficient matrix in the BEM linear system is at a local maximum suggesting that the solution of the system will be highly sensitive to small errors. If we further increase the resolution, this phase shift effect disappears, the condition number moves away from the maximum, and the solution given by the BEM becomes much more accurate.

When comparing Fig. 8.3a and Fig. 8.6a, the error now increases with frequency

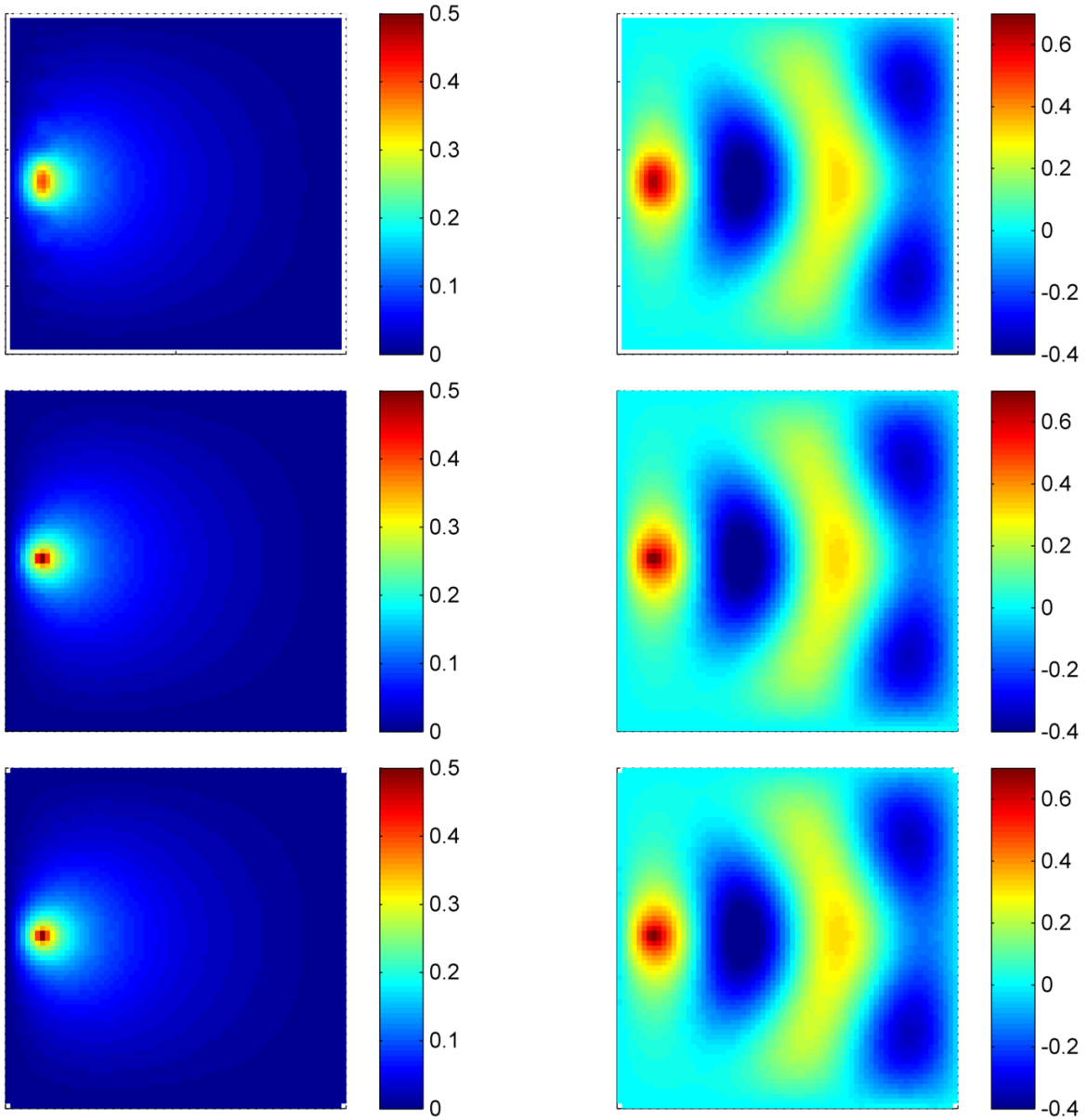

(a) f=20 (left column) and f=680 (right column)

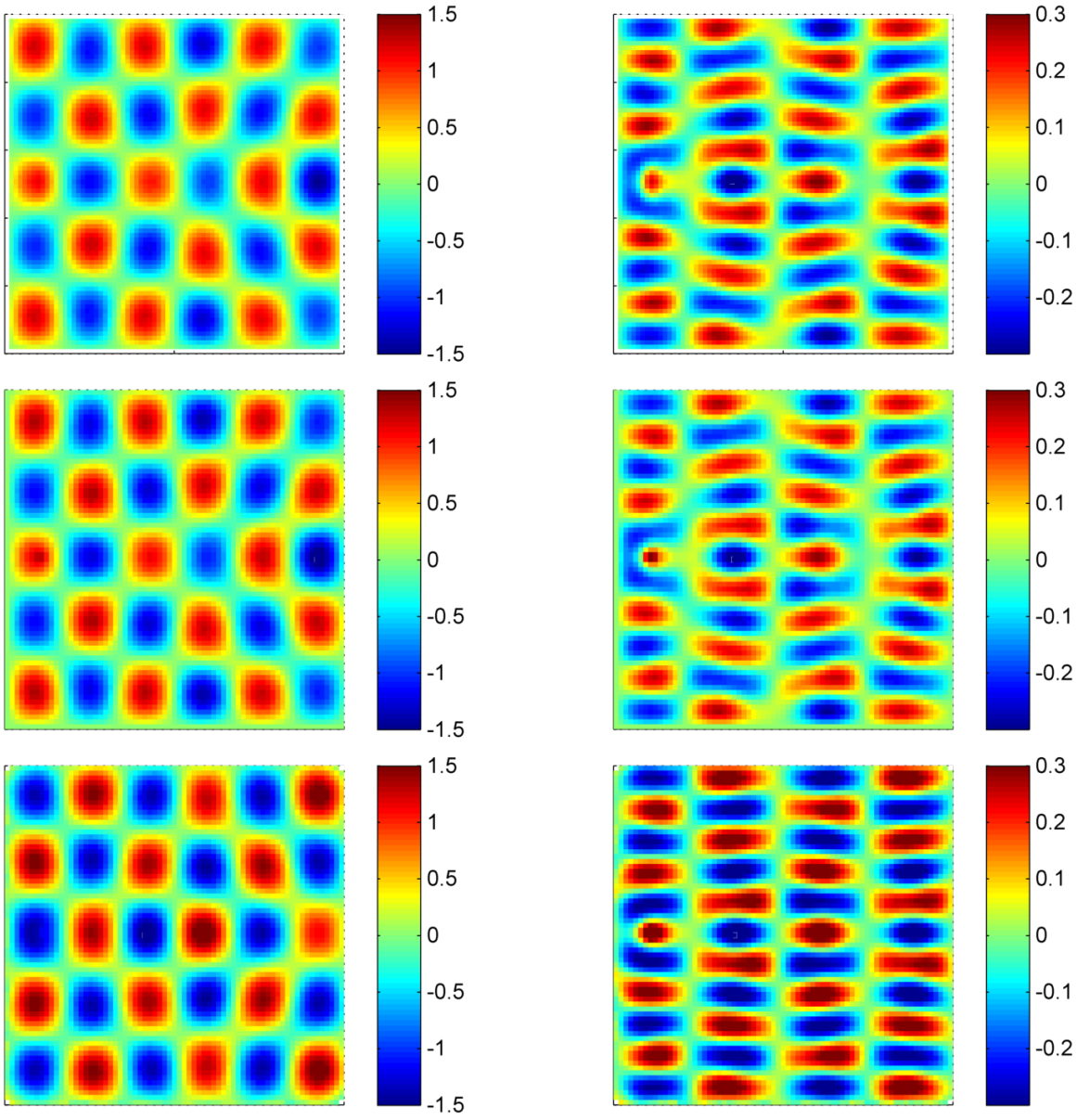

(b) f=1340 (left column) and f=2000 (right column)

Figure 8.5: Results for for the BEM n=12 (bottom row), analytical expression Eqn. (7.22) (middle row) and Sinc-Galerkin M=32 (top row) for a source near the boundary of the unit square

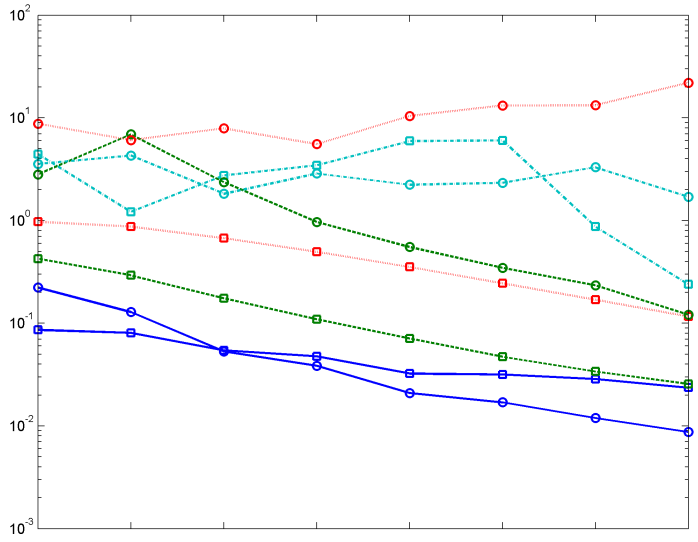

(a) f=20 (solid blue), f=680 (dashed green), f=1340 (dotted red), f=2000 (dot-dash cyan)

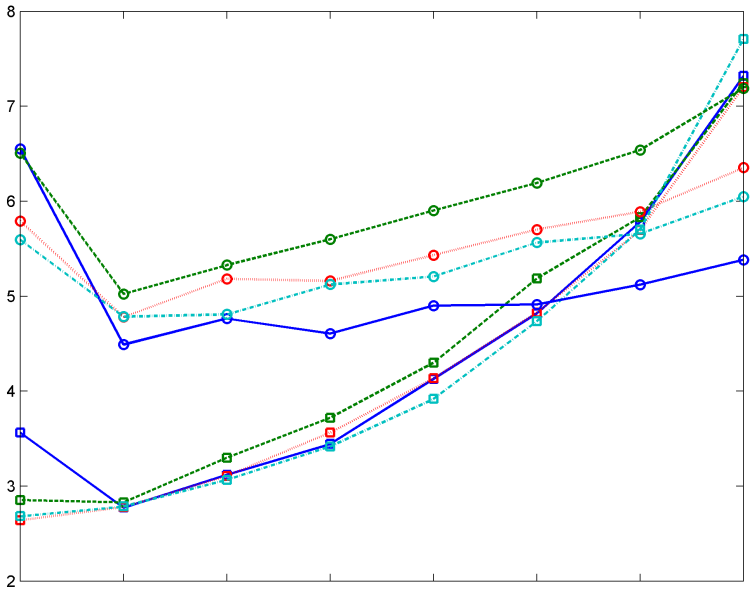

(b) f=20 (solid blue), f=680 (dashed green), f=1340 (dotted red), f=2000 (dot-dash cyan)

Figure 8.6: Relative error (top) and execution time in seconds (bottom) for Sinc-Galerkin (squares) and BEM (circles) for the range of mesh densities tested (horizontal axis) for a near-boundary source.

across the whole range tested unlike for the centred source. There is a slight increase in overall error in both methods but, as expected, the BEM suffers more significantly with the error at the highest two frequencies, struggling to converge with mesh density. In contrast, the Sinc-Galerkin converges better than $e^{-\sqrt{N}}$ regardless of frequency. It is less predictable at high frequencies, which is expected as more terms overall will be required for the expansion to represent the rapid changes in the solution. Even so, the robustness of the Sinc-Galerkin method means that a lack of mesh density manifests itself in a milder way compared with the BEM.

Figure 8.6b shows little sensitivity to source location when compared with Fig. 8.3b for both methods. This indicates that neither of the two source locations selected here are sufficiently close to the boundary as to cause any serious computational difficulties with either method. However, moving the source closer to the boundary does have a more pronounced effect on the BEM as expected which serves to highlight the robustness of the Sinc-Galerkin procedure.

8.3 Comparison Summary

Throughout this research, we have assessed three different methods and in this chapter have initiated appropriate comparisons to assess relative performance in terms of accuracy and execution time. Rather than leaving this information scattered throughout this document, we recap, for clarity, the main discussion points across all the methods under the headings laid out at the beginning of the chapter.

8.3.1 Accuracy

The degree of accuracy of the methods which we can reasonably expect to achieve using current computing resources is a particularly important property. Specifically, it is important to understand the features of the methods which limit the accuracy. In the previous three chapters, we have discussed the sources of error of the methods in detail. Here we bring this information together.

The accuracy achieved using the method based on the compact Green's function depends on how we define the terms in the first place. If 'accuracy' refers to how close

the numerical result matches the exact Green's function for the problem then the inaccuracies relate to the suitability of the conditions listed in Section 5.1 applied to a particular problem. Specifically, for the first order correction we compute to be viewed as appropriate, a decision needs to be made on whether the scatterer may be considered acoustically compact and whether the placement of the source and observer are as required. Quantitatively the implications may be understood by considering the higher-order terms in Eqn. (5.1). If, however, 'accuracy' refers to the ability of the numerical procedure to compute the first order correction (the Kirchhoff vector) precisely, attention shifts to the configuration of the conformal mapping involved. For this part of the procedure, we illustrated in Chapter 5 that the sources of error include the choice of computational domain and the degree of discretisation (referred to as polygon vertex density). Depending on the combination of the class of geometry and selected computational domain, the relative error in computing the potential flow (Kirchhoff vector components) for the test problems ranges from values of the order 10^{-4} to 10^{-9}.

The BEM, although to a certain extent, can be considered physics-based, does not share the advantages of the semi-analytical method based on the compact Green's function. In Chapter 6 we applied the method to both a finite and a semi-infinite geometry, the latter using a new formulation which allows any number of transparent boundaries. For the finite domain, the errors associated with the method are typical of the BEM. These errors included the error in application of quadrature to compute the influence coefficients; the error associated with the evaluation of internal points near the boundary; and the error associated with the level of discretisation. Of these, the last was seen to be the most influential, illustrated by the plane wave problem of Section 6.7 (Fig. 6.3a). This figure also illustrates a notable degree of dependency on the frequency of the waves being represented. Results achieved relative errors of the order 10^{-3} to 10^{-5}. However, as illustrated by Fig. 6.5, the extrapolated frequency-dependency indicates that a maintenance of this range, even for an absolute error, is likely to make the calculation prohibitively expense as the frequency exceeds those studied in Section 6.7, and accuracy is likely to be lower in practice, as indicated by the results of Section 8.2.

The inclusion of the DtN boundary condition introduced new source of error into the

BEM. The truncation of the non-local DtN series is of particular significance. Our results have corroborated the conclusions of Harari *et al.* [146], demonstrating that the inclusion of all propagating modes in the boundary conditions is a minimum requirement for the prevention of spurious reflections introduced by an inaccurate boundary condition. We further clarify that this is only true if all evanescent modes have decayed to a level by the boundary such that reflections would not contaminate the domain solution. Relative errors are of the order 10^{-3} for the semi-infinite problems studied over a wide range of frequencies.

There is plenty of evidence in the literature (see the citations of Section 7.1.0.1) of the Sinc-Galerkin procedure achieving absolute errors as low as $\mathcal{O}(10^{-9})$ or smaller. However, this considers the method applied to a limited class of problems – standard and singular differential equations which at worst feature regular singular points or boundary singularities. We have explored the application of the Sinc-Galerkin method to problems featuring domain singularities, which physically indicate regions of amplification due to scattering or otherwise. Such singularities are characteristic of Green's functions. Our studies have shown that the convergence of the method with mesh density is degraded but is still capable of achieving relative errors of the order 10^{-2} to 10^{-1} depending on the computational resources available. The detail of the singularity is poorly captured although qualitative results agree very well for the model problems tested. This error range is somewhat misleading as in Chapter 7, we see that the error is actually due to a combination of localised error at the 'tip' of the singularity and small errors in regions where the solution is close to zero. For this reason, the qualitative results still agree very well, better in fact than the BEM for the problem studied in Section 8.2, despite the relative errors appearing as high.

8.3.2 Execution Time

As a pre-processing step for existing hybrid noise predictions, it is important that the time taken to compute the Green's function, using one or a combination of the three methods developed here, not be unreasonably large. It has, therefore, been one of the foci of this work to assess the execution time of the Green's function computation. When linking the computation with an existing hybrid scheme, the combined time of

Green's function, flow field and sound field calculation must be considered and managed to ensure the efficiency gained from using a hybrid scheme over a exclusively numerical scheme is maximised.

In Chapter 5, the computation time for the compact method is seen to comprise mainly the time taken to compute the conformal and the time taken to map the grid points for evaluation. The significance of the latter depends on the problem and desired output and is seen in Fig. 5.13 to scale linearly with the grid density: for example, if a compactly distributed source is to be evaluated at just a single field point, this activity will take little time. However, if the value of the Green's function is desired over a large number of observer points, this step could dominate the time taken to execute. This is also pertinent to the BEM as discussed below.

In contrast, the time taken to construct the conformal map scales non-linearly with vertex density and can cause conditioning issues which slow the calculation further. Although this can have a pronounced impact on the overall execution time of the method, it is only an issue associated with very specific geometries. Geometries capable of being represented accurately by a minimum number of straight line segments will not encounter this issue. In fact, the backward-facing step problem treated in Section 8.1 maps the geometry in a fraction of a second. However, when the geometry is curved, we show in Section 5.4.2 that a large number of segments are need to represent the geometry and hence the computation time is significantly lengthened. However, this can be addressed by including the ability to map arcs using the theory of Bjorstad & Grosse [34].

In Section 8.1 and Section 8.2 we see that to achieve results of comparable accuracy, the BEM takes longer to execute than both the other two methods. Attached to this evidence is the caveat that we are comparing unoptimised benchmarks in both cases. The source of the time take to execute the BEM is attributed to the expensive evaluation of the influence coefficients, first to solve for unknowns on the boundary and for every internal point at which the solution is required. This is influenced by the number of quadrature points used (although this is largely insignificant) and the mesh density (the number of influence coefficients to be computed). However, as mentioned above, the size of the grid of internal points for evaluation is controlled by the user and there may be situations where a small grid of points will suffice. In such cases, the BEM

would become much quicker to execute, possibly of similar order of magnitude as the other two methods. For the problems studied earlier in this chapter, the grid of points is relatively dense and hence execution times can increase by an order of magnitude or more compared with the compact method and by a factor of 1.5 compared with the Sinc-Galerkin.

The execution time is seen in Fig. 6.7 to decreased with frequency due to the multi-threading of certain functions involved in the calculation of the influence coefficients. This only offsets the additional cost associated with increasing the mesh density and is more pronounced at higher frequencies. Fortunately, the inclusion of the DtN boundary condition adds little computational cost, as it avoids numerical integration, and in most practical cases, a relatively few number of terms in the DtN expansion are required for an accurate representation of boundary behaviour. Even so, for the largest number of terms tested in Chapter 6, the variation in execution time was negligible (Fig. 6.9).

In Chapter 7 we presented the execution time of a MATLAB implementation of the Sinc-Galerkin method as run on the Intel Core i7 870 CPU. Reproduction of investigations in the literature have shown the method to be extremely rapid, although details of the execution time of the original investigations are unavailable for comparison. The efficiency of the Sinc-Galerkin is due to a combination of the matrix system being kept small by a minimal set of basis functions, and the preclusion of numerical integration allowing for simple matrix system construction. Furthermore, where the equation being solved is linear, application of the Sinc-Galerkin method produces a linear system of equations. The results of Chapter 7 indicate that where the solution contains singular points within the domain, this exponential convergence rate is degraded and hence a larger basis set is required to maintain acceptable levels of accuracy. Furthermore, the execution time scales non-linearly with mesh density in the non-vectorised implementation used in this project.

As with the BEM, the evaluation of the solution over a grid of internal points can be a significant activity for the Sinc-Galerkin method as the solution is constructed by essentially superimposing the allowable 2D mode shapes multiplied by the computed coefficients. This procedure is accelerated by vectorising the code such that the evaluation is performed over all grid points simultaneously. This is not possible

for the BEM as the influence coefficient are computed anew for each internal point. Parallelisation of the process in the Sinc-Galerkin method is possible and is expected to produce notable speed up of this step.

8.3.3 Computational Resources

We next give a brief description of the computational resource demands of the methods. Where possible, we estimate the scaling of memory requirements based on the size of the systems assembled by each.

The compact method, like all the methods, requires storage of grid coordinates and nodal data. The size of the grid scales with the density of the grid points. Little additional storage is required other than the complex coordinates of the polygon and data associated with the mapping. Memory overruns were not observed while using this method, even when increasing the polygon vertex density beyond the limits of numerical stability of the mapping solution method.

The BEM stores the influence coefficients in two matrices which scale with the boundary mesh density. These variables dominate the storage requirements for the method and are additional to the variables holding the grid coordinates and nodal data. The size of these matrices equates to the size of the linear matrix system to be solved. While using the method throughout this research project, memory overruns were witnessed on desktop machines equipped with 8 GB of RAM. These occurrences were limited to situations in Chapter 6 where a maximum accuracy was being sought. Specifically, in order to achieve absolute errors as low as the threshold of hearing ($\mathcal{O}\left(10^{-5}\right)$), according to Fig. 6.5, we require 400 elements (nodes) per wavelength. This would require double-precision storage of values using memory in excess of 100 GB, not something widely available just yet. It is worth noting that the addition of the DtN boundary condition only added storage requirements characterised by a single double-precision (64-bit) vector of values with length equal to the number of terms in the expansion. As in most cases the number of terms may be kept to a value < 1000, the additional memory required would be < 16 kB.

The Sinc-Galerkin method, similar to the BEM, stores matrices of coefficient in addition to the grid data. Although the exponential convergence of the method can serve

to reduce system sizes, the tensor products expanding the system size significantly during solution and the process of building the solution once the problem has been solved can be expensive in terms of time (as discussed above) as well as memory. Vectorised code can be used to reduce the time taken to construct the solution but increases the storage requirements prohibitively. The reason for memory overruns in the vectorised case are due to the need to replicate a copy of the grid coordinates to a 3D array of depth $(2M+1)^2$. Each layer of the 3D array is evaluated for each combination of basis functions (of which there are also $(2M+1)^2$). The memory required to store this double-precision 3D array for $M = 80$ [143] is in excess of 2.6 GB. Add to this the storage requirements of the other parts of the procedure and the memory of a typical desktop is soon used up. There are questions as to the suitability of implementation used. However, this implementation is highly amenable to parallelisation which could introduce significant speed-up.

To summarise, the compact method may be viewed as significantly cheaper than the other two. The sensitivity to frequency of the BEM means that for high frequency problems, a dense mesh is required and hence storage requirements become large. However, the scaling is linear unlike the Sinc-Galerkin method. Due to the domain singularity, the Sinc-Galerkin must use a high number of basis functions to achieve the required accuracy which results in large memory usage. However, effective parallelisation could drastically reduce the resource demand.

8.3.4 Flexibility

The aim of this research is to examine the potential of three methods to compute the Green's function in arbitrary geometries. As geometrical configurations of acoustic problems can vary significantly, it is important that the means of computing the Green's function we suggest is capable of treating a wide range of geometries. We summarise now the flexibility of the methods to different configurations.

For the method based on the compact Green's function, the choice of computational domain is not automatic with different possibilities available for different classes of geometry. Our studies have shown that an infinite channel is more suitable than a semi-infinite half-plane as a continuity principle may be used to scale the transformed potential flow – demonstrated in Chapter 5 to be crucial to accuracy. However, not all

classes can be mapped to this geometry in a meaningful way and hence some judgement is required: for example, it was necessary in Section 5.4.2.1 to include a non-physical wall to allow the infinite strip domain to be used. Furthermore, the suitability of a particular compact approximation depends on the geometry and the availability of an analytical representation of a suitable starting form for correction. Although many model problems have available closed form Green's functions, there will be some for which the correction required is likely 'too large'. In other words, the realistic geometry is radically different from the closest geometry for which an analytical representation is available. In such cases, the compact Green's function is expected to be unsuitable. One useful advantage of the compact method is to be able to either specify the grid to represent sources or observers. This flexibility allows the practitioner to investigate the variation in source position on the radiated sound at an observer location in a single calculation. The compact method, in its present form, supports only rigid wall boundary conditions although modified formulations may be possible. Finally, the theory of Bjorstad & Grosse [34] may be used to treat curved geometries in a more robust manner and the inclusion of this theory in the existing conformal mapping code could be the subject of future work (see Section 9.1).

The BEM is the most versatile method in terms of both geometries and boundary conditions. The exceptions are mentioned in Section 6.1.2. However, this flexibility comes at a price, specifically in terms of execution time as discussed earlier. A decision must also be made on the design of the mesh, which can be difficult *a priori*. As we have shown in Section 8.1, a poor mesh design negatively impacts the accuracy of the solution. The disadvantage of this is that solution behaviour must be known (or at least estimated) *a priori*. Alternatively, a preliminary calculation may be necessary to identify areas of the mesh requiring local refinement. This preliminary calculation may be performed using one of the other two methods if appropriate. Where neither of these are possible, the mesh is constructed blind and can lead to poor results or the need for numerous recalculations.

The Sinc-Galerkin is inherently limited to rectangular geometries but can take into account semi-infinite and infinite boundaries with conformal transforms rather than the use of expensive and potentially inaccurate artificial boundary conditions. This, coupled with the rapid assembly and solution of the matrix system makes it an ideal

choice for such problems. Although not undertaken here as the task would form an individual research project in its own right, it may also form part of a domain decomposition algorithm to represent more complex geometries. We present in Section 7.7 a formulation which extends the method tested here to account for rigid wall boundary conditions. Consequently, mixed boundary conditions may also be treated. The ability for the Sinc-Galerkin to capture singularities in the domain is limited as the investigations of Chapter 7 show, but we also proposed a suitable used of domain decomposition which may counteract its influence involving the removal of the singularity to the boundary.

8.3.5 Ease of Use/Implementation

All methods require little user interaction. In the main, once key geometrical parameters are specified, the code is capable of generating meshes, seeding nodes or vertices and returning the solution data automatically. However, for the compact method, the choice of computational domain and analytical form for correction must be made in advance and the computational potential function specified. This may be challenging depending on the geometry and there may be a number of possibilities available.

The design of the BEM mesh needs to be a careful process and so the practitioner may decide to pass the process to specialised software or design the mesh manually. This latter approach would slow down the use of the method significantly. Furthermore, input files need to be specified for this method containing the coordinates of the boundary sections and the corresponding boundary conditions. These files will depend on the mesh design.

The mappings for the Sinc-Galerkin must be specified based on the patch geometry, although this function could be carried out automatically due to the limited choice available. When not part of a patching procedure, this method is the most automated of them all. The discretised equations generated by the Sinc-Galerkin procedure can be quite complicated, particularly for Neumann or mixed boundary conditions, where basis extension is required. Care must be taken during implementation to avoid mistakes which can be hard to find.

All of the methods are capable of producing the same output – the value of the Green's function for the problem over a grid of observer locations for a given source position.

It is expected that these values will be used directly in the Green's function method to compute the sound field due to an arbitrary source. If the techniques presented here are used for a range of source positions then the results may be used as part of a quadrature procedure over the source grid to compute the convolution Eqn. (4.2). In this case, the alignment between the source grid used for the Green's function calculation and the grid used for the hydrodynamic source calculation must be of paramount importance and should be investigated as part of future work.

8.4 Guidelines & Conclusions

Drawing the analysis of this chapter together, it is possible to formulate the following guidelines for method selection which we present here in graphical form (Fig. 8.7). These guidelines are formulated from the known assumptions and limitations of each of the methods discussed in Chapters 5 to 7. The intention of these guidelines is to provide practical assistance in the selection of one method over another for as broad a range of geometries as possible.

These guidelines do not incorporate all possible decisions which influence the suitability of one method over another but include the most influential. Furthermore, there may be exceptional circumstances where following the guidelines is not appropriate. However, this flowchart is something which can be implemented as software to automate the selection of a method for the practitioner as we discuss in Section 9.1.
It should be clear from Fig. 8.7 that there is no single method capable or suitable to treat every class of geometry. Through this flowchart we recommend treating the methods discussed here as a portfolio capable of accurately and efficiently computing the Green's function for the Helmholtz equation in many different geometries. Crucially, this flowchart illustrates the basic implementation of the portfolio and allows the Green's function to be computing numerically for a wide range of geometries for which analytical solutions would be difficult or impossible to construct.
The conditions for which the compact Green's function forms a good approximation to the exact Green's function for given problem are integrated into the left-hand side of the flow chart and must all be satisfied in order for the compact option to be selected. As discussed in Chapter 5, there is a large class of acoustic problems which meet

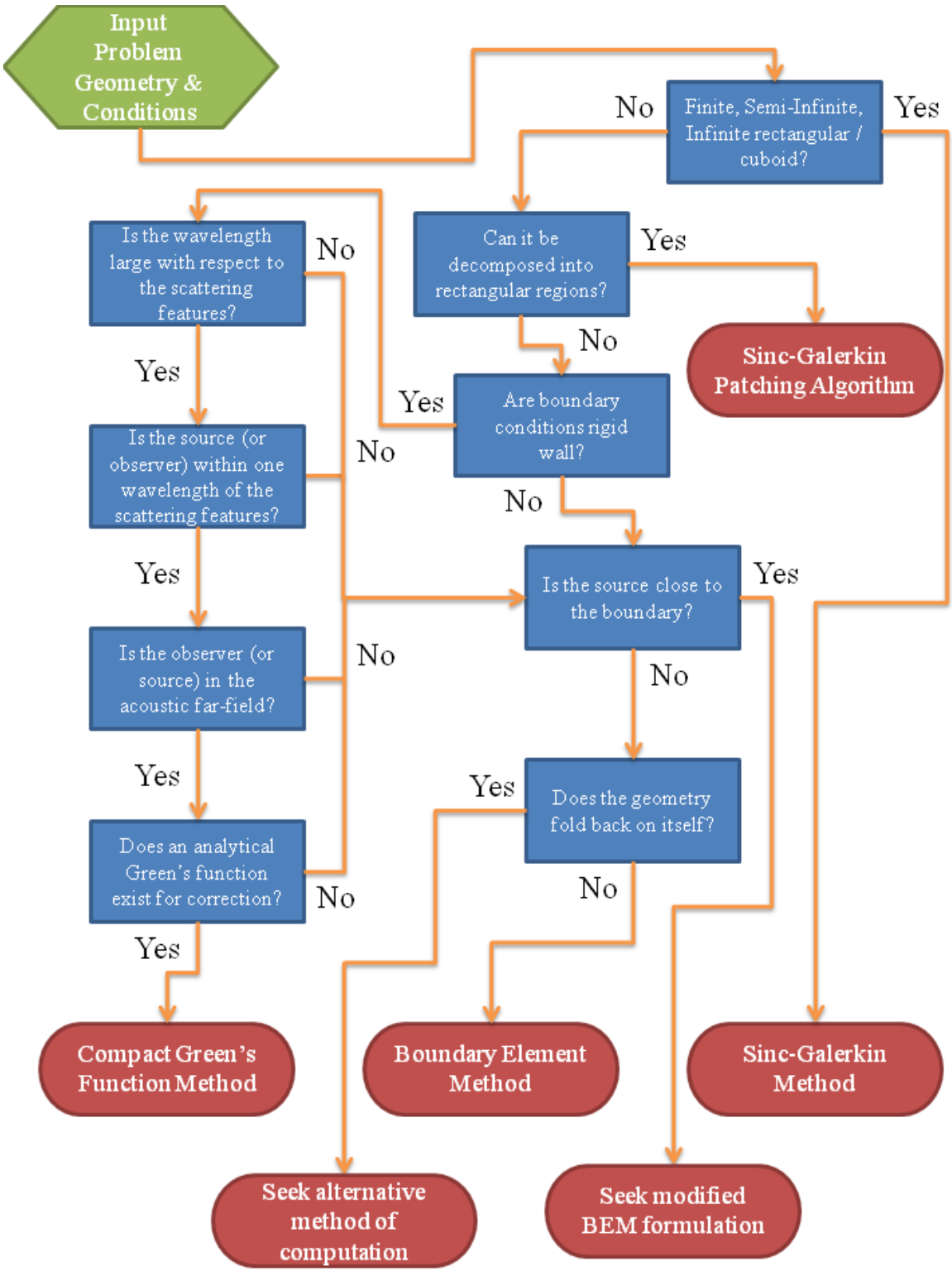

Figure 8.7: Graphical depiction of guidelines to aid selection of the most suitable method for calculation of the Green's function for the given problem. For clarity, the formal decision notation of a diamond has been changed to a rectangle.

these conditions. The Sinc-Galerkin method in its current form is restricted in direct application to a class of finite or infinite rectangular geometries which is reflected in the flow chart options. Furthermore, we have developed, but not implemented due to time constraints, a formulation suitable for Neumann (or indeed mixed) boundary conditions. Figure 8.7 allows for the use of Sinc-Galerkin for these problems too. The BEM, although generally more expensive, is suitable for problems which cannot be treated using the other two methods or variations thereon. Figure 8.7 also recognises the limitations of the BEM and advises the use of a modified formulation [218] where the source is close to the boundary. In the event that the particular acoustic problem does not meet any of the requirements, additional methods may be sought.

Chapter 9

Closing Remarks

The goal of this research output is to allow hybrid noise prediction to take place in a wider range of complex geometries by providing numerical representations of acoustic Green's functions. Hybrid noise prediction schemes utilise efficient integral-based propagation techniques such as the acoustic analogy. Previously, acoustic propagation using integral-based approaches was only possible for simple geometries due to the requirement for a closed-form representation of the Green's function. Such analytical Green's functions are rare and, for more complex geometries, are often challenging, if not impossible, to construct. For this reason we have investigated the use of numerical methods to evaluate the Green's function over a grid of points in the domain. This grid may then be used in place of the analytical Green's function in existing hybrid noise prediction schemes. Hence, these schemes may propagate noise through domains for which Green's functions are traditional unavailable, whilst exploiting the efficiency and accuracy of the integral-based approach.

This research has selected, developed and analysed three numerical methods for computing an approximation to the Green's function for the Helmholtz equation in several different classes of geometry. These methods were selected based on a set of requirements formulated after a survey of available options, namely (see Chapter 4):

- The method shall not unreasonably increase the overall execution time of an existing hybrid scheme.
- Where possible, the method shall satisfy a range of acoustic boundary conditions accurately without contaminating the domain solution.

- The method shall be robust for a wide range of geometries.

The methods have been compared and contrasted and, through understanding of the advantages and disadvantages, each contribute to a portfolio of numerical approaches suitable for computing numerical approximations to the Green's function for a wide range of acoustic problems. The pros and cons of each of the methods may be broader summarised as being:

- Compact Green's Function
  - ✓ Offers semi-analytical precision
  - ✓ Easily handles complicated geometries
  - ✗ Limited to compact class of problems
  - ✗ Curved surfaces can be computationally expensive
- Boundary Element Method
  - ✓ Can handle variety of geometries
  - ✓ Only discretisation of problem boundary required
  - ✗ Extra BCs required for semi-infinite domains
  - ✗ Matrix construction expensive and required for each individual internal point
- Sinc-Galerkin Method
  - ✓ No expensive numerical integration required
  - ✓ Can be parallelised and used in domain decomposition algorithms
  - ✗ Direct application limited to rectangular domains
  - ✗ Convergence degraded by domain singularities

The numerical approximations computed by the three methods have been compared to available analytical solutions for validation. Where appropriate, methods have been enhanced to increase their versatility. For example,

1. We used numerical conformal mapping to allow application of the compact Green's function method to more complex geometries;

2. We suggested a new implementation of non-reflecting boundary conditions for the boundary element method to allow treatment of semi-infinite domains;

3. We proposed an extension to the Sinc-Galerkin method to allow treatment of Helmholtz boundary value problems subject to Neumann boundary conditions.

The work has been concluded by providing guidelines as to the selection of one particular method over another based on knowledge of the acoustic problem. Details of the attributes of the methods have been summarised in Chapter 8.
In addition to providing a numerical representation of the Green's function for use in hybrid schemes, the Green's functions computed by the portfolio of methods offer important qualitative benefits. For example, in Section 6.9 and Section 6.10, we visualise the results which, from simple inspection, can provide insightful preliminary indications of key regions of scattering in a given geometry. This information could contribute to the design of a more complete acoustic investigation or a means to concentrate resources on a particular geometrical feature.

9.1 Future Work

The work presented in this document offers many opportunities for future research. First, the BEM and the Sinc-Galerkin methods have been developed here in 2D and written in MATLAB. Their extension to 3D is straightforward and would be a logical extension to the work presented here, especially if the code is to be used as part of existing hybrid schemes which would already be configured for 3D problems. The compact method is already available for use in 3D as it constructs the 3D solution from the constituent 2D problems (see Section 5.5).
The investigation into the use of the Sinc-Galerkin method used a simple formulation and considered problems on a single rectangular patch. Although a basic domain, it was possible to perform a suitable degree of analysis on this configuration. Further complexity would have been unnecessary and potentially would have obscured the manifestation of error. As well as extending the method to 3D, there is work to be done on developing domain decomposition and patching algorithms which will allow the Sinc-Galerkin to be applied to a wider range of geometries. This would be quite a

challenging but rewarding pursuit and essential for the continued used of the method. The code used to execute the methods has all been written in a serial sense. In practice, the code ought to run as efficiently and quickly as possible. One way of achieving this would be to recode into another language, which may use more efficient software implementations of the arithmetic operations. Furthermore, there are numerous means of parallelising all, or sections of, the original code. In particular, the construction of the Sinc-Galerkin solution is amenable to this treatment and would benefit significantly from it. Examination of the software with a view of parallelising the operations where possible is a useful activity for the future.

As remarked in Section 8.4, the guidelines for selecting a suitable method for a given geometry are suitable for software implementation. This research may be applied as a practical tool if this implementation were to be carried out. This 'master routine' would take in the problem geometry as well as other details such as source/observer locations, wavelength and boundary conditions. After applying the logic described by Fig. 8.7, the routine would select an appropriate method, perform the calculation and store the Green's function for use in the integral-based propagation step of the hybrid scheme. This activity could take place in parallel with the source region computation, immediately after the source region mesh is confirmed. Thus little additional time would be added to the calculation while ensuring the Green's function is known as the required grid points.

A related future task would be to incorporate the methods into an existing hybrid scheme and assess their performance. This task should consider the alignment between the Green's function grid and the grid of the hybrid calculation. Moreover, the impact of the errors associated with the Green's function calculation should be ascertained. Specifically, how the errors manifest themselves in the radiated sound field and how sensitive this behaviour is to changes in problem parameters. This task is of considerable size and scope but can build on the detailed examination of error sources performed in this research.

Bibliography

[1] J.-L. Adam, D. Ricot, F. Dubief, and C. Guy. Aeroacoustic simulation of automotive ventilation outlets. In *Acoustics 08*, 2008.

[2] A. Agarwal, P.J. Morris, and R. Mani. Calculation of sound propagation in nonuniform flows: suppression of instability waves. *AIAA Journal*, 42(1):80–88, 2004.

[3] J.B. Allen and D.A. Berkley. Image method for efficiently simulating small-room acoustics. *Journal of the Acoustical Society of America*, 65(4):943–950, 1979.

[4] J.S. Alonso and R.A. Burdisso. Green's function for the acoustic field in line ducts with uniform flow. *AIAA Journal*, 45(11):2677–2687, 2007.

[5] R.K. Amiet. Acoustic radiation from an airfoil in a turbulent stream. *Journal of Sound and Vibration*, 41(4):407–420, 1975.

[6] R.K. Amiet. Noise due to turbulent flow past a trailing edge. *Journal of Sound and Vibration*, 47(3):387–393, 1976.

[7] N. Andersson, L.E. Eriksson, and L. Davidson. Large-eddy simulation of subsonic turbulent jets and their radiated sound. *AIAA Journal*, 43(9):1899–1912, 2005.

[8] B. André, T. Castelain, and C. Bailly. Broadband shock-associated noise in screeching and non-screeching underexpanded supersonic jets. *ERCOFTAC Bulletin 90, March, Special Issues in Aeroacoustics (Invited)*, pages 10–14, 2012.

[9] W.T. Ang. *A Beginner's Course in Boundary Element Methods*. Universal Publishers, 2007.

[10] D. Appelö, T. Colonius, T. Hagstrom, and M. Inkman. Development of arbitrary-order hermite methods for simulation and analysis of turbulent jet noise. *Procedia Engineering*, 6:19–27, 2010.

[11] Daniel Appelö, Matthew Inkman, Thomas Hagstrom, and Tim Colonius. Hermite Methods for Aeroacoustic: Recent Progress. Technical report, California Institute of Technology, 2011.

[12] Tilo Arens, Kai Sandfort, Susanne Schmitt, and Armin Lechleiter. Analysing Ewald's method for the evaluation of Green's functions for periodic media. *IMA Journal of Applied Mathematics*, pages 1–27, 2011.

[13] R. Jeremy Astley. Numerical methods for noise propagation in moving flows, with application to turbofan engines. *Acoustical Science and Technology*, 30(4):227–239, 2009.

[14] A. Atangana. Drawdown in prolate spheroidal-spherical coordinates obtained via Green's function and perturbation methods. *Communications in Nonlinear Science and Numerical Simulation*, 19(5):1259–1269, May 2014.

[15] I. Aziz, Siraj Ul-Islam, and B. Sarler. Wavelets collocation methods for the numerical solution of elliptic BV problems. *Applied Mathematical Modelling*, 37(3):676–694, Feb 2013.

[16] M. Babiker, D.R. Tilley, E.L. Albuquerque, and C.E.T. Goncalves da Silva. Acoustic Green-Function for Superlattices. *Journal of Physics C: Solid State Physics*, 18(6):1269–1284, 1985.

[17] C. Bailly, W. Bechara, P. Lafon, and S. Candel. Jet Noise Predictions Using a K-Epsilon Turbulence Model. AIAA, 1993.

[18] C. Bailly, P. Lafon, and S. Candel. Subsonic and supersonic jet noise predictions from statistical source models. *AIAA Journal*, 35(11):1688–1696, 1997.

[19] Christophe Bailly, Christophe Bogey, and Xavier Gloerfelt. Some useful hybrid approaches for predicting aerodynamic noise. *Comptes Rendus Mécanique*, 333(9):666–675, 2005.

[20] Hélène Barucq, Rabia Djellouli, and Anne-Gaëlle Saint-Guirons. Exponential Decay of High-Order Spurious Prolate Spheroidal Modes Induced by a Local Approximate Dtn Exterior Boundary Condition. *Progress In Electromagnetics Research B*, 37:1–19, 2012.

[21] F. Bastin, P. Lafon, and S. Candel. Computation of jet mixing noise due to coherent structures: the plane jet case. *Journal of Fluid Mechanics*, 335:261–304, 1997.

[22] Alvin Bayliss, Max Gunzburger, and Eli Turkel. Boundary Conditions for the Numerical Solution of Elliptic Equations in Exterior Regions. *SIAM Journal on Applied Mathematics*, 42(2):430–451, 1982.

[23] Alvin Bayliss and Eli Turkel. Radiation boundary conditions for wave-like equations. *Communications on Pure and Applied Mathematics*, 33(6):707–725, 1980.

[24] Mario Bebendorf. Approximation of boundary element matrices. *Numerische Mathematik*, 86(4):565–589, 2000.

[25] W. Bechara, C. Bailly, P. Lafon, and S.M. Candel. Stochastic approach to noise modeling for free turbulent flows. *AIAA Journal*, 32(3):455–463, 1994.

[26] G. Beer and J.L. Meek. 'Infinite domain' elements. *International Journal for Numerical Methods in Engineering*, 17(1):43–52, 1981.

[27] G. Beer and J.O. Watson. Infinite boundary elements. *International Journal for Numerical Methods in Engineering*, 28(6):1233–1247, 1989.

[28] Jean-Pierre Berenger. A perfectly matched layer for the absorption of electromagnetic waves. *Journal of Computational Physics*, 114(2):185–200, 1994.

[29] Julien Berland, Christophe Bogey, Olivier Marsden, and Christophe Bailly. High-order, low dispersive and low dissipative explicit schemes for multiple-scale and boundary problems. *Journal of Computational Physics*, 224(2):637–662, 2007.

[30] C. Berman, G. Gordon, G. Karniadakis, and S. Orszag. Jet turbulence noise computations. *AIAA Paper (93-4365)*, (0146-3705), 1993.

[31] Gregory Beylkin, Christopher Kurcz, and Lucas Monzón. Fast convolution with the free space Helmholtz Green's function. *Journal of Computational Physics*, 228(8):2770–2791, 2009.

[32] A. Birkefeld and C.D. Munz. Simulations of Airfoil Noise with the Discontinuous Galerkin Solver NoisSol. *ERCOFTAC Bulletin 90, March, Special Issues in Aeroacoustics (Invited)*, pages 28–33, 2012.

[33] Andreas Birkefeld and Claus-Dieter Munz. A Hybrid Method for CAA. In Andreas Dillmann, Gerd Heller, Michael Klaas, Hans-Peter Kreplin, Wolfgang Nitsche, and Wolfgang Schröder, editors, *New Results in Numerical and Experimental Fluid Mechanics VII*, volume 112 of *Notes on Numerical Fluid Mechanics and Multidisciplinary Design*, chapter 58, pages 473–480. Springer Berlin Heidelberg, 2010.

[34] Petter Bjorstad and Eric Grosse. Conformal Mapping of Circular Arc Polygons. *SIAM Journal on Scientific and Statistical Computing*, 8(1):19–32, 1987.

[35] Daniel J. Bodony, George Zagaris, Adam Reichert, and Qi Zhang. Aeroacoustic predictions in complex geometries. *Procedia Engineering*, 6:234–243, 2010.

[36] D.J. Bodony and S.K. Lele. Current status of jet noise predictions using large-eddy simulation. *AIAA Journal*, 46(2):364–380, 2008.

[37] Christophe Bogey and Christophe Bailly. A family of low dispersive and low dissipative explicit schemes for flow and noise computations. *Journal of Computational Physics*, 194(1):194–214, 2004.

[38] Christophe Bogey and Christophe Bailly. Computation of a high Reynolds number jet and its radiated noise using large eddy simulation based on explicit filtering. *Computers & Fluids*, 35(10):1344–1358, 2006.

[39] S. Boluriaan and P.J. Morris. Numerical Prediction of Minor Losses in High Amplitude Acoustic Resonators. In *8th AIAA/CEAS Aeroacousitcs Conference & Exhibit*, 2002.

[40] W. Borth. Vibration and Resonance Phenomena in Pipes of Piston Fans. *Zeitschrift des VDI*, 60(28):565–569, 1916.

[41] M. Bouchon. A Review of the Discrete Wavenumber Method. *Pure and Applied Geophysics*, 160(3):445–465, 2003.

[42] Michel Bouchon. A numerical simulation of the acoustic and elastic wavefields radiated by a source on a fluid-filled borehole embedded in a layered medium. *Geophysics*, 58(4):475, 1993.

[43] K. Bowers and J. Lund. Numerical Solution of Singular Poisson Problems via the Sinc-Galerkin Method. *SIAM Journal on Numerical Analysis*, 24(1):36–51, 1987.

[44] C.A. Brebbia and J. Dominguez. *Boundary Elements An Introductory Course*. Computational Mechanics Publications McGraw-Hill Book Company, Southampton, 2nd edition, 1989.

[45] K.S. Brentner. An efficient and robust method for predicting helicopter rotor high-speed impulsive noise. *Journal of Sound and Vibration*, 203(1):87–100, 1997.

[46] James Bridges and Fazle Hussain. Direct evaluation of aeroacoustic theory in a jet. *Journal of Fluid Mechanics*, 240:469–501, 1992.

[47] Thomas F. Brooks, D. Stuart Pope, and Michael A. Marcolini. Airfoil self-noise and prediction. Technical report, NASA, 1989.

[48] Guillaume Brès, Franck Pérot, and David Freed. Properties of the Lattice Boltzmann Method for Acoustics. In *15th AIAA/CEAS Aeroacoustics Conference (30th AIAA Aeroacoustics Conference)*. American Institute of Aeronautics and Astronautics, 11-13 May 2009. doi:10.2514/6.2009-3395.

[49] Guillaume Brès, Franck Pérot, and David Freed. A Ffowcs Williams - Hawkings Solver for Lattice-Boltzmann Based Computational Aeroacoustics. In *16th AIAA/CEAS Aeroacoustics Conference*, Aeroacoustics Conferences. American Institute of Aeronautics and Astronautics, 2010. doi:10.2514/6.2010-3711.

[50] Guillaume A Brès, Tim Colonius, and Alexander V Fedorov. Acoustic properties of porous coatings for hypersonic boundary-layer control. *AIAA Journal*, 48(2):267–274, 2010.

[51] J.M. Buick, C.A. Greated, and D.M. Campbell. Lattice BGK simulation of sound waves. *EPL (Europhysics Letters)*, 43(3):235, 1998.

[52] Damiano Casalino, Michel Roger, and Marc Jacob. Prediction of sound propagation in ducted potential flows using Green's function discretization. *AIAA Journal*, 42(4):736–744, 2004.

[53] J. Casper and K.R. Meadows. Using high-order accurate essentially nonoscillatory schemes for aeroacoustic applications. *AIAA Journal*, 34(2):244–250, 1996.

[54] A.V.G. Cavalieri, P. Jordan, and Y. Gervais. Jet Noise and Coherent Structures. *ERCOFTAC Bulletin 90, March, Special Issues in Aeroacoustics (Invited)*, pages 34–39, 2012.

[55] Simon N. Chandler-Wilde, Ivan G. Graham, Stephen Langdon, and Euan A. Spence. Numerical-asymptotic boundary integral methods in high-frequency acoustic scattering. *Acta Numerica*, 21:89–305, 2012.

[56] S.N. Chandler-Wilde and D.C. Hothersall. A uniformly valid far field asymptotic expansion of the green function for two-dimensional propagation above a homogeneous impedance plane. *Journal of Sound and Vibration*, 182(5):665–675, 1995.

[57] C.J. Chapman. The Spiral Green-Function in Acoustics and Electromagnetism. *Proceedings of the Royal Society of London. Series A: Mathematical and Physical Sciences*, 431(1881):157–167, 1990.

[58] S. Chen and G.D. Doolen. Lattice Boltzmann method for fluid flows. *Annual Review of Fluid Mechanics*, 30(1):329–364, 1998.

[59] C.Y.R. Cheng, A.F. Seybert, and T.W. Wu. A multidomain boundary element solution for silencer and muffler performance prediction. *Journal of Sound and Vibration*, 151(1):119 – 129, 1991.

[60] Hongwei Cheng, Jingfang Huang, and Terry Jo Leiterman. An adaptive fast solver for the modified Helmholtz equation in two dimensions. *Journal of Computational Physics*, 211(2):616–637, 2006.

[61] J. Christophe, K. Kucukcoskun, and C. Schram. Analytical and Numerical Extensions of Amiet's Incoming Turbulence Noise Theory to Account for Near-field Effects. *ERCOFTAC Bulletin 90, March, Special Issues in Aeroacoustics (Invited)*, pages 45–49, 2012.

[62] C. Chung and P.J. Morris. Acoustic scattering from two-and three-dimensional bodies. *Journal of Computational Acoustics*, 6(3):357–375, 1998.

[63] Charlotte Clark and Stephen A. Stansfeld. The Effect of Transportation Noise on Health and Cognitive Development: A Review of Recent Evidence. *International Journal of Comparative Psychology*, 20(2):145–158, 2007.

[64] Andrea Colombi, Lapo Boschi, Philippe Roux, and Michel Campillo. Green's function retrieval through cross-correlations in a two-dimensional complex reverberating medium. *The Journal of the Acoustical Society of America*, 135(3):1034, 2014.

[65] T. Colonius and J.B. Freund. Reconstruction of large-scale structures and acoustic radiation from a turbulent M= 0.9 jet using proper orthogonal decomposition. *CIMNE Advances in Turbulence IX*, 2002.

[66] T. Colonius, S.K. Lele, and P. Moin. Boundary conditions for direct computation of aerodynamic sound generation. *AIAA Journal*, 31:1574–1582, 1993.

[67] T. Colonius, S.K. Lele, and P. Moin. Direct Computation of the Sound Generated by Two-Dimensional Mixing Layer. *AIAA Paper (93-4328)*, 1993.

[68] T. Colonius, S.K. Lele, and P. Moin. The sound generated by a two-dimensional shear layer: A comparison of direct computations and acoustic analogies. *AIAA Paper (95-036)*, 1995.

[69] T. Colonius, S.K. Lele, and P. Moin. Sound generation in a mixing layer. *Journal of Fluid Mechanics*, 330:375–409, 1997.

[70] T. Colonius, A. Samanta, and K. Gudmundsson. Parabolized stability equation models of large-scale jet mixing noise. *Procedia Engineering*, 6:64–73, 2010.

[71] Tim Colonius and Sanjiva K. Lele. Computational aeroacoustics: progress on nonlinear problems of sound generation. *Progress in Aerospace Sciences*, 40(6):345–416, 2004.

[72] Tim Colonius, Sanjiva K. Lele, and Parviz Moin. The scattering of sound waves by a vortex: numerical simulations and analytical solutions. *Journal of Fluid Mechanics*, 260:271–298, 1994.

[73] Andrew W. Correia, Junenette L. Peters, Jonathan I. Levy, Steven Melly, and Francesca Dominici. Residential exposure to aircraft noise and hospital admissions for cardiovascular diseases: multi-airport retrospective study. *BMJ*, 347, 2013.

[74] Martin Costabel. Time-Dependent Problems with the Boundary Integral Equation Method. In *Encyclopedia of Computational Mechanics*. John Wiley & Sons, Ltd, 2004.

[75] D.G. Crighton. Radiation from vortex filament motion near a half plane. *Journal of Fluid Mechanics*, 51(02):357–362, 1972.

[76] D.G. Crighton. Basic principles of aerodynamic noise generation. *Progress in Aerospace Sciences*, 16(1):31–96, 1975.

[77] D.G. Crighton. Goals for Computational Aeroacoustics. In D. Lee, R.L. Sternberg, and M.H. Schultz, editors, *Computational Acoustics: Algorithms and Applications*, Proceedings of 1st IMACS Symposium on Computational Acoustics. Elsevier, New Haven, 1988.

[78] D.G. Crighton and F.G. Leppington. On the scattering of aerodynamic noise. *Journal of Fluid Mechanics*, 46(03):577–597, 1971.

[79] Bernd Crouse, David Freed, Ganapathy Balasubramanian, Sivapalan Senthooran, Phoi-Tack Lew, and Luc Mongeau. Fundamental Aeroacoustics Capabilities of the Lattice-Boltzmann Method. In *12th AIAA/CEAS Aeroacoustics Conference (27th AIAA Aeroacoustics Conference)*. American Institute of Aeronautics and Astronautics, 2006. doi:10.2514/6.2006-2571.

[80] S.C. Crow. Aerodynamic sound emission as a singular perturbation problem. *Studies in Applied Mathematics*, 49:21–44, 1970.

[81] N. Curle. The Influence of Solid Boundaries upon Aerodynamic Sound. *Proceedings of the Royal Society of London. Series A: Mathematical and Physical Sciences*, 231(1187):505–514, 1955.

[82] Xiwen Dai, Xiaodong Jing, and Xiaofeng Sun. Vortex Shedding and its Nonlinear Acoustic Effect Occurring at a Slit. *AIAA Journal*, 49(12):2684–2694, 2011.

[83] P.J. Davis and P. Rabinowitz. *Methods of Numerical Integration*. Academic Press, London, 1975.

[84] A.S. Deakin and H. Rasmussen. Sparse Boundary Conditions on Artificial Boundaries for Three-Dimensional Potential Problems. *Journal of Computational Physics*, 129(1):111–120, 1996.

[85] Mehdi Dehghan and Faezeh Emami-Naeini. The Sinc-collocation and Sinc-Galerkin methods for solving the two-dimensional Schrödinger equation with nonhomogeneous boundary conditions. *Applied Mathematical Modelling*, 37(22):9379–9397, 2013.

[86] Andrew Dienstfrey, Fengbo Hang, and Jingfang Huang. Lattice sums and the two-dimensional, periodic Green's function for the Helmholtz equation. *Proceedings of the Royal Society of London. Series A: Mathematical, Physical and Engineering Sciences*, 457(2005):67–85, 2001.

[87] PE Doak. Fluctuating total enthalpy as the basic generalized acoustic field. *Theoretical and Computational Fluid Dynamics*, 10(1-4):115–133, 1998.

[88] H.J. Dong and S. Kim. Green's functions for parabolic systems of second order in time-varying domains. *Communications on Pure and Applied Analysis*, 13(4):1407–1433, 2014.

[89] A. Dravet, J. Julliard, M. Ah-Fa, and G. Rollin. Computation of jet mixing noise for confluent flow nozzles using k-ϵ turbulence model, 1998.

[90] T.A. Driscoll and L.N. Trefethen. *Schwarz-Christoffel Mapping*. Cambridge University Press, Cambridge, 2002.

[91] Tobin A. Driscoll. Algorithm 843: Improvements to the Schwarz-Christoffel toolbox for MATLAB. *ACM Transsactions on Mathematical Software*, 31(2):239–251, 2005.

[92] Wenbo Duan. *Acoustic signals for fluid-filled pipeline blockage detection*. PhD thesis, The University of Manchester, Manchester, 2010.

[93] Dean G. Duffy. *Green's Functions with Applications*. Chapman and Hall, 2001.

[94] Iain D.J. Dupère. *Sound Vortex Interaction in Pipes*. PhD thesis, Department of Engineering, University of Cambridge, 1997.

[95] John A. Ekaterinaris. Implicit High-Order-Accurate-in-Space Algorithms for the Navier-Stokes Equations. *AIAA Journal*, 38(9):1594–1602, 2000.

[96] John A. Ekaterinaris. High-order accurate, low numerical diffusion methods for aerodynamics. *Progress in Aerospace Sciences*, 41(3-4):192–300, 2005.

[97] M. El-Gamel and A.I. Zayed. Sinc-Galerkin method for solving nonlinear boundary-value problems. *Computers & Mathematics with Applications*, 48(9):1285–1298, 2004.

[98] Mohamed El-Gamel. A numerical scheme for solving nonhomogeneous time-dependent problems. *Zeitschrift für angewandte Mathematik und Physik ZAMP*, 57(3):369–383, 2006.

[99] Mohamed El-Gamel. A comparison between the Sinc–Galerkin and the modified decomposition methods for solving two-point boundary-value problems. *Journal of Computational Physics*, 223(1):369–383, 2007.

[100] Mohamed El-Gamel, S.H. Behiry, and H. Hashish. Numerical method for the solution of special nonlinear fourth-order boundary value problems. *Applied Mathematics and Computation*, 145(2–3):717–734, 2003.

[101] Mohamed El-Gamel and John R. Cannon. On the solution a of second order singularly-perturbed boundary value problem by the Sinc-Galerkin method. *Zeitschrift für angewandte Mathematik und Physik ZAMP*, 56(1):45–58, 2005.

[102] Mohamed El-Gamel, John R. Cannon, and Ahmed I. Zayed. Sinc-Galerkin method for solving linear sixth-order boundary-value problems. *Mathematics of Computation*, 73:1325–1343, 2004.

[103] Jeff D. Eldredge, Tim Colonius, and Anthony Leonard. A vortex particle method for two-dimensional compressible flow. *Journal of Computational Physics*, 179(2):371–399, 2002.

[104] David Elliott and Peter R. Johnston. Gauss-Legendre quadrature for the evaluation of integrals involving the Hankel function. *Journal of Computational and Applied Mathematics*, 211(1):23–35, 2008.

[105] Mark Embree and Lloyd N. Trefethen. Green's Functions for Multiply Connected Domains via Conformal Mapping. *SIAM Review*, 41(4):745–761, 1999.

[106] Bjorn Engquist and Hong-Kai Zhao. Absorbing boundary conditions for domain decomposition. *Applied Numerical Mathematics*, 27(4):341–365, 1998.

[107] Björn Engquist and Andrew Majda. Absorbing boundary conditions for numerical simulation of waves. *Mathematics of Computation*, 31(139):629–651, 1977.

[108] R.J. Epstein and D.B. Bliss. An Aeroacoustic Boundary Element Method using Analytical/Numerical Matching. AIAA, 1995.

[109] R.J. Epstein and D.B. Bliss. Aeroacoustic boundary element method using analytical/numerical matching. *AIAA Journal*, 35(2):244–254, 1997.

[110] V. Şeremet. A new approach to constructing Green's functions and integral solutions in thermoelasticity. *Acta Mechanica*, 225(3):735–755, 2014.

[111] V. Şeremet. Static equilibrium of a thermoelastic half-plane: Green's functions and solutions in integrals. *Archive of Applied Mechanics*, 84(4):553–570, 2014.

[112] R. Ewert, M. Meinke, and W. Schröder. Computation of trailing edge noise via LES and acoustic perturbation equations. *AIAA Paper (2002-2467)*, 2002.

[113] R. Ewert and W. Schröder. Acoustic perturbation equations based on flow decomposition via source filtering. *Journal of Computational Physics*, 188(2):365–398, 2003.

[114] F. Farassat. The Kirchhoff Formulas for Moving Surfaces in Aeroacoustics - The Subsonic and Supersonic Cases. Technical Report TM-110285, NASA, 1996.

[115] F. Farassat and M.K. Myers. Extension of Kirchhoff's formula to radiation from moving surfaces. *Journal of Sound and Vibration*, 123(3):451–460, 1988.

[116] S. Feng and D.L. Johnson. High-frequency acoustic properties of a fluid/porous solid interface. II. The 2D reflection Green's function. *Journal of the Acoustical Society of America*, 74(3):915–924, 1983.

[117] J.E. Ffowcs-Williams. The Noise from Turbulence Convected at High Speed. *Philosophical Transactions of the Royal Society of London. Series A, Mathematical and Physical Sciences*, 255(1061):469–503, 1963.

[118] J.E. Ffowcs-Williams and L.H. Hall. Aerodynamic sound generation by turbulent flow in the vicinity of a scattering half plane. *Journal of Fluid Mechanics*, 40(04):657–670, 1970.

[119] J.E. Ffowcs-Williams and D.L. Hawkings. Sound Generation by Turbulence and Surfaces in Arbitrary Motion. *Philosophical Transactions of the Royal Society of London. Series A, Mathematical and Physical Sciences*, 264(1151):321–342, 1969.

[120] J.B. Freund and T. Colonius. Turbulence and sound-field POD analysis of a turbulent jet. *International Journal of Aeroacoustics*, 8(4):337–354, 2009.

[121] J.B. Freund, S.K. Lele, and P. Moin. Calculation of the radiated sound field using an open Kirchhoff surface. *AIAA Journal*, 34(5):909–915, 1996.

[122] G. Gabard, R.J. Astley, P. Gamallo, and G. Kennedy. Physics-based computational methods for aero-acoustics. *Procedia Engineering*, 6(0):183–192, 2010.

[123] P.R. Garabedian. An integral equation governing electromagnetic waves. *Quarterly of Applied Mathematics*, 12:428–433, 1955.

[124] Gabriel N. Gatica. Variational formulations of transmission problems via FEM, BEM and DtN mappings. *Computer Methods in Applied Mechanics and Engineering*, 182(3-4):341–354, 2000.

[125] R. Gilbert and M.J. Ou. Near field representations of the acoustic Green's function in a shallow ocean with fluid-like seabed. *Georgian Mathematical Journal*, 14(1):109–122, 2007.

[126] R.P. Gilbert, Z.Y. Lin, and K. Hackl. Acoustic Green's Function Approximations. *Journal of Computational Acoustics*, 6(4):435–452, 1998.

[127] R.P. Gilbert, Y.Z. Xu, and D.H. Wood. Construction of approximations to acoustic Green's functions for nonhomogeneous oceans using transmutation. *Wave Motion*, 10(3):285–297, 1988.

[128] M.B. Giles. Nonreflecting Boundary Conditions for Euler Equation Calcultions. *AIAA Journal*, 28(12):2050–2058, 1990.

[129] Dan Givoli. A spatially exact non-reflecting boundary condition for time dependent problems. *Computer Methods in Applied Mechanics and Engineering*, 95(1):97 – 113, 1992.

[130] Dan Givoli. High-order local non-reflecting boundary conditions: a review. *Wave Motion*, 39(4):319–326, 2004.

[131] X. Gloerfelt, C. Bailly, and D. Juvé. Direct computation of the noise radiated by a subsonic cavity flow and application of integral methods. *Journal of Sound and Vibration*, 266(1):119–146, 2003.

[132] M. Goldstein. Recent developments in the application of the Generalized Acoustic Analogy to jet noise prediction. *International Journal of Aeroacoustics*, 10(2):89–116, 2011.

[133] M.E. Goldstein. A generalized acoustic analogy. *Journal of Fluid Mechanics*, 488:315–333, 2003.

[134] L. Grasedyck. Adaptive Recompression of -Matrices for BEM. *Computing*, 74(3):205–223, 2005.

[135] Stéphan Grilli, Torstein Pedersen, and Peter Stepanishen. A hybrid boundary element method for shallow water acoustic propagation over an irregular bottom. *Engineering Analysis with Boundary Elements*, 21(2):131–145, 1998.

[136] Chester E. Grosch and Steven A. Orszag. Numerical solution of problems in unbounded regions: Coordinate transforms. *Journal of Computational Physics*, 25(3):273–295, 1977.

[137] M. Grote and J. Keller. Exact Nonreflecting Boundary Conditions for the Time Dependent Wave Equation. *SIAM Journal on Applied Mathematics*, 55(2):280–297, 1995.

[138] Marcus J. Grote and Joseph B. Keller. On Nonreflecting Boundary Conditions. *Journal of Computational Physics*, 122(2):231–243, 1995.

[139] Marcus J. Grote and Christoph Kirsch. Dirichlet-to-Neumann boundary conditions for multiple scattering problems. *Journal of Computational Physics*, 201(2):630 – 650, 2004.

[140] K. Gudmundsson and Tim Colonius. Instability wave models for the near-field fluctuations of turbulent jets. *Journal of Fluid Mechanics*, 689:97–128, 2011.

[141] B.L.J. Gysen, E.A. Lomonova, J.J.H. Paulides, and A.J.A. Vandenput. Analytical and Numerical Techniques for Solving Laplace and Poisson Equations in a Tubular Permanent-Magnet Actuator: Part I. Semi-Analytical Framework. *IEEE Transactions on Magnetics*, 44(7):1751–1760, 2008.

[142] Philipp Hahn and Dan Negrut. Smoothed Particle Hydrodynamics in Acoustic Simulations. Technical report, University of Wisconsin-Madison, 2010.

[143] M.A. Hajji and Q.M. Al-Mdallal. Modified Sinc-Galerkin Method for Nonlinear Boundary Value Problems. *Journal of Mathematics*, 2013:10, 2013.

[144] W.S. Hall. Integration Methods for Singular Boundary Element Method Integrands. In C.A Brebbia, editor, *Boundary elements X: Mathematical and computational aspects*, volume 1, pages 219–236. Computational Mechanics Publications, Southampton, 1988.

[145] Anna L. Hansell, Marta Blangiardo, Lea Fortunato, Sarah Floud, Kees de Hoogh, Daniela Fecht, Rebecca E. Ghosh, Helga E. Laszlo, Clare Pearson, Linda Beale, Sean Beevers, John Gulliver, Nicky Best, Sylvia Richardson, and Paul Elliott. Aircraft noise and cardiovascular disease near Heathrow airport in London: small area study. *BMJ*, 347, 2013.

[146] Isaac Harari, Igor Patlashenko, and Dan Givoli. Dirichlet-to-Neumann Maps for Unbounded Wave Guides. *Journal of Computational Physics*, 143(1):200 – 223, 1998.

[147] J.C. Hardin and D.S. Pope. Sound Generation by a Stenosis in a Pipe. *AIAA Journal*, 30(2):312–317, 1992.

[148] J.C. Hardin and D.S. Pope. Sound generation by flow over a two-dimensional cavity. *AIAA Journal*, 33(3):407–412, 1995.

[149] M Harper-Bourne and M.J. Fisher. The noise from shock waves in supersonic jets. Technical report, AGARD, 1974.

[150] Michaela Herr and Werner Dobrzynski. Experimental Investigations in Low-Noise Trailing Edge Design. *AIAA journal*, 43(6):1167–1175, 2005.

[151] R. Hixon. On Increasing the Accuracy of MacCormack Schemes for Aeroacoustic Applications. Technical Report ICOMP-96-11, NASA, Cleveland, Ohio, 1996.

[152] S. Hong and R.F. Goodrich. Application of Conformal Mapping to Scattering and Diffraction Problems. In J. Brown, editor, *Electromagnetic Wave Theory Part 2*, volume 11, pages 907–914. Pergamon Press, 1st edition, 1965.

[153] Khalid M. Hosny, Ismail A. Ismail, and Awatef A. Hamed. Simulation of Shocked Acoustic Wave Using DRP Scheme. *University of Istanbul Faculty of Science the Journal of Mathematics*, 59:145–166, 2000.

[154] Peng-Fei Hou, Li Wang, and Tao Yi. 2D Green's functions for semi-infinite orthotropic thermoelastic plane. *Applied Mathematical Modelling*, 33(3):1674–1682, 2009.

[155] H. How, C. Vittoria, L.C. Kempel, and K.D. Trott. Green's function calculations on circular microstrip patch antennas. *IEEE Transactions on Antennas and Propagation*, 49(3):393–401, 2001.

[156] M.S. Howe. Contributions to the theory of aerodynamic sound, with application to excess jet noise and the theory of the flute. *Journal of Fluid Mechanics*, 71(04):625–673, 1975.

[157] M.S. Howe. The generation of sound by aerodynamic sources in an inhomogeneous steady flow. *Journal of Fluid Mechanics*, 67(03):597–610, 1975.

[158] M.S. Howe. The dissipation of sound at an edge. *Journal of Sound and Vibration*, 70(3):407–411, 1980.

[159] M.S. Howe. Structural and Acoustic Noise Produced by Turbulent Flow over an Elastic Trailing Edge. *Proceedings of the Royal Society of London. Series A: Mathematical and Physical Sciences*, 442(1916):533–554, 1993.

[160] M.S. Howe. The compact Green's function for a semi-infinite elastic plate, with application to trailing-edge noise and blade-vortex interaction noise. *Journal of the Acoustical Society of America*, 94(4):2353–2364, 1993.

[161] M.S. Howe. Trailing Edge Noise at Low Mach Numbers. *Journal of Sound and Vibration*, 225(2):211–238, 1999.

[162] M.S. Howe. Edge-source acoustic Green's function for an airfoil of arbitrary chord, with application to trailing-edge noise. *The Quarterly Journal of Mechanics and Applied Mathematics*, 54(1):139–155, 2001.

[163] M.S. Howe. *Theory of Vortex Sound*. Cambridge University Press, Cambridge, 2003.

[164] L.H. Howell. *Computation of Conformal Maps by Modified Schwarz-Christoffel Transformations*. PhD thesis, Massachusetts Institute of Technology, 1990.

[165] George C. Hsiao, Fengshan Liu, Jiguang Sun, and Liwei Xu. A coupled BEM and FEM for the interior transmission problem in acoustics. *Journal of Computational and Applied Mathematics*, 235(17):5213–5221, 2011.

[166] Fang Q. Hu. A Spectral Boundary Integral Equation Method for the 2D Helmholtz Equation. *Journal of Computational Physics*, 120(2):340–347, 1995.

[167] Z.W. Hu, C.L. Morfey, and N.D. Sandham. Sound radiation from a subsonic turbulent plane jet. *AIAA Paper (2002-2421)*, 2002.

[168] Z.Y. Huang and W.K. Jiang. An effective method calculating acoustic Green's function for closed rectangular cavity using the Ewald's summation technique. *Acta Acustica United with Acustica*, 93(5):853–856, 2007.

[169] J. Huijssen, M.D. Verweij, and N. de Jong. Green's Function Method for Modeling Nonlinear Three-dimensional Pulsed Acoustic Fields in Diagnostic Ultrasound Including Tissue-like Attenuation, 2008.

[170] Osamu Inoue and Nozomu Hatakeyama. Sound generation by a two-dimensional circular cylinder in a uniform flow. *Journal of Fluid Mechanics*, 471:285–314, 2002.

[171] Moshe Israeli and Steven A. Orszag. Approximation of radiation boundary conditions. *Journal of Computational Physics*, 41(1):115–135, 1981.

[172] K. Jansen, T. Maeder, and R. Reba. Finite-element based large-eddy simulation of the near-nozzle region of a compressible round jet. *AIAA Paper (2002-2358)*, 2002.

[173] X. Jiang, P.J. Li, and W.Y. Zheng. Numerical Solution of Acoustic Scattering by an Adaptive DtN Finite Element Method. *Communications in Computational Physics*, 13(5):1227–1244, 2013.

[174] X. Jing and X. Sun. Discrete vortex simulation on the acoustic nonlinearity of an orifice. *AIAA Journal*, 38(9):1565–1572, 2000.

[175] Kirk E. Jordan, Gerard R. Richter, and Ping Sheng. An efficient numerical evaluation of the Green's function for the Helmholtz operator on periodic structures. *Journal of Computational Physics*, 63(1):222–235, 1986.

[176] Sukky Jun and Do Wan Kim. Axial Green's function method for steady Stokes flow in geometrically complex domains. *Journal of Computational Physics*, 230(5):2095–2124, 2011.

[177] M. Kaltenbacher, M. Escobar, S. Becker, and I. Ali. Numerical simulation of flow-induced noise using LES/SAS and Lighthill's acoustic analogy. *International Journal for Numerical Methods in Fluids*, 63(9):1103–1122, 2010.

[178] Joseph B. Keller and Dan Givoli. Exact non-reflecting boundary conditions. *Journal of Computational Physics*, 82(1):172–192, 1989.

[179] S. Kirkup. *The Boundary Element method in Acoustics: a development in Fortran.* Integrated Sound Software, 1998.

[180] Omar M. Knio, Lu Ting, and Rupert Klein. Interaction of a slender vortex with a rigid sphere: Dynamics and far-field sound. *The Journal of the Acoustical Society of America*, 103(1):83–98, 1998.

[181] S.R. Koh, G. Geiser, H. Foysi, and W. Schröder. Impact of Inhomogeneous Density Distribution on Acoustic Sources in Turbulent Jets. *ERCOFTAC Bulletin 90, March, Special Issues in Aeroacoustics (Invited)*, pages 15–20, 2012.

[182] Sanoe Koonprasert and Kenneth L. Bowers. The fully Sinc-Galerkin method for time-dependent boundary conditions. *Numerical Methods for Partial Differential Equations*, 20(4):494–526, 2004.

[183] Rajneesh Kumar and Vijay Chawla. Green's functions in orthotropic thermoelastic diffusion media. *Engineering Analysis with Boundary Elements*, 36(8):1272–1277, 2012.

[184] H. Kurkcu, N. Nigam, and F. Reitich. An integral representation of the Green function for a linear array of acoustic point sources. *Journal of Computational Physics*, 230(8):2838–2856, 2011.

[185] Harun Kurkcu and Fernando Reitich. Stable and efficient evaluation of periodized Green's functions for the Helmholtz equation at high frequencies. *Journal of Computational Physics*, 228(1):75–95, 2009.

[186] P.K. Kythe. *Green's functions and linear differential equations: Theory, Applications and Computation*. Chapman & Hall/CRC Press, London, 2011.

[187] F. Ladeinde, K. Alabi, T. Colonius, K. Gudmundsson, R.H. Schlinker, and R.A. Reba. An Integrated RANS-PSE-Wave Packet Tool for the Prediction of Subsonic and Supersonic Jet Noise, 2010.

[188] D.J. Lee and S.O. Koo. Numerical study of sound generation due to a spinning vortex pair. *AIAA Journal*, 33:20–26, 1995.

[189] S. Lee, J. Kim, Y.H. Yu, and M.P. Isom. Prediction of Rotor High-Speed Impulsive Noise with a Combined CFD-Kirchhoff Method. *Journal of Sound and Vibration*, 207(4):453–464, 1997.

[190] Phoi-Tack Lew, Luc Mongeau, and Anastasios Lyrintzis. Noise prediction of a subsonic turbulent round jet using the lattice-Boltzmann method. *The Journal of the Acoustical Society of America*, 128(3):1118–1127, 2010.

[191] David L. Lewis, John Lund, and Kenneth L. Bowers. The space–time Sinc-Gallerkin method for parabolic problems. *International Journal for Numerical Methods in Engineering*, 24(9):1629–1644, 1987.

[192] X.Y. Li, X. Zhao, and Y.H. Li. Green's functions of the forced vibration of Timoshenko beams with damping effect. *Journal of Sound and Vibration*, 333(6):1781–1795, 2014.

[193] Y.L. Li, C.H. Liu, and S.J. Franke. Three-dimensional Green's function for wave propagation in a linearly inhomogeneous medium - the exact analytic solution. *The Journal of the Acoustical Society of America*, 87(6):2285–2291, 1990.

[194] M.J. Lighthill. On Sound Generated Aerodynamically. I. General Theory. *Proceedings of the Royal Society of London. Series A: Mathematical and Physical Sciences*, 211(1107):564–587, 1952.

[195] M.J. Lighthill. On Sound Generated Aerodynamically. II. Turbulence as a Source of Sound. *Proceedings of the Royal Society of London. Series A, Mathematical and Physical Sciences*, 222(1148):1–32, 1954.

[196] G.M. Lilley. On the noise from jets. Technical Report CP-131, AGARD, 1974.

[197] C. Linton. Lattice Sums for the Helmholtz Equation. *SIAM Review*, 52(4):630–674, 2010.

[198] C.M. Linton. The Green's Function for the Two-Dimensional Helmholtz Equation in Periodic Domains. *Journal of Engineering Mathematics*, 33(4):377–401, 1998.

[199] Y.S.K. Liow, B.T. Tan, M.C. Thompson, and K. Hourigan. Sound generated in laminar flow past a two-dimensional rectangular cylinder. *Journal of Sound and Vibration*, 295(1-2):407–427, 2006.

[200] S.C. Lo, K. Aikens, G. Blaisdell, and A. Lyrintzis. Numerical investigation of 3-D supersonic jet flows using large-eddy simulation. *International Journal of Aeroacoustics*, 11(7):783–812, 2012.

[201] J.F. Lu and D.S. Jeng. Green's function for a harmonic acoustic point source within seawater overlying a saturated poroelastic seabed. *Journal of Sound and Vibration*, 307(1-2):172–186, 2007.

[202] P.J. Lu, D. Pan, and D.Y. Yeh. Numerical simulation of trailing-edge acoustic/vortical interaction. *AIAA Journal*, 33(5):785–793, 1995.

[203] C. Lui and S.K. Lele. A numerical study of shock-associated noise. *AIAA Paper (2002-2530)*, 2002.

[204] John Lund and Kenneth L. Bowers. *Sinc Methods for Quadrature and Differential Equations*. Society for Industrial and Applied Mathematics, Philadelphia, 1992.

[205] C. Luo, M. Zhao, and Z.S. Rao. The analysis of structural-acoustic coupling of an enclosure using Green's function method. *International Journal of Advanced Manufacturing Technology*, 27(3-4):242–247, 2005.

[206] W. Luo, Z.P. Nie, and Y.P.P. Chen. Fast Analysis of Electromagnetic Scattering From Three-Dimensional Objects Straddling the Interface of a Half Space. *IEEE Geoscience and Remote Sensing Letters*, 11(7):1205–1209, 2014.

[207] Xuqiong Luo, Qikui Du, Hongying Huang, and Tianshu He. A Schwarz alternating algorithm for a three-dimensional exterior harmonic problem with prolate spheroid boundary. *Computers & Mathematics with Applications*, 65(8):1129–1139, 2013.

[208] T. Luostari, T. Huttunen, and P. Monk. The Ultra Weak Variational Formulation Using Bessel Basis Functions. *Communications in Computational Physics*, 11(2):400–414, 2012.

[209] Nancy J. Lybeck and Kenneth L. Bowers. The Sinc-Galerkin Schwarz Alternating Method for Poisson's Equation. In *Computation and Control IV*, volume 20 of *Progress in Systems and Control Theory*, pages 247–256. Birkhäuser Boston, 1995.

[210] Nancy J. Lybeck and Kenneth L. Bowers. Domain decomposition in conjunction with sinc methods for Poisson's equation. *Numerical Methods for Partial Differential Equations*, 12(4):461–487, 1996.

[211] A. Lyrintzis and Y. Xue. Versatile Kirchhoff code for aeroacoustic predictions. *AIAA Journal*, 35(1):198–200, 1997.

[212] A.S. Lyrintzis. Review: The use of Kirchhoff's method in computational aeroacoustics. *Journal of Fluids Engineering*, 116(4):665–676, 1994.

[213] V.P. Manno, S.H. Reitsma, and T.F. Tureaud. Developing numerical techniques for solving low Mach number fluid-acoustic problems. *AIAA Journal*, 31(11), 1993.

[214] E. Manoha, C. Herrero, P. Sagaut, and S Redonnet. Numerical prediction of airfoil aerodynamic noise. In *Proceedings of 8th AIAA/CEAS Aeroacoustics Conference, Breckenridge, Colorado, USA*, 2002.

[215] E. Manoha, B. Troff, and P. Sagaut. Trailing-edge noise prediction using large-eddy simulation and acoustic analogy. *AIAA Journal*, 38(4), 2000.

[216] S.W. Marcus. A hybrid (finite difference-surface Green's function) method for computing transmission losses in an inhomogeneous atmosphere over irregular

terrain. *IEEE Transactions on Antennas and Propagation*, 40(12):1451–1458, 1992.

[217] S. Marié, D. Ricot, and P. Sagaut. Comparison between lattice Boltzmann method and Navier-Stokes high order schemes for computational aeroacoustics. *Journal of Computational Physics*, 228(4):1056–1070, 2009.

[218] L. Marin, D. Lesnic, and V. Mantič. Treatment of singularities in Helmholtz-type equations using the boundary element method. *Journal of Sound and Vibration*, 278(1–2):39–62, 2004.

[219] Kelly M. McArthur, Kenneth L. Bowers, and John Lund. Numerical implementation of the Sinc-Galerkin method for second-order hyperbolic equations. *Numerical Methods for Partial Differential Equations*, 3(3):169–185, 1987.

[220] Kelly M. McArthur, Kenneth L. Bowers, and John Lund. The Sinc method in multiple space dimensions: Model problems. *Numerische Mathematik*, 56(8):789–816, 1990.

[221] R.S. McGowan and M.S. Howe. Compact Green's functions extend the acoustic theory of speech production. *Journal of Phonetics*, 35(2):259–270, 2007.

[222] R. Mehra, N. Raghuvanshi, M.C. Lin, and D. Manocha. Efficient GPU-based solver for acoustic wave equation. Technical Report TR10-007, Computer Science, University of North Carolina at Chapel Hill, 2010.

[223] H.H. Meinke. A survey on the use of conformal mapping for solving wave-field problems. In E.C. Jordan, editor, *Electromagnetic Theory and Antennas, Part 2*, volume 2, pages 1113–1124. Permagon Press, 1963.

[224] Y.A. Melnikov and M.Y. Melnikov. Computability of series representations for Green's functions in a rectangle. *Engineering Analysis with Boundary Elements*, 30(9):774–780, 2006.

[225] S. Mendez, M. Shoeybi, S. Lele, and P. Moin. On the use of the Ffowcs Williams-Hawkings equation to predict far-field jet noise from large-eddy simulations. *International Journal of Aeroacoustics*, 12(1):1–20, 2013.

[226] W. Möhring. On vortex sound at low Mach number. *Journal of Fluid Mechanics*, 85(04):685–691, 1978.

[227] L.M. Milne-Thomson. *Theoretical Hydrodynamics*. Macmillan, New York, 4th edition, 1960.

[228] D.C. Mincu and E. Manoha. Numerical and Experimental Characterization of Fan Noise Installation Effects. *ERCOFTAC Bulletin 90, March, Special Issues in Aeroacoustics (Invited)*, pages 21–27, 2012.

[229] Brian E. Mitchell, Sanjiva K. Lele, and Parviz Moin. Direct computation of the sound from a compressible co-rotating vortex pair. *Journal of Fluid Mechanics*, 285:181–202, 1995.

[230] Adel Mohsen and Mohamed El-Gamel. On the Galerkin and collocation methods for two-point boundary value problems using sinc bases. *Computers & Mathematics with Applications*, 56(4):930–941, 2008.

[231] Anne C. Morlet, Nancy J. Lybeck, and Kenneth L. Bowers. The Schwarz alternating sinc domain decomposition method. *Applied Numerical Mathematics*, 25(4):461 – 483, 1997.

[232] Anne C. Morlet, Nancy J. Lybeck, and Kenneth L. Bowers. Convergence of the sinc overlapping domain decomposition method. *Applied Mathematics and Computation*, 98(2–3):209 – 227, 1999.

[233] A. Moroz. Quasi-periodic Green's functions of the Helmholtz and Laplace equations. *Journal of Physics A: Mathematical and General*, 39:11247, 2006.

[234] Philip J. Morris. The scattering of sound from a spatially distributed axisymmetric cylindrical source by a circular cylinder. *The Journal of the Acoustical Society of America*, 97(5):2651–2656, 1995.

[235] Philip J. Morris and F. Farassat. Acoustic Analogy and Alternative Theories for Jet Noise Prediction. *AIAA Journal*, 40(4):671–680, 2002. doi: 10.2514/2.1699.

[236] J.R. Mosig. Static Green's functions with conformal mapping and MATLAB. *IEEE Antennas and Propagation Magazine*, 45(5):123–135, 2003.

[237] S. Mu and S. Mahalingam. Direct numerical simulation of acoustic/shear flow interactions in two-dimensional ducts. *AIAA Journal*, 34(2):237–243, 1996.

[238] J.L. Mueller and T.S. Shores. A new sinc-galerkin method for convection-diffusion equations with mixed boundary conditions. *Computers & Mathematics with Applications*, 47(4–5):803–822, 2004.

[239] D.V. Nance, K. Viswanathan, and L.N. Sankar. Low Dispersion Finite Volume Scheme for Aeroacoustic Applications. *AIAA Journal*, 35(2), 1997.

[240] Susheela Narasimhan, Kuan Chen, and Frank Stenger. A Harmonic-Sinc Solution of the Laplace Equation for Problems with Singularities and Semi-Infinite Domains. *Numerical Heat Transfer, Part B: Fundamentals*, 33(4):433–450, 1998. doi: 10.1080/10407799808915042.

[241] Susheela Narasimhan, Joseph Majdalani, and Frank Stenger. A First Step in Applying the Sinc Collocation Method to the non-linear Navier-Stokes Equations. *Numerical Heat Transfer, Part B: Fundamentals*, 41(5):447–462, 2002. doi: 10.1080/104077902753725902.

[242] J.N. Newman. The Green function for potential flow in a rectangular channel. *Journal of Engineering Mathematics*, 26(1):51–59, 1992.

[243] M.K. Ng. Fast iterative methods for symmetric sinc-Galerkin systems. *IMA Journal of Numerical Analysis*, 19(3):357–373, July 1999.

[244] Z. Niu and H. Zhou. The natural boundary integral equation in potential problems and regularization of the hypersingular integral. *Computers and Structures*, 82(2):315–323, 2004.

[245] Ahniyaz Nurmuhammad, Mayinur Muhammad, and Masatake Mori. Sinc–Galerkin method based on the DE transformation for the boundary value problem of fourth-order ODE. *Journal of Computational and Applied Mathematics*, 206(1):17–26, 2007.

[246] Assad A. Oberai, Manish Malhotra, and Peter M. Pinsky. On the implementation of the Dirichlet-to-Neumann radiation condition for iterative solution of the Helmholtz equation. *Applied Numerical Mathematics*, 27(4):443 – 464, 1998.

[247] F. Obermeier. The influence of solid bodies on low Mach number vortex sound. *Journal of Sound and Vibration*, 72(1):39–49, 1980.

[248] Stefan Oerlemans, Murray Fisher, Thierry Maeder, and Klaus Kögler. Reduction of wind turbine noise using optimized airfoils and trailing-edge serrations. *AIAA journal*, 47(6):1470–1481, 2009.

[249] W.F.J. Olsman and T. Colonius. Numerical Simulation of Flow over an Airfoil with a Cavity. *AIAA Journal*, 49(1):143, 2011.

[250] N. Papamichael. Numerical conformal mapping onto a rectangle with applications to the solution of Laplacian problems. *Journal of Computational and Applied Mathematics*, 28:63–83, 1989.

[251] M.J. Park, J.K. Park, and S.W. Nam. Efficient calculation of the Green's function for the rectangular cavity. *IEEE Microwave and Guided Wave Letters*, 8(3):124–126, 1998.

[252] M.C.A.M. Peters and H.W.M. Hoeijmakers. A vortex sheet method applied to unsteady flow separation from sharp edges. *Journal of Computational Physics*, 120(1):88–104, 1995.

[253] O.M. Phillips. On the generation of sound by supersonic turbulent shear layers. *Journal of Fluid Mechanics*, 9(01):1–28, 1960.

[254] A.R. Pilon and A.S. Lyrintzis. Development of an improved Kirchhoff method for jet aeroacoustics. *AIAA Journal*, 36(5):783–790, 1998.

[255] Alan Powell. Theory of Vortex Sound. *The Journal of the Acoustical Society of America*, 36(1):177–195, 1964.

[256] C. Prax, F. Golanski, and L. Nadal. Control of the vorticity mode in the linearized Euler equations for hybrid aeroacoustic prediction. *Journal of Computational Physics*, 227(12):6044–6057, 2008.

[257] I. Proudman. The Generation of Noise by Isotropic Turbulence. *Proceedings of the Royal Society of London. Series A. Mathematical and Physical Sciences*, 214(1116):119–132, August 7, 1952 1952.

[258] N. Raghuvanshi, R. Narain, and M.C. Lin. Efficient and Accurate Sound Propagation Using Adaptive Rectangular Decomposition. *IEEE Transactions on Visualization and Computer Graphics*, 15(5):789–801, 2009.

[259] H. Ran and T. Colonius. Numerical simulation of the sound radiated by a turbulent vortex ring. *International Journal of Aeroacoustics*, 8(4):317–336, 2009.

[260] J. Rashidinia, K. Maleknejad, and N. Taheri. Sinc-Galerkin method for numerical solution of the Bratu's problems. *Numerical Algorithms*, 62(1):1–11, 2013.

[261] J. Rashidinia and M. Nabati. Sinc-Galerkin and Sinc-Collocation methods in the solution of nonlinear two-point boundary value problems. *Computational & Applied Mathematics*, 32(2):315–330, 2013.

[262] R. Reba, S. Narayanan, and T. Colonius. Wave-packet models for large-scale mixing noise. *International Journal of Aeroacoustics*, 9(4):533–558, 2010.

[263] R. Reba, S. Narayanan, T. Colonius, and T. Suzuki. Modeling jet noise from organized structures using near-field hydrodynamic pressure. In *Proceedings of the 11th AIAA/CEAS Aeroacoustics Conference, Monterey, California, USA*, 2005.

[264] E. Redon, A.-S. Bonnet-Ben Dhia, J.-F. Mercier, and S. Poernomo Sari. Non-reflecting boundary conditions for acoustic propagation in ducts with acoustic treatment and mean flow. *International Journal for Numerical Methods in Engineering*, 86(11):1360–1378, 2011.

[265] J.J. Rego Silva, H. Power, and L.C. Wrobel. Numerical Implementation of a Hypersingular Boundary Element Formulation for Acoustic Radiation Problems. In C.A. Brebbia, J. Dominguez, and F. Paris, editors, *Boundary Elements XIV: Field problems and applications*, volume 1, pages 199–216. Computational Mechanics Publications & Elsevier Applied Science, 1992.

[266] Jean-Michel Roche, Laurent Leylekian, Grégory Delattre, and François Vuillot. Aircraft Fan Noise Absorption: DNS of the Acoustic Dissipation of Resonant Liners. In *15th AIAA/CEAS Aeroacoustics Conference (30th AIAA Aeroacoustics Conference)*. American Institute of Aeronautics and Astronautics, 2009. doi:10.2514/6.2009-3146.

[267] D. Rodríguez, A. Samanta, A.V.G. Cavalieri, T. Colonius, and P. Jordan. Parabolized stability equation models for predicting large-scale mixing noise of turbulent round jets. In *Proceedings of the 17th AIAA/CEAS Aeroacoustics Conference, Portland, Oregon, USA*, 2011.

[268] V. Rokhlin. Rapid solution of integral equations of classical potential theory. *Journal of Computational Physics*, 60(2):187–207, 9/15/ 1985.

[269] V. Rokhlin. Rapid solution of integral equations of scattering theory in two dimensions. *Journal of Computational Physics*, 86(2):414–439, 2// 1990.

[270] M.T. Rose and P.R. Voke. Transition of a Flat Plate Boundary Layer due to Long Wavelength Disturbances. Technical Report ME-FD/95.45, Department of Mechnical Engineering, University of Surrey, 1995.

[271] C.W. Rowley, T. Colonius, and A.J. Basu. On self-sustained oscillations in two-dimensional compressible flow over rectangular cavities. *Journal of Fluid Mechanics*, 455(2):315–346, 2002.

[272] C.W. Rowley, T. Colonius, and R.M. Murray. POD based models of self-sustained oscillations in the flow past an open cavity. *AIAA Paper (2000-1969)*, 2000.

[273] R.D. Sandberg and L.E. Jones. Direct Numerical Simulations of Airfoil Self-Noise. *ERCOFTAC Bulletin 90, March, Special Issues in Aeroacoustics (Invited)*, pages 4–9, 2012.

[274] J.A.F. Santiago and L.C. Wrobel. Modified Green's functions for shallow water acoustic wave propagation. *Engineering Analysis with Boundary Elements*, 28(11):1375–1385, 2004.

[275] J.A.F. Santiago and L.C. Wrobel. An efficient Green's function for acoustic waveguide problems. *Communications in Numerical Methods in Engineering*, 23(7):703–719, 2007.

[276] S. Sarkar and M.Y. Hussaini. Computation of the sound generated by isotropic turbulence. Technical Report ICASE-93-74, NASA, 1993.

[277] M. Sato, S. Yoshiyoka, K. Tsukui, and Yuuki R. Accurate numerical integration of singular kernels in the two-dimensional boundary element method. In C.A. Brebbia, editor, *Boundary Elements X*, pages 279–96. Springer Berlin Heidelberg, 1988.

[278] L. Sbardella. CFD Analysis of Noise Propagation. Technical Report VUTC/C/97004, Imperial College London, London, 1997.

[279] Harry A. Schenck. Improved Integral Formulation for Acoustic Radiation Problems. *The Journal of the Acoustical Society of America*, 44(1):41–58, 1967.

[280] R. Schinzinger and P.A.A. Laura. *Conformal Mapping: Methods and Applications*. Dover Publications, Mineola, New York, 2003.

[281] R.H. Schlinker, J.C. Simonich, R.A. Reba, T. Colonius, and F. Ladeinde. Decomposition of high speed jet noise: Source characteristics and propagation effects. In *Proceedings of the 14th AIAA/CEAS Aeroacoustics Conference, Vancouver, Canada*, 2008.

[282] Johan B.H.M. Schulten. Unsteady Leading-Edge Suction Effects on Rotor-Stator Interaction Noise. *AIAA Journal*, 38(9):1579–1585, 2000.

[283] Aydin Secer and Muhammet Kurulay. The sinc-Galerkin method and its applications on singular Dirichlet-type boundary value problems. *Boundary Value Problems*, 2012(1):126, 2012.

[284] Aydin Secer, Muhammet Kurulay, Mustafa Bayram, and Mehmet Akinlar. An efficient computer application of the sinc-Galerkin approximation for nonlinear boundary value problems. *Boundary Value Problems*, 2012(1):117, 2012.

[285] A.P.S. Selvadurai. *Partial Differential Equations in Mechanics: Vol. 1 Fundamentals, Laplace's equation, diffusion equation, wave equation.*, volume 1. Springer-Verlag, New York, 2000.

[286] Tapan K. Sengupta, Manoj K. Rajpoot, and Yogesh G. Bhumkar. Space-time discretizing optimal DRP schemes for flow and wave propagation problems. *Computers & Fluids*, 47(1):144–154, 2011.

[287] Christelle Seror, Pierre Sagaut, and Alain Bélanger. A Numerical Aeroacoustic Analysis of a Detailed Landing Gear. In *10th AIAA/CEAS Aeroacoustics Conference*, Aeroacoustics Conferences. American Institute of Aeronautics and Astronautics, 2004. doi:10.2514/6.2004-2884.

[288] F. Sgard, N. Atalla, and J. Nicolas. Coupled FEM-BEM approach for mean flow effects on vibro-acoustic behavior of planar structures. *AIAA Journal*, 32(12):2351–2358, 1994.

[289] W. Shao and C.K. Mechefske. Acoustic analysis of a finite cylindrical duct based on Green's functions. *Journal of Sound and Vibration*, 287(4-5):979–988, 2005.

[290] S.C. She and Y.Y. Lu. Improved Dirichlet-to-Neumann map method for scattering by circular cylinders on a lattice. *Journal of the Optical Society of America a-Optics Image Science and Vision*, 29(9):1999–2004, 2012.

[291] Scott E. Sherer and James N. Scott. High-order compact finite-difference methods on general overset grids. *Journal of Computational Physics*, 210(2):459–496, 2005.

[292] A. Shidfar and A. Babaei. The Sinc-Galerkin method for solving an inverse parabolic problem with unknown source term. *Numerical Methods for Partial Differential Equations*, 29(1):64–78, 2013.

[293] Haiqing Si, Tongguang Wang, and Du Chen. Grid-optimized upwind DRP finite difference scheme on curvilinear grids for computational aeroacoustics. *Aerospace Science and Technology*, 15(2):90–102, 2011.

[294] Camilo Silva, Franck Nicoud, and Stéphane Moreau. Extracting the Acoustic Pressure Field from Large Eddy Simulation of Confined Reactive Flows. In *16th AIAA/CEAS Aeroacoustics Conference*. American Institute of Aeronautics and Astronautics, 2010. doi:10.2514/6.2010-3867.

[295] B.A. Singer, D.P. Lockard, and G.M. Lilley. Hybrid acoustic predictions. *Computers & Mathematics with Applications*, 46(4):647–669, 2003.

[296] Bart A. Singer, David P. Lockard, and Kenneth S. Brentner. Computational Aeroacoustic Analysis of Slat Trailing-Edge Flow. *AIAA Journal*, 38(9):1558–1564, 2000.

[297] R. Singh, J. Kumar, and G. Nelakanti. Approximate series solution of fourth-order boundary value problems using decomposition method with Green's function. *Journal of Mathematical Chemistry*, 52(4):1099–1118, 2014.

[298] B. Sjögreen and H.C. Yee. Multiresolution Wavelet Based Adaptive Numerical Dissipation Control for High Order Methods. *Journal of Scientific Computing*, 20(2):211–255, 2004.

[299] Wesley C.H. Slemp and Rakesh K. Kapania. Imposing boundary conditions in Sinc method using highest derivative approximation. *Journal of Computational and Applied Mathematics*, 230(2):371–392, 2009.

[300] R. Smith, G. Bogar, K. Bowers, and J. Lund. The Sinc-Galerkin Method for Fourth-Order Differential Equations. *SIAM Journal on Numerical Analysis*, 28(3):760–788, 1991.

[301] Ralph C. Smith, Kenneth L. Bowers, and John Lund. A fully Sinc-Galerkin method for Euler–Bernoulli beam models. *Numerical Methods for Partial Differential Equations*, 8(2):171–202, 1992.

[302] Roel Snieder, Huub Douma, and Ivan Vasconcelos. Extracting the Green's function from measurements of the energy flux. *The Journal of the Acoustical Society of America*, 131(4):EL309–EL315, 2012.

[303] Philippe Spalart and Michael Shur. Variants of the Ffowcs Williams - Hawkings equation and their coupling with simulations of hot jets. *International Journal of Aeroacoustics*, 8(5):477–491, 2009.

[304] K.P. Sridhar and R.T. Davis. A Schwarz-Christoffel Method for Generating Two-Dimensional Flow Grids. *Journal of Fluids Engineering*, 107(3):330–337, 1985.

[305] Frank Stenger. A 'Sinc-Galerkin' method of solution of boundary value problems. *Mathematics of Computation*, 33(145):85–109, 1979.

[306] Frank Stenger. Summary of sinc numerical methods. *Journal of Computational and Applied Mathematics*, 121(1-2):379–420, 2000.

[307] Masaaki Sugihara and Takayasu Matsuo. Recent developments of the Sinc numerical methods. *Journal of Computational and Applied Mathematics*, 164 & 165(0):673–689, 2004.

[308] A. Tadeu, J. Antonio, and L. Godinho. Applications of the Green functions in the study of acoustic problems in open and closed spaces. *Journal of Sound and Vibration*, 247(1):117–130, 2001.

[309] A.J.B. Tadeu, P.F.A. Santos, and E. Kausel. Closed-form integration of singular terms for constant, linear and quadratic boundary elements. Part 1. SH wave propagation. *Engineering Analysis with Boundary Elements*, 23(8):671–681, 1999.

[310] George R.C. Tai and Richard Paul Shaw. Helmholtz-equation eigenvalues and eigenmodes for arbitrary domains. *The Journal of the Acoustical Society of America*, 56(3):796–804, 1974.

[311] M Talei, M Brear, and E Hawkes. A numerical solution of Lighthill's acoustic analogy for acoustically excited laminar premixed flames. In *Proceedings of the 18th Australasian Fluid Mechanics Conference*, 2012.

[312] Christopher K.W. Tam. Jet Noise: Since 1952. *Theoretical and Computational Fluid Dynamics*, 10(1):393–405, 1998.

[313] Christopher K.W. Tam. Computational Aeroacoustics: An Overview of Computational Challenges and Applications. *International Journal of Computational Fluid Dynamics*, 18(6):547–567, 2004.

[314] Christopher K.W. Tam. Recent advances in computational aeroacoustics. *Fluid Dynamics Research*, 38(9):591–615, 2006.

[315] Christopher K.W. Tam, Nikolai N. Pastouchenko, and K. Viswanathan. Extension of the near acoustic field of a jet to the far field. *Procedia Engineering*, 6(0):9–18, 2010.

[316] Christopher K.W. Tam and Jay C. Webb. Dispersion-Relation-Preserving Finite Difference Schemes for Computational Acoustics. *Journal of Computational Physics*, 107(2):262–281, 1993.

[317] C.K.W. Tam. Computational aeroacoustics: issues and methods. *AIAA Journal*, 33(10):1788–1796, 1995.

[318] C.K.W Tam. Computational Aeroacoustics: An Overview. North Atlantic Treaty Organisation Research and Technology Organisation, 2001.

[319] C.K.W. Tam and L. Auriault. Jet mixing noise from fine-scale turbulence. *AIAA Journal*, 37(2):145–153, 1999.

[320] C.K.W. Tam and H. Ju. Finite difference computation of acoustic scattering by small surface inhomogeneities and discontinuities. *Journal of Computational Physics*, 228(16):5917–5932, 2009.

[321] C.K.W. Tam and K.A. Kurbatskii. Microfluid dynamics and acoustics of resonant liners. *AIAA Journal*, 38(8):1331–1339, 2000.

[322] C.K.W. Tam and K.A. Kurbatskii. Multi-size-mesh Multi-time-step Dispersion-relation-preserving Scheme for Multiple-scales Aeroacoustics Problems. *International Journal of Computational Fluid Dynamics*, 17(2):119–132, 2003.

[323] C.K.W. Tam, K.A. Kurbatskii, K.K. Ahuja, and R.J. Gaeta Jr. A Numerical and Experimental Investigation of the Dissipation Mechanisms of Resonant Acoustic Liners. *Journal of Sound and Vibration*, 245(3):545–557, 2001.

[324] Zhen-Huan Teng. Exact boundary condition for time-dependent wave equation based on boundary integral. *Journal of Computational Physics*, 190(2):398 – 418, 2003.

[325] M. Terracol, E. Manoha, C. Herrero, E. Labourasse, S. Redonnet, and P. Sagaut. Hybrid methods for airframe noise numerical prediction. *Theoretical and Computational Fluid Dynamics*, 19(3):197–227, 2005.

[326] Kevin W. Thompson. Time dependent boundary conditions for hyperbolic systems. *Journal of Computational Physics*, 68(1):1–24, 1987.

[327] O.K.G. Tietjens. *Fundamentals of Hydro- and Aero-Mechanics*. Dover, New York, 1957.

[328] Lu Ting and Michael J. Miksis. Exact boundary conditions for scattering problems. *The Journal of the Acoustical Society of America*, 80(6):1825–1827, 1986.

[329] Victor D. Topalian and Jonathan B. Freund. Acoustic Resonance in a Model Ducted-Jet System. *AIAA Journal*, 48(7):1348–1360, 2010.

[330] A. Torabi, A.A. Shishegar, and R. Faraji-Dana. An Efficient Closed-Form Derivation of Spatial Green's Function for Finite Dielectric Structures Using Characteristic Green's Function-Rational Function Fitting Method. *IEEE Transactions on Antennas and Propagation*, 62(3):1282–1292, 2014.

[331] Anna-Karin Tornberg and Björn Engquist. Numerical approximations of singular source terms in differential equations. *Journal of Computational Physics*, 200(2):462–488, 2004.

[332] B.E. Treeby and B.T. Cox. A k-space Green's function solution for acoustic initial value problems in homogeneous media with power law absorption. *Journal of the Acoustical Society of America*, 129(6):3652–3660, 2011.

[333] B.E. Treeby and J. Pan. A practical examination of the errors arising in the direct collocation boundary element method for acoustic scattering. *Engineering Analysis with Boundary Elements*, 33(11):1302–1315, 2009.

[334] L.N. Trefethen. Numerical computation of the Schwarz-Christoffel transformation. *SIAM Journal on Scientific and Statistical Computing*, 1:82–102, 1980.

[335] L.N. Trefethen and T.A. Driscoll. Schwarz-Christoffel Mapping in the Computer Era. Proc. Int. Congress Mathematicians, 1998.

[336] Semyon V. Tsynkov. Numerical solution of problems on unbounded domains. A review. *Applied Numerical Mathematics*, 27(4):465 – 532, 1998.

[337] Eli Turkel, Dan Gordon, Rachel Gordon, and Semyon Tsynkov. Compact 2D and 3D sixth order schemes for the Helmholtz equation with variable wave number. *Journal of Computational Physics*, 232(1):272 – 287, 2013.

[338] A. Uzun, G.A. Blaisdell, and A.S. Lyrintzis. 3-D large eddy simulation for jet aeroacoustics. *AIAA Paper (2003-3322)*, 2003.

[339] H. Vagh and A.B. Wadji. Distributed-elementary-source self-regularized dyadic Green's functions for modeling the massloading effect in acoustic devices. *Engineering Analysis with Boundary Elements*, 36(5):665–674, 2012.

[340] F. Van Herpe, D.G. Crighton, and P. Lafon. Noise generation by turbulent flow in a duct obstructed by a diaphragm. *AIAA Paper (95-035)*, (0146-3705), 1995.

[341] V. Vavrycuk. Acoustic and elastodynamic 3D Green's functions for isotropic media with a weak velocity gradient. *Wave Motion*, 31(3):223–236, 2000.

[342] E. Vergnault, O. Malaspinas, and P. Sagaut. A time-reversal lattice Boltzmann method. *Journal of Computational Physics*, 230(22):8155–8167, 2011.

[343] K. Viswanathan and L.N. Sankar. Toward the direct calculation of noise: fluid/acoustic coupled simulation. *AIAA Journal*, 33(12):2271–2279, 1995.

[344] M. Wang, S.K. Lele, and P. Moin. Computation of quadrupole noise using acoustic analogy. *AIAA Journal*, 34(11):2247–2254, 1996.

[345] M. Wang, S.K. Lele, and P. Moin. Sound radiation during local laminar breakdown in a low-Mach-number boundary layer. *Journal of Fluid Mechanics*, 319:197–218, 1996.

[346] Meng Wang, Jonathan B. Freund, and Sanjiva K. Lele. Computational prediction of flow-generated sound. *Annual Review of Fluid Mechanics*, 38(1):483–512, 2006.

[347] R. Wang. A simple orthonormalization method for stable and efficient computation of Green's functions. *Bulletin of the Seismological Society of America*, 89(3):733–741, 1999.

[348] V.L. Wells and A.Y. Han. Acoustics of a moving source in a moving medium with application to propeller noise. *Journal of Sound and Vibration*, 184(4):651–663, 1995.

[349] J. Whitmire and S. Sarkar. The computation of flow-generated sound using an acoustic analogy. *AIAA Paper (95-038)*, 1995.

[350] E.T. Whittaker. On the Functions Which are Represented by the Expansions of the Interpolation Theory. *Proceedings of the Royal Society of Edinburgh*, 35:181–194, 1915.

[351] Andreas Wilde. Calculation of sound generation and radiation from instationary flows. *Computers & Fluids*, 35(8-9):986–993, 2006.

[352] A. Witkowska, D. Juvé, and J.G. Brasseur. Numerical study of noise from isotropic turbulence. *Journal of Computational Acoustics*, 5(3):317–336, 1997.

[353] L.C. Wrobel. *The Boundary Element Method: Applications in Thermo-Fluids and Acoustics*, volume 1. John Wiley & Sons, Chichester, UK, 2002.

[354] L.C. Wrobel, J.C.F. Telles, W.J. Mansur, J.P.S. Azevedo, L.C.M. Meniconi, and F.M. Farias. A Boundary Element System for Cathodic Protection Design. In F.L.L.B. Caniero, R.C. Batista, and A.J. Ferrante, editors, *Offshore Engineering*, volume 5, pages 753–768. Pentech Press, 1985.

[355] Xionghua Wu, Wenbin Kong, and Chen Li. Sinc collocation method with boundary treatment for two-point boundary value problems. *Journal of Computational and Applied Mathematics*, 196(1):229–240, 2006.

[356] Xionghua Wu, Chen Li, and Wenbin Kong. A Sinc-collocation method with boundary treatment for two-dimensional elliptic boundary value problems. *Journal of Computational and Applied Mathematics*, 196(1):58–69, 2006.

[357] Hui Xu and Pierre Sagaut. Optimal low-dispersion low-dissipation LBM schemes for computational aeroacoustics. *Journal of Computational Physics*, 230(13):5353–5382, 2011.

[358] Toshihiro Yamamoto. Toward the sinc-Galerkin method for the Poisson problem in one type of curvilinear coordinate domain. *Electronic Transactions on Numerical Analysis*, 23:63–75, 2006.

[359] Q. Yang, Y. Wang, and M. Zhang. Calculation of propeller's load noise using LES and BEM numerical acoustic coupling methods. In C.A Brebbia and V. Popov, editors, *Boundary Elements and Other Mesh Reduction Methods XXXIII*, pages 85–97. WIT Press, Southampton, 2011.

[360] De-hao Yu. *Natural boundary integral method and its applications*. Mathematics and its applications. Kluwer Academic Publishers and Science Press, London, 2002.

[361] De-hao Yu and Longhua Zhao. Natural boundary integral method and related numerical methods. *Engineering Analysis with Boundary Elements*, 28(8):937–944, 2004.

[362] S.I. Zaman. A Comprehensive Review of Boundary Integral Formulations of Acoustic Scattering Problems. *Science and Technology Special Review*, pages 281–310, 2000.

[363] M. Zarebnia and M. Sajjadian. The sinc–Galerkin method for solving Troesch's problem. *Mathematical and Computer Modelling*, 56(9–10):218–228, 2012.

[364] X. Zhang, X.X. Chen, C.L. Morfey, and P.A. Nelson. Computation of spinning modal radiation from an unflanged duct. *AIAA Journal*, 42(9):1795–1801, 2004.

[365] Chongbin Zhao and S. Valliappan. A dynamic infinite element for three-dimensional infinite-domain wave problems. *International Journal for Numerical Methods in Engineering*, 36(15):2567–2580, 1993.

[366] Z.C. Zheng, B.K. Tan, and W. Li. On compact Green's functions and asymptotic expansions for flow-induced sound predictions. *Electronic Journal "Technical Acoustics"*, 8, 2006.

[367] B. Zhou and S.A. Greenhalgh. Composite boundary-valued solution of the 2.5-D Green's function for arbitrary acoustic media. *Geophysics*, 63(5):1813–1823, 1998.

[368] O.C. Zienkiewicz, C. Emson, and P. Bettess. A novel boundary infinite element. *International Journal for Numerical Methods in Engineering*, 19(3):393–404, 1983.

[369] O.C. Zienkiewicz, D.W. Kelly, and P. Bettess. The coupling of the finite element method and boundary solution procedures. *International Journal for Numerical Methods in Engineering*, 11(2):355–375, 1977.

[370] Y. Özyörük and L.N. Long. Progress in Time-Domain Calculations of Ducted Fan Noise: Multigrid Acceleration of a High-Resolution CAA Scheme. *AIAA Paper (96-1771)*, 1996.